Post-print note

Main results from this thesis have been summarized in the article *Ref1* listed below. This article covers part 3, 4 and partially part 6 of this thesis in a more concise way. Thank you for using this official peer-reviewed publication if reference to these parts are needed. This thesis is made accessible online since the access via DTU library was difficult. Further work from the author on the topic may be found in *Ref2* which presents an analytical tip-loss factor and study the effect of wake expansion. Simpler expressions(and typo-free) for the helical vortex filament solution presented in appendix A.2 can also be found in *Ref2*. The earlier article *Ref3* is a less detailed version than *Ref2*. Some figure references in this document may be undefined due to confidential restrictions.

- *Ref1*: Emmanuel Branlard, Kristian Dixon, Mac Gaunaa - "Vortex methods to answer the need for improved understanding and modelling of tip-loss factors" - 2013 - IET Renewable Power Generation - ISSN 1752-1416 - doi: 10.1049/iet-rpg.2012.0283
- *Ref2*: Emmanuel Branlard, Mac Gaunaa - "Development of new tip-loss corrections based on vortex theory and vortex methods". In: Proceedings of Torque 2012, the science of making torque from wind. 2012.
- *Ref3*: Emmanuel Branlard, Kristian Dixon, Mac Gaunaa - "An improved tip-loss correction based on vortex code results". In: Proceedings of EWEA 2012 - European Wind Energy Conference & Exhibition. EWEA - The European Wind Energy Association, 2012.

E. Branlard, May 2013

SIEMENS

Technical University of Denmark DTU

Master's Thesis

Wind turbine tip-loss corrections

Review, implementation and investigation of new models

Emmanuel Branlard

September 2011

Risø DTU
National Laboratory for Sustainable Energy

Master's Thesis

Wind turbine tip-loss corrections

Review, implementation and investigation of new models

Emmanuel Branlard

September 2011

Wind turbine tip-loss corrections
Review, implementation and investigation of new models

Author	Emmanuel Branlard (s090961)
Supervisors	Mac Gaunaa (Risø-DTU) Kristian Dixon (Siemens) Kevin Standish (Siemens)

Time Period	April 18th - September 30th
Firt Release Date	September 30th
Edition	09/05/2013
Category	Partially confidential
Comments	This report is part of the requirements ro achieve the Master of Science in Wind Energy at the Technical University of Denmark.
Credits	30 ECTS

Risø National Laboratory
Technical University of Denmark
P.O.Box 49
DK-4000 Roskilde
Denmark
Tel: (+45) 4677 4004
Fax: (+45) 4677 4013
www.risoe.dk

Risø DTU
National Laboratory for Sustainable Energy

Siemens Energy Inc.
Renewables - Wind
1050 Walnut St. - Suite 303
Boulder, Co 80302
USA
Tel: (+01) 303 895 2100
Fax: (+01) 303 895 2101
www.energy.siemens.com

SIEMENS

Abstract

The focus of this study is the use of a lifting-line free wake vortex code to derive tip-loss corrections that could be implemented in Blade Element Momentum (BEM) codes. The different theories and three dimensional effects that are related to tip-losses are progressively introduced: lifting-line concepts, wake dynamics and its vortex modelling, far-wake analysis. The different tip-loss corrections found in the literature are reviewed with a focus on the main theories, namely the work of Betz, Prandtl, Goldstein and Theodorsen, and the different implementations in BEM codes found in the literature are presented. The method of Okulov to compute Goldstein's factor at a reasonable computational cost is provided with details. The computation of Goldstein's factor being accessible, a method to use this factor in the BEM method is presented. Various form of Prandtl's tip-loss factor are also listed for reference. Tip-losses are investigated using a free wake vortex code and with Computational Fluid Dynamics(CFD), and results from both approaches are compared and discussed. For the use of CFD data, the question of definition of the local induction factor on the blade is risen and different method to define it are investigated. The author introduces the naming of "performance tip-loss" factor, which is a correction to the airfoil coefficients due to the tri-dimensionality of the flow at the tip. A preliminary model for the performance tip-loss function is introduced. For the representation of various circulation shapes, a new method using the formulation of Bézier curves is described and developed. Such method can be widely used to describe curves such as lift, circulation or chord distribution. Last, a method to determine tip-losses using a vortex code is described and implemented. From this method, a new tip-loss model is implemented in a BEM code in order to reproduce the 3D effects inherently present in a vortex code.

Contents

Introduction

Context and motivations Early investigations of wind turbine performances revealed that the power produced was lower than the one expected by the blade element momentum theory, the production was as if the size of the rotor had been reduced in a proportion of approximately 3%. The main reason for this power loss is the circulation of flow around the tip of the blade which is a well known phenomenon in the study of aircraft wings where a vortex is emitted at the extremity of each wing. These vortices are commonly known as they can be observed under some particular pressure and humidity characteristics of the air. At the beginning of the 20$^{\text{th}}$ century, Prandtl was among the first to investigate the losses accounted by these vortices for a wing and later for a propeller. The losses appear for the former when the wing has a finite span, and for the later when the rotating devises has a finite number of blades. Prandtl's research led to the introduction of a tip-loss factor which is now widely used in wind turbine aerodynamic codes to account for the tip-losses. The load reduction at the tip due to this effect has a dramatic influence on the produced power because the tip being at a great distance to the hub it has the possibility to generate a lot of torque by a simple lever arm rule. Summing up over the entire range of operation of a wind turbine these losses can represent a reduction of 10% on the Annual Energy Production. A proper blade design can reduce the power losses and thus increase the productivity of the blade but this require of course a better understanding of tip-losses. It is the purpose of this document to focus on this aspect.

Approach description The notion of tip-losses requires for its understanding a wide picture of the different theories applied to wind turbines but also general notions of wing and wind turbines 3D aerodynamics. Historically, tip-losses appeared in the context of investigation of optimal propellers with an important contribution from authors of the German school: Prandtl, Betz, and Goldstein. Glauert in a later work applied these notions and integrated them into a wind turbine performance prediction algorithm called the Blade Element Momentum(BEM) theory. The formulations and notions of these theories will be presented in this study. A pragmatic approach will have to be taken when studying the different tip-loss functions and their implementations for they have and are still rising debates in the scientific community. These foundations established, tools like vortex codes and Computational Fluid Dynamics (CFD) will be used to investigate further the notion of tip-losses and possibly improve the performances of BEM codes.

Content This document is structured with a succession of six chapters which follow the approach mentioned in the above paragraph. All chapters are progressively built upon each other, except for chapters 4 and 5 that can be read in different order. Different chapters were placed in appendices for a clearer and smoother reading, despite the fact that a large part of the corpus rely on them. In a first chapter, the different theories and three dimensional effects that are connected to tip-losses are progressively introduced. In a second time, the different tip-loss corrections found in the literature are reviewed with a focus on the main theories and their implementations. The next chapters both investigate tip-losses using a specific code. The focus of this study was to use a vortex code to derive tip-loss corrections that could be implemented in BEM codes. The study of CFD data give rise to more discussion and interesting results comparisons which be summarized in a final chapter.

Contribution from this work The different aspects on which this study contributes to existing work on the matter of tip-losses can be listed as follow:

- This document is the first one to the author's knowledge to be entirely dedicated to wind turbine tip-losses. Along this line, a listing of all the different tip-loss corrections implemented was performed and important distinctions were made.
- In this study, a new method to determine tip-losses using a vortex code has been described and implemented. From this method, a new tip-loss model was implemented in a BEM code in order to reproduce the 3D effects inherently present in a vortex code.
- A method to fit curves using the formulation of Bézier curves was described and developed. Such method can be widely used to describe curves such as lift, circulation or chord distribution.
- The author introduced the naming of "performance tip-loss" factor, which is a correction to the airfoil coefficients due to the tri-dimensionality of the flow at the tip. Such corrections have been investigated for instance in [98] in a slightly different way. A model for the performance tip-loss function is introduced in Sect. 5.2.6.
- In Appendix A, a detailed description of Goldstein's article from 1929[36] can be found. This article is generally considered as a complex article so that the details presented in this report is intended to help the curious reader to go quickly through this essential reference on the topic of tip-losses.
- In Sect. A.2, the method of Okulov[79] to compute Goldstein's factor at a reasonable computational cost is provided with more details than in the original article in order to share it.
- Eighth order polynomial that fits Goldstein's factor for different operating conditions are also provided in Sect. A.4.
- The computation of Goldstein's factor being accessible, a method to use this factor in the BEM method was presented in Sect. 3.4.1.
- Analysis from [43] and [48] use CFD to investigate the axial induction. In this study similar analysis were performed with focus this time on the tip-loss factor.
- Along the same line than the point above, the question of definition of the local induction factor a_B on the blade was risen. Different method to define it were investigated in Sect. 5.1
- All the figures are done with the wind turbine convention, rotating clockwise and with a relative wake velocity in the opposite of the stream direction. When studying the theory of helical wakes, most references uses different or inconsistent conventions.

About this document This document was entirely written by the author. All the figures present in this document are from the author, either drawn or generated using Matlab or Mathematica. If a figure was inspired by others a reference is mentioned. The author borrowed figures from his own previous work, mainly[15]. All references cited in this document have been consulted by the author except for the following which were not available[90][68][91][16][89][45][95][21]. This document was written in LaTeX using a template from the author. The paper size chosen is A4.

Notations

Lower case letters

a	Axial induction factor
a'	Tangential induction factor
a_B	Axial induction factor local to the blade
$\hat{a}$	Axial induction factor from 2D momentum theory
$\overline{a}$	Azimuthally averaged axial induction factor
c	Chord
h	Helix pitch
h_B	Apparent pitch h/B
$\overline{h}$	Normalized pitch h/R
l	Helix torsional parameter
$\overline{l}$	Normalized torsional parameter l/R
n_{rot}	Rotational speed in revolutions per second: $\Omega/(2\pi)$
p	Static pressure
r	Radial position along the blade
$\overline{r}$	Dimensionless radial position r/R
s	Normal distance between two vortex sheets
u_{i_θ}	Tangential induced velocity
u_{i_z}	Axial induced velocity
w	Wake relative longitudinal velocity
z_0	Surface roughness length

Upper case letters

A	Area
AR	see Abbreviations
B	Number of blades
C_Γ	Dimensionless circulation
C_d	Drag coefficients
C_l	Lift coefficients
C_n	Normal component of the aerodynamic coefficients
C_p	Power coefficient
C_Q	Torque coefficient
C_t	Tangential component of the aerodynamic coefficients
C_T	Thrust coefficient
D	Drag force
D	Rotor diameter
F	Tip-loss factor
F_a	Tip-loss factor based on axial induction
F_Γ	Tip-loss factor based on circulation
F_{C_l}	Performance tip-loss factor
F_{Go}	Goldstein's tip-loss factor
F_{Gl}	Glauert's tip-loss factor
F_{Pr}	Prandtl's tip-loss factor
F_{Sh}	Shen's tip-loss factor
I_t	Turbulence intensity
L	Lift force
P	Power

Q	Rotor torque
R	Rotor radius
S	Rotor surface
T	Thrust force
U	Longitudinal velocity at the rotor in 1D
$\boldsymbol{U}$	Relative velocity at the rotor
U_0	Longitudinal velocity far upstream
U_i	Induced velocity in 1D
U_n	Velocity normal to the rotor
U_t	Velocity tangent to the rotor
U_w	Longitudinal velocity in the far wake in 1D
V	Velocity vector
V_n	Normal velocity in the far wake
V_{r}	Rotor velocity Ωr
V_{rel}	Relative velocity
V_t	Tangential velocity in the far wake
$\boldsymbol{W}$	Induced velocity vector at the rotor

Lower case Greek letters

α	Angle of attack
β	Twist angle
γ	Distributed circulation
ϵ	Pitch angle of the wake helix screw
$\varepsilon_{l/d}$	Lift-over-drag ratio
η	Efficiency
θ	Azimuthal coordinate in polar coordinates, same as ψ
κ	Goldstein's factor
λ	Tip speed ratio $= \Omega R/U_0$
λ_r	Local speed ratio $= \lambda r/R$
μ	Dynamic viscosity [kg m^{-1} s^{-1}]
ν	Kinematic viscosity $= \mu/\rho$ [m^2 s^{-1}]
ρ	Air density ≈ 1.225 kg/m^3
σ	Local blade solidity $= Bc/2\pi r$
τ	Shear stress
ϕ	Flow angle
ψ	Azimuthal coordinate, positive with the rotor rotation, same as θ
ω	Rotational speed of the wake

Upper case Greek letters

Γ	Circulation [m^2 /s]
Φ	Velocity Potential
Ψ	Stream function
Ω	Rotational speed of the rotor

Abbreviations

1D	One dimension
2D	Two dimensions
3D	Three dimensions

AD	Actuator Disk
AEP	Annual Energy Output
AR	Aspect ratio of a wing: length squared divided by its surface
BEM	Blade Element Momentum
BET	Blade Element Theory
CFD	Computational Fluid Dynamics
DOF	Degree of Freedom
IEC	International Electrotechnical Commission
MT	Momentum Theory
VL	Vortex Lattice
WS	Wind speed
WD	Wind direction
WT	Wind Turbine
LSS	Low Speed Shaft
HSS	High Speed Shaft

Chapter 1

Tip-losses: context and challenges

1.1 Tip-losses in the historical context of wind turbine aerodynamics

The origin of the most common tip-loss correction, Prandtl's correction, comes from the broader problem of loss minimization for lifting devises. An historical review of the topic will reveal the intellectual path followed by the scientists at the beginning of the 20th century with the study of problems of growing complexity, while also shedding light on the different theoretical tools available and on the assumptions under which they operate. The problem is first taken as the determination of induced power losses in general to further focus on the tip-loss aspects only. Notions of local aerodynamics of the blade will be required to understand how tip-losses can affect the angle of attack and the airfoil performances. The tip-loss factor will be defined in Sect. 1.3 where preliminary considerations on this challenging topic will be introduced.

1.1.1 Losses inherent to a rotating extracting device

1D momentum theory - Rankine-Froude's theory The 1D momentum theory is the simplest method to assess the induced power losses. It's derivation has been obtained by R. Froude[29] from the discussions and contributions of Rankine[89] and W.Froude[30]. In this theory the flow is assumed to be purely axial with no rotational motion and the induced velocities at the rotor are uniform over the whole swept area. The rotor is replaced by the concept of an actuator disk, which is responsible for creating an artificial pressure drop while allowing the flow to be continuous through it. The actuator disk can be seen as two contra-rotative rotors with infinite number of blades but no details on the actual energy extracting device are used and its rotation is not even implied. The flow slows down to a velocity $U_0 - u_i$ at the rotor disk across which it releases momentum due to the pressure drop created by the actuator disk. The flow returns to its original pressure far downstream where it has eventually reached a velocity of $U_0 - 2u_i$ according to Bernoulli's theorem and the conservation of mass. The accurate demonstration of this result needs to take into account the pressure force on the streamtube. The proper way to derive the result is to consider it as the limit of a finite case where either the streamtube is in an channel[35][38], either it is pressure-constrained at its boundary[38], and then expand the walls to infinity. Most authors ignore this problem or implicitly add another assumption to this theory by using the fact that: the streamtube is surrounded by atmospheric pressure, or the longitudinal velocity in the by-pass flow is equal to the infinite velocity[42].

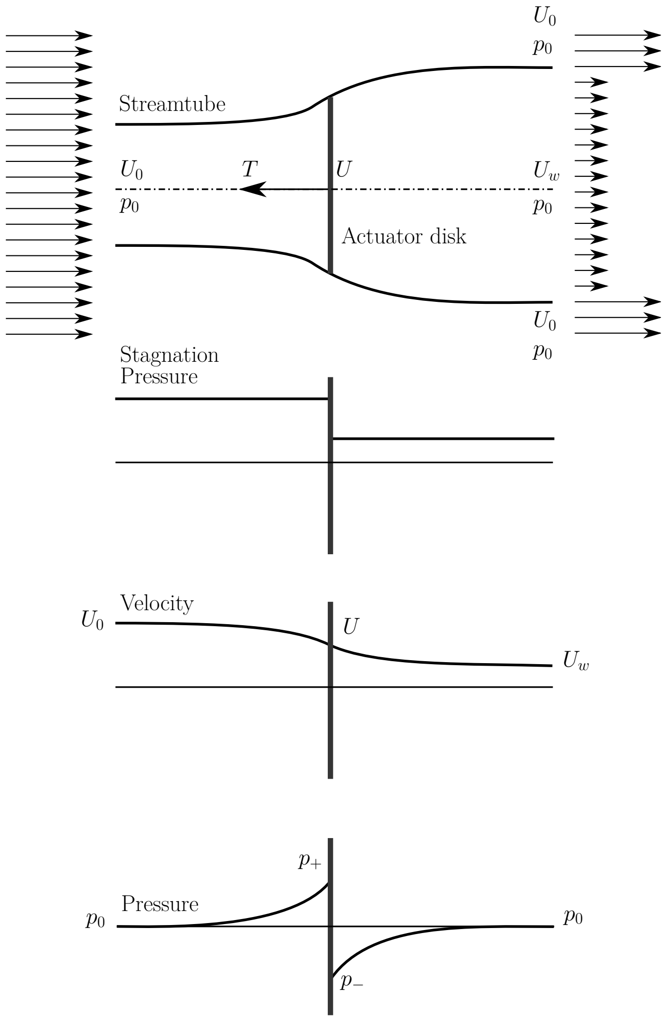

Figure 1.1: One dimensional momentum theory.

Parallel work down within 5 years from the authors Lanchester[58, (1915)], Joukowski[1][51, (1920)] and Betz[10, (1920)], led to the theoretical limit of power than can be extracted: the Betz-Joukowski limit[2] with a value of power coefficient of 16/27. It should be noted that some authors found that the power coefficient tends to infinity for low tip speed ratio but it has been argued[104] that this is the result of neglecting the pressure forces on the streamtube for highly-loaded rotors. Below, it will be seen that the theoretical Betz-Joukowski limit has to be reduced in practice while releasing assumptions from the momentum theory.

2D momentum theory The 2D momentum theory as derived by Joukowski[50] in 1918, reported by Glauert[35] in 1935 and further formalized in 2010 by Sørensen and van Kuik[104] uses an actuator disk that impart a pressure drop and a tangential rotational speed to the fluid without discontinuity in the axial and radial flow passing the disk. No friction losses are considered in this theory which is why the rotation of the flow has to be introduced artificially by the actuator disk and also why the rotational velocity in front of the disk is zero. This theory allows for radial variations of velocities and pressure at the rotor and at the wake, and accounts for pressure changes due to wake rotation. Nevertheless the theory leads to a system of equations which is not closed. Either two variables needs to be given or assumptions made to simplify the theory. The Joukowski model uses the assumption of constant circulation, which imply that the flow is irrotational everywhere except along the axis of rotation and that the rotational momentum of the slipstream in the wake ωr^2 is constant for each radial elements. Under this assumption, it is found that in general the axial induced velocity in the wake is not twice the one at the rotor. Nevertheless, the results get really close for tip speed ratio above 2. To avoid inconsistency near the rotor center, a Rankine vortex core can be used instead of a line vortex for a better representation of the flow[104]. In this case, the equations become more complex, but still lead to a closed form solution.

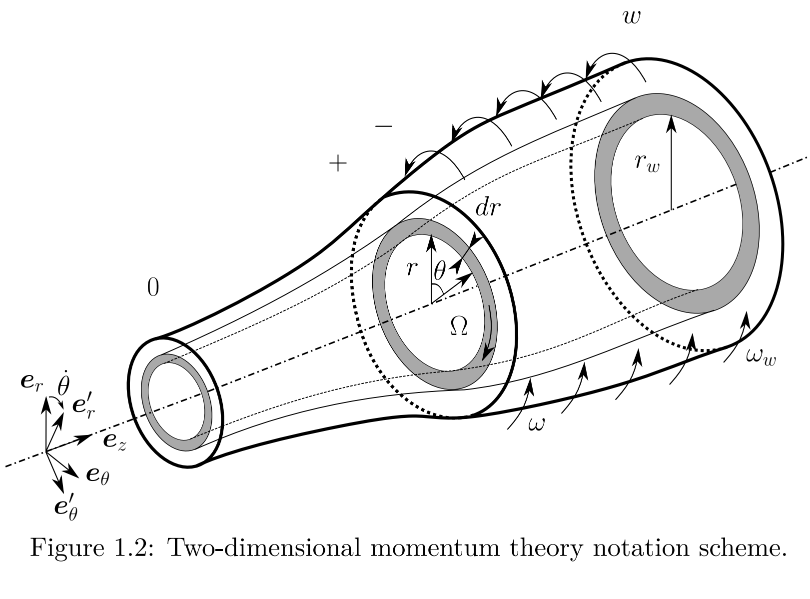

Figure 1.2: Two-dimensional momentum theory notation scheme.

Simplified equations are obtained by adding the assumption that the rotor is lightly loaded and the rotation of the wake is small compared to the rotational speed of the rotor. This can be interpreted as the pressure in the far wake equals the pressure upstream. Consequently the thrust and axial induction results from the 1D momentum apply and the tangential axial induction factor can be determined as a function of the local speed ratio and the axial induction factor. This relation is often drawn as a velocity triangle and can also be interpreted as an energy equation. The final

[1] Nikolai Egorovich Zhukovsky, different writing of this name can be found when using latin alphabet.

[2] In 2007[113] the naming Lanchester-Betz-Joukowski limit was suggested, but further historical research[81] attributed this result to the independent work of Betz and Joukowski.

equations resulting from the use of 2D momentum theory results linked to 1D momentum results will be further referred to as “simplified-2D momentum theory”. It should be kept in mind that only under the assumption of this simplified theory holds the fact that the induced velocity in the wake is twice the one at the rotor.

1.1.2 Introducing notions used for the study of three dimensional effects

Limitation of momentum theory The methods mentioned above do no fully capture the variations of the flow nor the physics of the energy extraction device. The momentum theory gives an upper limit for the maximum power that can be extracted from the flow but does not give indication on the design of the device itself. Also the assumption of uniform induced velocity at the rotor used in the momentum theory does not hold for a real flow where three dimensional effects takes place and the rotor obviously does not have an infinite number of blades. One example of these effects in the appearance of vortices at the tip of a finite span wing as described among the following paragraphs. Tip-vortices have been first investigated for aircrafts by Prandtl who derived the lifting line theory to determine the losses related to this vorticity.

Simulation of actuator disks Under the 1D and simplified-2D momentum theory, the inductions factors are assumed uniform over the entire disk. The validity of these assumptions were studied using computational fluid dynamic tools to model the actuator disk[103, 67, 73, 66]. Results from these analysis showed that the axial velocity was underestimated(a overestimated) in the inner part of the disk due to the neglecting of the pressure term from wake rotation. On the outer part of the blade the axial velocity is overestimated(a underestimated) due to the neglecting of the radial expansion of the streamtube. The assumption of uniform axial induction factor is thus not valid, and it will be expected to be, among others, a function of the radius:

$$a = a(r, \dots) \tag{1.1}$$

Such variations are captured by the general 2D momentum theory in which the axial induction is purely a function of radius, written in this document $\hat{a} = \hat{a}(r)$. Despite this radial-dependency, it is worth mentioning that using both a simple vortex model and a actuator disk model, it has been found[110] that each annular element seem to behaves locally as predicted by the 1D momentum theory, meaning that in a first approximation each annular strip can be reasonably considered independent.

Finite number of blades The concept of actuator disk used previously is equivalent to the assumption of infinite number of blades, which is that all particles passing through the disk will experience the same change of momentum due to the presence of the blades. This no longer holds for a rotor with a finite number of blades for which the local axial induction will be larger close to the blades than in between the blades. As a result of this, an azimuthal dependency of the axial induction factor should be accounted for on top of the radial dependency mentioned in the above paragraph, viz.

$$a = a(r, \psi, \dots) \tag{1.2}$$

The local induction factor at the blade which characterize the incoming speed on the blade and thus determine the local aerodynamic load is written distinctively a_B. The average axial induction factor $\overline{a}(r)$ is defined as:

$$\overline{a}(r) = \frac{1}{2\pi}\int_0^{2\pi} a(r,\psi)d\psi \qquad [\text{ - }] \tag{1.3}$$

In the case of infinite number of blade a_B and $\overline{a}$ are the same. Axisymmetric flows, i.e. flow azimuthally independent such as the one described by 2D momentum or 2D vortex theories can only be found for wind turbines with infinite number of blades. With finite number of blades, these theories no longer apply but are still used in BEM codes by introduction of a "tip-loss factor" (see discussion on Sect. 1.3 and Sect. 3.2).

Tip vortex Complex aerodynamic laws[3] causes pressure differences to arise between the two sides of an airfoil which in turn result in aerodynamic forces. The low pressure upper surface is called the suction side and the lower surface the pressure side. The pressure difference has to vanish if no airfoil is present so that pressure equalization between the pressure and the suction side should occur at the extremity of any lifting surface such as an aircraft wing or a wind turbine blade. This causes a spanwise pressure gradient so that the flow from the lower surface will go around the blade tip to reach the upper surface generating a vortex known as a tip-vortex. The higher the loading, the higher the pressure gradient and hence the intensity of the tip-vortex. The pressure gradient will imply a radial motion with the flow from the lower surface having a radial component heading towards the tip while the flow from the upper surface will go in the other direction. This is illustrated on Fig. 1.3, and CFD results example are shown in Sect. D.4.

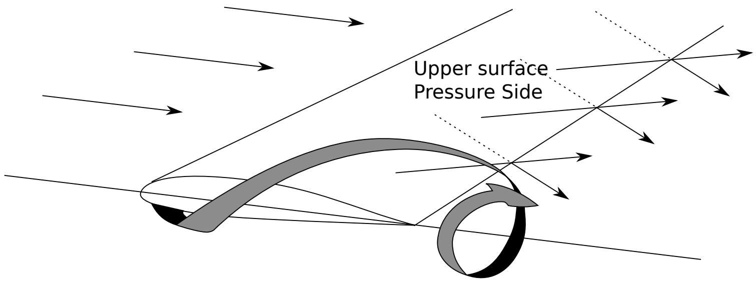

Figure 1.3: Tip-vortex formation and radial flow on the upper and lower surface at the tip. The flow from the upper surface has a radial component towards the root, while the flow from the pressure side is directed towards the tip.

When meeting at the trailing edge the flow from the two surfaces reaches a common axial velocity but keeps this radial difference of velocity. This jump in tangential velocity has to be associated with a vortex sheet which is known to have the properties of such discontinuity surface. This vortex sheet is formed at the trailing edge and for this reason will be referred to as trailing vorticity. The tangential velocities stay discontinuous across this sheet whereas the pressure is continuous. The intensity of this vortex sheet is directly related to the jump of tangential velocity:

$$[\![V_t]\!] = \boldsymbol{\Gamma} \times \boldsymbol{n} \tag{1.4}$$

In fact, the tip-vortices observed are the result from the roll-up of the vortex sheet which occur under the influence of the induced velocities created from the whole vortex sheet. The notion of induced velocity will be developed below.

Vortices in the context of potential flow Under the assumption of incompressible and irrotational flow, the equations of motion reduce to the well known Laplace's equation where the velocity is expressed by a potential. Among the particular solutions from this equation lay the vortex, source and doublet solutions. The linearity of Laplace's equation implies that any potential flow can be described as a combination of these elementary solutions if properly distributed to satisfy the boundary conditions. This makes the foundations for numerical vortex methods. For profiled bodies under small angles of attack, separation can be omitted and the assumptions of potential flow can be used to determine the lift force. Vortices in viscous flow will be discussed in section Sect. 1.1.6.

[3]Laws that does not involve wrong assertions such as "upper and lower paths have different lengths". Rigorous understanding of lift can be found in[11]

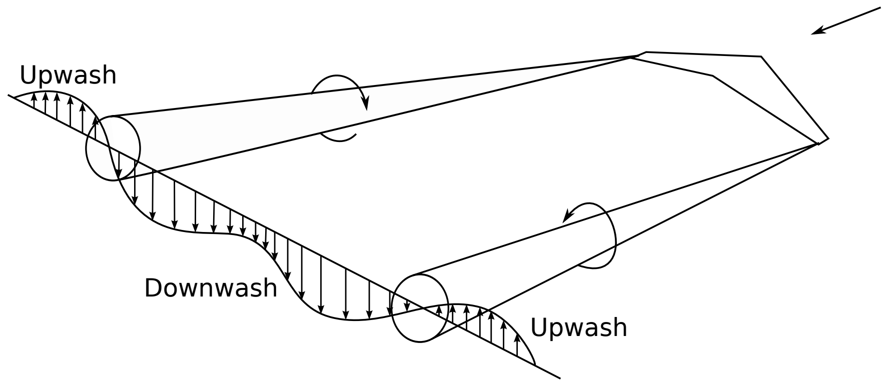

Figure 1.4: Formation of tip vortices at the tip of a wing and resulting induced velocities in the wake.

Notion of induced drag

Kutta-Joukowski relation At this stage it is required to introduce the Kutta-Joukowski relation which is extensively used in aerodynamics. This relation strictly applies to potential flows but is commonly used in the presence of viscosity as well in a fashion described below. The Kutta-Joukowski theorem named from the two authors who developed it independently at the beginning of the 20^{th} century, states that the force per unit of span at a given point is related to the velocity and the circulation around this point:

$$\boldsymbol{L} = \rho \boldsymbol{V}_{\text{rel}} \times \boldsymbol{\Gamma} \qquad [\text{N/m}] \tag{1.5}$$

This direct relationship between lift and circulation is the foundations for lifting line theories where the airfoil is replaced by a vortex filament. The assumptions of the Kutta-Joukowski relation are often relaxed and the frictional Drag is introduced[4]. The force obtained from the Kutta-Joukowski theorem contributes fully to the lift. The drag is calculated if the lift over drag ratio $\varepsilon_{l/d}$ of the airfoil is known. The drag has the same direction as the incoming flow and is obtained as:

$$\boldsymbol{D} = \frac{\|\boldsymbol{L}\|}{\varepsilon_{l/d}} \frac{\boldsymbol{V}_{\text{rel}}}{\|\boldsymbol{V}_{\text{rel}}\|} = \frac{1}{\varepsilon_{l/d}} \rho \Gamma \boldsymbol{V}_{\text{rel},} \qquad [\text{N/m}] \tag{1.6}$$

In the above the velocity V_{rel} refers to the velocity projected into the cross sectional plane of the airfoil.

Biot-Savart law The Biot-Savart law is named after the two scientists who developed it in 1820 for application in induction in electromagnetism. It also applies for aerodynamics to determine the velocity induced by a vortex distribution. This law is obtained from the classical resolution of Poisson's equation by convolution with the Green function. The velocity field produced at the point $M(x, y, z)$ by a volumic vortex distribution γ in a domain Ω is found as:

$$\boldsymbol{u_i}(M) = \frac{1}{4\pi} \cdot \int_{\Omega} \frac{\boldsymbol{\gamma} \times \boldsymbol{M_0 M}}{\|\boldsymbol{M_0 M}\|^3} d\Omega(M_0) \tag{1.7}$$

Notion of induced velocity The finite span of a wing generates vorticity which propagates in the wake. The term "induced velocity" is used to refer to the part of the total velocity field which is different from the uniform infinite velocity upstream. In potential flows, this field can be associated for instance with a distribution of sources and vortices. There is a complete equivalence between the knowledge of the distribution of sources and vortices and their associated wind field. There is thus no cause and effect relationship between them, so that the term "induced" is considered by some authors inappropriate[25]. This notion is found in 2D unsteady flow where vorticity is shed and in three dimensions due to the formation of a wake. It is introduced artificially to highlight the differences with 2D steady flow.

[4]The Pressure drag is zero in potential flow, which is D'Alembert's paradox.

In three dimensional flow the wake induces a downwash[5] velocity at any radial position of the wing so that the local angle of attack is reduced compared to the one expected if calculated from the infinite upstream velocity. The actual lift can thus be seen as rotated accordingly downstream and if projected on the direction of the upstream velocity, a force component colinear with the upstream velocity is found. This force is called drag induced by the lift in aircraft terminology, it can represent up to 80% of the total drag in climb and account for about 40% of the fuel used in a commercial planes[57]. Figure 1.5 illustrates how the component of the lift induces drag due to the downwash.

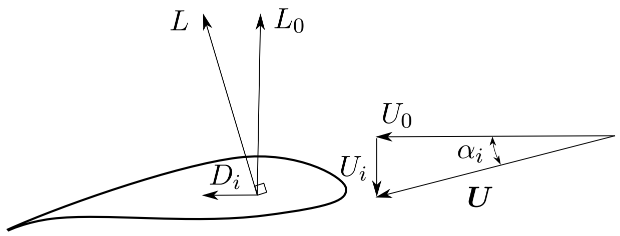

Figure 1.5: Illustration of the notion of induced drag

Loss minimization The apparition of losses due to three dimensional effects raises the challenge of minimizing these losses. For this reason many investigations have been carried out in order to find the optimal lift or circulation distribution that would minimize the induced loss for a wing, a propeller or a rotor. The theoretical work concerning wings is attributed to Prandtl[86] and Munk[76], for propellers and air-screw to Betz[9], Prandtl(in the appendix to Betz article), and Goldstein[36]. Later, minimum induced losses for wind mills, propellers and helicopters has been investigated by Larrabee[59] and is still studied with new numerical methods[19]. The motivation for these investigation is that the losses can be minimized for a given thrust if an efficient circulation distribution is present at the rotor, and thus if an efficient design is implemented.

1.1.3 Description of the wake dynamics

In this section three dimensional effects which concerns the structure and dynamics of the wake that forms behind a turbine is presented. The description of 3D aerodynamic effects which affects the performance of the blade airfoil locally is discussed in a separate section (Sect. 1.2). References in aerodynamics appreciated by the author are [12] and [46]. For specific 3D wind turbine aerodynamics the following references can be used [17, 70, 42] which are in turn highly inspired by the work of Glauert[35].

Generality for wings To describe precisely the vorticity system associated with a wing, the distinction between bound, trailed and shed circulation is to be done. As seen from the Kutta-Joukowski theorem in Eq. (1.5), the lift from a wing is associated with a circulation around the airfoil called *bound circulation* and further noted Γ. In stationary flow, this bound circulation corresponds to the starting vortex generated when the upstream flow started its motion according to Kelvin's theorem. Due a consequence of Helmotz's theorem stating that vortex line going along the wing span cannot end in the fluid, the vorticity associated to this circulation has to be trailed into the wake from the trailing edge and the wing extremities(the blade root and the tip for a rotor). This streamwise component of vorticity emanating from the airfoil is referred as *trailed vorticity*. If the circulation is constant along the wing span, vortices are trailed only from wing

[5]In aerodynamics the notion of downwash or upwash is relative to the lift and not the vertical. A downwash velocity is a velocity in opposite direction of the lift.

extremities, whereas if the circulation varies along the blade span, trailing vortices are created from each radial position r forming a continuous vortex sheet. The strength per unit of length of the trailed vorticity is directly equal to the bound circulation's gradient which writes:

$$\Gamma_t(r) = -\frac{\partial \Gamma(r)}{\partial r} dr \qquad [\mathrm{m}^2/\mathrm{s}] \tag{1.8}$$

For a real flow, the bound circulation gradient along the span will obviously be present because the circulation has to vanish continuously at the wing extremities. As a result of this, the strength of the vortex sheets usually increases towards the wing extremities where the circulation gradient is expected to be the highest. These higher intensities of trailed vorticity at the tip will induce a roll-up of the wake into concentrated tip-vortex. Prandtl neglected this roll-up to develop his lifting-line theory where the blade was modelled as a superposition of horseshoe vortices laying on the wing and expending towards infinity.

The last form of vorticity found is the one generated by time variations of the bound circulation which shed spanwise vorticity in the wake. This *shed circulation* is directly related to the change of vorticity on the blade as:

$$\Gamma_s(r) = \frac{\partial \Gamma(r)}{\partial t} dt \qquad [\mathrm{m}^2/\mathrm{s}] \tag{1.9}$$

The vorticity sheets are convected downstream with the wake velocity. According to Biot-Savart law, the distributed vorticity from the wake and the blade induces a velocity field in the domain. In particular this field acts on the fluid particle of the wake sheet which then tends to roll-up into concentrated tip-vortex as it propagates downstream. It should be noted that in potential flow, there can be no flow through these surfaces and they can be considered impermeable. An illustration inspired and adapted from [93] of the different type of circulations involved is found on Fig. 1.6. The above discussion is valid for rotary wings, but the structure of the wake is more complex and will deserve more attention in the following.

Rotor wake specificity For a rotating wing, the vorticity structures are mainly transported downstream in the axial direction and because they are continuously shed from different azimuthal location due to the rotation of the rotor the resulting wake shape "looks" helical. The influence of the wake on itself will distort the wake shape so that the wake does not hold its nominal helical shape. For instance, the edges of the vortex sheet roll up into concentrated tip vortices. For simplicity this roll-up can be ignored, as for the propeller case for instance where the high axial velocity in the streamwise direction transport the wake quickly downstream. For airplane propeller and helicopters the induced velocities are often small compared to the speed of flight but this is not the case for wind energy applications in which they are appreciable and moreover opposite to the streamwise direction. As the wake propagates downstream, the distance between the different vortex sheets tend to decrease while the wake radius expands. The stability of the wake is quite complex and depends mainly on the loading of the rotor. The loading can be related to the thrust coefficient, which in turns is related to the inductions factors and the tip speed ratio. Studies of wake stability can be found in [78], but in all theoretical derivations presented in this study the wake is assumed stable.

Lightly-loaded assumption When a rotor is lightly-loaded it is argued that the wake expansion behind the rotor is small and so is its distortion. When the assumption of lightly-loaded rotor is made, it thus implies no wake expansion and distortion, so that the wake shape is a perfect helix held in a cylinder with periodicity between the vortex sheet. For applications where the thrust coefficient is low(usually high wind speed, low tip-speed ratio), the lightly-loaded assumption is often used for its convenient simplicity.

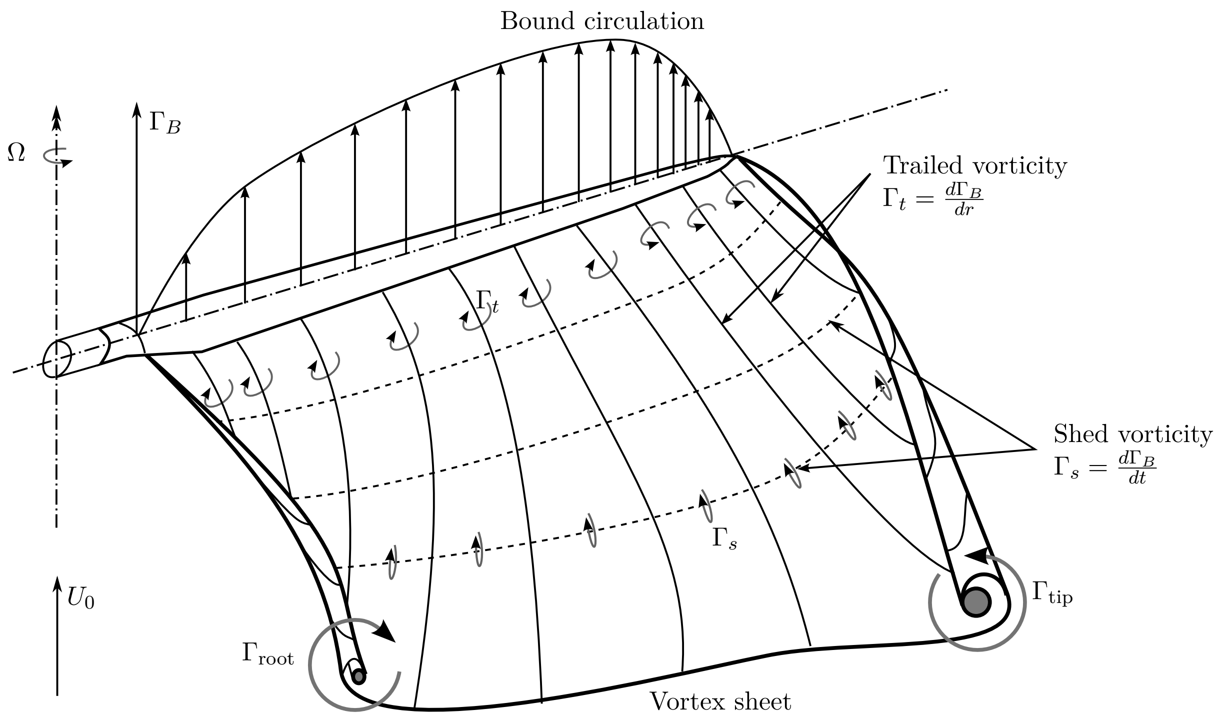

Figure 1.6: Vortex sheet forming behind a wind turbine blade. The variation of bound circulation along the span generates trailed vorticity, while its time variation generates shed vorticity. The influence of the vortex sheet on itself induces a roll-up of the sheet at the root and the tip which concentrates into a tip and root vortex.

Constant circulation The case of an hypothetical rotor uniformly loaded with hence a constant circulation along its blades is sometimes referred as the Joukowski's model. In this case a single vortex is continuously emitted from the tip and from the root. This can be understood by looking at the ill-definition of Eq. (1.8) at the blade extremities. In this simplified model, the discontinuity of circulation at the tip will induce an infinite downwash at the tip. An illustration of the hypothetical vortex system that would exist in this case can be seen on Fig. 1.7 where the hub radius is assumed to be zero. For a simple aircraft made of two symmetric wings joined together, the bound circulations of the wings are equal and have the same sign. There is thus no discontinuity of circulation and hence no vorticity is trailed at the junction between the two wings. For a two-bladed wind turbine(with or without hub) the bound circulation on each blade has opposite sign so that vorticity is trailed at the root. In case where the hub radius is zero, the root vortices are trailed along the rotor axis in a straight line with intensity:

$$\Gamma_{\mathrm{axis}} = -B\,\Gamma_{\mathrm{blade}} = -B\,\Gamma_{\mathrm{tip}} \tag{1.10}$$

The tip-vorticity line convects downstream with the wake velocity forming an helix of constant pitch and radius. If the hub radius is none zero, then B vortex lines of intensity Γ_{blade} are emitted at the root and convects downstream in a helical shape.

For a wind turbine configuration, the axial component of the tip and root vorticity is such that it induces a swirl in the wake in the opposite direction as the rotor rotation but no flow rotation outside of the wake. The azimuthal component of the tip and root[6] vortex induces an axial velocity inside the wake in the upstream direction hence slowing down the flow inside the wake. More generally, the axially induced velocity is in the opposite direction of the thrust, so that for a propeller, the directions in the above needs to be inverted.

[6]In presence of a hub radius.

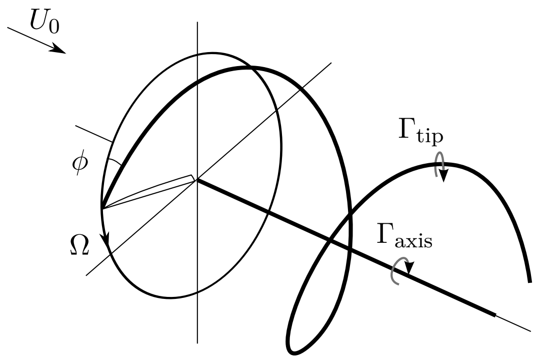

Figure 1.7: Single helical vortex-line trailing from the tip under the assumption of constant circulation at the blade and zero hub radius.

Despite the uniform loading the axial induction factor is not uniform due to the finite number of blade. Instead it takes larger values in the vicinity of the blades and hence lower values elsewhere. This can be demonstrated by implementing a simple vortex code using discrete line elements. The influence of the bound's circulation on each blade cancels out, and, if the hub radius is zero, the circulation on the axis does not contribute to the axial induced velocity. As a results of this, only the influence of the helical tip vortices of each blade needs to be computed. Results from such simulation are displayed on Fig. 1.8. Despite the azimuthal variation it should be noted that the azimuthally averaged value of a is uniform:

$$\forall r, \quad \overline{a} = \frac{1}{2\pi}\int_0^{2\pi} a(r,\psi)d\psi = \text{cst} \tag{1.11}$$

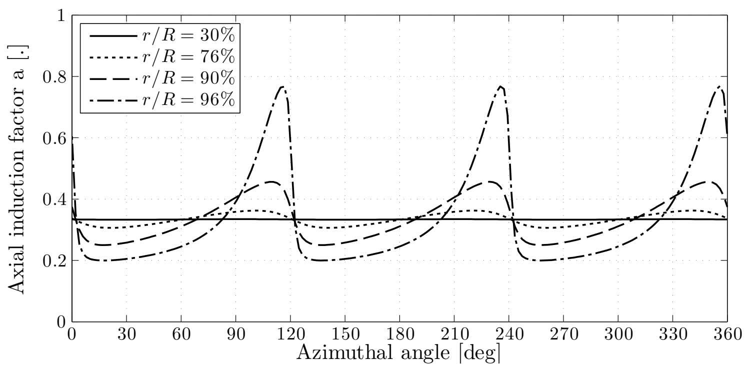

Figure 1.8: Azimuthal variation of a for different radial positions. It can be observed that the azimuthally average value of a is uniform. These results were obtained using vortex line elements describing a three bladed rotor operating at $\lambda = 6$, $a = 1/3$ and $C_T = 0.89$, with a uniform circulation along the span equal to $\Gamma = C_T \pi R U_0/(B\lambda)$. Each of the three helical curve extends 40 radii downstream and is modelled by 10000 vortex line elements.

Span-varying circulation When the circulation is not uniform each blade sheds a continuous sheet of vorticity from its trailing edge that is transported downstream so that the resulting wake shape can be compared to one of a screw. Thetypical notations and conventions are represented on Fig. 1.9, while the non-expanding wake shape are detailed onFig. 1.10. In analogy with Eq. (1.10), the center of the wake contains vorticity which is such that the flow outside the streamtube does not have a tangential velocity. Its strength is equal to the axial components of the trailing vorticity. As was mentioned above, the wake does not keep its canonical helical shape, it expands, distorts, and rolls-up into concentrated tip-vortices. As most theories uses a non-expanding helical shape as a starting point, Fig. 1.10 has been drawn to help visualize this wake shape. It should be noted that the wind turbine convention of rotor that rotates in the clockwise direction has been used for clarity. To the author's knowledge, the other references(e.g. [79, 80]), always represents these wake shapes in the counter clockwise direction(which is common in propellers and helicopters references), which could confuse the reader. This explains why the author has chosen to detail Fig. 1.10. On Fig. 1.11, the wake from the three blades is represented.

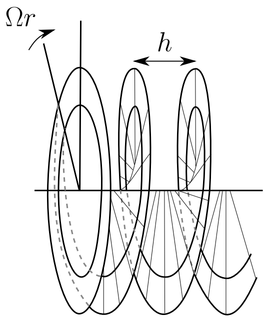

Figure 1.9: Continuous vortex sheet trailed by a rotor with span varying circulation - Convention

Velocities induced by the wake at the rotor The wake vorticity and the blade's bound vorticity[7] induce velocities that alter the velocity field at any location and in particular about the rotor. The induced velocities has an influence in $1/r^3$ according to Biot-Savart law. As a result of this the contribution from the vortex close to the rotor will be predominant. A CFD study[120] shows that resolving only the near wake, $0.5D$, was giving induction results only 1.2% different than the one for a simulation resolving a wake of $7D$. Nevertheless, this grid size study result can not be directly transfered to vortex codes where larger grid sizes are expected to be required[96]. The exact induced velocity at the rotor is the result of the contribution of the entire wake, and is thus a result of the whole circulation history. The numerical vortex methods that will be introduced in Sect. 1.1.6 are used to calculate the induced velocity at the rotor from a given circulation history at the rotor.

1.1.4 Methods to overcome the limitations of the momentum theory

In Sect. 1.1.2 the limitations of the momentum theory have been introduced and basic elements related to three dimensional effects have been described. A better insight of the three dimensional structure of the flow has been acquired through Sect. 1.1.3. Methods to account for these effects and provide a better view of the details of the flow should now be presented.

Different philosophy Methods that investigate the flow can be distinguished between "near wake" analysis where the flow is sought at the rotor and "far wake" analysis where the flow is studied far downstream. The term "near wake" is used for the region where the properties of the rotor can be discriminated, which is taken between half or one rotor diameter downstream. In the far-wake, the effects due to the specificity of the rotor are assumed to be dissipated. Near-wake analysis are the one commonly used obviously because in most application the interest is on the details of the flow and loads close to the rotor and on the specificity of the rotor itself. Nevertheless, far-wake analysis are used for theoretical derivations whose results are in turn applied for methods that investigates the flow in the near-wake. Far-wake results will be the object of the next section (Sect. 1.1.5)

[7] For a perfectly symmetric rotor the bound vorticity influences of each blade cancels out

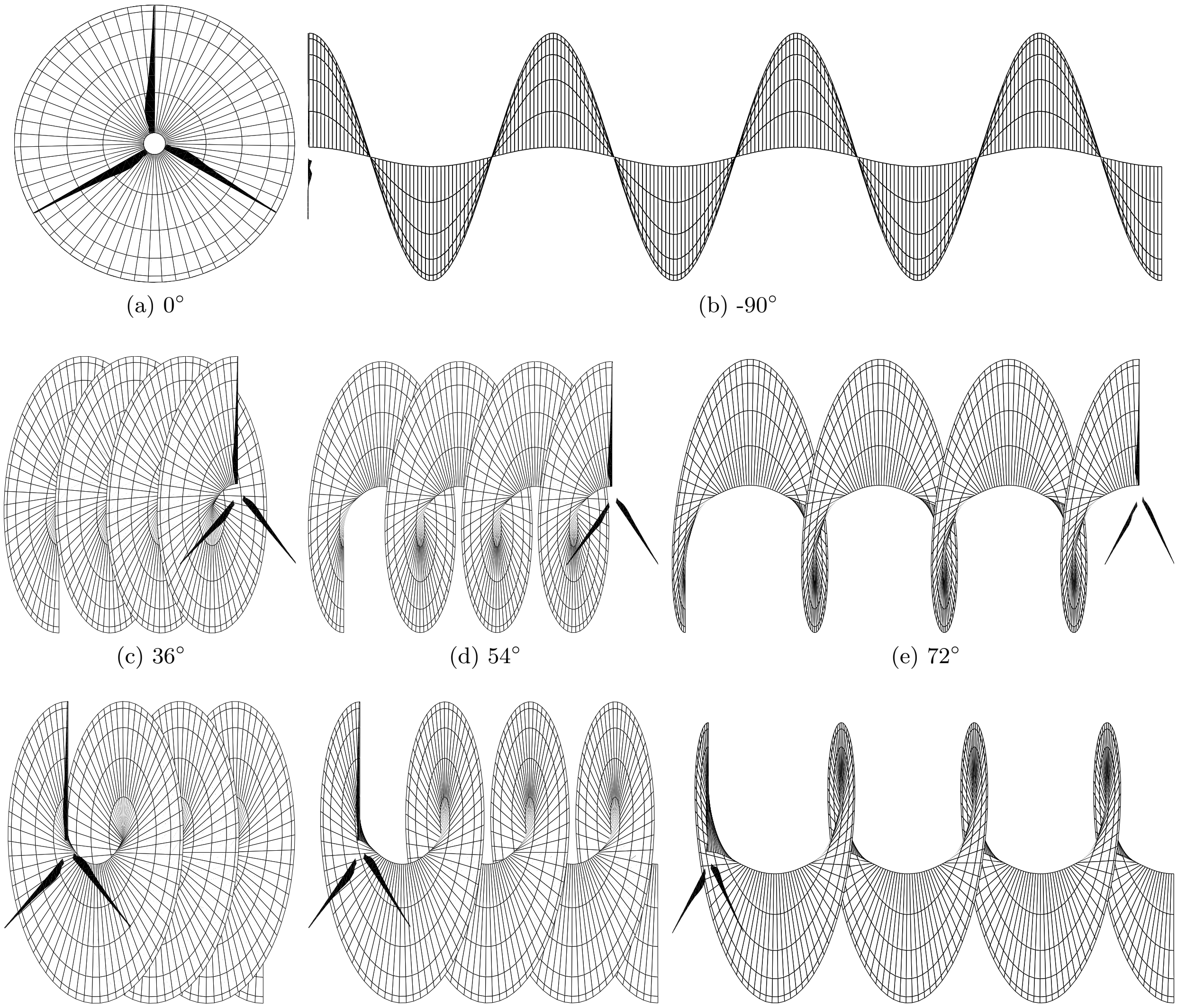

(a) 0°

(b) -90°

(c) 36°

(d) 54°

(e) 72°

(f) -36°

(g) -54°

(h) -72°

Figure 1.10: Visualization of the ideal helical wake with the proper wind turbine convention. The wake of only one blade is displayed for clarity. All the plots follow the convention of a wind turbine turning in the clockwise direction. These plots are different view of a same helical wake when the camera is rotated in the wake plane by the angle presented below each figures. The axis of rotation is follows the blade pointing up.

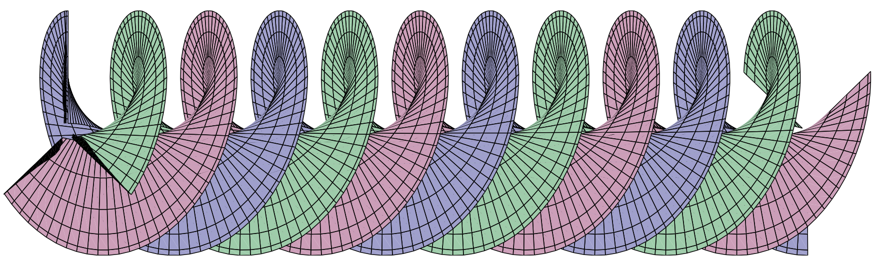

Figure 1.11: Ideal helical wake behind a turbine generated by the three blades.

Vortex theory The knowledge of the wake vorticity distribution allows the calculation of the induced velocity at the rotor. Analytical solution are limited to vortex lines, tubes and recently helix[79] so that such methods are inherently oriented towards numerical implementation. Such numerical methods will be described in Sect. 1.1.6.

Blade element theory The blade element theory derived by W. Froude[30] and mainly S. Drzeweicki[27] takes into account the blade geometry and aerodynamic properties at every blade location to determine the loads acting on an elementary blade portion assuming two-dimensionality of the flow. Nevertheless, this theory by itself does not allow the determination of the flow at the rotor. Combined with the momentum theory, it yields to the Blade Element Momentum Method, which will be briefly commented in Sect. 1.3.4 and detailed in Appendix C.

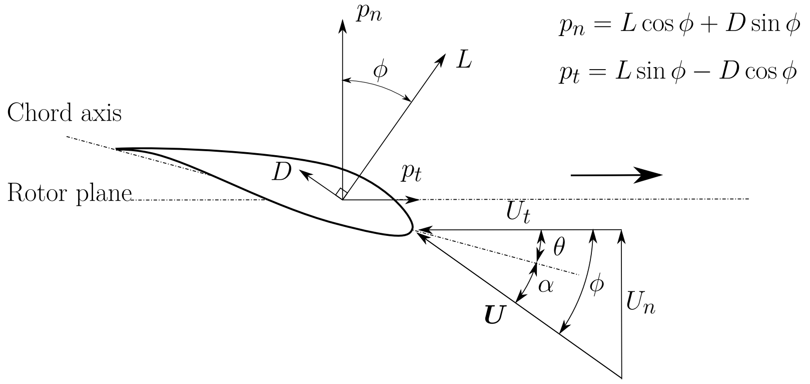

Figure 1.12: Blade velocity triangle and resulting aerodynamic forces for the blade element theory

The use of the Kutta-Joukowski theorem By application of the Kutta-Joukowski theorem the forces along the blades can be determined and by integration one can obtain the total aerodynamic forces and moments acting on the turbine. Such method requires the knowledge of both the circulation and the induced velocity distribution. If the circulation is known, simulations using vortex method can be used to determine the induced velocity distribution. Experimentally, pressure sensors on the blade can be used to determine the lift and then the circulation at different locations. Different flow visualization techniques from smoke to Particle Image Velocimetry(PIV) can be used to determine the induced velocities or the geometry of the wake.

Prandtl lifting line theory - Spanwise loading distribution Prandtl found the optimal circulation distribution for a fixed wing by modelling the wake by a series of horseshoe vortices placed along the wing span(mentioned in Sect. 1.1.3). His theory is based on two assumptions: the wing is thin and has a wide span. From these hypotheses, the wake vortex-sheet is assumed to be planar and the wing reduces to a bound vortex segment called Prandtl's lifting-line. The whole vortex sheet is composed by an infinite number of horseshoe vortices. The two trailing semi-infinite segments from a horseshoe vortex located at the spanwise position y have the intensity $d\Gamma/dy$. On one hand the lift coefficient can be computed by definition using the Lift(i.e. the circulation from the Kutta-Joukowski relation), the chord and the relative velocity(approximated to the infinite velocity). On the other hand the lift coefficient can be computed using thin airfoil theory. For the latter, the effective angle of attack is used, which is determined by computing the induced velocities from the vortex sheet. Equating the two formulae of the lift coefficient leads to Prandlt's integral equation. From the expression of the lift and the downwash, the induced drag as defined in Sect. 1.1.2 is obtained. One approach used by Prandtl consists in defining a lift distribution $L(y)$ as an infinite Fourier series. This leads to a none trivial equation involving the Fourier coefficients. Taking only the first term of the Fourier series leads to an elliptical distribution of lift. More details on this can be found in e.g. [46, 57]. In his analysis, Prandtl showed that the elliptical distribution was the one inducing the least drag. This result was also derived by Munk[76] using a far-wake analysis.

1.1.5 Far wake analysis: optimal distribution and the birth of tip-losses

Introduction Far wake theories applies under the assumptions of inviscid and irrotational flow, and they rely on the fact that there is a direct relation between the loading and hence the circulation at the lifting devise and the momentum in the wake. Such theories are often quite complex and require a high level of abstraction so that only few historical elements and basic concepts are referenced in this section. They are introduced in this study because all theoretical derivations concerning tip-losses are based in the far-wake.

The motivations for such analysis is that the flow is way more complicated in the near wake due to the interaction with blades, boundary layers at the blade and separation effects. These effects dissipates and are thus no more present in the far wake. For helicopter flows the blade tip reaches transonic speeds so that compressibility effects should be accounted for. For wind turbines such speeds are not found but the Mach number can be found to be quite larger than 0.3[8] which is the upper limit usually taken to justify incompressibility. In the far wake the induced velocities are reduced so the assumptions of inviscid and irrotational flow can be further justified.

Far wake analysis - elliptical wing elliptical distribution By applying momentum theory on a box surrounding the wing and extending the boundaries to infinity, only the plane perpendicular to the direction of flight in the far wake is left in the calculation of the drag[57, chap. 9]. This conceptual plane or “front view”, called the Trefftz plane, leaves the chord as a secondary consideration by focusing on the wake at the Trefftz plane only. The lift and drag at the lifting devise can be determined by integration of the velocity potential in the Trefftz plane, and by application of the Gauss theorem, reduces to a line integral on the wake. By using a variation method on the velocity potential, Munk[76] derived the minimum drag and found the result of elliptic lift distribution in a different way than Prandtl.

Betz Following an analogous far wake analysis as Munk[76], Betz derived the optimum circulation distribution which minimizes the power losses for a propeller rotor with infinite number of blades[9]. To do so he calculated the thrust and power in the far wake and minimized the power for variations of the circulation. This yielded to the condition of the flow being locally perpendicular to the wake surface. The optimal circulation is obtained for this flow condition at any radial position by integrating the velocity around a path surrounding the propeller axis. For this optimal condition the flow in the far wake is the same as if the vortex surface formed by the trailing vortices was an impermeable rigid body that translated downstream with a constant velocity w. In the propeller case, this velocity is oriented in the stream direction going away from the rotor, whereas for wind turbines, w is pointing towards the rotor. This analysis was performed under the assumption of lightly-loaded rotor(low-thrust) and the system of vortex sheets was thus taken as a perfect screw(no wake expansion). Betz referred to it as the “rigid-wake” condition but it should be noted that the flow in itself does not follow a rigid rotation nor a rigid translation. The flow has to move locally perpendicular to the screw surface which has an helix angle which changes with radius as illustrated in Fig. 1.13, so that the flow actually has an axial and an azimuthal component. It is important to note as well that the w is the apparent velocity of translation of the wake, but an elementary wake surface at radius r would move at a velocity $w \cos \epsilon(r)$, as illustrated on Fig. 1.13.

[8] Temperature plays a role as well with higher Mach number at lower temperature. See e.g. [14] for study of wind turbines in cold climates.

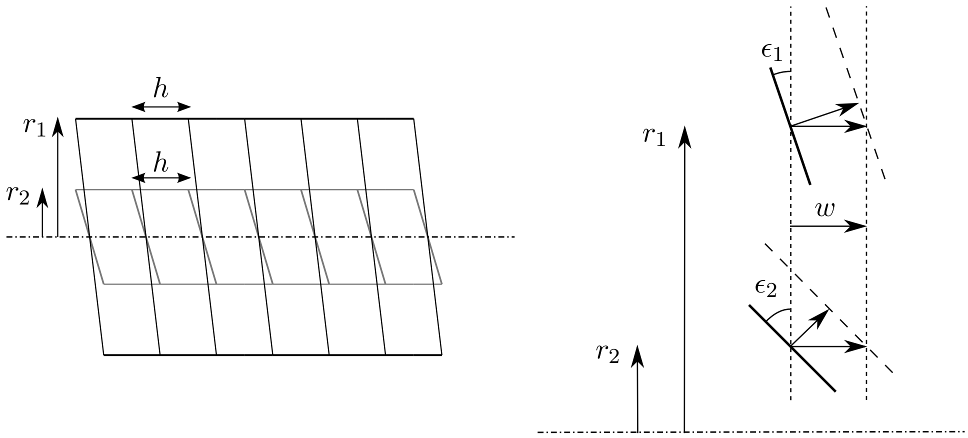

(a) (b)

Figure 1.13: Helix angle change with radius. (a) Side-view of an helix of pitch h for two different radii - (b) Close up on the change of helix angle ϵ along r and decomposition of the helix velocity along the normal of the helix surface. Each wake section has a velocity equal to $w \cos \epsilon(r)$. The apparent translation velocity of the wake w has been represented for the case of a propeller, its sign should be opposite for a wind turbine.

Prandtl As a discussion following the work of Betz, Prandtl derived an approximation to correct for the finite number of blades [88]. By doing so, he introduced a correction factor which made the optimal circulation from Betz go to zero at the tip of the blade. This physical effect is referred as tip-losses and the correction factor called the tip-loss factor usually noted F. A more detailed study of Prandtl tip-loss factor will follow in Sect. 2.3.

Goldstein Advised by him, Goldstein[36] completed the work from Betz using the same assumptions except with a finite number of blades and derived an exact solution as opposed to the approximation from Prandtl. He used Betz's results stating that the optimal circulation distribution for a given thrust was producing the same far-wake flow: a rigid screw moving axially with a constant velocity. Goldstein took advantage of the periodicity of the flow between two screw surfaces to solve Poisson's equation which reduces to solving both the homogeneous and the inhomogeneous modified Bessel differential equations. Goldstein's makes use of infinite series to solve these equations with the proper boundary conditions. Once the potential is known he determines the circulation at a given radial position, for a given tip-speed ratio by the jump of potential across the sheet at this radial position(in the far wake). The velocity at any point of the far wake is obtained by differentiation of the potential ($\boldsymbol{V} = \text{grad}\,\phi$). With the no-wake expansion assumption, the velocities at the rotor are found as twice as much as the velocity in the far-wake and the flow-angle can be derived. The calculation of the thrust and torque follow with and without the presence of profile drag using the Kutta-Joukowski theorem. A guide to follow Goldstein's article can be found in Appendix A and overview of the results and challenges from his theory will follow in Sect. 2.4.1.

1.1.6 Numerical vortex methods

Vortex methods determine the induced velocities at the rotor generated by the bound and wake vorticity of the wake by using the Biot-Savart law. As opposed to the momentum theory, the vortex theory is based on local flow characteristics and can thus provide more information about the flow. It is important to note that the vortex theory gives the same results as the momentum theory when using the same assumptions, that is, assuming an infinite number of blade, with the vorticity distributed throughout the wake volume[49, 84]. Different vortex methods are found depending on the way the vorticity is modeled. The different options originate from the fact that Poisson's equation, which is linear, admits several infinitesimal solutions which can be used by superposition to find any solutions satisfying the given boundary conditions of the problem. The equivalence between a potential flow and a distribution of vortex elements is illustrated on Fig. 1.14, adapted from [112].

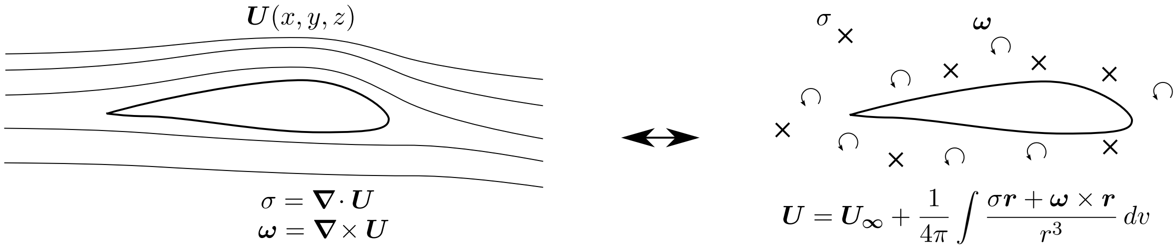

Figure 1.14: Illustration of the equivalence between a given flow and a continuous distribution of sources and vortices.

Different vortex code implementations exist also depending on the purpose of the code. Some codes guess and prescribe the wake geometry to calculate the flow at the rotor for a steady situation, while other codes reproduce the vorticity shedding, propagation and deformation of the wake. Several variations of vortex codes have been implemented for this study as described in Appendix B. A small overview is presented in this section.

Different dimensions of vorticity The size of the problem can be reduced in several degrees to simplify it by integrating the distributed vorticity distribution and concentrating it into surfaces lines, or even points. The different formulations changes the character of the flow in the vicinity of the vortex elements which reduces to so called singularities. Far from the vortex elements though the different configurations should give similar flow fields. The reduction of vorticity dimensions is illustrated on Fig. 1.15, adapted from both [25] and [112].

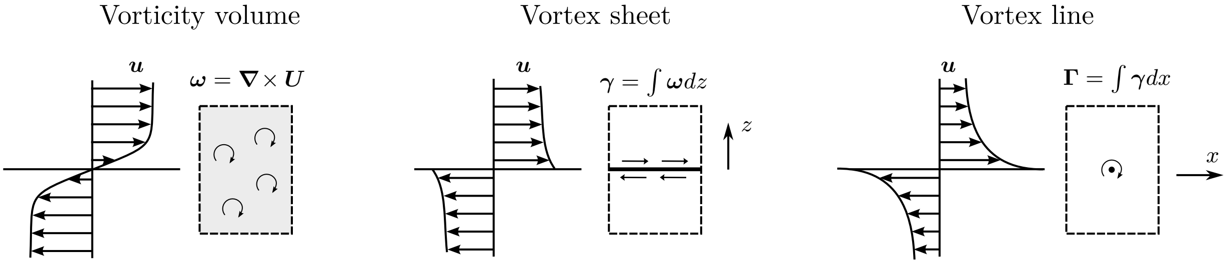

Figure 1.15: Reduction of vorticity dimensions by integration. The concentration of vorticity introduces singularities in the velocity field close to the vortex elements.

Different vortex codes From the different dimensions of vorticity presented above, different vortex code formulations can be derived. These vortex codes are illustrated on Fig. 1.16 and they will be further described in the following paragraphs.

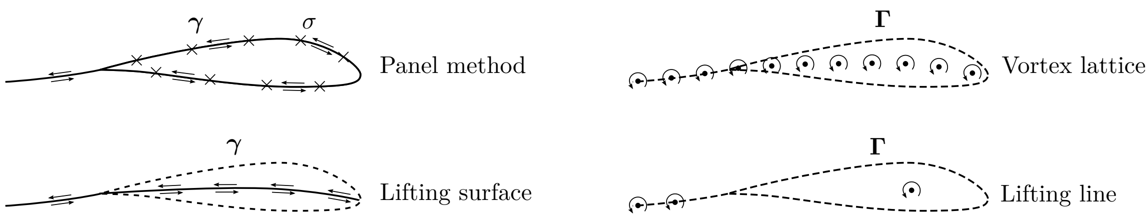

Figure 1.16: Different vortex codes using different dimension of vorticity.

Lifting-line code Prandtl's analytical lifting line theory for a wing has been presented above in Sect. 1.1.4. This theory cam be applied numerically for any lifting devises satisfying the assumption that the extension of the geometry in the span-wise direction is predominant compared to the ones in chord and thickness direction. For a wind turbine, under this assumption, each blade can be modelled with a line, made of bound vortex segments, passing through the quarter chord point of each cross section. All the flow field in chord-wise direction is concentrated in that point and at each cross section of the blade the lift is assumed to act at the quarter chord location. From each extremity of the bound vorticity segments, two trailing vortex segments emanates of the blade and convects downstream. Segments parallel to the bound segments are also shed if the circulation varies with time. The resulting wake shapes resembles a lattice justifying the appellation sometimes used of "vortex-lattice code". The implementation of such code varies. It can be made by using segments, horseshoe vortex, or vortex rings. All formulation are identical but varies in the concept of attribution of circulation value to the segments. For instance, in a vortex ring formulation, each rings as one circulation value. Two adjacent rings in the spanwise direction will have one trailed segment in common. The concept of the algorithm is such that the segment is counted positive for one ring and negative for the other ring, so that by computing the total contribution for the two rings, by linearity it is equivalent to computing the trailed segments only once with the circulation value equal to the difference of the two circulations. For code optimization, this is obviously required to avoid computing the influence of a same segments twice.

In this study a lifting line code has been implemented as described in Appendix B. Another example of lifting-line code is the one from ECN called AWSM[37, 112]. In AWSM the effect of viscosity is taken by using polars of the lift, drag and pitching moment as function of the local flow direction. To avoid singularities for velocities evaluated close to the vortex line elements, a "cut-off radius" is used in the denominator of the Biot-Savart law to ensure it is never 0.

Lifting surface code with vortex-lattice The difference between such code and a lifting-line code is that the wing or blade is modelled with several elements in the chordwise direction and hence takes into account the chord dimension. The wake model is identical, and the same concepts of vortex rings, horseshoe vortex, or trailed and shed segments can be chosen. The difficulty in this code come when it is used in combination with airfoil data. The notion of angle of attack needs to be defined together with the chordwise repartition of lift and hence circulation. Methods using known chordwise distribution from flat plates and elliptical wings are used in[82].

Lifting surface code with continuous distribution As opposed to the previous method, the vorticity distribution is modelled continuously in each "rings" or quadrilateral forming the lattice. This method is at midway between the vortex-lattice and the panel code formulation.

Panel code In a panel code the thickness of the geometry can be modelled offering the possibility to compute complex flow cases. Many variations of panels code can be found, as referenced for instance in[52].

Mixed representation For steady simulations in the light of optimizing propellers, steady lifting-line codes are developed[18, 19]. Such methods requires iterations to find a physical solution.

Challenges Due to the law in $1/r^2$ the induced velocity close to a vortex element tend to infinity. Such phenomenon is observed within the hypothesis of potential flow, but in a viscous flow, even a strong vortex will generate finite induced velocity due to viscous shear forces within the fluid elements[4]. The vorticity is diffused into a small tube called the vortex-core. Vortex methods circumvent the infinite velocity by introducing these vortex core to simulate viscous effects[52, 49]. Nevertheless, the choice of the core size is empirical and affects significantly the results. In numerical vortex methods where the vortex elements are allowed to move freely, numerical instabilities can arise if two elements become too close to each other, even if a vortex core model is used.

Wake model The wake shape formed by the vortex elements has a critical influence on the induced velocities found at the rotor. It has been seen that for real flow the wake convects, expands, rolls up and distorts. To capture these phenomena, the induced velocities at every point of the wake should be calculated and used to determine how each vortex element will move and what will be their location at the next time step. Such model is referred to as a free wake model. Running such a model requires an important computational time and raises different problems such as the handling of vortex elements as they get close to each other(viscous model, re-meshing) and the modelling of the stretching of vortex elements. These problems are often circumvented by using a prescribed wake model which specifies the wake shape and hence the locations of each vortex elements. The determination of the wake shape is usually empirical or based on free-wake simulations. For a given prescribed wake the induced velocities at the rotor are known in a deterministic way, so that the accuracy of the solution is entirely dependent on how realistic the wake shape is. Given the large number of parameters influencing the wake shape(C_T, λ, Γ, etc.) prescribed wake models clearly appears limited. Nevertheless, a common approach consists in using mixed representation setting the close-wake free in order to capture local phenomena, while modelling the far-wake as a prescribed helix of constant pitch and radius. Wake modelling for vortex methods has an important number of variations which are beyond the scope of this document(see for instance [33]).

1.2 Considerations on the local aerodynamics of a rotating blade

The understanding of the 3D aerodynamics of a rotating blade is fundamentally required in this study. The 3D effects influencing the airfoil performance are investigated because they need to be the modelled in BEM codes and sometimes vortex codes as well. The challenge in these codes is to use tabulated 2D airfoil data which by essence does not reveal three dimensional effects. Two main levers are found:

- The angle of attack: a wrong assessment of the angle of attack will lead to a wrong data from the table.
- The airfoil performances: the relevance of 2D airfoil data for wind turbine is rather limited[114], the airfoil performances have to be known for the exact flow conditions(stall, radial flow, extension of the boundary layer, etc.) they are evaluated at.

The problem is really critical for simulation quality but also really challenging. The notion of tip-loss is greatly implicated in this problem as it is used to determine the flow angle and thus the angle of attack either in direct or inverse BEM codes. Inversed BEM codes can be used to find the local angle of attack for a given load distribution on the blade. For this reason a wrong tip-loss implementation will not value a good 3D correction model, and an inaccurate 3D correction model will give no hope to find a good tip-loss correction. An uncertainty analysis was carried out[74] by students from Georgia Tech that showed that the uncertainty on the airfoil coefficients was the one which had the greatest influence on the determination of Goldstein's tip-loss factor(see Sect. 2.4.1). On the other hand, rotational effects and stall are mainly found in the inner part of the blade, so it is likely that the tip-losses won't have effects in this area. It has also been observed[32], that as long as the airfoil section is not stalled, the 2D data were a good approximation in wind energy applications.

In Sect. D.2 a comparative study between the airfoil coefficients found with 3D CFD compared to the one found with 2D CFD is presented. These data will be used in Sect. 5.2 to assess a “lift coefficient” tip-loss factor. It will be indeed seen that tip-losses can (partially) by viewed as airfoil corrections (as defined e.g. by Eq. (1.28)). The following paragraphs will be useful to discuss this definition.

1.2.1 Angle of attack

Definition of angle of attack The notion of angle of attack is only well defined in a 2D situation whereas in 3D the introduction of span-wise velocity and induced velocities make it ill-defined. In two dimensions, the angle of attack is defined as the angle between the velocity vector and the chord direction vector. In the 2D lifting line theory, the angle of attack has been found to be defined as the angle between the local chord direction and the local effective velocity which is taken as the sum of the undisturbed velocity and the velocity induced by the wake. This definition is made more general, by considering the projection of the total velocity into the plane of the airfoil section. This distinction is important when radial flows are present and in the case of swept and coned blades.

In [101] the induced velocities used for the angle of attack are taken as the one resulting from all vorticity except the one from the bound vortices. In a same fashion, Pitot tube measurements on a rotating blade must be corrected to account for the bound circulation and for the finite number of blade. In the BEM method(see Appendix C), such considerations are not needed because the induced velocities will not be calculated using the Biot-Savart law, but using a force-momentum equilibrium law.

Inverse methods to determine the angle of attack Using the BEM formalism presented in Appendix C, the angle of attack can be determined if the load distribution is known. The load distribution can be determined by integration of pressure measurement or CFD computation. It is likely that when integrating pressure from measurement, a coordinate system attached to the airfoil chord will be used and hence the load in the chordwise and perpendicular direction will be known. Using data from CFD, depending on the post processor, the data might be exported in another reference system, such as the global blade coordinate system. The pitch angle and twist angle being known, the axial and tangential forces per length, p_n and p_t, are here used as input variables for this inverted BEM code.

The second linkage equations Eq. (C.13) and (C.14) have to be solved for a and a'.

$$\frac{Bp_n}{4\pi\rho r U_0^2} = aF\left(1-a\right) \tag{1.12}$$

$$\frac{Bp_t}{4\pi\rho r U_0^2\lambda_r} = a'F\left(1-a\right) \tag{1.13}$$

It should be noted that the tip-loss factor has been inserted in these equations using Glauert's formalism. Also, the "hat" notation $\hat{a}$, has been dropped not to surprise the reader with this notation. Other implementations of the tip-loss and BEM equations are possible as described in Sect. 3.2. Only the principle of inverse BEM codes is described here. The flow angle is then determined with the first linkage equation:

$$\phi = \operatorname{atan}\frac{(1-a)u_0}{(1+a')\lambda_r} \tag{1.14}$$

Once again, strictly speaking, the local axial inductions on the blade a_B and a'_B should be used in these equations, but several variations of BEM formulation exist. The angle of attack, and lift and drag forces per length immediately follow:

$$\alpha = \phi - \theta \tag{1.15}$$

and the aerodynamic coefficients:

$$C_l = \frac{1}{\frac{1}{2}\rho \boldsymbol{U}^2 c}\left(p_n\cos\phi + p_t\sin\phi\right) \tag{1.16}$$

$$C_d = \frac{1}{\frac{1}{2}\rho \boldsymbol{U}^2 c}\left(p_n\sin\phi - p_t\cos\phi\right) \tag{1.17}$$

If the tip-loss functions are not function of a and a', then the resolution is done, otherwise an iterative procedure is required. For this the tip-loss function can be initialized to 1. For instance, all functions can be taken as the Glauert tip-loss correction, F_{Gl}. As it will be seen in Sect. 3.1, this factor depend on $\phi(r)$, which in turn depend on a and a', justifying the iterative procedure. Both in experimental and computational methods, the force normal to the chord axis is the one obtained with the most accuracy so it is expected that the lift force will be determined more accurately than the drag force. Moreover, a small error in the determination of the angle of attack will results in a large error in the induced drag due to commonly large values of the lift over drag ratio $\varepsilon_{l/d}$ (see Eq. (1.6)).

In a similar fashion, it is possible to use a vortex code in an inverse fashion, using iterations to find the angle of attack corresponding to a given loading. More details on such methods can be found in [94] and [32].

Other methods to determined the angle of attack The averaging technique is probably the most widely used method to determine the angle of attack for CFD data. This method presented in [43, 48] consists in averaging the axial induction in annuli located at different distance to the rotor to extrapolate the value of the axial induction at the rotor. In its simplest form, only two annuli symmetric with respect to the rotor can be used. In [97] an iterative method is presented which can be used for both CFD and Pitot tubes measurements. This method uses the loading on the blade and the flow angle parameter to determine the bound circulation and the corresponding induced velocities, that will in turn modify the flow angle. A similar method, but using this time a distributed circulation instead of a point vortex to assess the induced velocities is presented in[47]. The advantage of this method, is that it is less dependent on the distance to the leading edge where the velocity is evaluated.

1.2.2 Rotational effects

Rotational effects In the middle of the 20^{th} century, Himmeslkamp[45] has observed on aircraft propellers that the lift coefficients of the airfoils were increased due to rotational effects implying radial flows. This observation was mainly seen in the smaller radial sections where it was also observed that the stall was occurring at higher angle of attack. One of the first simulation that could include rotational effects and carried out for a wind turbine was done by Sørensen in 1986[102]. The effects of lift increase and stall delay were found in these simulations and confirmed by observations of Savino and Nyland[95, 1985], and later by Rasmussen et al.[90, 1988], Madsen and Rasmussen[68, 1988], Ronsten[91, 1991], Bruining[16, 1993], with other references found in[63] and a throughout comparison in[62].

- Lift coefficient: In the inner part of the blade, increase of lift coefficient up to 30% can be found. Nevertheless, the quantification of increase of lift is difficult and clearly airfoil dependent. As a general trend, the difference between the 2D and 3D lift coefficients increases going from the mid-span to the hub, in the region where stall occurs. It was also found that the 3D aerodynamic coefficients mainly starts to differ from the 2D coefficient from the angle of attack of maximum lift.

- Radial component: It was found that the laminar flow was hardly influenced by rotational effects and followed the chord direction from the leading edge. Nevertheless, when the flow encounters an adverse pressure gradient and separates, the fluid is significantly moved outwards by the centrifugal force. This effect is referred as “centrifugal pumping”.

- Drag coefficient: Studies of the NREl phase VI experiment[62, 107] showed an increase of drag near the root and a small decrease near the tip. In his study, Sørensen found almost no difference but slightly lower C_d. In general, there is no full consensus yet concerning the drag coefficient, though it has been observed that the pressure in the 3D separated zone is lower than the one in 2D, resulting in higher drag. The tapered ratio of the tip is likely to have an influence on the drag coefficient towards the tip.

- Separation Point: Stall can be delayed of few percent of the chord length.

The current understanding of rotational effects can be described as follow. The centrifugal loads acts on all volume of air for which the relative tangential velocity differs from the relative velocity of the blade, Ωr. This radial flow can only occurs in regions of strongly retarded flows as the separated boundary layer and separation bubble present on the suction side of the blade. Due to centrifugal loads the air is accelerated radially towards the tip of the blade. This radial velocity component will induce a Coriolis acceleration in the main flow direction, acting as a favourable pressure gradient. The displacement thickness of the separated boundary layer is decreased, leading to less de-cambering and higher lift coefficients[101]. .

1.2.3 Airfoil corrections

Data for large angles of attack Data for large angles of attack are usually not available from wind tunnel measurement so extrapolation techniques are often used. For high incidences(e.g. $\alpha \in [-170\ ;\ -30] \cup [30\ ;\ 170]$) airfoil characteristics are considered to become rather independent of the geometry so that data from a flat plate can be used. This is for instance mentioned in [98] but with the flat plate airfoil characteristics reduced by a factor of 85%. In [5] the fully separated(fs) coefficients for high angle of attack are computed as:

$$C_{L,\text{fs}} = 2\cos\alpha\sin\alpha \tag{1.18}$$

$$C_{D,\text{fs}} = 1.3\sin^2\alpha \tag{1.19}$$

$$C_{m,\text{fs}} = -\frac{1}{4}C_n \quad \text{with} \quad C_n = 1.0\sin\alpha \tag{1.20}$$

and a function g is used to ensure a smooth transition between the original data and the extrapolated data, as $C_\bullet = gC_\bullet + (1-g)C_{\bullet,\text{fs}}$, with e.g. the function g defined with three parameters α_d, α_0 and $\Delta\alpha$ as:

$$g(\alpha) = 0.5 + 0.5\tanh\left[\frac{\alpha_d + \alpha_0 - |\alpha|}{\Delta\alpha}\right] \tag{1.21}$$

Another model is the one from Viterna and Corrigan[115] which extrapolates the airfoil coefficients after stall. The authors looked at a way to obtain an idealized stall that would keep a constant torque at high wind speeds and thus high angles of attack. This approach was developed to fit measured and predicted performances of two specific stall regulated wind turbine. This correction requires that the lift over drag ratio at the initial angle of attack matches the lift over drag ratio of a flat plate. This is unfortunately not a common case and in[107] it is argued that an incomplete understanding of the stall process existed at the time of this method's development. In[107], the Viterna's method is applied with as input the angle of attack and the average aerodynamic coefficients values over the blade span for which the lift over drag ratio matches the flat plate theory. A review of aerodynamics coefficients at high angles of attack can be found in [61].

Airfoil data 3D corrections The 2D airfoil coefficients found from measurements in wind tunnel or by simulations such as CFD or panel methods tools such as Xfoil[26], are usually corrected to be used in BEM or aeroelastic codes. It should be noted that though there are uncertainties in simulations results, measurements data also have quite a spread as seen in the comparison of results from 4 different renown wind tunnels [69]. Most 3D correction methods can be written in the following form:

$$C_{\bullet,\text{3D}} = C_{\bullet,\text{2D}} + f_{C_\bullet}\Delta C_\bullet \tag{1.22}$$

where $\bullet$ stands for L, D, m, the indexes of Lift, Drag and moment coefficients. $\Delta C_\bullet$ is the difference between the coefficient $C_\bullet$ estimated in inviscid flow(i.e. without separation) and its its steady 2D value evaluated for instance from a wind tunnel measurement(where obviously separation will occur). The inviscid lift coefficient can be approximated with the one for the Joukowski's airfoil family[46] approximated for a thin airfoil of trailing edge parameter a, chord of $\approx 4a$, at small angle of attack α and small camber parameter β :

$$C_{l,\text{inv,thin}} \approx 8\pi\frac{a}{c}\sin(\alpha+\beta) \approx 2\pi(\alpha - \alpha_0) \tag{1.23}$$

Nevertheless, the author would like to point out that such approximations is often inappropriate for airfoils used in wind energy. This remark will also apply when commenting the performance tip-loss correction from Lindenburg in Sect. 3.1. The result from Eq. (1.23) apply to thin airfoils and the slope 2π is only obtained when the thickness tend to zero. In Abbot and Von Doenhoff[1], a similar conformal transformation is used for symmetric airfoils that leads to(see [1, p 53]):

$$C_{l,\text{inv,thin}} \approx 2\pi\left(1+\frac{4}{3\sqrt{3}}\frac{t}{c}\right)\sin(\alpha-\alpha_0) \approx 2\pi\left(1+0.77\frac{t}{c}\right)\sin(\alpha-\alpha_0) \tag{1.24}$$

where the thickness ratio has been taken as $(3\sqrt{3}/4)\epsilon/a \approx 1.299\epsilon/a$ according to Abbot and Von Doenhoff's notations. This formula shows that the slope for thick airfoil can be expected to be higher than the theoretical results of 2π extensively used in engineering methods. The author does not recommend in particular to use Eq. (1.24) which could lead to tremendously large slopes for thick airfoils. Instead, a linear fit of 2D viscous tabulated data in the linear region (e.g. $[\alpha_0\ ;\ \alpha_0+8]$) should be used to determine the slope $C_{l,\alpha}$. The inviscid coefficient could then be determined as:

$$C_{l,\text{inv}} = C_{l,\alpha}\sin(\alpha-\alpha_0-0.01) \tag{1.25}$$

The constant 0.01 is suggested in order to ensure that the inviscid data are slightly always than the viscous one.

A brief overview of the models of Snel et al[101], Lindenburg[62, 63], Du and Selig[28] and Chaviaropoulos and Hansen[20] which all increases the lift coefficient in the root section can be seen Tab. 1.1. None of the methods presented in this table uses a correction for the moment coefficient, i.e. $f_{C_m}=0$. This table also presents the engineering model that has been derived by Sant[93] for the NREL phase VI rotor[40] using different polynomials P of degree 3 and 4 in c/r. The model of Bak et al[7] is probably the most complex one at this moment as it uses a model for the C_p distribution depending on the angles of attack where the separation occurs from the leading edge and where the separation starts from the trailing edge. This model of C_p tries to reproduce the difference between C_p distributions from 3D measurements and 2D data. It is also the only model that presents a correction for the moment coefficient. Among the other existing corrections used for wind turbine, one can mention the methods to extrapolates coefficients for unclean blades(ice, dirt, insects). Such extrapolation methods are referenced in [14].

Table 1.1: Corrections of airfoil coefficients for 3D effects according to Eq. (1.22)

Model	$\mathbf{f_{C_L}}$	$\mathbf{f_{C_D}}$
Snel et al.[101]	$3\left(\frac{c}{r}\right)^2$ or $3.1\left(\frac{c}{r}\right)^2$	0
Lindenburg[63]	$3.1\left(\frac{\Omega r}{V_{\text{rel}}}\frac{c}{r}\right)^2$	0
Du & Selig[28]	$\frac{1}{2\pi}\left[\frac{1.6(c/r)}{0.1267}\frac{a-(c/r)^{\frac{dR}{\Lambda r}}}{b+(c/r)^{\frac{dR}{\Lambda r}}}-1\right]$ with $\Lambda=\Omega R/\sqrt{V_0^2+(\Omega r)^2}$, $a=b=d=1$	$-\frac{1}{2\pi}\left[\frac{1.6(c/r)}{0.1267}\frac{a-(c/r)^{\frac{dR}{2\Lambda r}}}{b+(c/r)^{\frac{dR}{2\Lambda r}}}-1\right]$
Chaviaropoulos & Hansen[20]	$a\left(\frac{c}{r}\right)^h\cos^n\beta$ with $a=2.2$, $h=1$ and $n=4$	$a\left(\frac{c}{r}\right)^h\cos^n\beta$
Sant [93]	$K_L(\alpha)\left[1-e^{-0.003(\max(\alpha,\alpha_s)-\alpha_s)^3}\right]$ with $K_\bullet=g_\bullet(n_\bullet-m_\bullet\alpha)e^{-a_\bullet(\alpha-\alpha_s)}$, $g,n,m,a=P(\frac{c}{r})$	$K_D(\alpha)\left[1-e^{-0.003(\max(\alpha,\alpha_s)-\alpha_s)^3}\right]$

Stall Delay The most common stall delay model is the one from Corrigan and Shillings[21, 62]. Most models for stall delay modify only the lift coefficient, but not exclusively. For wind turbines applications, a modification of the drag coefficient is most probably required due to difference of pressure intensity observed in the separated regions between 2D and 3D stall.

Tip-losses The tip-loss correction of Shen et al.[98] suggests of correction on C_n and C_t to account for the pressure equalization at the tip of the blade which should lead to the loads vanishing. This correction will be presented in more details in Sect. 3.1.3 and 3.2.2. In his PhD thesis[93], Sant suggests a correction for the lift and drag coefficient in a similar fashion than Shen. This correction is presented in Sect. 3.1.3.

1.3 Preliminary considerations for the study and modelling of tip-losses

1.3.1 Physical considerations expected to be modelled

- The force on the blade should go to zero at the tip due to the pressure balance between the upper surface and the lower surface

- The relative velocity at the blade tip cannot be equal to the upstream velocity due to shear at the boundary of the "ideal" streamtube and to the presence of the tip vortex that will clearly modify the flow structure at this particular location.

- The average axial induction drops towards zero at the tip, but does not have to be exactly zero at the tip. The radial and rotational flow at the tip due to the tip-vortex transfers axial kinetic energy towards rotational kinetic energy so that the flow is not likely to have it's full upstream velocity at the tip. This is supported by the considerations of the previous point, and CFD simulations.

- The relative velocity is not uniform in a annular section to the limited number of blades. The axial and tangential induction factor are thus azimuthally dependent.

- The flow has a radial component, simply due to the expansion of the streamtube and also more subtly due to 3D aerodynamic effects[67]. As a result of this the 2D airfoil coefficients could not be suitable to give the exact aerodynamic loads.

- The circulation along the blade is not constant due to e.g. root and hub losses. This will imply a radial dependency of the induction factors.

- The optimal circulation distribution derived by Goldstein and reasonably simplified by Prandtl are never obtained in reality. Moreover they are derived for optimal frictionless rotors, so their applicability to rotors in general is uncertain.

1.3.2 Definition of the tip loss factor

It will be seen that several definitions and interpretations of the tip-loss factor can be found in the literature. These definitions will be introduced in this section, but more detailed will be found throughout this document, particularly in chapter 2 where the theoretical work are presented. As a result of these different definitions, the implementation of the tip-loss factor will also have several variations. This will be the focus of Sect. 3.2.

Definition in terms of axial induction The fact that the axial induction factor is azimuthally dependent suggests the introduction of the average induction factor in an annulus $\overline{a}$ (see Eq. (1.3)). It is also expected that this factor will reach an extremum in the vicinity of the blade so that the particular value taken at the blade is relevant and will be denoted a_B. With these definition, the tip-loss factor F has been defined by Glauert as the ratio between the azimuthally averaged axial induction factor and its value at the blade:

$$F = \frac{\overline{a}}{a_B} \tag{1.26}$$

The difference between $\overline{a}$ and a_B can be read on Fig. 1.8. Reading the plot at the azimuthal positions of the blades(e.g. 120°), and doing the ratio of the inductions factors at different radial position, the tip-loss factor as defined by Eq. (1.26) can be visualized. A shape similar to Fig. 2.12 is obtained.

Definition in terms of circulation The tip-loss factor can also be seen as the ratio between the maximum theoretical circulation for a rotor with an infinite number of blades to the actual circulation for a rotor with finite number of blades:

$$F = \frac{B\Gamma}{\Gamma_\infty} \tag{1.27}$$

This definition corresponds to the work of Prandtl and Goldstein, whose work will presented

Definition in terms of aerodynamic efficiency In Sect. 1.2 the local aerodynamics near the blade has been discussed. At the blade tip the flow is likely to differ significantly from 2D aerodynamics due to the formation of the tip-vortex(see e.g. **??**). The performance of the airfoil at the tip is hence lower than expected and a tip-loss factor can be defined accordingly as:

$$F_{C_l} = \frac{C_{l,3D}}{C_{l,2D}} \tag{1.28}$$

This tip-loss factor is likely to be dependent on the tip geometry and on the rotor operating condition. It will be investigated using CFD data in Sect. 5.2. This tip-loss factor can be seen independently of the one from Eq. (1.26) which predicts a reduction of angle of attack near the tip.

1.3.3 Distribution of axial induction

Given the definition from Eq. (1.26), a throughout understanding of how the axial induction is distributed around the wind turbine is required. Several figures will be and have been presented to illustrate the variations of the axial induction. Observing these figures, several general remarks are drawn:
- Figure 1.1: From the 1D momentum theory, it is known that the axial induction increases progressively from upstream to a given value downstream
- Figure 1.8: Using a vortex code with a constant circulation along the blade, it was seen that the axial induction increases azimuthally when approaching the blade azimuth and drops after that. This increase of induction is more important at the tip of the blade.
- Figure 4.7: The bound circulation is responsible for the jump in axial induction from both side of the blade when looking at different azimuthal position. The wake is responsible for the main part of the axial induction. In a sense, the blockage of the flow is performed by the wake.
- Figure 6.3: The axial induction increases when going further downstream. The local effects are smoothen out and the presence of the nacelle becomes barely noticeable. It is seen that the average axial induction goes to zero with the radial coordinate, but is not zero at the tip.
- Figure 1.17: The thrust coefficient has an important influence on how the axial induction is distributed before and after the rotor. The higher the thrust coefficient, the more flow is blocked in front of the rotor. Radial variations of the axial induction in the wake are of course dependent on the axial induction on the blade. Important variations of axial induction are found at the tip. Velocities higher than the free stream velocity can be found at the tip, implying that negative axial induction can occur at the tip. As said above, The velocity does no reaches the free stream velocity exactly at the blade tip.

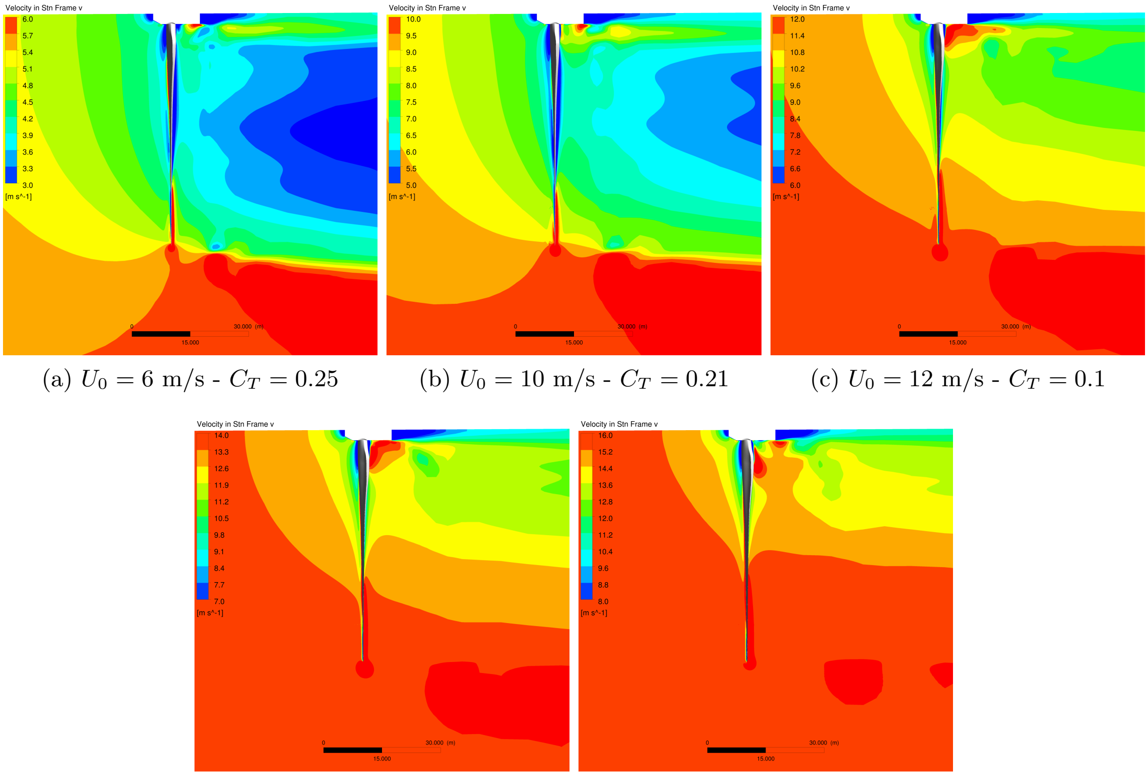

(a) $U_0 = 6$ m/s - $C_T = 0.25$ (b) $U_0 = 10$ m/s - $C_T = 0.21$ (c) $U_0 = 12$ m/s - $C_T = 0.1$

(d) $U_0 = 14$ m/s - $C_T = 0.06$ (e) $U_0 = 16$ m/s - $C_T = 0.03$

Figure 1.17: Side view of the turbine showing the variation of velocity(or axial induction) found with CFD

1.3.4 Subtleties of the BEM method relevant for this study

For clarity, the common BEM method is presented in annex Appendix C whereas this section is more dedicated to the subtleties of this method. The blade element momentum(BEM) method is attributed to Glauert[35] and results in the combination of the momentum theory and the blade element theory. The momentum theory applied to an annular element provides the corresponding elementary thrust and torque for a given set of induction factors. This relation between induction factors and loads is invertible. The velocity triangle from the momentum theory also gives an expression of the flow angle as function of a and a'. On the other hand, the blade element theory requires the airfoil characteristics, the angle of attack(or the flow angle) and the relative velocity to calculate the forces of lift and drag applied to the blade element, and by projection the elementary thrust and torque. For a given rotor geometry and a given wind condition, a physical solution will be found if both methods returns the same loads for all the different stripes. In order to find this solution, the methods are linked together to form a converging iterative process. The author likes to emphasize two links, or linkage, to clearly distinguish the difference of the methods and how they interact. The first linkage is obtained by comparing the velocity triangles of the two methods(energy equation). The second linkage consists in equalizing the loads obtained from both methods. Figure 1.18 illustrates the BEM process, the use of the different theory and the two links between them.

Context of applicability

Assumptions 1.1: Simplified 2D Momentum theory

(H 1.1a) - Homogeneous, incompressible, steady state fluid flow

(H 1.1b) - No frictional drag

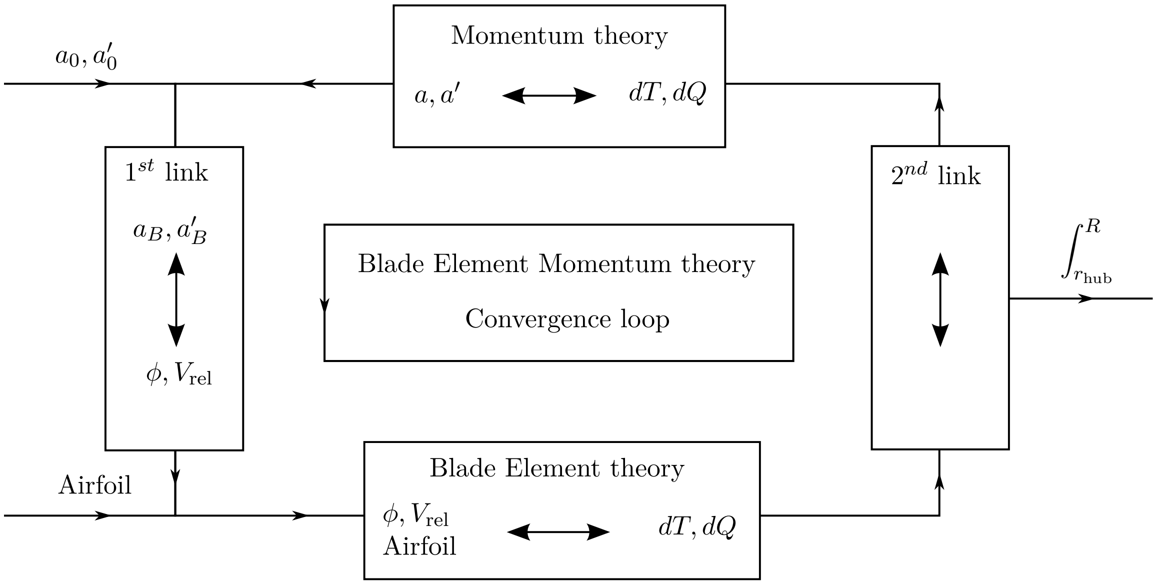

Figure 1.18: Parameters needed and results obtained with the different method used. The Blade Element Momentum(BEM) method results in the combination of both the momentum theory and the blade element theory

(H 1.1c) - Actuator disk generates a pressure drop and rotates the flow downstream(infinite number of blades)

(H 1.1d) - Uniform circulation/thrust over the rotor area and thus uniform induction

(H 1.1e) - Lighlty loaded rotor

(H 1.1f) - The static pressure far upstream and downstream is equal to the undisturbed ambient static pressure(ω small compared to Ω)

Assumptions 1.2: Blade element theory

(H 1.2a) - No aerodynamic interaction between the annular elements

(H 1.2b) - Forces on the blade can be calculated using airfoil aerodynamic characteristics

Assumptions 1.3: BEM

(H 1.3a) - The assumptions of momentum theory can be relaxed

(H 1.3b) - The forces of the B blade elements are responsible for the change of momentum of the air which passes through the annulus swept by the elements

A justification on how (H1.1d) can be relaxed can be found in [70, p 63]. This relaxation is primordial to justify the common use of the BEM method.

Pros and cons Doing a listing of advantages and shortcomings of a BEM code is bound to raise clichés and debates, so the reader is invited to evaluate them parsimoniously:
Advantages

- Fast
- Known and well tested models to unsteady flows
- Proved some accuracy

Shortcomings:

- Not possible to model winglets of sweep-back blades
- 3D effects, yaw, non-stationary effects and stall are only modelled
- No investigation of the flow possible(boundary layer, pressure distribution, wake)

Observed performance of BEM codes The performance of BEM codes will be extremely dependent on the model implemented. As an illustrations of this, several observations found in the literature are listed. It is see that these observations are sometimes contradictory and they should thus not be taken as general. Different observations are found when comparing with measurements.
- Underprediction of power, especially after stall [92].
- Underprediction of power in the stalled conditions[102].
- Overprediciton of power for 2-bladed rotors[62]
- Prandtl tip loss correction overestimate the loads at the tip[98]
- Under prediction of the power coefficient in the inner part of the blade and over prediction in the outer part of the blade (without tip or hub corrections) [66, 67]

Debate on the drag In linking the blade element theory and the momentum theory, it is argued that the drag should not be included.
- References advising not to include the drag:[117, 62, 23, 70]
- References including the drag:[42, 6]
- References arguing both:[70]

From an analysis of the following references [17, 62, 46, 117], the following can be mentioned concerning the debate on the inclusion of the drag. The viscous effects emerging from the boundary layer of the airfoil are propagated in the wake into helical filaments enclosed by vorticity. The velocity deficit caused by drag is confined to this narrow wake emerging from the trailing edge. It is argued that these filaments are diffused behind the rotor and are only a feature of the wake, so that they induced no velocity in the rotor plane. The momentum equations uses the induced velocities at the rotor plane and thus from the argument above the drag coefficient should not be used.

This argumentation requires the understanding and distinction of pressure drag and friction drag. Friction drag comes from the tangential component of the strain vector at the wall which arises from viscosity. Pressure drag is the result of the normal component of the strain vector. For profiled bodies at high Reynolds number, at a first approximation separation can be neglected and the pressure solution would be close to the one found for the corresponding potential flow[9]. The pressure drag force could then be neglected as a general result of potential flow. Nevertheless, the frictional drag associated with the viscous strain in the boundary layer is non zero and makes the most part of the total drag. In the contrary, when separation clearly occurs, the pressure drag is likely to be the predominant term in the total drag. The friction drag is barely dependent on the relative thickness of the profile whereas the pressure drag clearly is. Assuming attached flow at high Reynolds number then, the pressure drag could be considered as zero and thus the drag would not contribute to the pressure drop across the rotor. This analysis though is to be taken with care and its results can be argued.

Steady BEM Code patches BEM Code patches listed here with a minimum of detail. The representation as a list of different items should be taken with care as most of them are overlapping or interlinked.
- Momentum theory break down: The actuator disk stops all the fluid if $a = 1/2$, but this cannot be stored it has to flow away so correction is needed. The common corrections are the one from Spera or Glauert. Typically $C_T = f(a)$ inverted in $a = f(C_T)$
- Hub and tip losses due to 3D effects and the intrinsic generation of vorticity from the lift
- Corrections of airfoil coefficients accounting for 3D effects, extrapolation, smoothing of airfoil data

[9]For moderate Reynolds number though, the pressure drag due to the presence of the boundary layer, even if thin, can be quite important.

- Stall delay model accounting for some 3D effects

Each of these "patches" offers a different levers to correct for the difference between the simplified theory and the real situation. There are indeed different physical phenomenon observed such as centrifugal pumping, stall delay, tip losses, and it seems reasonable to treat these different problem independently, but obviously non-linearity in the overall problem will make the modelling and verification difficult. The different models mentioned above have proven good when combined all together in the BEM algorithm, but there is no guarantee that improving one model with more physical sense will make the overall BEM code more accurate.

1.3.5 Final remarks

Note on potential flows The 1D and 2D momentum theory relies on the assumption of potential flow, which mainly implies that the drag is zero. The blade element theory on the other hand does not have this constraint. Using both the simplified 2D momentum theory and the BET, the BEM equations should in theory be constraint to the absence of drag but nevertheless BEM codes are used with drag. The same apply to vortex theory which relies on potential flow, and vortex codes which are sometimes used as predictive wind turbine tools, using drag. All wind turbine codes all have to relax the assumptions on which they are based, hence loosing rigour and introducing potential inconsistency.

Pragmatic approach All of the above being kept in mind the physical problem of tip-losses will be investigated. Such investigation will require the observation of this phenomenon through experiments and simulation, together with an interpretation and understanding of its physics. By studying the different existing models, understanding their limitations and confronting them to different datasets, an insight of the challenges raised when modeling this problem will be acquired. Due to the different "BEM patches" acting as as many levers, a global view of the field of influence of each of them is necessary. Such analysis should eventually give suitable basis for trying to search for improvements.

Chapter 2

Theories of optimal circulation and tip-losses

2.1 Introduction

As seen in the historical review(Sect. 1.1), the notion of tip-losses appeared in the research of the optimal circulation distribution that would give the minimum losses for a given thrust. The theories from Prandtl and Munk[76] for the elliptical distribution applied on a finite-span wing are not described here. Nevertheless, the theories that apply for propellers and wind turbine directly follow their early analysis. The main articles presenting the optimal circulation for rotors are further studied below, including the one from Betz[9] with its comment from Prandtl[87], written in german, they are reported by Prandtl in english in [88]. Advised by Betz, Goldstein[36] extended the theory and the work of all the mentioned authors is reported by Glauert[35] in 1935.

All theories are based on a prescribed wake shape made of helix surfaces. For this reason, the literal, mathematical and physical formalism of the helical wake surface will be presented first before approaching the different theories. This introduction will also allow to tackle the different theories in a slightly more general way than presented originally by the authors. The following analysis is performed in light of the modern wind energy references such as [117, 17, 42], and modern research articles as [79, 80], and tries to reduce the confusion a reader can encounter when following the old and modern references with their different (sometimes implicit) assumptions.

2.1.1 Preliminary remarks and notations

Notes on old references Going through the old references on this subject requires a lot of care:

- The references uses different notations from one to another, which is of course not a big issue, but some of them are extremely confusing. As an advise, care should be taken when reading variables: r, r', x, λ, μ, h, l.

- The convention used in the old references is the convention for propellers, so that the axial induced velocity has actually an opposite sign to the one given in this document. Also, the longitudinal relative wake of a propeller is in the downwind direction whereas it is in the upstream direction for a wind turbine.

- Most references apply under the assumption of lightly loaded rotor, and omit the induce velocities in the velocity triangle. Some references mentioned as an appendix that their formulae should be modified to include the induced velocities. Two modifications are often mentioned an exact one, and an approximation. The exact one account for both induced velocity, whereas the approximation accounts only for the axial induced velocity.

Index notation To distinguish the theories between each authors, the first two letters of their last name are used as indices:

$$\begin{aligned} \text{Be} &\rightarrow \text{Betz} \\ \text{Pr} &\rightarrow \text{Prandtl} \\ &\text{etc.} \end{aligned}$$

Definitions When referring to the wake screw surface special care is required on the definitions and notations. Different notations and conventions are sometimes found between different publications[79, 80, 31], so that a clarification of notations and definition is presented on Tab. 2.1. Most definitions from Tab. 2.1 are summarized on Fig. 2.1 and 2.4.

Table 2.1: Notations and definitions for the wake screw surface. The lasts columns contain the notations used by Prandtl, Theodorsen and Okulov.

Definition		Expression	Units	Pr	Th	Ok
Pitch: longitudinal distance between two turns of the same surface	h	$2\pi r \tan\epsilon = \text{cst}$	[m]	h	H	h
Pitch angle: angle formed by the screw surface	ϵ	$\text{atan}\,\frac{dz}{rd\theta} = f(r)$	[rad]	ϵ		ϕ
Apparent pitch: longitudinal distance between two consecutive sheets generated by two consecutive blades	h_B	$\frac{h}{B}$	[m]			h
Normal distance: perpendicular distance apart of the edges of two consecutive blades' screw surface	s	$\frac{h}{B}\cos\epsilon_R$	[m]	a		
Torsional parameter: introduced in the mathematical formalism describing the helix	l	$\frac{h}{2\pi}$	[m]	r'		
Normalized pitch	$\bar{h}$	$\frac{h}{R} = \frac{2\pi l}{R}$	[.]			
Normalized torsional parameter or advance ratio	$\bar{l}$	$\frac{l}{R} = \frac{h}{2\pi R} = \tan\epsilon_R$	[.]		λ	l
wake relative longitudinal velocity	w	$f(u_{i_{z,w}}, u_{i_{\theta,w}}, \epsilon)$	[m/s]	w'	w	w
Axial induced velocity at the rotor	u_{i_z}	$f(w,\phi)$	[m/s]	w_a		u_{z_0}
Tangential induced velocity at the rotor	u_{i_θ}	$f(w,\phi)$	[m/s]	w_t		u_{θ_0}
Axial induced velocity in the wake	$u_{i_{z,w}}$	$f(w,\epsilon)$	[m/s]	w_a		u_z
Tangential induced velocity in the wake	$u_{i_{\theta,w}}$	$f(w,\epsilon)$	[m/s]	w_t		u_θ

Mathematical formalism of the helix In Cartesian and polar coordinates the equation of an helical sheet as function of a dimensionless parameter $\bar{t}$ is:

$$\begin{cases} x(\bar{t}) = r\cos\bar{t} \\ y(\bar{t}) = r\sin\bar{t} \\ z(\bar{t}) = l\bar{t} \end{cases} \leftrightarrow \begin{cases} r(\bar{t}) = r \\ \theta(\bar{t}) = \bar{t} \\ z(\bar{t}) = l\bar{t} \end{cases} \tag{2.1}$$

Using the polar coordinates, one finds that $\theta = z/l$ so that by definition the tangent of the pitch angle for an helix is:

$$\tan\epsilon = \frac{dz}{rd\theta} = \frac{l}{r} = \frac{h}{2\pi r} \tag{2.2}$$

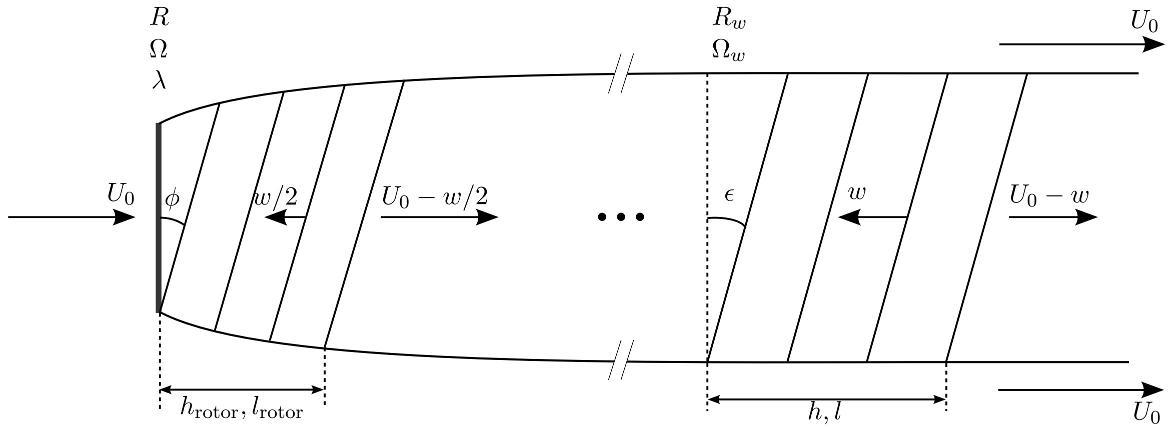

Figure 2.1: Side view of the helical wake behind a wind turbine. An important distinction is made between parameters from the near-wake and the far-wake

Introducing kinematics The wake vortex sheet rotates at an angular velocity Ω_w and moves downwind with the velocity $U_0 - w$, which means $\theta(t) = \Omega_w t$ and $z(t) = (U_0 - w)t$. By identification with Eq. (2.1), one finds $\bar{t} = \Omega_w t$, and $l = \frac{U_0 - w}{\Omega_w}$, so that the tangent of the pitch angle is:

$$\tan \epsilon = \frac{U_0 - w}{\Omega_w r} \leftrightarrow h = 2\pi \frac{U_0 - w}{\Omega_w} \leftrightarrow l = \frac{U_0 - w}{\Omega_w} \tag{2.3}$$

If one considers the sheet generated by the blade number b, then a phase offset should be added to the azimuthal coordinate as:

$$\theta(t) = \Omega_w t + \frac{2\pi(b-1)}{B} \tag{2.4}$$

The velocity triangles resulting from the kinematics study of the near and far wake helices is found on Fig. 2.2.

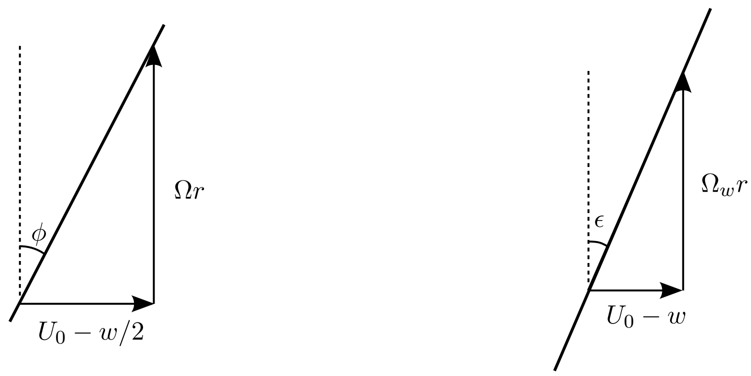

Figure 2.2: Velocity triangle resulting from the mathematical and kinematic study of helix. (left) Near wake - (right) Far wake

Boundary conditions on the screw surface On the screw surface, the motion imparted to the air is normal to the surface. This a known result for screws. The screw surface is moving at a velocity w along its axis. The velocity of the screw surface is entirely determined by the induced velocities on the surface itself.

Goldstein[36] considers the rotating frame in the far wake $(U_0, \Omega_w r)$ and writes the equality of

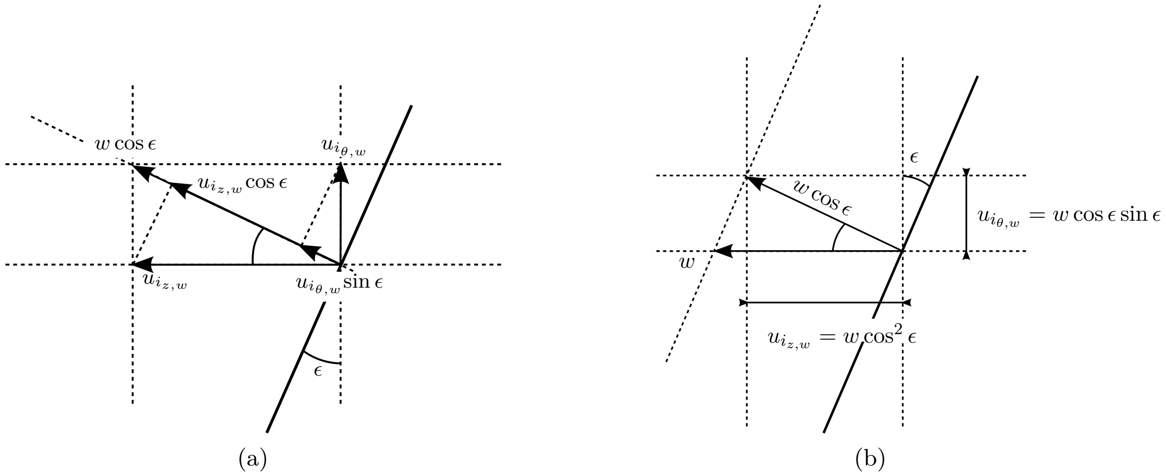

Figure 2.3: Induced velocity in the far wake. (a) Projections of velocities on the normal - (b) Induced velocities as function of the wake velocity w

normal velocities on the wake sheet as seen on Fig. 2.3a to get the relation:

$$w \cos\epsilon = u_{i_{z,w}} \cos\epsilon + u_{i_{\theta,w}} \sin\epsilon \tag{2.5}$$

which simplifies to

$$w = u_{i_{z,w}} + u_{i_{\theta,w}} \tan\epsilon \tag{2.6}$$

In the above equation, the velocity of the screw surface has been determined as function of the induced velocities. Looking at Fig. 2.3b, the induced velocities can be expressed as function of the screw velocity as well:

$$u_{i_{z,w}} = w \cos^2\epsilon \tag{2.7}$$

$$u_{i_{\theta,w}} = w \cos\epsilon \sin\epsilon \tag{2.8}$$

Inserting the boundary condition from Eq. (2.6) into the kinematic relation given by Eq. (2.3), leads to :

$$\tan\epsilon = \frac{U_0 - u_{i_{z,w}}}{\Omega_w r + u_{i_{\theta,w}}} \tag{2.9}$$

Nevertheless it will be seen that this relation is not used historically.

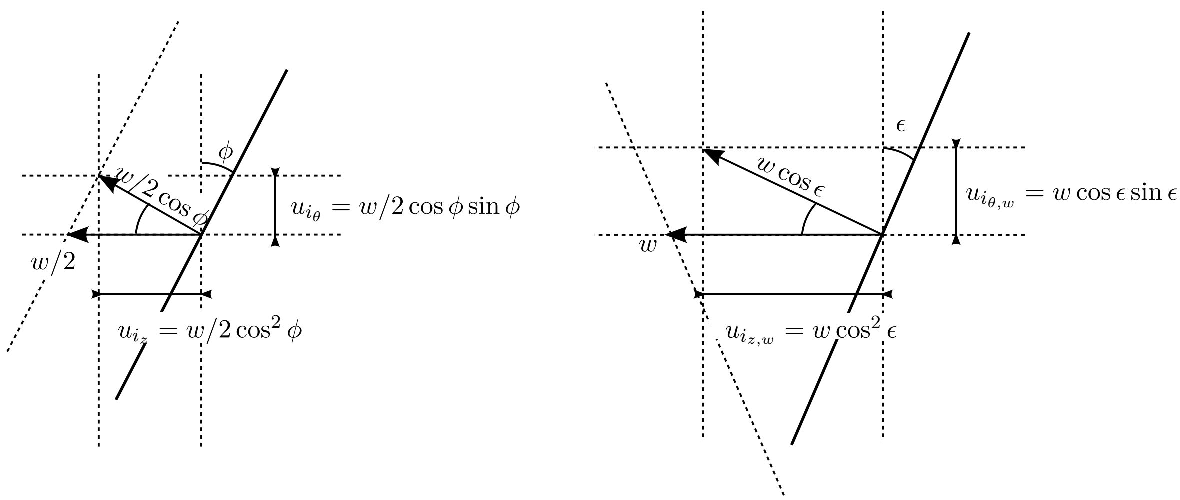

Figure 2.4: Near wake and far wake notations.

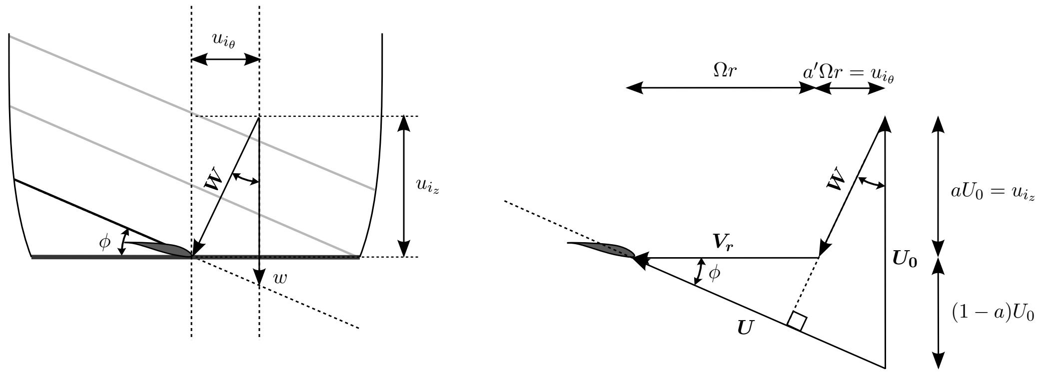

Figure 2.5: Velocity triangle at the rotor related to the near wake notations of Fig. 2.4

2.1.2 Relation with rotor parameters

One of the problem of the far wake analysis is that it uses values of parameters in the far wake. For this analysis to be usable in practise the far wake parameters should be linked to the parameters at the rotor. This is done in different ways in the literature.

Relation on induced velocities In absence of wake expansion, the induced velocities at the rotor are taken to be half the one in the far wake:

$$u_{i_\theta} = \frac{1}{2} u_{i_{\theta,w}} \;, \quad u_{i_z} = \frac{1}{2} u_{i_{z,w}} \tag{2.10}$$

Using the above equations and the definition of the flow angle yield to:

$$\tan\phi = \frac{U_n}{U_t} = \frac{U_0 - u_{i_z}}{\Omega r + u_{i_\theta}} = \frac{U_0 - u_{i_{z,w}}/2}{\Omega r + u_{i_{\theta,w}}/2} \tag{2.11}$$

It is reasonable to postulate that the flow angle at the rotor corresponds to the pitch of the screw surface at the rotor. Nevertheless, this angle will in general be different from the angular pitch in the far wake.

First relation used historically For simplicity, Prandtl, Betz and Goldstein define the wake screw surface such that its pitch angle is the ratio of the “velocity of flight” U_0 to the rotational velocity of the blade Ωr.

$$\tan\epsilon = \frac{U_0}{\Omega r} \leftrightarrow h = \frac{2\pi R}{\lambda} \tag{2.12}$$

Nevertheless, the three authors argued that the screw's pitch angle should be modified according to the induced velocity at the rotor in the following way:

$$\tan\epsilon = \frac{U_0 - u_{i_{z,w}}/2}{\Omega r - u_{i_{\theta,w}}/2} \tag{2.13}$$

Prandtl also mention that the following approximation can be useful:

$$\tan\epsilon = \frac{U_0 - w/2}{\Omega r} \tag{2.14}$$

In 1944, Theodorsen[108] expands Goldstein's theory to the case of highly loaded rotors by defining the tangent of the tip vortex angle in the ultimate wake as:

$$\tan\epsilon_R = \frac{U_0 - w}{\Omega R} \tag{2.15}$$

which is consistent with the kinematic relation Eq. (2.3) with $\Omega_w = \Omega$.

Relation in the general case In order to include all the possible situations discussed in the literature, generic variables will be used for the normal and tangential velocity which are used to assess the angle of pitch of the screw. The screw's pitch angle ϵ is written to be generically equal to:

$$\tan\epsilon = \frac{V_n}{V_t} \tag{2.16}$$

This should avoid repetition of formulae and unify the different studies and assumptions. The screw's pitch angle is allowed to be different from the flow angle ϕ at the rotor defined by Eq. (2.11):

This is introduced because of the difference of definitions presented in the previous paragraph concerning old references, and also because some authors (Lock[64], and Burton et al. [17]) argue that the vortex theory assumes no rotation of the inflow. This means that U_t and V_t should be allowed to be different. From the work of Theodorsen[108], the axial components U_n and V_n will be likely to be different as well.

Common modern relation Assuming the relative velocity of the wake behind the rotor is half the relative velocity in the far wake, with analogy with what has been done when studying the kinematics of the far wake, the near-wake pitch angle is set to;

$$\tan\phi = \frac{U_0 - w/2}{\Omega r} \tag{2.17}$$

The correponding pitch is then:

$$h_{\text{rotor}} = 2\pi\frac{U_0 - w/2}{\Omega} \tag{2.18}$$

The rotor tip speed ratio is easily introduced in this relation to give:

$$\lambda = 2\pi\frac{R}{h_{\text{rotor}}}\left(1 - \frac{\overline{w}}{2}\right) \tag{2.19}$$

with $\overline{w} = w/U_0$. The conservation of circulation across all cross section of the wake implies[80] that the pitch at the rotor is the same than the pitch at the far wake: $h_{\text{rotor}} = h$. The far wake pitch is hence introduced in Eq. (2.19):

$$\lambda = 2\pi\frac{R}{h}\left(1 - \frac{\overline{w}}{2}\right) = \frac{1}{\overline{l}}\left(1 - \frac{\overline{w}}{2}\right) \tag{2.20}$$

Equation (2.20) provides the missing relation required to link the rotor parameters λ, R to the far wake parameters h, w. It should be noted that Eq. (2.17) and the assumption $h_{\text{rotor}} = h$ will lead to inconsistencies such as $w = 0$ if h is assessed with the relations from Eq. (2.12) and (2.15) used at the beginning of the 20^{th} century by Prandtl and Theodorsen. Equation (2.20) assumes in general $\Omega_w \neq \Omega$.

2.1.3 Final remarks

Dimensionless circulation The circulation distribution will be made dimensionless: using the pitch of the helix h and the backward velocity of the wake w:

$$C_\Gamma = \frac{\Gamma}{hw} \tag{2.21}$$

Using $h = 2\pi r\tan\epsilon$ yields to :

$$C_\Gamma = \frac{B\Gamma V_t}{2\pi r w V_n} \tag{2.22}$$

In the particular case where $V_t = \Omega r$ and $V_n = U_0 + w$, which is used by [108, 79] it writes:

$$C_\Gamma = \frac{B\Omega\Gamma}{2\pi w(U_0 + w)} \tag{2.23}$$

In the particular case where $V_t = \Omega r$ and $V_n = U_0$, which is used by [36, 35] it writes:

$$C_\Gamma = \frac{B\Omega\Gamma}{2\pi w U_0} \tag{2.24}$$

Tip-loss factor The total circulation found by Betz, Γ_∞, is used as a reference case as it corresponds to an infinite number of blades. Obvisouly this is not a circulation per blade. If one uses the result of Betz and distributes it artificially over the B blades of the rotor, then each blade would have a reference circulation Γ_∞/B. For a given blade circulation distribution Γ, the tip loss factor is expressed with respect to the reference distribution[1]:

$$F = \frac{\Gamma}{\Gamma_\infty/B} \tag{2.25}$$

Dependency in r In the following, most parameters are dependent on the radial position r but this dependence is not formally written. Nevertheless, when parameters are evaluated at a particular position, like $r = R$, then this dependence is explicitly written.

2.2 Betz theory of optimal circulation

2.2.1 Betz's optimal circulation

In the following the results of Betz optimal circulation are presented. In a second time, elements of the demonstration are given but the reader is invited to refer to the original articles of Betz[9] and Munk[76] for a throughout understanding of the derivation of optimum lifting devises.

Assumptions 2.1:

(H 2.1a) - Inviscid, irrotational fluid

(H 2.1b) - Lighlty-loaded rotor

(H 2.1c) - Infinite number of blades

(H 2.1d) - Uniform flow

Betz[9] obtained the fact that for the optimum rotor, the flow far behind the rotor is the same as if the wake surface formed by the trailing vortices was rigid and moved downstream with a constant velocity. This assumption is hence added to the list above:

(H 2.1e) - Optimal rotor ("rigid wake")

Assumption (H2.1c) deserves a little attention regarding the definition of the circulation. If $\Gamma_B(r)$ designs the circulation around one blade at radius r, then the circulation for an infinite number of blade is

$$\Gamma_\infty(r) = \lim_{\substack{B\to\infty \\ \Gamma_B\to 0}} B \cdot \Gamma_B(r) \tag{2.26}$$

[1]This can of course be thought inversely as the comparison of the total circulation $B\Gamma$ with respect to the total circulation Γ_∞ of Betz's rotor

and the above limit is assumed to be finite. Historically, Betz uses the helix angle from Eq. (2.12), that will be replaced here for general purposes by Eq. (2.16). The boundary conditions on the "rigid wake" Eq. (2.8) and Eq. (2.7) then writes:

$$u_{i_{z,w}} = w\frac{V_t^2}{V_n^2 + V_t^2} \tag{2.27}$$

$$u_{i_{\theta,w}} = w\frac{V_n V_t}{V_n^2 + V_t^2} \tag{2.28}$$

Integrating the tangential velocity along a circle of radius r gives Betz optimum circulation:

$$\Gamma_\infty(r) = \int_0^{2\pi} u_{i_{\theta,w}} r d\theta = 2\pi r u_{i_{\theta,w}} = 2\pi\frac{wV_n}{\Omega}\frac{V_t^2}{V_n^2 + V_t^2} \tag{2.29}$$

Assuming this results apply for a rotor with B blades then the circulation of each blade is:

$$\Gamma_{\text{Be}} = \frac{\Gamma_\infty}{B} = \frac{2\pi}{B}\frac{wV_n}{\Omega}\frac{V_t^2}{V_n^2 + V_t^2} \tag{2.30}$$

which writes in dimensionless form:

$$C_{\Gamma_{\text{Be}}} = \left(\frac{V_t}{\Omega r}\right)\frac{V_t^2}{V_n^2 + V_t^2} \tag{2.31}$$

In the special and historical case of $V_t = \Omega r$ and $V_n = U_0$,i.e. using the helix angle from Eq. (2.12), the Betz circulation reduces to:

$$\Gamma_{\text{Be},0} = \frac{2\pi}{B}\frac{wU_0}{\Omega}\frac{\lambda_r^2}{1 + \lambda_r^2} \tag{2.32}$$

and in dimensionless form:

$$C_{\Gamma_{\text{Be},0}} = \frac{\lambda_r^2}{1 + \lambda_r^2} \tag{2.33}$$

2.2.2 Overview of Betz's demonstration

Betz demonstration relies on quite advanced statements and theorems which make the reproduction of the demonstration quite difficult. The major elements of the demonstration are here mentioned for reference.

- The "staggered theorem": This theorem derived by Munk states that the total drag of any lifting system is always independent of longitudinal coordinate of the lifting elements. These elements can be displaced in the direction of flight if the lift force stays the same(the angle of attack might change but not the effective angle of attack)[76]. An equivalent theorem was derived by Betz, though its formulation is more complex due to the fact that the vortex system considered has the shape of a screw. The result is that lifting elements can be displaced along the screw lines without changing the total energy-loss.

- The principle of determination of minimum induced drag found by Munk is somehow extended by Betz in terms of work loss(for wind energy, this translates to maximum power extraction). The basics of these two formulations consists in the consideration of two lifting elements. The optimal distribution of circulation is obtained if the displacements of these two elements(by means of the staggered theorem) while keeping the total thrust (or total lift in case of a wing) unchanged does not reduces the energy loss. By reductio ad absurdum, if this was not the case then the energy loss could be reduced using the new distribution of circulation. In the case of the wing, a condition of constant downwash along the span is found. In the case of a propeller, this conditions writes:

$$\frac{w_n}{r \sin \epsilon} = \text{cst} \tag{2.34}$$

- The last part of the demonstration consider the velocity component normal to a rigid screw surface moving at a constant streamwise velocity w. By using the formalism of helix and the definition of the pitch , a relation is found that takes the same form than Eq. (2.34). from this results, a suitable choice of the longitudinal velocity of the screw w can be made so that Eq. (2.34) is satisfied. In that case, $w_n = w \cos \epsilon$ and Betz condition writes:

$$\frac{w \cos \epsilon}{r \sin \epsilon} = \text{cst} \qquad \text{i.e.} \qquad r \tan \epsilon = \text{cst} \tag{2.35}$$

This leads to Betz results of the “rigid wake” analogy, which translated by Prandtl reads: “The flow behind a propeller having the least loss in energy is as if the screw surfaces passed over by the propeller blades were solidified into a solid figure and these were displaced backward in the non viscous fluid with a given small velocity”.

2.2.3 Inclusion of drag

In Glauert’s report[35], another derivation of Eq. (2.32) is found attributed to the work of Helmbold[44]. This derivation leads to the following form of solution:

$$\Gamma = \frac{2\pi}{B} \frac{U_0^2}{\Omega} A \frac{\lambda_r^2}{1 + \lambda_r^2} \tag{2.36}$$

Which is equivalent to Eq. (2.32) if A is taken as w/U_0. Glauert then follows a similar demonstration, in which he includes the effect of profile drag, assuming a constant lift over drag ratio $\varepsilon_{l/d}$ along the blade. In this case, the optimal circulation found is:

$$\Gamma = \frac{2\pi}{B} \frac{U_0^2}{\Omega} \left(A - \frac{\lambda_r}{\varepsilon_{l/d}} \right) \frac{\lambda_r^2}{1 + \lambda_r^2} \tag{2.37}$$

If $A = w/U_0$, then the above can be written in dimensionless form(different than Glauert’s one though):

$$C_\Gamma = \left(1 - \frac{\lambda_r w}{\varepsilon_{l/d} U_0} \right) \frac{\lambda_r^2}{1 + \lambda_r^2} \tag{2.38}$$

The author then argues that due to the high values usually taken by $\varepsilon_{l/d}$, the ratio $\lambda_r/\varepsilon_{l/d}$ is small near the root of the blade and thus the formula of optimal circulation Eq. (2.36) applies in this region. Going towards the tip though, the circulation reaches an optimal and falls to zero when $\lambda_r = A\varepsilon_{l/d}$. Once again, given the high values of $\varepsilon_{l/d}$, and the rather small tip-speed ratio values of wind turbine operations, it is likely that $\lambda < A\varepsilon_{l/d}$ and thus the circulation is non zero at the tip. The difference between the optimum circulation without drag ($\varepsilon_{l/d} = \infty$) and with drag is illustrated on Fig. 2.6. As expected, for high lift-over-drag ratio, the circulation is close to the optimal one without drag. The same is observed for higher inductions (i.e. A higher).

2.3 Generalized Prandtl’s theory

Assumptions 2.2:

(H 2.2a) - Inviscid, irrotational fluid

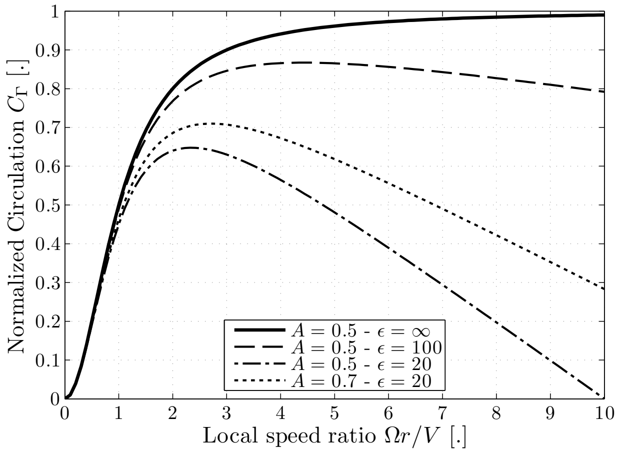

Figure 2.6: Betz's optimum circulation with and without drag with $\lambda = 10$.

(H 2.2b) - Lighlty-loaded rotor

(H 2.2c) - Finite number of blades

(H 2.2d) - Uniform flow

(H 2.2e) - The problem is approximated in 2D using a succession of semi-infinite aerofoils separated by a distance s

2.3.1 Qualitative description

In the case of the rigid wake screw with a large number of blades, the surfaces of the screw are close together and it can be assumed that under the lightly loaded assumption, the flow remain contained in the cylindrical slipstream. On the other hand, with a smaller number of blades, the flow will have a tendency to flow around the edges of the impermeable screw surface and a radial component appears on top of the rotational component. Fluid particles will go around the edges of the sheets weaving from one side of a sheet to the other. The lower the axial velocity of a particle, the closer it will get to the rotational axis.

Prandtl replaces the vortex sheets by material disks that will make the flow go around these disks in a similar fashion than described above. The material sheets introduced are moving with the velocity of the wake to ensure this model reproduce in its best the developed wake flow. The velocity of the wake being $U_0 - U_{i,w}$, and the free stream velocity U_0, then in the referential of the wake(i.e. the material sheets), the free stream flow will have the velocity $U_{i,w}$. For simplicity, azimuthal symmetry is assumed so that the problem reduces to two dimensions and the disks are replaced by semi-infinite lines. This model is illustrated on Fig. 2.7. A simple[2] conformal transformation exists that transforms this layout into a simpler flow so that the problem can be solved analytically(see Sect. 2.3.2).

The freestream particles weaves in and out between the sheets[17, p84] adding kinetic energy to the wake flow. The axial velocity will thus increase from the wake velocity to the freestream velocity when going towards the edge of the sheets. The more apart the sheets, the deeper the free-stream air would penetrate and the more kinetic energy is added to the wake flow.

The distance separating the disks, s, is taken as the normal distance between two helical sheets at the wake radius. This distance is thus a function of the number of blades and the pitch of the

[2] A conformal transformation always exists

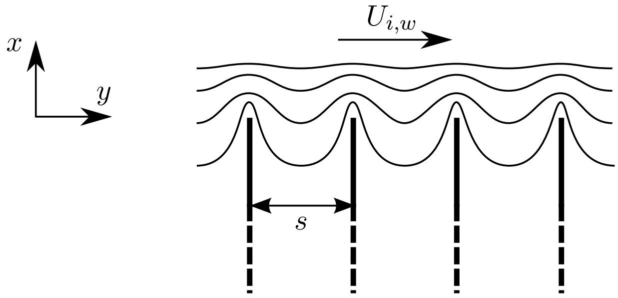

Figure 2.7: The system of material sheets introduced by Prandtl. This figure is drawn in the referential of the material sheets in which the relative velocity of the free stream is $U_{i,w}$.

wake-screw, which in turn is related to the tip speed ratio of the turbine[3]. As a result of this, for high tip speed ratio, the distance s is small compared to the rotor radius. From the above paragraph, a small distance between the disks will imply that the distance from the rotational axis where the wake velocity is unaffected by the free-stream is large. This is observed on Fig. 2.12a, where the effect of tip-losses is concentrated at the tip for large tip-speed ratios.

2.3.2 Detailed derivation of Prandtl's tip-loss factor

In the following the mathematical derivation of Prandtl tip-loss factor is done. The derivation present no difficulty but is not found in detail in any references to the author's knowledge. By looking at Fig. 2.8, the distance s is easily found to be:

$$s = \frac{h}{B} \cos \epsilon(R) \tag{2.39}$$

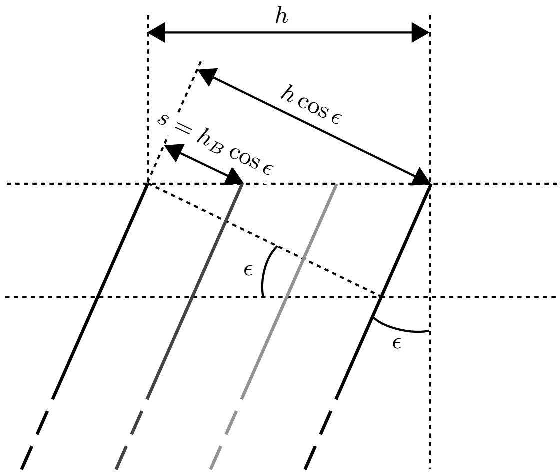

Figure 2.8: Distance between two helical vortex sheets at the "tip". Illustration for three blades

Determination of the conformal transformation The 2D plane of Fig. 2.7 will be further referred as the z-plane, using the complex coordinates $z = x + iy$. The system of material lines are then described with $x \in [-\infty \; ; \; 0]$ and $y = ks$, with $k \in \mathbb{Z}$. The idea is to find a conformal mapping that would transform the system of all material lines into another complex plane, the Z-plane, in which the system and hence the flow are simplified. The first simple mapping that could come into

[3] In which proportion this relation occurs is more complex. In most articles from the beginning of the 20^{th} century, this relation is taken as $\lambda = 1/\bar{l}$.

mind is the logarithm one which transforms concentric circle in the Z planes into parallel lines in the z planes. The problem is that the flow around an infinite number of concentric circles is not known so this idea should be discarded. Clearly a way to simplify the problem and remove the fact that an infinite number of lines are present should be found. By looking at the symmetry of the problem, and by the knowledge of the periodicity of the complex exponential function, this reduction can easily be done. Writing $y = k\pi\frac{s}{\pi}$, then the semi-infinite lines are transformed by the exponential to:

$$e^{\frac{\pi z}{s}} = e^{\frac{\pi x}{s}} e^{ik\pi} = e^{\frac{\pi x}{s}} \begin{cases} 1 & k \in 2\mathbb{Z} \\ -1 & k \in 2\mathbb{Z}+1 \end{cases} \tag{2.40}$$

Given the values of $x \in [-\infty\ ;\ 0]$, $e^{\frac{\pi x}{s}}$ covers the segment $[0\ ;\ 1]$, and $e^{\frac{\pi z}{s}}$ covers the segment $[-1\ ;\ 1]$. By using the transformation

$$z = \frac{s}{\pi} \log Z \tag{2.41}$$

the problem of reducing the complexity of the infinite number of lines has been solved. The problem reduces to determining the flow around a segment. This is a well known problem in fluid dynamics which is solved by using another conformal mapping: Joukowski's conformal mapping.

The most famous conformal mapping in aeronautics is the one from Joukowski, defined as :

$$z = \frac{1}{2}\left(Z + \frac{1}{Z}\right) \tag{2.42}$$

The idea is that the flow around a circle in the Z plane is analytically known by superposition of three elementary potential solutions: the uniform flow, a vortex and a doublet, the two latter being at the circle's center. All the circles considered by Joukowski intersect the real axis at coordinate 1. The transformation is such that depending on the location of the circle's center a different airfoil profile is obtained in the z plane by inverse transformation. The typical example is the one of the unitary circle, which is transformed by Eq. (2.42) into the segment $[-1\ ;\ 1]$. This is easily seen by inserting $Z = e^{i\theta}$ into Eq. (2.42).

$$z = \frac{1}{2}\left(e^{i\theta} + e^{-i\theta}\right) = \cos\theta \tag{2.43}$$

From the two paragraphs above the pieces are easily put together to derive the conformal mapping that transforms the infinite system of semi-infinite segments into the unit-circle around which the flow is known. The transformation writes:

$$z = \frac{s}{\pi} \log\left[\frac{1}{2}\left(Z + \frac{1}{Z}\right)\right] \tag{2.44}$$

It should be noted that the function $z(Z)$ is an injection which covers only two semi infinite lines if the complex logarithm is defined with an imaginary part in $[\pi\ ;\ \pi[$. A definition of the logarithm as function of the argument of Z should be used to cover the infinite number of lines, viz.

$$\log(re^{i\theta}) = \log r + i\theta \qquad \text{with } \theta \in \mathbb{R} \text{ and } r \in \mathbb{R}^+ \tag{2.45}$$

Determination of the complex velocity It was said above that the flow around a circle is known from the superposition of the infinite flow, a vortex and a doublet. In the current problem, only the induced velocities due to the circulation flow is sought so that only the vortex contribution is considered. It is recalled that the complex potential $\mathcal{F}$ is defined in term of the potential function Φ and the stream function Ψ as:

$$\mathcal{F}(Z) = \Phi + i\Psi \tag{2.46}$$

For a single vortex located at the origin the complex potential is known to be of the form:

$$\mathcal{F}(Z) = -i\frac{\Gamma}{2\pi}\log Z \tag{2.47}$$

where the circulation Γ is a constant to be determined. The variable Z can be eliminated between Eq. (2.44) and (2.47), to yield:

$$Z = \exp\left[\frac{2\pi}{\Gamma}(\Phi + i\Psi)\right] \tag{2.48}$$

Inserting Z back into Eq. (2.44) gives:

$$z = \frac{s}{\pi}\log\cos\left[\frac{2\pi}{\Gamma}(\Phi + i\Psi)\right] \tag{2.49}$$

The potential can be solved by considering the streamline $\Psi = 0$ which corresponds to the surface formed by the unit circle (or the equivalent vortex lines), and by equating the real parts:

$$\Phi = \pm\frac{\Gamma}{2\pi}\operatorname{acos}\exp\frac{x\pi}{s} \tag{2.50}$$

The uncertainty on the sign comes from the inversion of the cosine(cf. $\cos(x) = \cos(-x)$). The complex velocity w_Z in the Z plane is defined as $d\mathcal{F}/dZ$, which can be related to the complex velocity w_z in the z plane as:

$$w_z = \frac{d\mathcal{F}}{dZ}\cdot\frac{dZ}{dz} \tag{2.51}$$

The two parts of this product are:

$$\frac{d\mathcal{F}}{dZ} = -\frac{i\Gamma}{2\pi}\frac{1}{Z} \tag{2.52}$$

$$\frac{dz}{dZ} = \frac{s}{\pi Z}\frac{Z^2-1}{Z^2+1} \tag{2.53}$$

Eventually, the complex velocity in the z-plane is:

$$w_z = -i\frac{\Gamma}{2s}\frac{Z^2+1}{Z^2-1} \tag{2.54}$$

It should be remembered that the real velocity components are obtained by taking the conjugate of the complex velocity, i.e. $u = \operatorname{Re} w_z$ and $v = -\operatorname{Im} w_z$. In order to find a multiplicative factor for the velocity, Prandtl defines the potential in such way that the free stream velocity is equal to 1. Making $|Z| \to \infty$ in Eq. (2.54), this condition leads to the determination of the constant Γ as:

$$\Gamma = 2s \tag{2.55}$$

Equation (2.54) is enough to draw the streamlines around the vortex lines by using different concentric circles in the $Z-$plane. Nevertheless, this equation is a little disappointing for it expresses the velocity in the z plane as function of the Z coordinate instead of the z coordinate. It is possible to obtain a closed form equation but only between two vortex lines due to the fact that $z(Z)$ is an injection as was discussed above. This problem is of course minor because given the periodicity of the flow solving it between two lines is enough. Writing for simplicity $e = \exp(\pi z/a)$, and with the minimum rigor required, Eq. (2.44) is written:

$$Z^2 - 2Ze + 1 = 0 \tag{2.56}$$

which can be solved as:

$$Z = e \pm i\sqrt{1-e} \tag{2.57}$$

Using Eq. (2.56), Z^2+1 and Z^2-1 can easily be expressed and Eq. (2.54) writes:

$$w_z = \frac{e}{i\,(e-1/Z)} = \frac{\pm e}{\sqrt{1-e^2}} = \frac{\pm \exp\left(\frac{\pi z}{a}\right)}{\sqrt{1-\exp\left(\frac{2\pi z}{a}\right)}} \tag{2.58}$$

The velocity field found from Eq. (2.54)a is displayed on Fig. 2.9 for a series of concentric circles in the Z planes.

The work of Prandtl Using the scaling constant from Eq. (2.55), the velocity potential is:

$$\Phi = \pm\frac{s}{\pi}\,\mathrm{acos}\exp\frac{x\pi}{s} \tag{2.59}$$

The shape of the velocity potential is displayed in Eq. (2.54)b. Prandtl interprets the surface formed by this figure, which is the integral of the difference of potential along the vortex lines, as a factor which can be directly used for the determination of the lift(see examples of applications in e.g. [88]). From this point, the derivation of the tip-loss factor can be done in different ways. The induced velocities between two vortex lines can be integrated analytically. This was presented by Glauert and will be described in the next paragraph. Another way of seeing it consists in looking at the difference of potential on both side of a vortex line, which is related to the circulation. By dividing this difference by the distance between two vortex lines s, a factor between 0 and 1 is obtained, which corresponds to the tip-loss factor :

$$F = \frac{2}{\pi}\,\mathrm{acos}\exp\frac{\pi x}{s} \tag{2.60}$$

In his article[87] Prandtl uses this factor as a multiplicative factor for the optimal circulation found by Betz, viz:

$$\Gamma = F\cdot\frac{\Gamma_\infty}{B} \tag{2.61}$$

Prandtl also computes the distance of which the lines must be reduced in order to have the same overall losses but a constant velocity between the vortex lines. In the English version of his report[88] though, a typographic error is found, the correct expression of this distance being:

$$a' = \frac{s}{\pi}\log 2 \tag{2.62}$$

In the original papers $\log(2)/\pi$ is approximated by 0.2207, whereas a more accurate rounding would be 0.2206. Different ways of determining this factor are possible, by looking at the velocity, the potential, etc. A simple numerical way is to look at the area lost compared to unity:

$$a' = \int_{-\infty}^{0}(1-F)dx \tag{2.63}$$

For an analytical derivation it is easier to consider the velocity as done in[35].

The work of Glauert Instead of using the scaling to unity from Eq. (2.55), Glauert[35] uses the relative velocity outside of the system of lines that he writes v'. Equation (2.58) is simply modified by multiplying it by v'. From the discussion of Sect. 2.3.1, the relative velocity of the free stream outside the system of lines is $v' = U_{i,w}$. The notation v' will be kept below for harmony with this reference. Glauert uses Eq. (2.58) as a starting point to derive Prandtl's tip-loss factor. It will

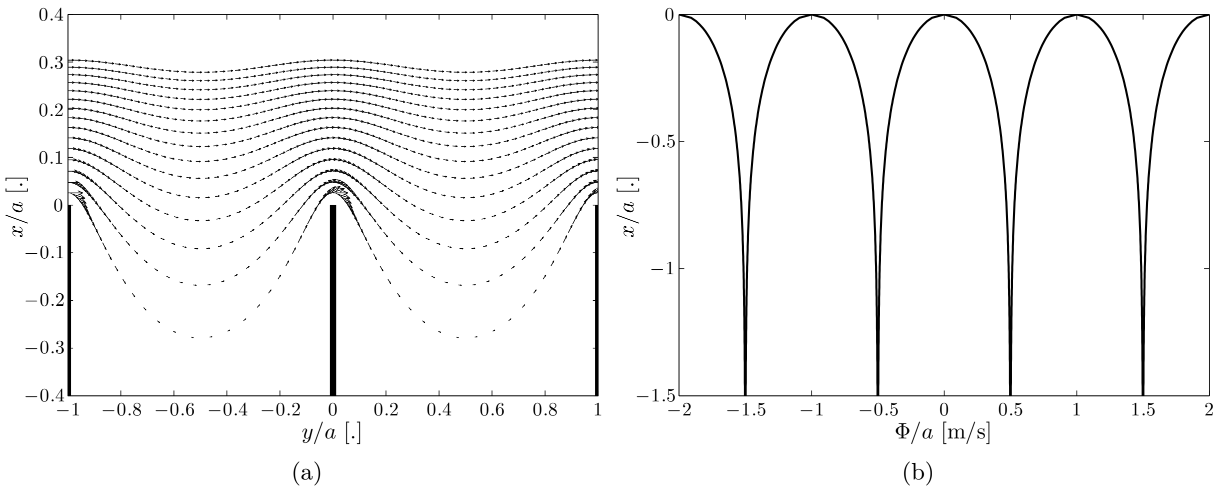

Figure 2.9: Prandtl velocity field and potential. (a) Velocity field around the vortex lines obtained using Eq. (2.54) for equidistant circles in the Z planes - (b) Surface formed by the velocity potential

be shown here how the two approaches are equivalent. The idea is here to compute the average longitudinal velocity between two vortex lines on a segment of abscissa x, i.e. the segment A-D seen in Fig. 2.10. This average velocity is computed as:

$$\overline{v} = \frac{1}{s}\int_0^s v\,dy = \frac{1}{s}\,I(AD) \tag{2.64}$$

where the notation $I(AD)$ has been introduced to represent the integral between points A and D. To evaluate this integral, one can use the chain rule with the intermediate points B and C displayed in Fig. 2.10.

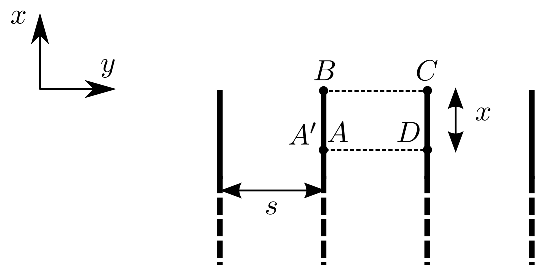

Figure 2.10: Definition of the points used to integrate the average velocity between two sheets.

Using our knowledge of the symmetry of the flow, and assuming that the velocity between B and C is constant equal to v', the evaluation of the integral is:

$$\begin{aligned} I(AD) &= I(AB) + I(BC) + I(CD) \\ &= I(AB) + I(BA') + I(BC) \\ &= 2I(AB) + I(BC) \\ &= 2I(AB) + v's \end{aligned}$$

The integral $I(AB)$ is easily derived using the change of variable $\cos\theta = \exp\left(\pi x/s\right)$:

$$I(AB) = \int_x^0 \frac{-v'\exp\left(\frac{\pi x'}{a}\right)}{\sqrt{1-\exp\left(\frac{2\pi x'}{a}\right)}}dx' = \frac{v's}{\pi}\int_{\text{acos}\exp(\pi x/s)}^{0} d\theta = -\frac{v's}{\pi}\,\text{acos}\exp\left(\frac{\pi x}{s}\right) \tag{2.65}$$

So that the average velocity eventually writes

$$\overline{v} = \frac{1}{s}\left(v's - 2I(AB)\right) = v'\left[1 - \frac{2}{\pi}\operatorname{acos}\exp\left(\frac{\pi x}{s}\right)\right] \tag{2.66}$$

from which the factor F is defined as:

$$F = \frac{2}{\pi}\operatorname{acos}\exp\frac{\pi x}{s} \tag{2.67}$$

Transferring Eq. (2.66) back to the referential of the ground velocity(i.e. adding $U_0 - v'$) and re-establishing our notation $v' = U_{i,w}$, the average velocity between two vortex sheets of the wake is:

$$\overline{U}_w = U_0 - FU_{i,w} \tag{2.68}$$

Using the 1D momentum theory results for the induced velocity in the far wake, $U_{i,w} = 2aU_0$, the above writes:

$$\overline{U}_w = U_0(1 - 2aF) \tag{2.69}$$

which is assumed to be extended to the rotor as well, viz:

$$\overline{U} = U_0(1 - aF) \tag{2.70}$$

Going back to the rotor geometry The system of vortex sheets in the z plane as an x coordinate that extends from $-\infty$ to 0. The analogy with the rotor is done by replacing x by $R-r$, so that eventually the tip-loss factor is derived as:

$$F = \frac{2}{\pi}\operatorname{acos}\exp\left[-\pi\frac{R-r}{s}\right] \tag{2.71}$$

Literal expression From the analysis above, the tip-loss factor is usually decomposed into two expressions interpreted as follow by Larrabee[59]:

$$F = \frac{\text{Average fluid velocity}}{\text{Vortex line velocity}} = \frac{2}{\pi}\operatorname{acos}\exp(-f) \tag{2.72}$$

$$f = \pi\frac{\text{Edge distance}}{\text{Vortex line spacing}} = \pi\frac{R-r}{s} \tag{2.73}$$

2.3.3 General expression

The demonstration done by Prandtl[87] is followed but this time in the idea of extending his work to the most general case where the tangent of the helix angle is determined by the arbitrary ratio of V_n and V_t. By doing so the following circulation is found:

$$\Gamma_{\mathrm{Pr}} = \frac{2\pi}{B}\frac{wV_n}{\Omega}\frac{V_t^2}{V_n^2 + V_t^2}\frac{2}{\pi}\operatorname{acos}\exp\left[-\pi\frac{R-r}{s}\right] \tag{2.74}$$

In this equation one recognizes the expression of Γ_∞ so that the tip-loss factor stands out easily:

$$F_{\mathrm{Pr}} = \frac{2}{\pi}\operatorname{acos}\exp\left[-\pi\frac{R-r}{s}\right] \tag{2.75}$$

The distance between two screw surface at the tip defines s as :

$$s = \frac{h(R)}{B}\cos\left(\epsilon(R)\right) \tag{2.76}$$

In the most general case the screw pitch h is not simply $2\pi U_0/\Omega$ as used by Prandtl, it actually depends on the radius and writes:

$$h(r) = 2\pi r \tan(\epsilon(r)) = 2\pi r \frac{V_n(r)}{V_t(r)} \tag{2.77}$$

This leads to the following general expressions for s:

$$s = \frac{2\pi R}{B} \sin(\epsilon(R)) = \frac{2\pi R}{B} \left. \frac{V_n}{\sqrt{V_n^2 + V_t^2}} \right|_{r=R} \tag{2.78}$$

and the tip-loss factor to be:

$$\begin{aligned} F_{\mathrm{Pr}} = \frac{2}{\pi} \operatorname{acos} \exp\left[-\frac{B}{2}\frac{R-r}{R\sin(\epsilon(R))}\right] &= \frac{2}{\pi} \operatorname{acos} \exp\left[-\frac{B}{2}\ \frac{R-r}{R}\ \sqrt{1+\frac{V_t^2(R)}{V_n^2(R)}}\right] \\ &= \frac{2}{\pi} \operatorname{acos} \exp\left[-\frac{B}{2}\left(1-\frac{\lambda_r}{\lambda}\right)\sqrt{1+\frac{V_t^2(R)}{V_n^2(R)}}\right] \end{aligned} \tag{2.79}$$

By using this general expression, it will be straightforward to unify all the different variation of the "Prandtl" tip-loss functions found in the literature. A list of these expressions will be provided in Sect. 2.3.4. Comparison between the optimal circulation of Betz and the one from Prandtl can be seen in Fig. 2.11. The effect of wind speed, tip-speed ratio and number of blades on the tip-loss factor can be seen in Fig. 2.12.

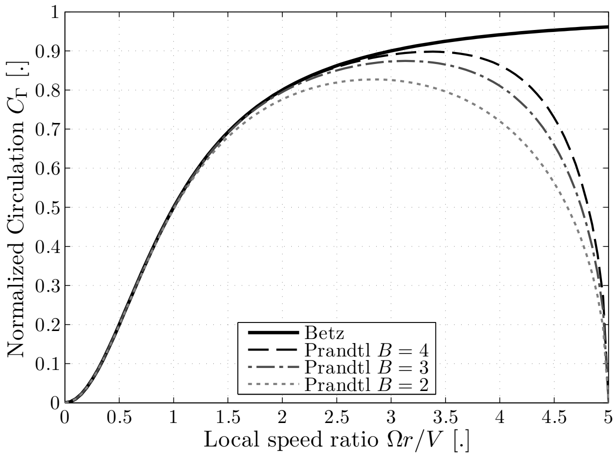

Figure 2.11: Comparison between Betz and Prandtl's circulation function.

2.3.4 Different uses of Prandtl's generalized tip-loss factor

From the general expression of Eq. (2.79), several expressions of the tip loss factor can be derived.

- Assume $U_n = V_n$ and $U_t = U_t$, then[4] $\phi = \epsilon$. This is the most common relation stated as a starting

[4] Modulo $2\pi\ldots$

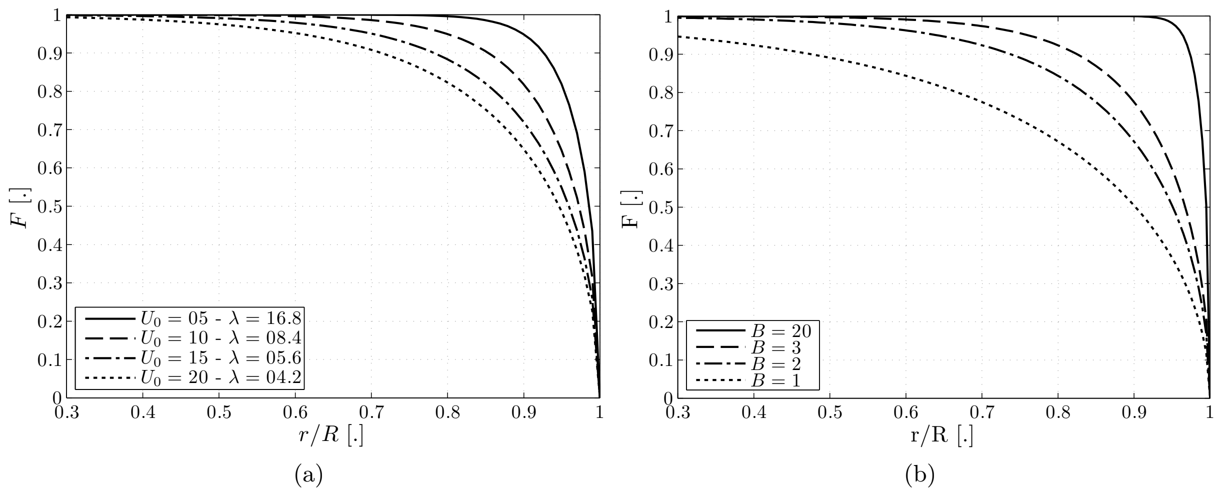

Figure 2.12: Prandtl's tip loss factor. (a) Influence of wind speed - (b) Influence of number of blades, for a constant $\lambda = 8$

point for Prandtl's tip loss correction:

$$F_{\mathrm{Pr},1} = \frac{2}{\pi}\operatorname{acos}\exp\left[-\frac{B}{2}\left(1-\frac{\lambda_r}{\lambda}\right)\frac{1}{\sin\left(\phi(R)\right)}\right] \tag{2.80}$$

- Assume $U_n = V_n = U_0$, $U_t = V_t = \Omega r$, then $\phi = \epsilon$. This results is the one originally found in Prandtl's article from 1919[87], and used by Goldstein[36] for comparison with his own theory:

$$F_{\mathrm{Pr},0} = \frac{2}{\pi}\operatorname{acos}\exp\left[-\frac{B}{2}\left(1-\frac{\lambda_r}{\lambda}\right)\sqrt{1+\lambda^2}\right] \tag{2.81}$$

- Assume $U_n = V_n$, $U_t = V_t$, and $R\sin\left(\phi(R)\right) \approx r\sin\left(\phi(r)\right)$. This is suggested by Glauert[35], and according to Wilson and Lissaman[117] it is also suggested by Lock[64]. The form below is as well found in the "Wind Energy Explained"[70]. It is the form used in most BEM code, supposedly more conveniently because the flow at the tip can be unknown while evaluating values at station r.

$$F_{\mathrm{Gl}} = \frac{2}{\pi}\operatorname{acos}\exp\left[-\frac{B}{2}\left(\frac{\lambda}{\lambda_r}-1\right)\frac{1}{\sin\phi}\right] \tag{2.82}$$

- Assume $U_n = V_n$, $U_t = V_t$, $R/\sqrt{U_n(R)^2+U_t(R)^2} \approx r/\sqrt{U_n^2(r)+U_t^2(r)}$, $U_t = \Omega r$(i.e. $a' = 0$), $U_n = U_0(1-a)$. This is done by Burton et al.[17] in the "Wind Energy Handbook".

$$F_{\mathrm{Bu}} = \frac{2}{\pi}\operatorname{acos}\exp\left[-\frac{B}{2}\left(\frac{\lambda}{\lambda_r}-1\right)\sqrt{1+\left(\frac{\lambda_r}{1-a}\right)^2}\right] \tag{2.83}$$

- Assume $V_n = U_0(1-a)$ and $V_t = \Omega r(1+a')$. This is the "exact" correction suggested by Betz and Prandtl in their articles [9, 88].

$$F_{\mathrm{Pr},2} = \frac{2}{\pi}\operatorname{acos}\exp\left[-\frac{B}{2}\left(1-\frac{\lambda_r}{\lambda}\right)\sqrt{1+\lambda^2\left(\frac{1+a'(R)}{1-a(R)}\right)^2}\right] \tag{2.84}$$

- Assume $V_n = U_0(1-a)$ and $V_t = \Omega r$. This is the "approximate" correction suggested by Betz and Prandtl in their articles [9, 88].

$$F_{\mathrm{Pr},3} = \frac{2}{\pi}\operatorname{acos}\exp\left[-\frac{B}{2}\left(1-\frac{\lambda_r}{\lambda}\right)\sqrt{1+\left(\frac{\lambda}{1-a(R)}\right)^2}\right] \tag{2.85}$$

- Assume $V_n = U_0(1 - \sqrt{F}\frac{a}{2})$ and $V_t = \Omega r(1 + 2\sqrt{F}\frac{a'}{2})$. This is an interesting suggestion from Lindenburg[62] to account for more realistic wake dynamics that will deserve a justification of the assumptions in Sect. 3.1.2.

$$F_{\mathrm{Li}} = \frac{2}{\pi}\,\mathrm{acos}\exp\left[-\frac{B}{2}\left(1 - \frac{\lambda_r}{\lambda}\right)\sqrt{1 + \lambda_r^2\left(\frac{1 + 2\sqrt{F_{\mathrm{Li}}}\,a'/2}{1 - \sqrt{F_{\mathrm{Li}}}\,a/2}\right)^2}\,\right] \tag{2.86}$$

The list is probably not an exhaustive list as some assumptions can be combined, it certainly appears confusing but should unify the different forms of tip-loss corrections accounted for the work of Prandtl and Glauert in the literature.

2.4 Goldstein's optimal circulation

Despite its relevancy for this study it is not in the scope of this report to explicit the article of Goldstein from 1929[36]. Instead, a short guide to read through this article is suggested because this theory is often left apart for its complexity whereas it provides a more suitable representation of the flow's potential than Prandtl's theory. The reader is thus invited to follow this short guide in Appendix A which is followed by a detailed description on how to calculate the Goldstein's factor using Okulov's method[79].

2.4.1 Goldstein's theory and its derivatives

The assumptions of Goldstein's work are as follow:

Assumptions 2.3:

(H 2.3a) - Inviscid, irrotational fluid

(H 2.3b) - Lighlty-loaded rotor

(H 2.3c) - Optimum rotor in Betz's sense("rigid wake" with constant velocity)

(H 2.3d) - Finite number of blades

(H 2.3e) - Uniform flow

(H 2.3f) - $U_n = V_n = U_0$, $U_t = U_t = \Omega r$

Goldstein used infinite series, sometimes referred as Kaptain series, to find a solution for the potential flow. The circulation found for a propeller with finite number of blades corresponding to a minimum energy loss in the slipstream for a prescribed thrust is obtained as[5]:

$$\Gamma_{\mathrm{Go}} = \frac{2\pi}{B}\frac{wU_0}{\Omega}\left[\frac{8}{\pi^2}\sum_{m=0}^{\infty}\frac{T_{1,\nu}\left(\nu\lambda_r\right)}{(2m+1)^2} + \frac{2}{\pi}\sum_{m=0}^{\infty}a_m\frac{I_\nu\left(\nu\lambda_r\right)}{I_\nu\left(\nu\lambda\right)}\right] \tag{2.87}$$

where $\nu = B\left(m + \frac{1}{2}\right)$. The corresponding tip-loss factor is thus:

$$\kappa = F_{\mathrm{Go}} = \left(\frac{\lambda_r^2}{1+\lambda_r^2}\right)^{-1}\left[\frac{8}{\pi^2}\sum_{m=0}^{\infty}\frac{T_{1,\nu}\left(\nu\lambda_r\right)}{(2m+1)^2} + \frac{2}{\pi}\sum_{m=0}^{\infty}a_m\frac{I_\nu\left(\nu\lambda_r\right)}{I_\nu\left(\nu\lambda\right)}\right] \tag{2.88}$$

This tip-loss factor was historically called the Goldstein factor and can be found noted as κ in several references[109, 85]. Using the formal calculator Mathematica[71], Goldstein's factor has been calculated for this study and an example of optimal circulation distribution for different tip-speed ratio is found in Fig. 2.13 for a two and three bladed rotor. It is seen that the difference

[5] See Appendix A

between Goldstein's and Prandtl's circulation distribution is reduced as the number of blades or the tip-speed ratio increases.

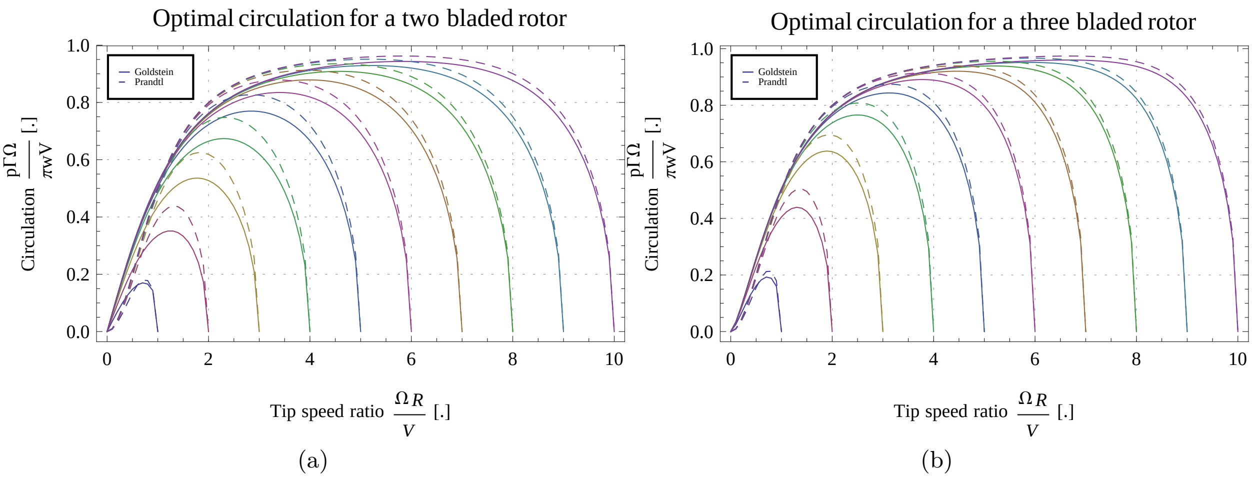

Figure 2.13: Comparison of Goldstein's circulation distribution with Prandtl's approximation for different tip-speed ratio. (a) Two bladed rotor - (b) Three bladed rotor. Prandtl's approximation is plotted using dashed lines. The computation of the infinite series was performed by the author using the software Mathematica

The work of Theodorsen In 1944, Theodorsen[108] presented a methodology for propeller design using Goldstein's theory. In his work though he uses $V_n = U_0 + w$ for a generalization of Goldstein's theory, to remove the assumption of lightly-loaded rotor. Theodorsen uses the following notation for his derived "Goldstein" tip loss factor:

$$G(r) = \frac{\Gamma(r)}{hw} \tag{2.89}$$

By doing so, wake expansion[79] and highly loaded rotor can be assumed to be studied using the Goldstein's function. The question remains on finding the link between the screw pitch angle and the tip-speed ratio as was discussed in Sect. 2.1.2.

2.4.2 Computation of Goldstein's factor

As mentioned at the end of Appendix A, the computation of F_{Go} requires care but is not unsuperables. Historical computation and tabulations include the work of Kramer in 1939[56], Tibery and Wrench in 1964[109]. Nevertheless, it has been observed that due do the slow convergence of the series, the computational time is quite important even for modern computers. In 1944, Theodorsen used the analogy with electromagnetism and used an experimental setup with different manufactured helical surfaces to measure Goldstein's factor.

Recently, the computation of this factor was carried out by modelling the wake-screw as the superposition of multiple single helical vortex filaments[79]. This method presents is fast, it presents no numerical issue and shows perfect agreement with tables from Tibery and Wrench[109]. A detailed description can be found in Sect. A.2 and the results from its implementation are displayed on Fig. 2.14 and A.2.

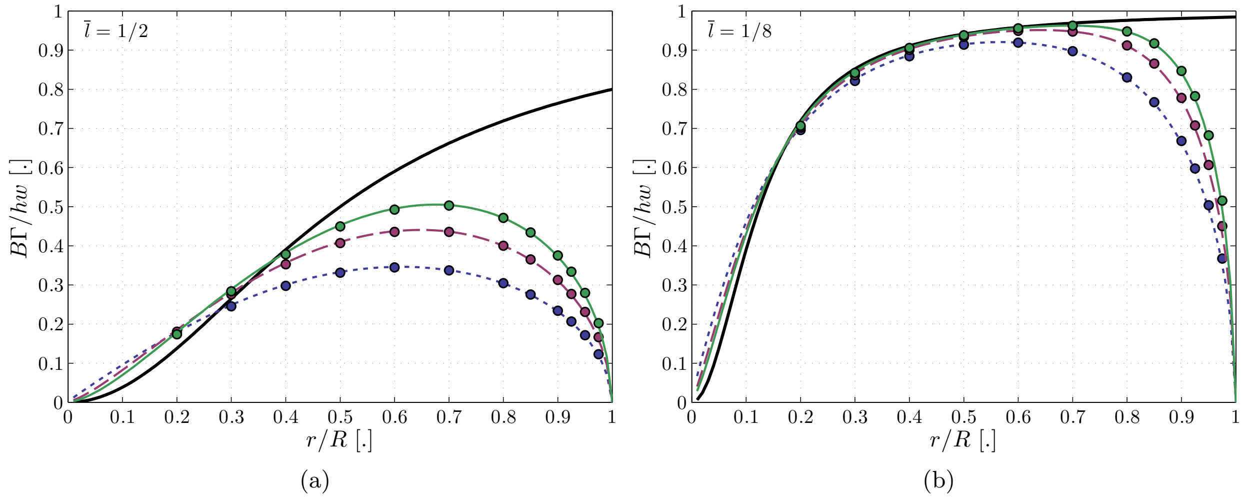

Figure 2.14: Comparison of Goldstein's circulation with Betz's circulation for different values of $\bar{l}$. (a) $\bar{l} = 1/2$ - (b) $\bar{l} = 1/8$. The computation of Goldstein's factor is performed using the superposition of helical vortex. In this case 150 vortices per blade were used. The thick line represent Betz's circulation. Goldstein's circulation is computed for $B = 2$(dotted), $B = 3$(dashed) and $B = 4$(thin). Dots are taken from the tables of Tibery and Wrench[109].

2.4.3 Comparison with Prandtl's factor

Figure 2.15 shows the comparison between the different circulation functions and tip-loss functions from the work of Betz, Prandtl and Goldstein for different tip-speed ratio.

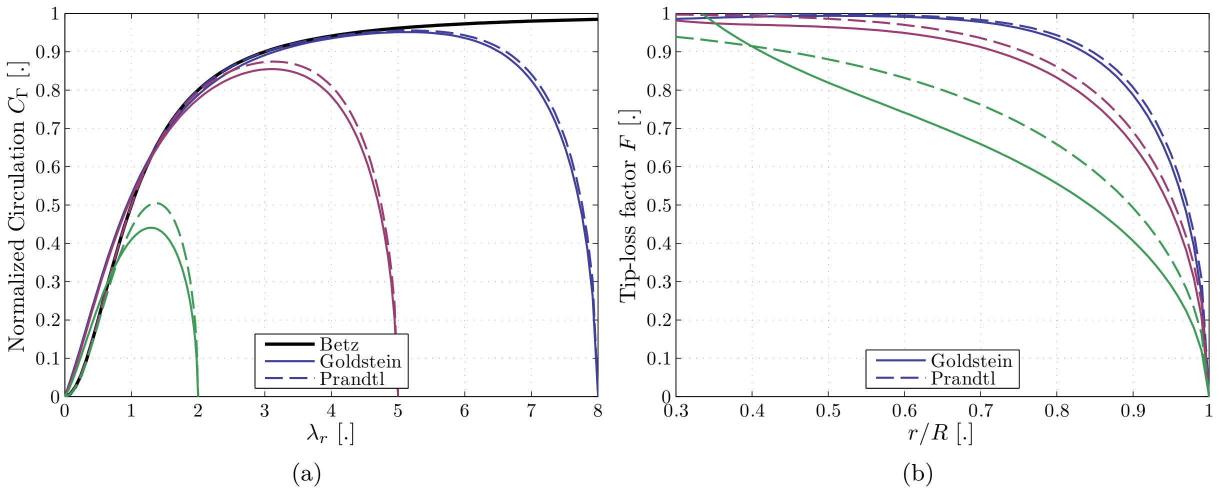

Figure 2.15: Comparison between Betz, Prandtl and Goldstein theory for a three bladed rotor. (a) Normalized Circulation - (b) Tip-loss factor. The colors represent the different values of tip speed ratio taken: 2,5 and 8. The computation of Goldstein's factor is done using Okulov's method. The link used between the tip-speed ratio and the helical pitch is: $h = 2\pi R/\lambda$.

Chapter 3

Tip-loss corrections and their implementation

3.1 Overview of the different tip-loss corrections

The main "theoretical" tip-losses correction have already been presented in chapter 2, they will be briefly repeated here for the sake of establishing a brief summary of the different tip-losses correction found in the literature. This time, empirical relation will be presented as well. The different ways to implement the tip-loss factor will be described in the following section(Sect. 3.2).

3.1.1 Theoretical tip-loss corrections

The derivations from these theories assume no expansion and distortion of the wake, which corresponds to the assumption of lightly-loaded rotors. It is recalled that λ is the tip-speed ratio, λ_r the local speed ratio and B the number of blades.

Prandtl's tip-loss correction Betz derived the optimal circulation for a rotor with infinite number of blades in [9] and as an appendix to his article Prandtl suggested a correction for a finite number of blades(reported in english in[88]). The tip-loss correction introduced by Prandtl is the following:

$$F_{Pr,0} = \frac{2}{\pi}\,\mathrm{acos}\left[\exp\left(-\frac{B}{2}\left(1-\frac{\lambda_r}{\lambda}\right)\sqrt{1+\lambda^2}\right)\right] \tag{3.1}$$

The reader is referred to Sect. 2.3.4 were several variations of Prandtl's tip-loss factor were presented.

Goldstein's tip-loss correction Using Goldstein's notations[36] of the T functions, the tip-loss correction derived by Goldstein writes:

$$F_{\mathrm{Go}} = \left(\frac{\lambda_r^2}{1+\lambda_r^2}\right)^{-1}\left[\frac{8}{\pi^2}\sum_{m=0}^{\infty}\frac{T_{1,\nu}\left(\nu\lambda_r\right)}{(2m+1)^2} + \frac{2}{\pi}\sum_{m=0}^{\infty} a_m \frac{I_\nu\left(\nu\lambda_r\right)}{I_\nu\left(\nu\lambda\right)}\right] \tag{3.2}$$

where $\nu = B\left(m+\frac{1}{2}\right)$. A detailed description of Goldstein's article can be followed in Appendix A.

Glauert's correction Contrary to Goldstein and Prandtl who focused on the optimal circulation, Glauert uses this correction in the Blade Element Method. Glauert reported[35] the work of Prandtl and derived the tip-loss correction in the following terms:

$$F_{Pr,1} = \frac{2}{\pi} \operatorname{acos}\left[\exp\left(-\frac{B}{2}\frac{R-r}{R\sin\phi_R}\right)\right] \tag{3.3}$$

where ϕ_R is the flow angle at the tip. The above formula is modified in most BEM codes as advised by Glauert to use the local flow angle ϕ instead, which leads to:

$$F_{\mathrm{Gl}} = \frac{2}{\pi} \operatorname{acos}\left[\exp\left(-\frac{B}{2}\frac{R-r}{r\sin\phi}\right)\right] \tag{3.4}$$

Several variations of Prandtl tip-loss factor including the one from Glauert were also presented in Sect. 2.3.4. Glauert uses this tip-loss factor to correct the axial induction factor a only, but does not uses this correction on the mass flux. This will be discussed in Sect. 3.2.

Just like Prandtl correction, Glauert's correction is accurate for low tip speed ratio and high number of blades. Its accuracy decreases as the tip speed ratio increases, or as the number of blade decreases (usually less than three). These statements can be observed for instance on Fig. 2.13 and 2.15.

3.1.2 Semi-Empirical tip-loss corrections

Xu and Sankar Xu and Sankar[92, 75] developed an empirical model based on CFD data simulating the NREL Phase VI experiment[40]. The empirical correction suggested for this specific wind turbine is the following:

$$F_{\mathrm{X,S}} = \begin{cases} \frac{1}{2}\left(F_{\mathrm{Gl}}^{0.85} + 0.5\right) & \text{when } r/R \geq 0.7 \\ 1 - \frac{r}{R}\frac{1-F_{\mathrm{X,S}}(r=0.7R)}{0.7} & \text{when } r/R < 0.7 \end{cases} \tag{3.5}$$

In this model the tip loss factor does no go to zero at the tip which is for some authors considered physically unrealistic whereas argued to be required by other authors.

Lindenburg The following correction is suggested in[62] for application in ECN codes PHATAS and BLADEMODE.

$$F_{\mathrm{Li}} = \frac{2}{\pi} \operatorname{acos}\exp\left[-\frac{B}{2}\left(1-\frac{\lambda_r}{\lambda}\right)\sqrt{1+\lambda_r^2\left(\frac{1+2\sqrt{F_{\mathrm{Li}}}\,a'/2}{1-\sqrt{F_{\mathrm{Li}}}\,a/2}\right)^2}\,\right] \tag{3.6}$$

This correction uses the velocity triangle just behind the rotor because, at it has already been seen in Sect. 1.1.3, this is the part of the wake which has the most influence on the induced velocities. The screw's pitch angle is assessed behind the rotor[1] where the radial velocity is $\Omega r(1+2a')$ and the axial velocity $U_0(1-a)$. Prandtl defines the pitch angle at the wake radius, but Lindenburg argues that the trailing vorticity is not concentrated at the tip, but rather distributed mainly over the outer part of the blade. As a result of this, the pitch angle is assessed using averaged induced velocities. In absence of tip vortex, the induced velocities from the momentum theory would be used (i.e. multiplied by 1), and in presence of a concentrated tip-vortex, the induced velocity should be multiplied by F according to Prandtl's theory. In between those two situations, to account for the distributed trailing vorticity, a factor of $\sqrt{F}$ is retained to assess the average tip-vortex velocity. Due to the recursion introduced, this factors is evaluated using the tip-loss value at the previous BEM iteration step. Moreover, in comparison with roller bearings between two surfaces, Lindenburg assumes that the tip vortices travel with a velocity averaged between the outside and the inside of the wake. This explains the factor $1/2$ applied on both induction factors.

[1] This definition differs from the pitch screw angle of Prandtl and Goldstein which are presumably considered in the far wake

3.1.3 Semi-Empirical performance tip-loss corrections

In this section tip-loss factors that applies to the airfoil coefficients are presented. The definition of such tip-loss factor was presented in Eq. (1.28). The implementation is discussed in Sect. 3.2.

Shen et al. A new correction is suggested by Shen[98] for which the flow angle at the tip is not zero but the forces tend to zero at the tip owing to pressure equalization between the upper and lower surface of the blade. This correction differ from the above in the way the tip-loss factor is applied. It is actually a second tip-loss correction applied this time on the airfoil data and which is is used together with the classical Prandtl's correction. The airfoil coefficients C_l and C_d, are indirectly corrected by multiplying the normal and tangential force coefficient, C_n and C_t, by a same factor F_{Sh}. Whether the drag should be included in the computation of the inductions is discussed, and eventually the drag is discarded(see Sect. 3.2). The correction takes a form similar to the one suggested by Glauert:

$$F_{C_n,\mathrm{Sh}} = \frac{2}{\pi}\operatorname{acos}\exp\left[-g(\lambda)\frac{B(R-r)}{2R\sin\phi_R}\right] \tag{3.7}$$

where

$$g(\lambda) = \exp\left[-c_1(B\lambda - c_2)\right] + c_3 \tag{3.8}$$

and the two first constants fitted from experimental data and the third one empirically suggested as $(c_1, c_2, c_3) = (0.125, 21, 0.1)$.

Lindenburg In [62] an empirical correction is suggested for the lift coefficient based on the NREL phase VI[40] experiment. This correction writes:

$$F_{C_l,\mathrm{Li}} = 1 - \left(\frac{\Omega r}{V_{\mathrm{rel}}}\right)^2 \cdot e^{-2\,\mathrm{AR}_{\mathrm{out}}} \cdot \frac{C_{l,\mathrm{inv}} - C_{l,\mathrm{2D}}}{C_{l,\mathrm{inv}}} \tag{3.9}$$

This formula as been adapted to the formalism of the current document(i.e. Eq. (1.28)), so that the 3D lift coefficient is obtained as:

$$C_{l,\mathrm{3D}} = F_{C_l,\mathrm{Li}} \cdot C_{l,\mathrm{2D}} \tag{3.10}$$

In the above, $C_{l,\mathrm{inv}}$ refers to the inviscid, or potential, 2D lift coefficient that Lindenburg suggests to take as $2\pi\sin(\alpha-\alpha_0)$, as in Eq. (1.23). Nevertheless, in Sect. 1.2.3, it was discussed by the author that such approximation is not suitable for wind turbines, and a method such as Eq. (1.25) is recommended to avoid having negative values of the difference of $C_{l,\mathrm{inv}} - C_{l,\mathrm{2D}}$ when the 2D slope is actually higher than 2π. The definition of $\mathrm{AR}_{\mathrm{out}}$ is the "aspect-ratio[2] of the part of the blade outboard of the section under consideration".

Sant Together with the stall delay correction presented in Sect. 1.2.3, Sant[93] suggest an engineering tip-loss correction for the NREL Phase VI rotor[40]. As for the Shen correction, the tip-loss factor is applied on the airfoil data, but this time, directly on C_l ad C_d. The corrective factor is given as:

$$F_{C_l,\mathrm{Sa}} = \frac{2}{\pi}\operatorname{acos}\exp\left[-18\frac{1-r/R}{r/R}\right] \tag{3.11}$$

[2] See Notations on page 3

It should be noted, that a root correction is also included in the original formula of Sant. Also, this correction is applied on the coefficients corrected for stall delay, which, according to Eq. (1.22) writes:

$$C_{\bullet,3D,\mathrm{Sa}} = F_{\mathrm{Sa}}\left[C_{\bullet,2D} + f_{\bullet,\mathrm{Sa}}\Delta C_{\bullet}\right] \tag{3.12}$$

with the symbol $\bullet$ referring to both L and D.

3.1.4 The historical approach of radius reduction

At the time where the BEM had to be computed manually, a common method to account for the tip-losses was to reduce the size of the rotor by a given factor. Prandtl[87] suggested for instance to reduce the rotor radius by his integrated factor:

$$\frac{R_e}{R} = (1 - \frac{\log 2}{\pi}\frac{s}{R}) \tag{3.13}$$

where $s = h/B\cos\epsilon(R)$ is the distance between two vortex-sheets in Prandtl's analysis of the tip-loss. Glauert[35] adapted this correction into the following:

$$\frac{R_e}{R} = 1 - \frac{1.386}{B}\frac{\lambda}{\sqrt{1+\lambda^2}} \tag{3.14}$$

In [106], the following radius correction are mentioned:

$$\frac{R_e}{R} = 1 - 0.5\frac{\overline{c}}{R} \tag{3.15}$$

where $\overline{c}$ is the average blade chord. Sissingh[100] suggested the following correction:

$$\frac{R_e}{R} = 1 - c_{\mathrm{root}}\frac{1 + 0.7e_{\mathrm{taper}}}{1.5R} \approx 1 - 3.56\frac{\overline{c}}{\pi R} \tag{3.16}$$

where c_{root} is the chord at the root of the blade and e_{taper} is the taper ratio defined as $c_{\mathrm{root}}/\overline{c}$. In 1944 Wald[106] presented a correction as function of the thrust coefficient:

$$\frac{R_e}{R} = 1 - 1.98\sqrt{\frac{C_T}{B}} \tag{3.17}$$

These corrections are now left apart due to the advancement of computers and the possibility to run fast BEM code computations.

3.2 On the applicability of the tip-loss factor

3.2.1 Introduction

Different interpretations The way the tip-loss factor is applied mainly depends on its definition. The following interpretations can be found:
- Circulation: the tip-loss can be seen as a loss in circulation compared to the circulation found with momentum theory.
- Induced velocities: the tip-loss factor can be applied to the induced velocities. The way this affect the momentum and the mass flow will be discussed below.
- Thrust coefficient: in a similar fashion than the circulation correction, the thrust coefficient can be corrected with the tip-loss factor.
- Airfoil coefficients: on top of the above corrections, a performance tip-loss factor is sometimes applied to the airfoil coefficients

In the following, the practical applicability and implementation of the tip-loss factor described by several authors in the literature will be presented. In a second time, different critics found in the literature will be mentioned to give a perspective of the debates the applicability of the tip-loss factor raises.

Axial induction To best follow the concepts used by the different authors, the distinctions on the axial induction factors that were used earlier in this document are recalled:
- $a = a(r, \psi)$ refers to the local axial induction at a given point on the rotor plane. The three dimensionality effects and the finite number of blades are accounted for.
- $\hat{a} = \hat{a}(r)$ refers to the 2D momentum theory axial induction, i.e. the axial induction for an actuator disk(infinite number of blades and no tip-losses). This is often simply written as a when presenting BEM equations (as was done in Appendix C). In this section, the distinction will be done for clarity.
- $\overline{a} = \overline{a}(r)$ refers to the azimuthally averaged axial induction defined by Eq. (1.3). At a first approximation, the results from the 2D momentum theory can be applied to an annulus, or stripe, using this average axial induction. Nevertheless, if the 2D momentum theory is applied on its own, the axial induction $\hat{a}(r)$ that would be found would be different than $\overline{a}$. Indeed for a 3D flow, with finite number of blades $\overline{a}$ decreases towards the tip. The two would match only if the circulation is constant along the blade.
- $a_B = a_B(r)$ refers to the axial induction at the blade. This should be used in the Blade Element Theory, to determines the proper velocity triangle and hence aerodynamic loads. Its definition is rather difficult due to the spatial extent of the blade and the strong variations of the flow around the blade due to the bound circulation.

The definitions and notations above are further extended to the tangential induction factor a'. From the above it is seen that a definition of the tip-loss factor as $F = \frac{\hat{a}}{a_B}$, $F = \frac{\overline{a}}{\hat{a}}$ or $F = \frac{\overline{a}}{a_B}$ can be envisaged. These distinctions will appear when studying the work of the different authors.

3.2.2 Applications in the literature

The equations from the BEM method presented in Appendix C have to be modified to introduce the effects of tip-losses. The tip-loss function is applied either on the circulation, the induced velocity or the thrust. The different ways this is performed in the literature is presented here without comments and argumentations on the validity of the application. The discussion is postponed to Sect. 3.2.3.

Glauert Glauert follows the demonstration of Prandtl's tip-loss factor(see Sect. 2.3), and hence look at this factor as a change in the longitudinal average induced velocity between two vortex sheets (vortex lines). Quoting his report[35, p267]:

> The physical fact represented by the tip correction is virtually that the maximum increase of axial velocity $2\hat{a}U_0$ in the slipstream occurs only on the vortex sheets and that the average increase of axial velocity in the slipstream is only a fraction F of this velocity. [...] Similarly also the angular momentum equation [...]

In this correction, it is the change of velocity between the upstream and wake velocity $U_0 - U_w = 2\hat{a}U_0$ which is corrected to $2\hat{a}FU_0$, not the velocity on the rotor. Following the momentum theory equations, this leads to the multiplication of the thrust and torque by the factor F as:

$$dT = \frac{1}{2}\rho U_0^2(2\pi r dr)\left[4\hat{a}F(1-\hat{a})\right] \tag{3.18}$$

$$dQ = \frac{1}{2}\rho U_0^2(2\pi r dr)r\left[4\hat{a}'F(1-\hat{a})\lambda_r\right] \tag{3.19}$$

From the above it is seen that the definition $F = \frac{\overline{a}}{\hat{a}}$ is used, which is to say that the azimuthally averaged axial induction $\overline{a}$ decreases towards the tip, which is not the case of the actuator disk axial induction $\hat{a}$. In the above $\hat{a}F$ should be replaced with $a_B F$ to correspond with Shen's analysis. The mass flux is not corrected here.

Wilson and Lissaman In their document from 1974, Wilson and Lissaman[117] present the same correction as Glauert. They also suggest a refinement by assuming that the axial mass flux should also be corrected due to tip-losses. From momentum theory, the mass flux expressed at the rotor in an annular element is $\dot{m} = \frac{1}{2}\rho dAU_0(1-\hat{a}(r))$. This flux is corrected in $\frac{1}{2}\rho dAU_0(1-F\hat{a}(r))$. The authors argue that this should affect the coefficient a but not a'.

$$dT = \frac{1}{2}\rho U_0^2(2\pi r dr)\left[4\hat{a}F(1-F\hat{a})\right] \tag{3.20}$$

$$dQ = \frac{1}{2}\rho U_0^2(2\pi r dr)r\left[4\hat{a}'F(1-\hat{a})\lambda_r\right] \tag{3.21}$$

The authors argue that the drag should not be used in the analysis therefore only C_l is used in this model for the blade element theory.In the above $\hat{a}F$ should be replaced with $a_B F$ to correspond with Shen's analysis.

De Vries To satisfy the orthogonality of the induced velocity with the relative velocity, De Vries derived a correction in the mass flux in the tangential momentum equation. Higher order corrections are also suggested which are beyond the scope of this report. For more information the reader should refer to the following reference[23].

Larrabee In his article from 1983[59], Larrabee suggests to modify the BEM equations by modifying the angle of attack by using an analogy with the lifting line theory. Larrabee provides a complex expression for the induced angle of attack as:

$$\alpha_i = \mathrm{asin}\left[\frac{1}{4}\frac{\sigma\sqrt{\lambda_r^2+1}}{F}\frac{\sqrt{(\lambda_r^2+1)\left\{\lambda_r^2+\left(1+\frac{w}{2U_0}\right)^2\right\}-\left(\frac{w}{2U_0}\right)^2}}{\lambda_r^2+\left(1+\frac{w}{2U_0}\right)^2}C_l\right] \tag{3.22}$$

which he approximates for small values of w/U_0 (i.e. low axial induction, lightly loaded rotor) with:

$$\alpha_i = \frac{1}{4}\frac{\sigma\sqrt{\lambda_r^2+1}}{F}C_l \tag{3.23}$$

Application using the circulation Phillips[85] uses the circulation to introduce the tip-loss correction. The circulation per blade can be calculated from the BEM code and corrected by a tip-loss factor. Such applications are nevertheless not used anymore.

Application on the airfoil coefficients If a correction is to be applied on the airfoil coefficients, no difficulty is found for the implementation. Depending on the interpretation chosen, the lift, the drag, the normal or the tangential coefficients are multiplied by a tip-loss factor. This tip-loss factor, referred in this document as performance tip-loss factor is physically different to the other one. There is no reason for instance for Prandtl tip-loss factor to be applied on the lift coefficients.

3.2.3 Critics in the literature

Wilson and Lissaman correction Shen et al. said there is an inherent inconsistency in this method if the chord is non-zero, because approaching the tip, $a_B \to 1$, $\phi \to 0$ but $C_l \to$ constant. The details of the demonstration and argumentation are found in Shen's paper[98]. De Vries also disagrees with Wilson and Lissaman's model because it does not satisfy the orthogonality condition between the induced velocity and the relative velocity.

De Vries correction Shen et al. showed that the inconsistency mentioned above for Wilson and Lissaman's model is also raised in De Vries model. It is also said that the use of De Vries correction gives results really close to the ones from Wilson and Lissaman.

3.3 Comparisons of the different tip-loss factors

In the following, different tip-loss functions are compared with respect to each other using a BEM code and a wind turbine model corresponding to the NREL rotor. The tip-loss implementation of Glauert has been chosen for all tip-loss factors except the one from Shen which has a specific implementation.

Important note In this study, not much time was used in the modelling of the NREL rotor. The results in this part do not intend to reproduce the results from the NREL phase six experiment. No corrections to the airfoil coefficients were applied, a constant rotational speed of 71.93 RPM was used for all simulation with a pitch of 5°.

3.3.1 Comparison for one BEM run

In a first time, the different tip-loss corrections are compared with respect to one BEM computation at 7m/s. The resulting axial induction, and angle of attack, tip-loss factor and normal loads are compared on Fig. 3.1. Eventually, the differences in power coefficient are found on Fig. 3.2.

.

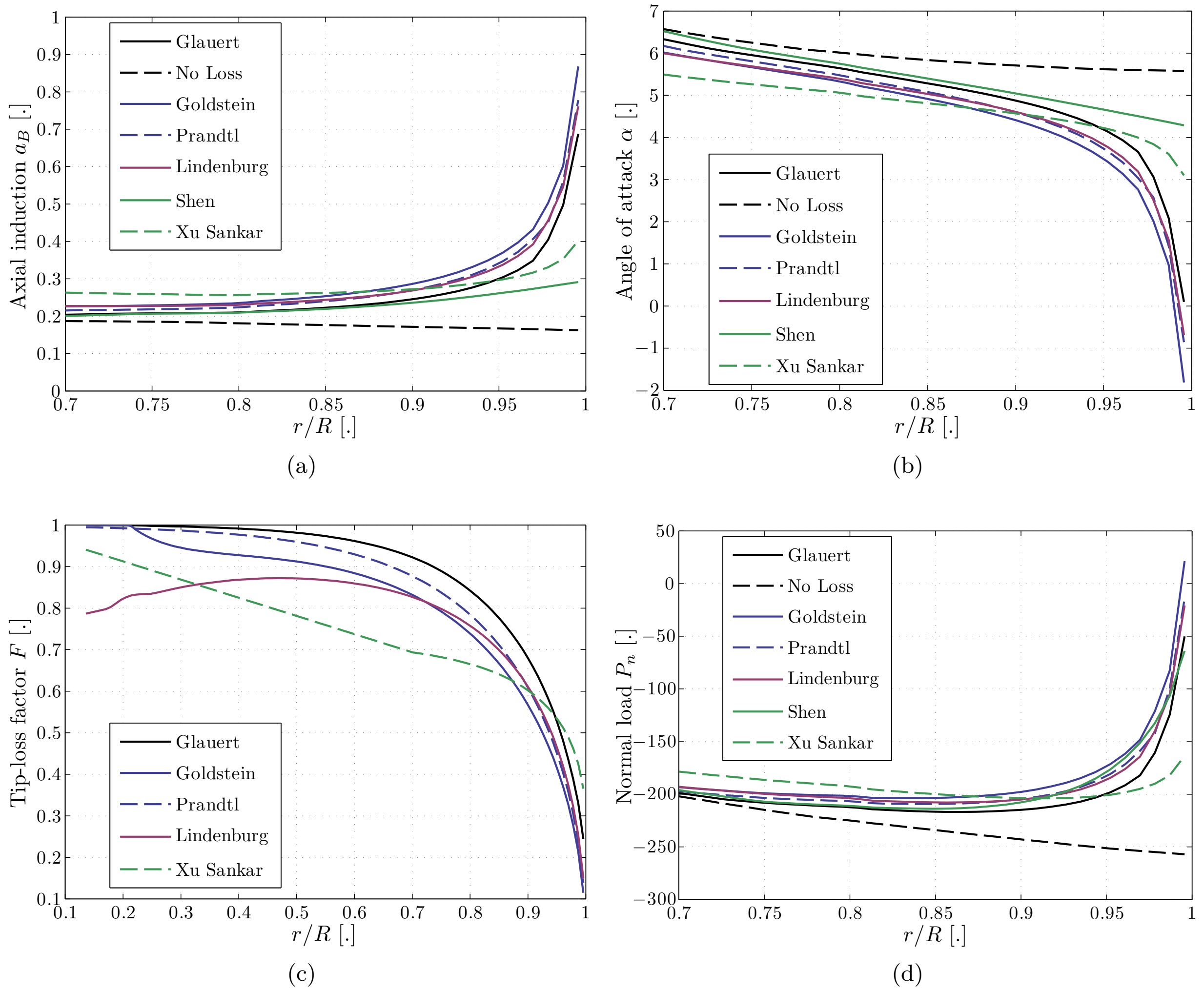

Figure 3.1: Comparison of the different tip-loss factors when used in a BEM code. (a) Axial induction - (b) Angle of attack - (c) Tip-loss factors - (d) Normal Load

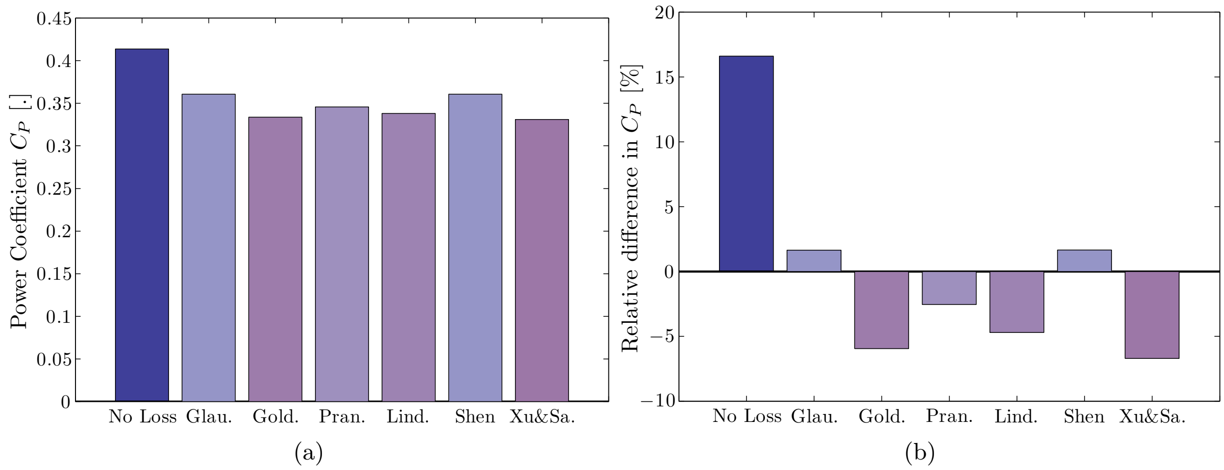

Figure 3.2: Differences in power coefficient when different tip-loss factors are used. (a) Power coefficient - (b) Relative difference between the power coefficient of one simulation and the mean value between all simulations

3.3.2 Impact on performances

A small impact study on the overall performance of the turbine when computed with a BEM code with different tip-loss factors is done. BEM simulations are performed for the operating range of wind speeds in order to derive a power curve as seen on Fig. 3.3a. Two different Weibull distributions(see e.g. [13]) are used for the assessment of the Annual Energy Output (AEP) as displayed on Fig. 3.3b. To derive the AEP from the aerodynamic power curve, losses of 0.03%

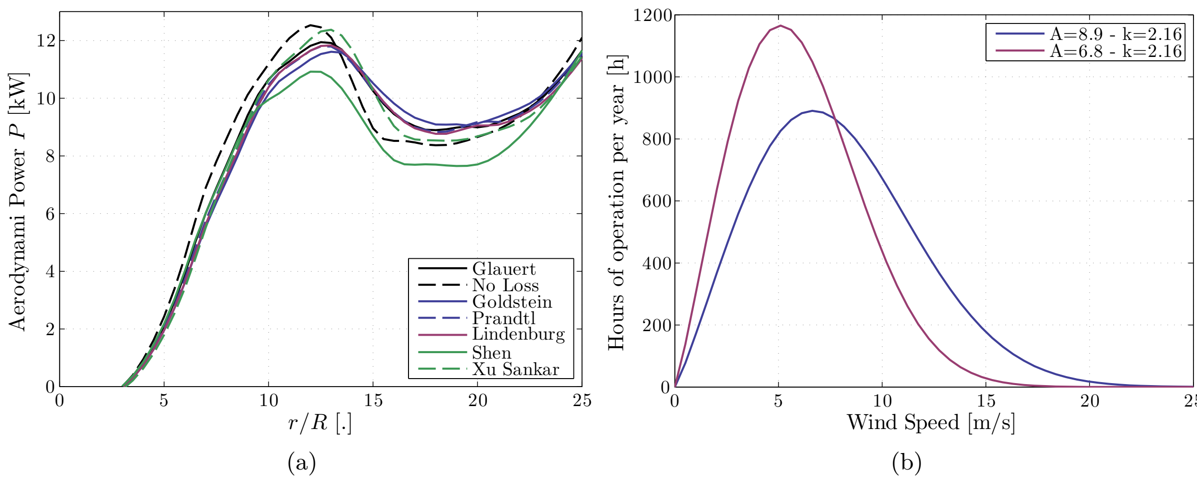

Figure 3.3: Power curves and wind distribution used for the computation of AEP. (a) Aerodynamic Power curves - (b) Weibull distribution expressed in hours of operation per year. Important variations in power curves are seen between the different tip-loss functions.

were assumed between the aerodynamic power and the electrical power and the wind turbine was assume to be operational 0.99% of the time. Results for the two different wind distributions are seen on Fig. 3.4 and on Fig. 3.5. As expected, strong variations in Annual energy production are found when different tip-loss factors are used. Two different wind distributions were used to illustrate that no conclusions should be drawn were comparing one tip-loss correction with respect to another: the relative differences in AEP for a same tip-loss factor can be quite different from one wind distribution to the other, as seen when comparing Fig. 3.4b with Fig. 3.5b and looking for instance at Shen and Xu&Sankar tip-loss correction results.

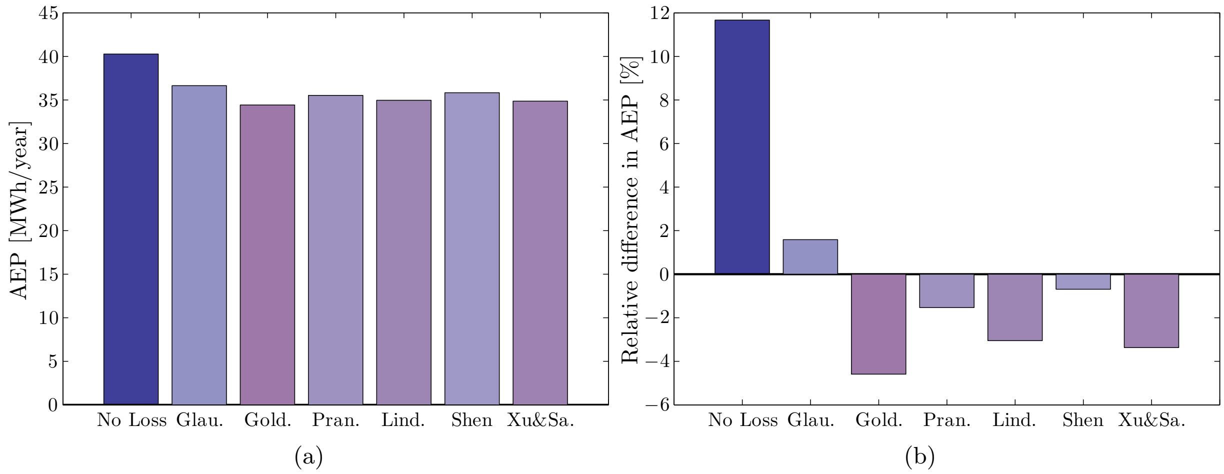

Figure 3.4: Annual energy production for the first wind distribution. (a) AEP - (b) Relative difference between the AEP obtained with one tip-loss factor with respect to the average between all the different simulations.

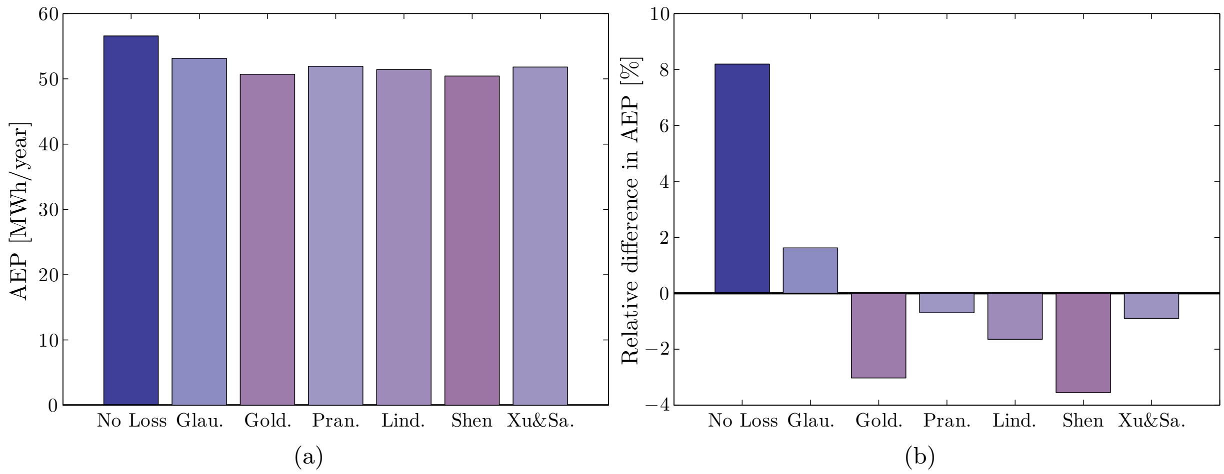

Figure 3.5: annual energy production for the second wind distribution. (a) AEP - (b) Relative difference between the AEP obtained with one tip-loss factor with respect to the average between all the different simulations.

3.4 New applications and methods

3.4.1 Possible new applications using the Goldstein factor

With the method described in Sect. A.2, the computation of Goldstein's factor is made at a really low computational cost and its use in BEM codes can be considered. The methods described below, and more certainly the second one, on how to implement the Goldstein's factor in a BEM code, are not known by the author to be present in the literature. The reading of Sect. 2.1.2 is advised for the considerations of the following paragraphs.

Simplest method - $F_{\mathbf{Go}} = F_{\mathbf{Go}}(\lambda, B) = F_{\mathbf{Go}}(\bar{l}, B)$ In its original form, the tip loss factor from Prandtl, $F_{\mathrm{Pr},0}$ was a direct function of the tip-speed ratio λ (see Sect. 2.3.4). The same can apply for the Goldstein function if Eq. (2.12) is used to relate the far-wake parameters to the rotor parameters. This relation writes $\lambda = 1/\bar{l}$, and it can be seen that under these conditions the Goldstein tip-loss factor $F_{\mathrm{Go}} = B\Gamma_{\mathrm{Go}}/\Gamma_\infty$ is independent of w, and a function of λ and B only. Using the numerical method described in Sect. A.2 or the engineering fit provided in Sect. A.4, the Goldstein circulation Γ_{Go} is computed. In this context the Betz circulation is

$$\Gamma_\infty = 2\pi \frac{wU_0}{\Omega} \frac{\lambda_r^2}{1+\lambda_r^2} \tag{3.24}$$

and the tip-loss factor is easily derived. This method was used for comparison of the Betz, Prandtl and Goldstein circulation on Fig. 2.15.

Iterative method - $F_{\mathbf{Go}} = F_{\mathbf{Go}}(\lambda, B, w) = F_{\mathbf{Go}}(\bar{l}, B, w)$ Using Eq. (2.20) to relate the far-wake parameters to the rotor parameters, then the Goldstein's factor is not anymore linear in w and an iterative method must be used to compute the tip-losses. In its simpliest form, the method would be:

1. Initialize $\overline{w}$ to 0. The computation of $F_{\mathrm{Go}} = F_{\mathrm{Go}}(\lambda, B)$ reduces to the method described in the previous paragraph, the dimensionless pitch is simply $\bar{l} = 1/\lambda$.

2. Perform BEM computation using the previously computed tip loss factor.

3. Compute a value for $\overline{w}$. Unlike the Betz theory, it is unlikely that the induction will be constant along the span, and thus velocity of the wake w is not a constant anymore. To match with the theory, w is kept a constant by defining it as e.g. the mean longitudinal wake induced velocity along the span[3]:

$$w = \int_0^{R_w} u_{i_{z,w}} dr \quad \rightarrow \quad \overline{w} \approx 2\int_0^R a dr \tag{3.25}$$

4. Compute a new value of $\bar{l}$ using Eq. (2.20):

$$\bar{l} = \frac{1}{\lambda}\left(1 - \frac{\overline{w}}{2}\right) \tag{3.26}$$

5. Compute the Goldstein circulation $\Gamma_{\mathrm{Go}} = \Gamma_{\mathrm{Go}}(\bar{l}, B, \overline{w})$ using the new values of $\bar{l}$ and $\overline{w}$.

[3]Other choice of relation than the mean can be considered

6. To eventually compute the new tip-loss factor $F_{\mathrm{Go}} = B\Gamma_{\mathrm{Go}}/\Gamma_{\infty}$, the Betz circulation is required. For the simplicity of the model this circulation is taken in its simpliest form from Eq. (3.24) but more general formulation such as the one presented in Sect. 2.2 can be considered.

7. Repeat steps 2-6 till the value of the pitch parameter $\bar{l}$ has converged.

The convergence of the process above is neither guaranteed nor enforced but the experience showed no divergence problem.

3.4.2 Further applications

In the following part of this study different methods to obtain and apply the tip-loss factor will be developed. Each of these methods and their applicability will be described in their corresponding sections: chapter 4, chapter 5.

Chapter 4

Using a vortex code to investigate tip-losses

4.1 Approach description

4.1.1 Introduction

During the period of time accorded to this study, a vortex code has been implemented to further study tip-losses. Different vortex code versions have been implemented as described in Sect. B.1. The wake geometry can be prescribed, set free, or set as a combination of the two. The influence velocities can be computed using line by line methods, or ring by ring methods. The blade can be modelled using several rings elements along the chord, or just one ring element so that the code reduces to a simple lifting-line code. Examples of applications of these different variation of vortex code and their validation can be found in Sect. B.2. In this section, the lifting-line version of the code is used. The first portion of the wake is set free and is progressively forming behind the rotor just like other unsteady free vortex code(e.g. AWSM[112]). Behind this free wake, a prescribed helical wake is attached to model the far wake.

The interest of such a vortex code is that it intrinsically contains or models 3D effects such as tip vortices, wake roll-up and expansion. As a result of this, this code does not need to be corrected with a tip-loss function as the BEM code. Contrarily, it can be used to determine the tip-loss function resulting from these 3D effects for further application in BEM codes. The methodology used to perform this is described in the following paragraph.

4.1.2 Method description

In order to find tip-loss functions that could be used for BEM codes, a representative samples of characteristics simulations need to be found. For this, the parameters expecting to influence the tip-loss function need to be found. The parameters selected are the circulation distribution along the blade and two “rotor state” parameters: the tip-speed ratio λ and the thrust coefficient C_T. The number of blade B has a critical importance, but it is here chosen to restrict this study to three bladed wind turbines. The idea is then to determine tip-loss functions for representative sets of these parameters so that these tip-loss functions can then be used directly for a BEM simulations which corresponds to a set of these parameters. The question that remains is to find a way to characterize all the different shapes of circulation that can be found in wind energy. Obviously to parametrize a curve that varies along the blade, several parameters will have to be used. This specific topic will be discussed in Sect. 4.2.

The vortex code can be run with a prescribed circulation, a defined tip-speed ratio and a defined geometry. The geometry dependence obviously has to be dropped for generality, and a way to circumvent the fact that the thrust coefficient is dependent on the circulation has to be found. The geometry dependence is only based on the rotor radius. The chord and twist distribution should not have an influence on the lifting line code which reduces the blade to a simple segment. An existing wind turbine geometry will be used, with the rotor radius scaled to unity. All the simulation will be run with this generic rotor which makes the definition of the tip-speed ratio somehow independent of the rotor radius. The second step is to solve the problem of interdependence between the total thrust coefficient and the circulation. To do this, the circulation as a parameter is normalized to unity. The thrust coefficient wanted for a given simulation will determine the multiplicative factor that should be applied to the normalized-circulation. To find this multiplicative factor prior to the vortex code simulation, a specific BEM code that takes as input a prescribed circulation was implemented. This BEM code uses no drag in his formulation according to the Kutta-Joukowski formula, so that the lift coefficient is determined as:

$$C_l = \frac{2\Gamma}{V_{\text{rel}} c} \tag{4.1}$$

An iterative procedure is used to find the multiplicative factor that should be applied to the normalized-circulation so that the BEM code returns the desired thrust coefficient for the right tip-speed ratio and normalized-circulation shape. This multiplicative factor is then used as input to the vortex code. At the end of the vortex code simulation, the thrust coefficient is computed to check if the right multiplicative constant was found. In all cases, the two thrust coefficients matched within less than 2% of error, hence validating the procedure.

Using the above approach, the vortex code was run for all the chosen characteristic sets of parameters. For each simulation, the tip-loss function was computed according to Eq. (1.26):

$$F = \frac{\langle a \rangle}{a_B}$$

In a lifting-line code the definition of the rotor plane is rather simple as it indeed reduces to a plane surface or a coned-surface if the rotor is coned. In this case, the typical rotor chosen does not have a cone angle as the context of applicability for a BEM code is the 2D momentum theory[1]. Each tip-loss function obtained is stored in a database for further use in a BEM code. The way this tip-loss function can be implemented in a BEM code is described in Sect. 4.3.3.

The advantages of such a method is that it will provide tip-loss functions more adapted to the rotor configuration than the specific and simplified function derived by Prandtl. This tip-loss function includes wake expansion effects, local aerodynamics on the blade, uses a realistic wake geometry (compared to the system of vortex planes of Prandtl). Other interesting aspects will be discussed in Sect. 4.3.3.

4.2 Family of circulation curves

In order to establish a database of tip-loss corrections for different family of circulation curves, a parametrization of these curves needs to be found.

[1]Of course, BEM codes are extended to coned rotor, but from the independence of the streamtube, the representation behind it is as if all the annular segments of the coned rotor where in the same plane.

4.2.1 Existing parametrization

In [33], a set of load cases are generated to study the aerodynamic performance of rotors with winglets using a prescribed and a free wake code. The circulation is modelled at the tip and root using the form of Prandtl hub and tip-loss factor. Further, a spanwise linear variation of the circulation is added to load the tip and the root in different ways. The model takes the form:

$$\Gamma = F_{\text{tip}} \cdot F_{\text{root}}, \Gamma_{\text{lin}} \tag{4.2}$$

with

$$F_{\text{tip}} = \frac{2}{\pi} \operatorname{acos} \exp\left(-C_{\text{tip}}(1-\overline{r})\right) \tag{4.3}$$

$$F_{\text{root}} = \left[\frac{2}{\pi} \operatorname{acos} \exp\left(-C_{\text{root}}\overline{r}\right)\right]^{1.5} \tag{4.4}$$

$$\Gamma_{\text{lin}} = \overline{r}\Gamma_{\text{tip}} + (1-\overline{r})\Gamma_{\text{root}} \tag{4.5}$$

The author defines the constants as function of the tip-speed ratio and uses multiplicative constants to define different load case scenarios. Examples of load cases as defined in the original reference[33] can be found on Fig. 4.1.

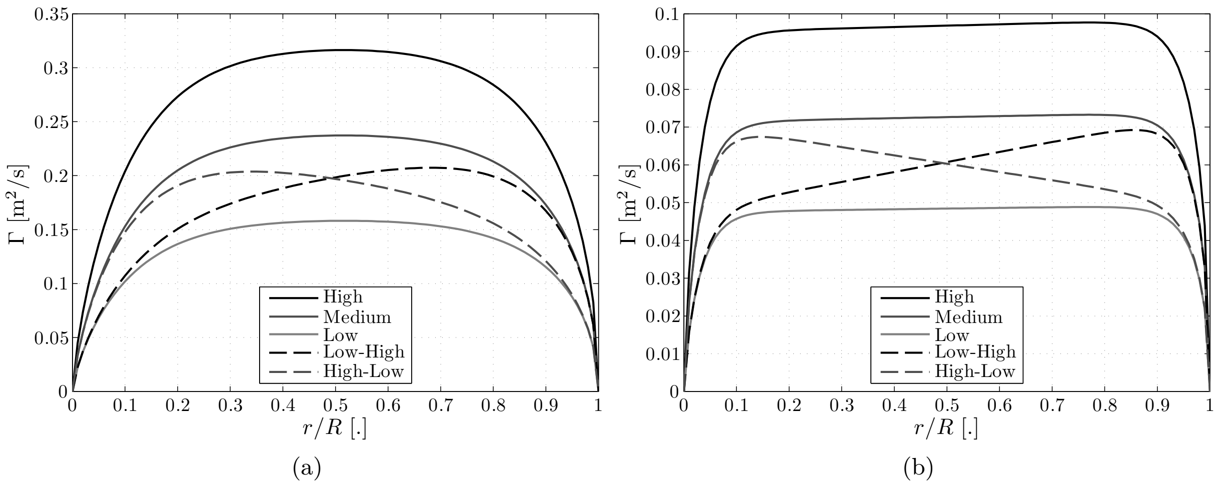

Figure 4.1: Different circulation translating different loading cases for two different tip-speed ratios. The model from [33] has been used. The constants in Eq. (4.2) have been determined in the same way than the original author to define the different loading cases: High, Medium, Low, High-Low and Low-High. (a) $\lambda = 3$ - (b) $\lambda = 10$

4.2.2 Parametrization using Bézier curves

Examples of modelled circulation have been seen on Fig. 4.1 and more examples from existing blades can be found on Fig. 4.4. From the variety of shapes the circulation curve can take, an explicit mathematical formalism is hard to find to parametrize all of them. From the knowledge of Bézier curve, it has been decided to develop a curve-fitting method to parametrize circulation curves using this formalism. The formalism of Bézier curve is attributed and named after French engineer Pierre Bézier who used them for the body design of the Renault car in the 1970's. Since then, they have been used by the drawing industry for fonts and vectorial drawing. The parametric

Bézier curve function defined by n control points P_k in any vectorial space is

$$B(t) = \sum_{k=0}^{n} \frac{n!}{k!(n-k)!} t^{n-k}(1-t)^k P_k \tag{4.6}$$

where t evolves in $[0\ ;\ 1]$. Given the complexity of the circulation curves, and the double change of concavity that could occur, a minimum of five control points seems to be required to model them. For $n = 5$, Eq. (4.6) develops as:

$$B(t) = (1-t)^4 P_0 + 4t(1-t)^3 P_1 + 6t^2(1-t)^2 P_2 + 4t^3(1-t) P_3 + t^4 P_4 \tag{4.7}$$

In two dimensions, a total of 10 parameters defining the coordinates of the points P_k determines the shape of the curve. An illustration of a Bézier curve with five points is plotted on Fig. 4.2.

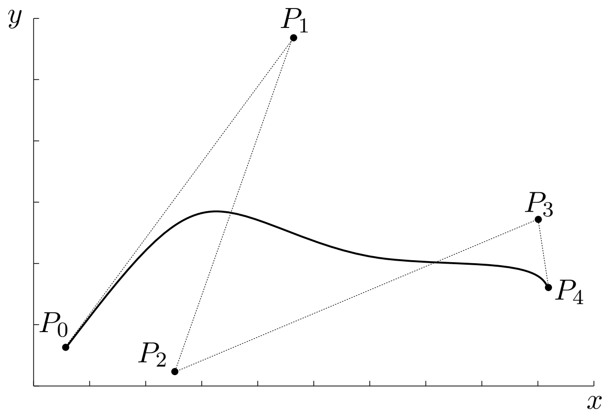

Figure 4.2: Bézier curve defined by five points. Illustration and notations. The curve always passes through the end points and is tangent to the line between the last two and first two control points.

A further reduction of the number of parameters or unknowns is now to be performed. The circulation curves will be described in the square-unity with the first points being located at $(0, 0)$ and the last point at $(1, 0)$. With these two assumptions four unknowns are dropped and the curve is now determined by six parameters. Writing Eq. (4.7) along the x and y coordinates leads to:

$$x(t) = 4t(1-t)^3 x_1 + 6t^2(1-t)^2 x_2 + 4t^3(1-t) x_3 + t^4 \tag{4.8}$$
$$y(t) = 4t(1-t)^3 y_1 + 6t^2(1-t)^2 y_2 + 4t^3(1-t) y_3 \tag{4.9}$$

The slope of the tangent at any regular points, if defined, is $m(t) = y'(t)/x'(t)$. For clarity, the derivative are explicitly written:

$$x'(t) = 4(1-t)^2(1-4t)x_1 + 12t(1-t)(1-2t)x_2 + 4t^2(3-4t)x_3 + t^4 \tag{4.10}$$
$$y'(t) = 4(1-t)^2(1-4t)y_1 + 12t(1-t)(1-2t)y_2 + 4t^2(3-4t)y_3 \tag{4.11}$$

For convenience, two other parameters, t_0 and x_0 are added as they will ironically make the reduction of parameters easier. These parameters define the maximum of the curve such that:

$$\begin{aligned} m(t_0) &= 0 \\ x(t_0) &= x_0 \\ y(t_0) &= 1 \end{aligned} \tag{4.12}$$

Dummy variables $a - h$ which are purely determined by t_0 are used in the following to simplify notations. They are defined through:

$$x(t_0) = ax_1 + bx_2 + cx_3 + g \tag{4.13}$$
$$y(t_0) = ay_1 + by_2 + cy_3 \tag{4.14}$$
$$x'(t_0) = dx_1 + ex_2 + fx_3 + h \tag{4.15}$$
$$y'(t_0) = dy_1 + ey_2 + fy_3 \tag{4.16}$$

From the knowledge of Bézier curves and the shapes of the circulation curves it is further assumed that the point P_3 will lay parallel to the y axis, and thus $x_3 = 1$. Developing and solving Eq. (4.12) leads to an expression for three parameters:

$$y_2 = \frac{1}{db/a - e}\left(\frac{d}{a} + y_3\left(f - \frac{dc}{a}\right)\right) \tag{4.17}$$
$$y_1 = \frac{1}{a}\left(1 - by_2 - cy_3\right) \tag{4.18}$$
$$x_1 = \frac{1}{a}\left(x_0 - bx_2 - c - g\right) \tag{4.19}$$

The problems is now reduced to four parameters (x_0, x_2, y_3, t_0) with

$$x_0 \in [0\ ;\ 1] \tag{4.20}$$
$$x_2 \in [-\infty\ ;\ 1] \tag{4.21}$$
$$y_3 \in [0\ ;\ +\infty] \tag{4.22}$$
$$t_0 \in [0\ ;\ 1] \tag{4.23}$$

Reduction constraints are added in order to reproduce realistic curves:

$$y_1 \in [0\ ;\ +\infty] \tag{4.24}$$
$$x_1 \in [0\ ;\ x_0 y_1] \tag{4.25}$$
$$\tag{4.26}$$

Other empirical constraints have been added to reduce the number of parameters sets based on the fitting of existing circulations. An example of the different curve shapes that can be obtained with this parametrization is displayed on Fig. 4.3 for $x_0 = 0.2$. The set of parameters used for this plot can be found on Tab. 4.1. Out of the 1089 different combination of parameters, 63 are retained with the added constraints discussed above.

4.2.3 Illustration of the parametrization using existing circulation curves

In order to demonstrate the wide range of applications of the parametrization described in Sect. 4.2.2, different circulation curves are fitted against this model. The original circulation curves are scaled to fit in the square unity by dividing them by their maxima Γ_0 and by reducing the radial blade span to $[0\ ;\ 1]$. A least square difference criteria between the fitted and the original curves is used to determine the set of parameters best describing the original circulation. Examples of circulation curves fitting are shown on Fig. 4.4. It can be seen that the parametrization is well suited for all different kind of circulation shapes.

Important note on the fit It should be noted, that as the focus is on the tip of the blade, the fitting algorithm has been set so that the curve is fitted from the maxima of circulation to the tip. Spanwise variation of circulation determines the intensity of the trailed circulation. At

Table 4.1: Range and discretization of the different parameters used for Fig.4.3

Parameter	Start	Step	End
x_2	-1	0.25	1
y_3	0	0.25	2.5
t_0	0.2	0.05	0.7

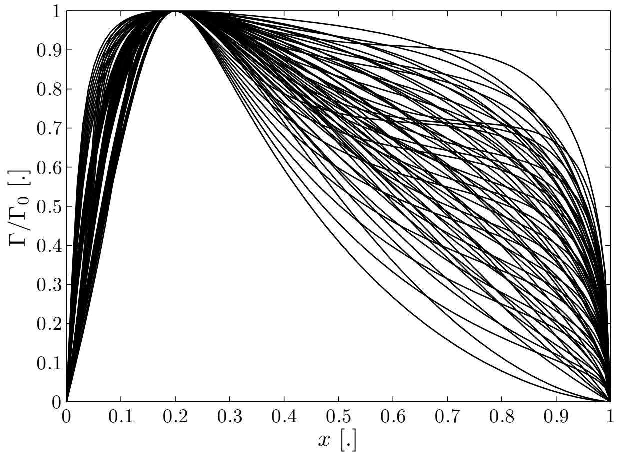

Figure 4.3: Example of different family of curve that can be obtain with the current parametrization. The different parameter values of Tab. 4.1 were used while the parameter x_0 was kept constant equal to 0.2.

the maximum circulation, the trailed vorticity is zero. It is expected that the way the circulation reduces from the maxima to the tip will be the parameter influent on the tip-loss. By focusing the fit on this part of the circulation curve, more resolution is obtained, and more detailed from the original curve are reproduced by the fitted curve. In opposite, the inner part of the blade is not considered by the fitting algorithm. It is obviously possible to fit and parametrize the entire circulation curve, but at the cost of increasing the number of parameters or loosing resolution at the tip of the blade.

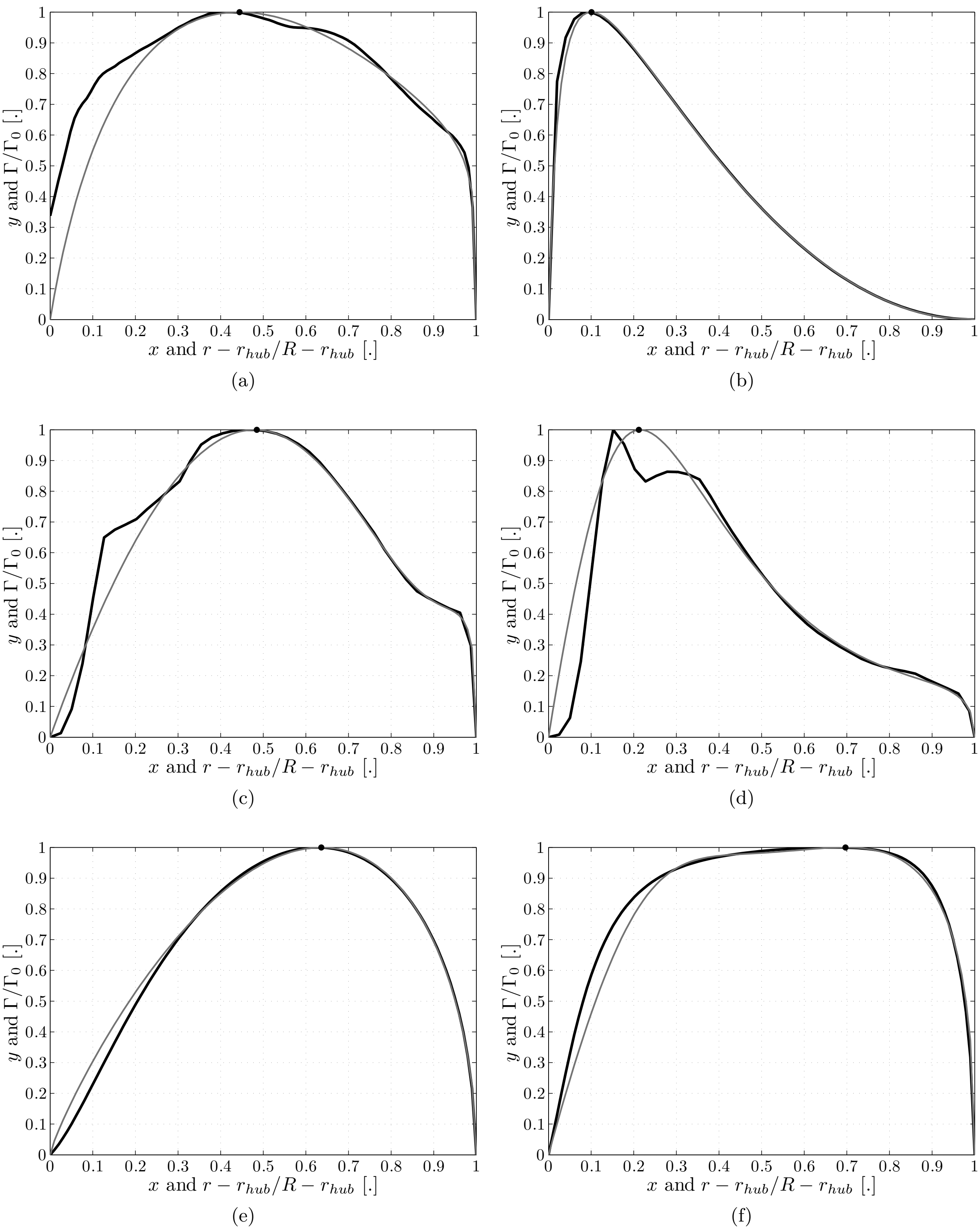

Figure 4.4: Illustration of the model and fitting method developed for circulation curves. Original curves are plotted in black thick lines and fitted curve in gray thin lines. The black dots represent the maximum of the fitted curve at coordinate $(x_0, 1, t_0)$. The parametrized model developed in Sect. 4.2.2 is fitted to the portion of the original curve between this dot and the tip. It can be seen that the parametrization works for high (a) and low (b) lift concepts, it allows specific inflexion at the tip as in (c) and (d) and fits the Goldstein circulation curves as in (e) and (f).

4.3 Sensitivity analysis

To ensure the reliability of the method described in Sect. 4.1 a sensibility analysis is performed on the different external parameters that could potentially introduce variability in the tip-loss function. For the method to be validated it is needed that only the six parameters of choice $\{x_0, x_2, y_3, t_0, \lambda, C_T\}$ influence the tip-loss function. In a first time, its independence on the external parameters is investigated and demonstrated. In a second time, the relative proportion in which the chosen parameters affects the tip-loss function is studied.

4.3.1 External parameters

The influence of external parameters is studied using the same prescribed circulation. The wind speed is fixed at 8m/s and the tip-speed ratio at 7.5. The design of a given wind turbine is scaled to a blade length of 1m with the chord scaled proportionally and the hub radius fixed to 0.02.

Number of blades As mentioned in the introduction, the database of tip-loss correction has been established for three bladed wind turbines but can be extended to turbines with any number of blades. The dependence on the number of blades follow the same trend than the one from Glauert correction as can be seen on Fig. 4.5.

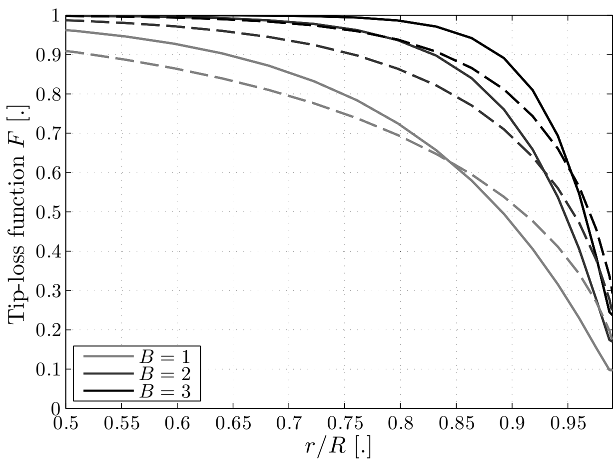

Figure 4.5: Dependence of the tip-loss function on the number of blades. Plain lines correspond to the tip-loss function obtained with the current method, while dashed lines are the one obtained for the same turbine configuration using Glauert's BEM-adapted method.

Sensitivity to Bound circulation From the review of the methods to determine the angle of attack from CFD(Sect. 1.2.1), it was seen that some methods try to remove the influence of the bound circulation which affects strongly the flow around the blade. For the vortex code, the axial induction on the blade is evaluated on the lifting line exactly. In the current algorithm, if the velocity is evaluated exactly on a vortex element, the velocity is always zero regardless of the vortex core model. Such behavior can of course be discussed. As a result of this, the axial induction a_B is the same with or without accounting for the bound circulation. For the average axial induction $\overline{a}$ though, one can ponder if the two approaches would give the same results. It is expected to be so due to the symmetry of the velocity field generated by the bound circulation on both side of a segment. This results is verified on Fig. 4.6 and for illustration the decomposition of the axial induction between the contribution of the bound circulation and the rest of the wake is plotted on Fig. 4.7.

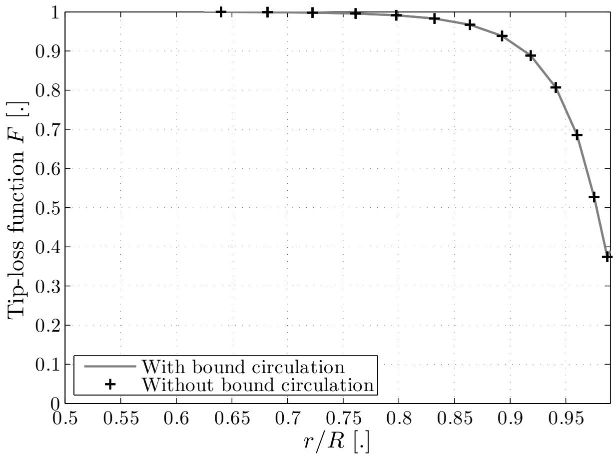

Figure 4.6: Tip-loss function obtained with and without the influence of the bound segments. a_b is the same in the case due to a choice of implementation of the singularity at the very location of a vortex element without respect of the vortex core model. $\overline{a}$ is the same due to the symmetry of the velocity field generated by a bound vortex element.

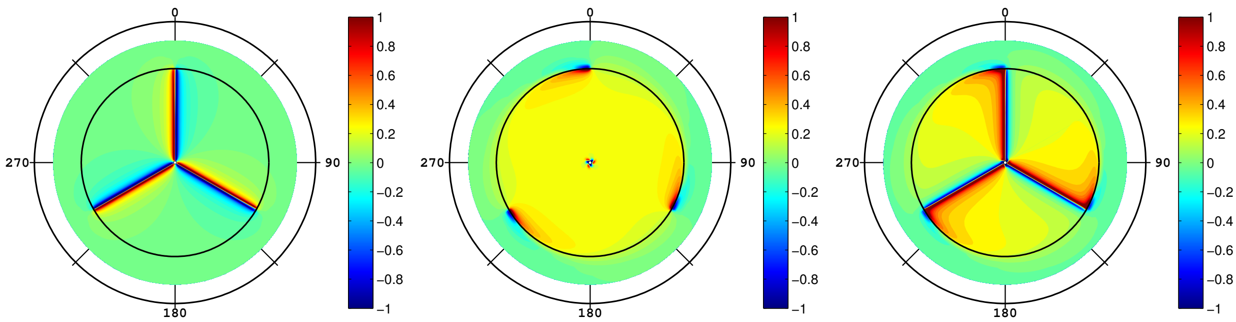

(a) (b) (c)

Figure 4.7: Axial induction computed by the vortex code at the rotor plane. (a) Bound circulation alone - (b) All without bound circulation - (c) All

Sensitivity to Chord distribution Given the lifting-line assumption for which the span-wise dimension prevails over the chord-wise and thickness-wise dimensions, it is expected that the results obtained for different chord distribution will have a negligible influence on the tip-loss correction obtained with the lifting-line code. Results from five different chord distribution as displayed on Fig. 4.8 confirm this statement.

Sensitivity to twist In the same line than the chord distribution sensitivity study, five different twist distributions are tested. On Fig. 4.9 it is seen that the twist distribution does not influence the tip-loss function.

Sensitivity to viscous model One of the critical parameters of vortex code is the way the singularity is handled as a control point gets close to a vortex element. Several models are presented

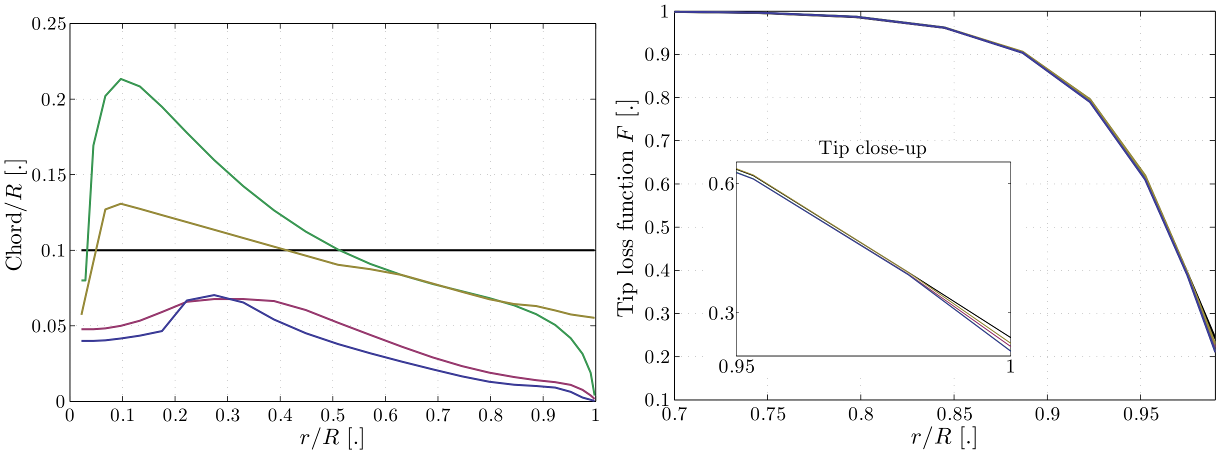

(a) (b)

Figure 4.8: Tip-loss function obtained for different chord distributions. (a) Chord distributions - (b) Corresponding tip-loss functions using the same color scheme. The expected independence of the result on the chord distribution is confirmed in these five different cases.

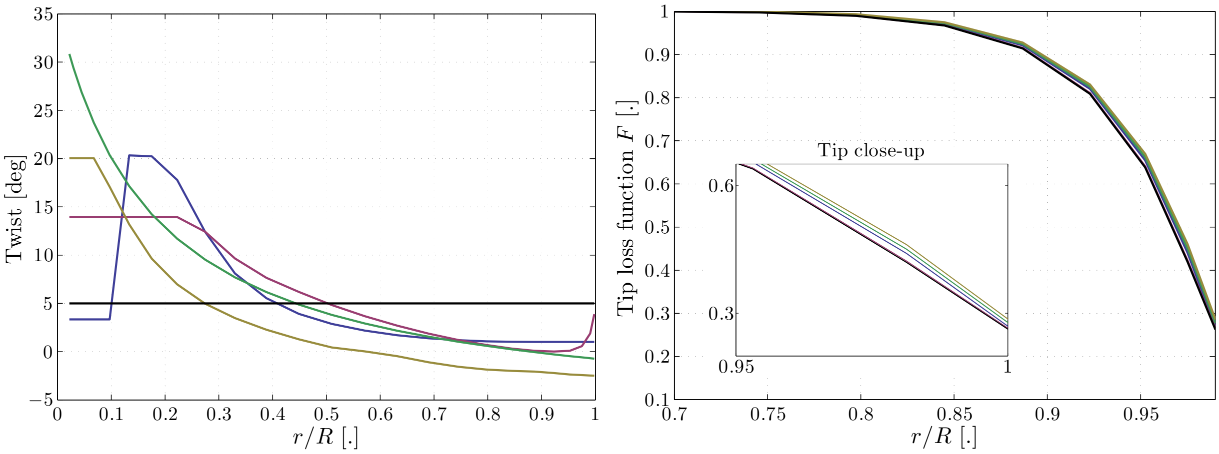

(a) (b)

Figure 4.9: Tip-loss function obtained for different twist distributions.

in Sect. B.1 and they are here tested against the resulting tip-loss function shape. Though a dependence on the viscous model is expected the results from the analysis presented on Fig. 4.10 tend to show that only the outermost portion of the tip-loss function is really affected.

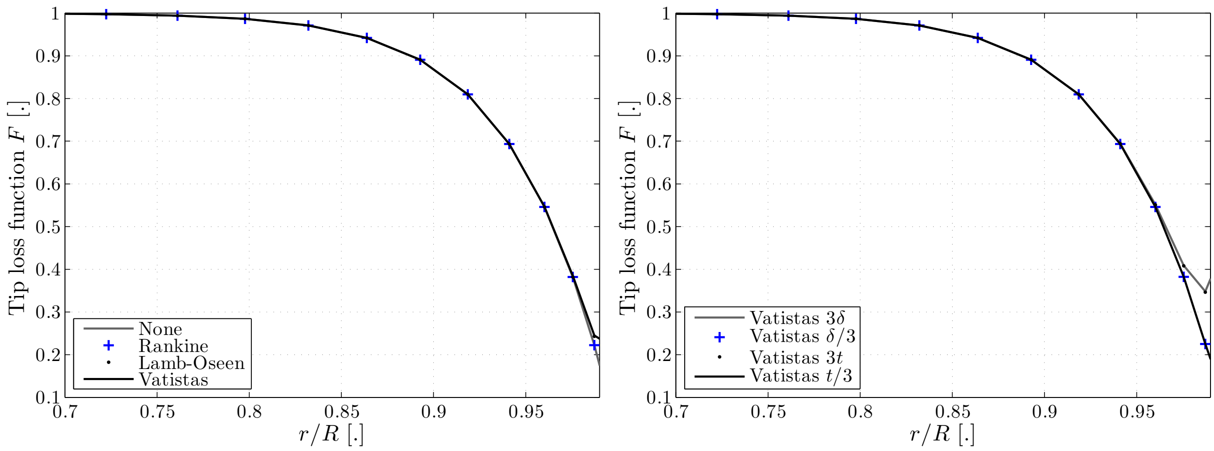

(a) (b)

Figure 4.10: Sensitivity of the tip-loss function with respect to the different viscous models. (a) Various models - (b) The Vatistas $n = 2$ model for different values of parameters δ and t.

Sensitivity to grid complexity The different parameters that affects the computational time are studied on Fig. 4.11. Once again, only small fluctuation in the resulting tip-loss function are observed when these parameters are changed.

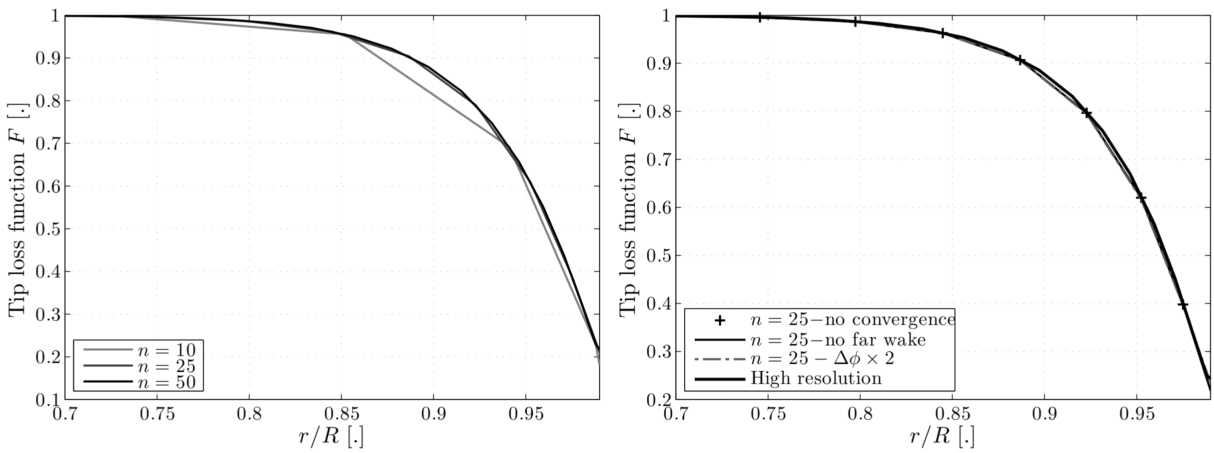

(a) (b)

Figure 4.11: Sensitivity of the tip-loss function with respect to the grid size. (a) Influence of the number of vortex rings n along the blade - (b) Influence of other parameters influencing the computational time: the resolution in azimuth $\Delta\phi$, the presence of a far-wake, and the possibility for the algorithm to stop after the induced velocities have converged and are constant over time.

4.3.2 Sensitivity to the database parameters

Wind turbine state For the given prescribed circulation displayed on Fig. 4.12, the vortex code has been run for different turbine states determined by the couple of parameters $\{\lambda, C_T\}$. The tip-loss functions resulting in these runs can be found on Fig. 4.13.

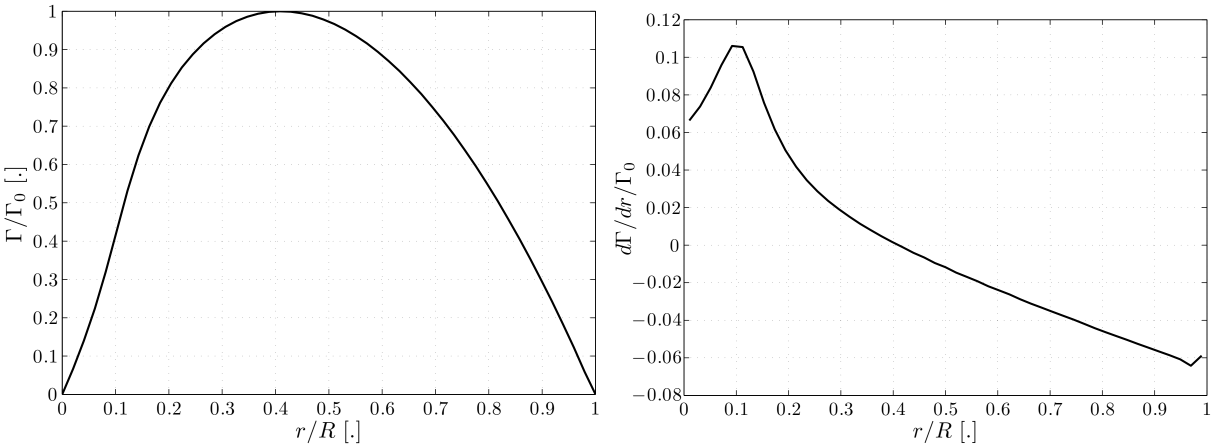

(a) (b)

Figure 4.12: Prescribed circulation used for the sensitivity analysis on the wind turbine state. (a) Circulation - (b) Derivative of the circulation

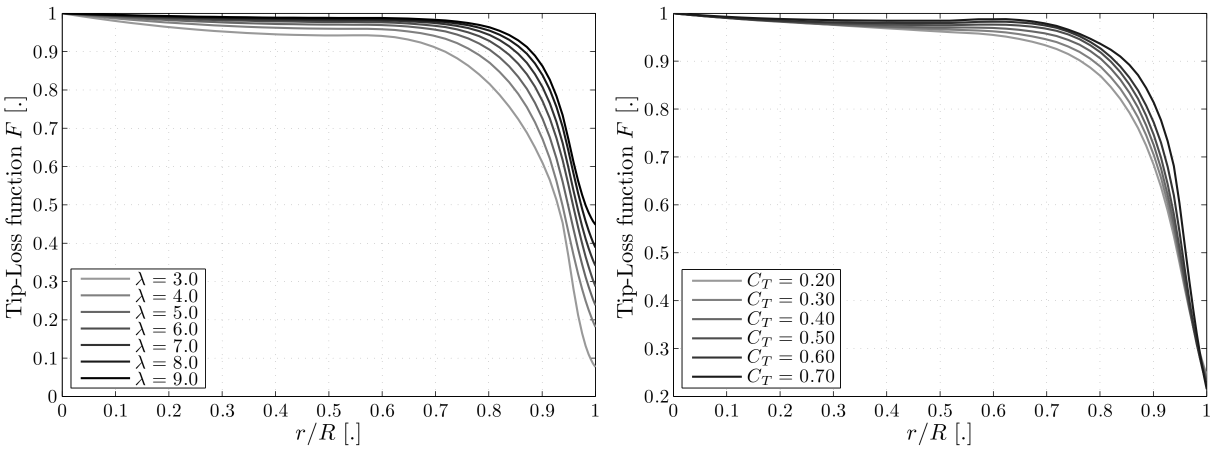

(a) (b)

Figure 4.13: Influence of the turbine state $\{\lambda, C_T\}$ on the tip-loss function. (a) Influence of λ for $C_T = 0.4$ - (b) Influence of C_T for $\lambda = 5$. All cases have been run with the prescribed circulation found on Fig. 4.12

Circulation shape On Fig. 4.14 the tip-loss function obtained for different circulation curves is displayed.

4.3.3 Discussion, preliminary results and method implementation

Implementation Once the database of tip-loss function has been established for a wide set of the four different circulation curve parameters and the two rotor state parameters, it is ready to be used in the BEM code. To initialize it the BEM code is run first using Glauert's tip-loss factor with a low resolution for a fast computation. The results from this simulation is used to asses the thrust coefficient. It is indeed expected that with or without the new tip-loss model, the thrust

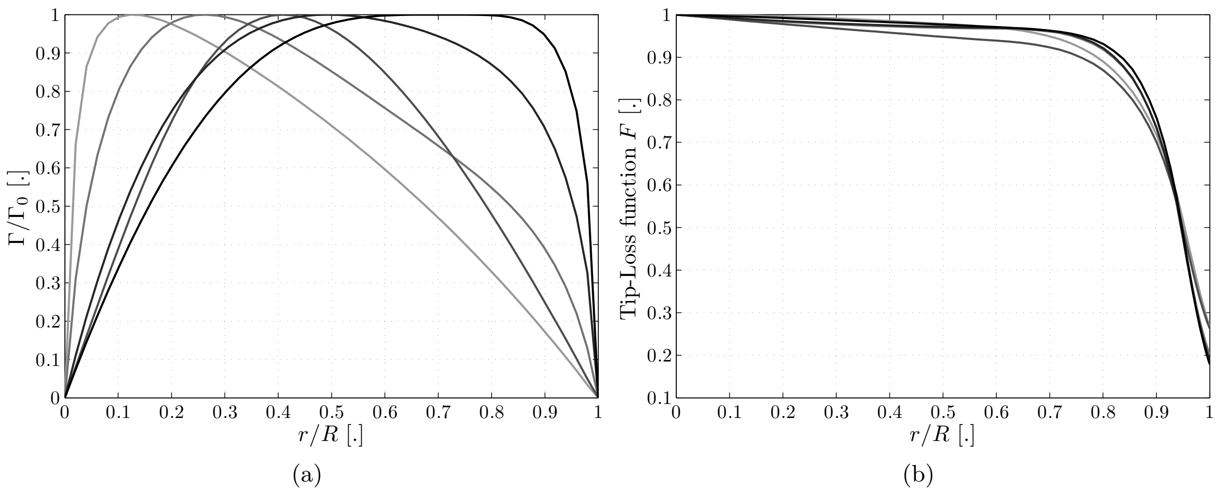

Figure 4.14: Influence of the circulation distribution on the tip-loss function. (a) Circulation curves - (b) Corresponding tip-loss function. The wind turbine state is $C_T = 0.2$ and $\lambda = 5$

coefficient will only slightly change:a maximum change of the order of 1% was observed. The database resolution in the thrust coefficient does not have to be high. The tip-speed ratio being a given parameter of a BEM simulation, the two rotor states parameters are hence known. The circulation curves and the tip-loss function from the database corresponding to this rotor state are loaded. A new BEM run is then launched with initialized parameters the end result of the prior BEM computation. At each iteration state, the circulation along the blade is compared to all the circulations curves present in the database. The closest one to the current BEM circulation is retained and the corresponding database tip-loss function is used for this BEM iteration. If the circulation from one iteration to the other barely changes, then the comparison with all the circulation curves from the database is not done. It would take computational time to eventually find that the selected database circulation is the one than the one selected at the previous iteration steps. The iterations are repeated till the BEM code converges (e.g. a tolerance criteria on the axial induction).

It should be noted that this BEM code requires an outer loop on the iterations and an inner loop on the radial elements. This requirements can be seen as an advantage, because the inner loop on the elements can be avoided and replaced by vectorial computations so that all informations along the blades are computed at the same time. The downside is that in the BEM code, the independence of the annular elements is such that some elements converges faster than others. Typically the hub and tip takes longer to converge, and sometimes never do due to the momentum theory breakdown. The number of maximum iterations is thus a key parameters for the computational time. Nevertheless, from the authors experience the choice of the imbrication order between the element loop and the iteration loop appear to have both advantage and shortcomings in computational time, so that the two methods are comparable. If the outer loop is the iterative loop, then the elements vector-wise implementation clearly accelerates the code(e.g. in Matlab). Nevertheless, the converged elements are re-computed till the non-converged elements converges. If the outer loop is the elements loop, than most of the elements of the blades converges rapidly and don't have to "wait" for the tip and root elements to converges. Nevertheless, two loops are requires which slows down the computation.

Discussion Preliminary results of the tip-loss shape have been presented on Fig. 4.13 and Fig. 4.12. From a first overview it is seen that the same behavior than the existing corrections are observed. It is rather surprising that a small sensitivity on the circulation distribution was observed on Fig. 4.14. The distribution studied on this figure had a wide spread of gradient, implying different trailed vorticity, hence different mechanism of vortex emission and roll-up. It seems that the importance of the parameters governing the tip-loss function are in decreasing priority order the tip-speed ratio, the thrust coefficient then the circulation shape.

An interesting aspect of the corrections obtained with the vortex code is that they don't necessarily drop to zero at the tip. It is believed by the author that this result is somehow desired as was discussed in Sect. 1.3: the average axial induction, though dropping to zero towards the tip, does not have to be zero at the tip. The same is then expected for the axial induction tip-loss factor here considered. The fact that the loads might have to go to zero at the tip due to the pressure balance will be discussed in the next chapter in Sect. 5.2.6.

As mentioned at the beginning of this chapter, the tip-loss function derived with this method have several advantages compared to the specific and simplified function derived by Prandtl or Goldstein. It should be recalled from chapter 2, that neither Prandtl or Goldstein's theory includes wake expansion. Goldstein's theory applies only if a specific optimal circulation is present at the rotor. The wake structure used is purely helical and does not include wake deformation and roll-up which are described by the vortex code. Goldstein's and Prandtl's theories do not account for the induced velocities when evaluating the velocity triangle at the rotor or the wake screw angle. This reduces once again to slightly loaded rotors. Goldstein's theory is a far wake analysis, which is hard to apply at the rotor as was discussed in chapter 2. In this sense, the vortex code captures more local, near wake characteristics of the flow which are relevant for application with the blade element theory. The wake model of Prandtl with infinite flat plates, though elegant and efficient, is rather simplified compared to the more realistic wake geometries that are obtained with a lifting line code. For all the above, it appears obvious than better tip-loss functions will be obtained from the methodology derived in this thesis.

BEM results The results of the implementation of the tip-loss model will be presented in Sect. 6.2.

Further work From the database of tip-loss correction, a general tip-loss function could be derived as function of the 6 parameters. This could be done by parametrizing the tip-loss functions using for instance the same Bezier curve formalism. Three parameters should be enough to parametrize all the tip-loss functions of the database. Using a neural network approach, a general tip-loss function matching the input database parameters and the output tip-loss parameters could be found. No time was allowed for this, but such an investigation would allow a generic function of a simple form that could be directly used in a BEM code without having to fit the circulation curve with all the database ones.

Chapter 5

Using CFD to investigate tip-losses

5.1 Tip-losses and axial induction

5.1.1 Introduction

The first approach considered here is the definition of the tip-loss factor in terms of axial induction as described in Sect. 1.3.2, Eq. (1.26):

$$F_a = \frac{\overline{a}}{a_B}$$

with $\overline{a}$ the azimuthally averaged axial induction defined by Eq. (1.3) and a_B the axial induction on the blade which is here to be defined. In case of a lifting line code indeed it is possible to define the axial induction on the blade by computing the induced velocity on the lifting line. Such method is not possible with CFD data and a way to reduce the complex velocity field around the blade to one value has to be determined.

5.1.2 Data available and methods investigated

For a single CFD simulation case[1], 3D velocity fields have been outputted in different planes parallel to the rotor plane. Due to the assumed symmetry of the flow only the sector of 120°sectors containing one of the three blades is used. These planes are located at distances $\{-3.3, -1.3, 1.3, 3.3\}$ from the rotor plane where the lengths are expressed in % of the blade radius, and counting negative values for upstream locations. For a rotor radius R of 60m this corresponds to locations $\{-2.0, -0.8, 0.8, 2.0\}$m. Using the velocity fields of two planes located symmetrically with respect to the rotor plane, an estimate of the tip-loss factor at the rotor is sought. The velocity field in the rotor plane is assumed to be the average of the velocity field in the two surrounding planes(see a scheme of the planes on Fig. 5.1a). The flow field at the rotor plane can not be determined otherwise due to the presence of the blade and the fast variation of the flow around the blade. This first averaging smears out the complex longitudinal variation of the flow and $\overline{a}$ can now be computed. This method to determine the axial induction can be seen as a simple version of the one suggest in [48] that was discussed in Sect. 1.2.1.

To determine a_B a second averaging needs to be performed to account for the spatial extent of the blade projected in the rotor plane. The three methods suggested and studied here are illustrated on Fig. 5.1b where the dark-gray area represents the area over which the axial induction is averaged to

[1] Blade 1, three-bladed rotor, 12rpm and 10m/s

obtain an estimate of a_B. The circular and rectangular methods are straight forward and depends respectively on the chosen angle θ and rectangle side-length L. The third method uses different central angles θ_i so that the arc formed at a given radius r_i is equal to a certain proportion k of the chord c_i at this location, i.e. $\theta_i r_i = kc_i$.

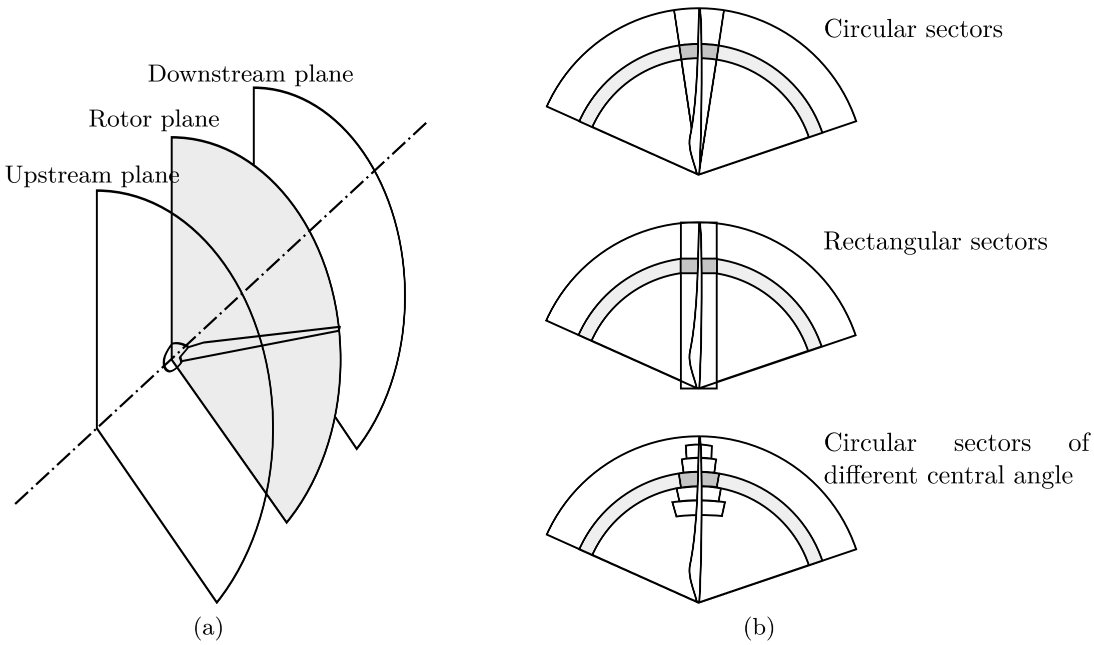

Figure 5.1: Determination of the tip-loss factor with CFD data. (a) Planes upstream and downstream the rotor where the velocity is outputted. The velocity field at the rotor plane is taken as the average between these two planes. - (b) Three different methods to determine an average velocity near the "blade" (dark-gray) at a given radial position. The ratio between the azimuthally averaged axial velocity $\overline{a}(r)$ (light-gray) and the "blade" averaged axial velocity $a_B(r)$(dark gray) is computed to give an estimate of the tip-loss factor at the rotor plane.

The effect of the averaging method on the estimate of a_B is studied on Fig. 5.2. The numerical values used for the circular and rectangular methods are of course dependent on the Rotor radius, which is here $R = 60m$. The circular method is clearly not using an area large enough at the inner part of the rotor for the estimate of a_b to be a proper average over the blade's area. The rectangular method does not have this problem but breaks by nature the azimuthal structure of the problem. The final method appears as a good solution offering a suitable area characteristic of the blade's surface at any radial position.

5.1.3 Results

It has been seen that the method and the method parameter (θ, L or k) used to assess a_B have a strong influence on its resulting value and so will it be on the tip-loss factor. By looking at Fig. 5.2 this dependence appear to be less important on the outer part of the blade but still exists as illustrated on Fig. 5.3. From this figure, conclusions are difficult to draw above $0.98R$.

The influence of the location of the planes used to average the velocity at the rotor is expected to have a strong influence as well. To illustrate this, the tip-loss factor obtained for the sets of planes at $\pm 1.3\%R$ and $\pm 3.3\%R$ are compared. The further apart the planes, the smaller the effect due to the finite number of blades is and the more local rotor information is lost. The above is observed

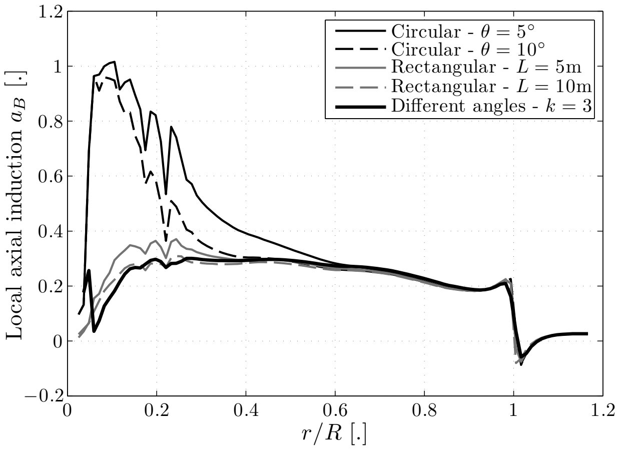

Figure 5.2: Estimate of the axial induction on the blade a_B using CFD data at planes $\pm 1.3\% R$. Out of the three methods presented on Fig. 5.1b, the one using different central angles is expected to give the more representative estimate of a_B.

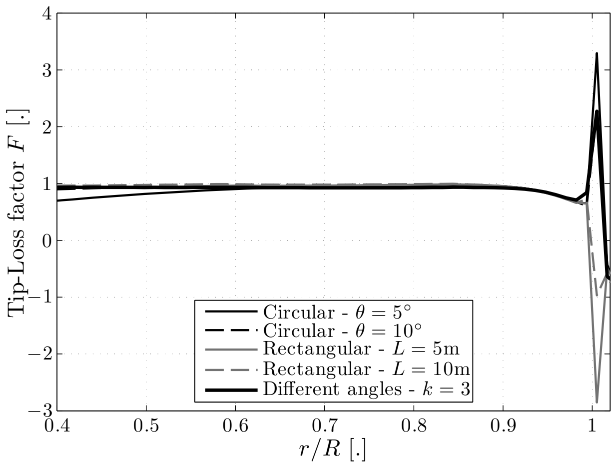

Figure 5.3: Influence of the averaging method determining a_B on the tip-loss factor near the tip. For radial position above $0.98R$ a strong dependency on the method is observed.

on Fig. 5.4.

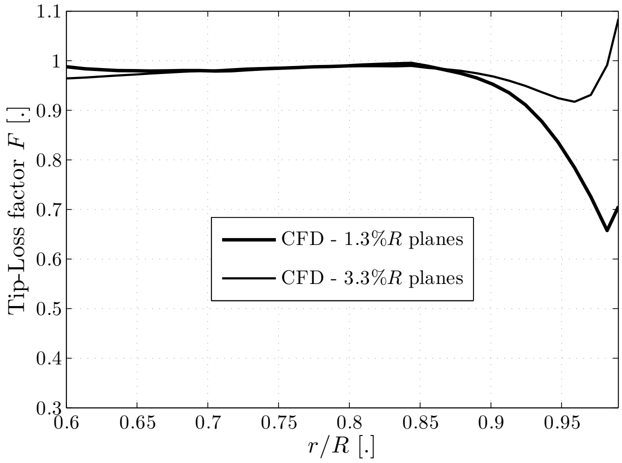

Figure 5.4: Tip-loss factor estimated using different planes apart from the rotor. The effect of finite number of blades is less captured when considering planes further apart from the rotor.

5.2 Tip-losses and aerodynamic coefficients

5.2.1 Introduction

In Sect. 1.3.2 Eq. (1.28), a tip-loss factor describing the airfoil performances at the tip has been defined as:

$$F_{C_l} = \frac{C_{l,3D}}{C_{l,2D}}$$

This factor has been defined because the pressure equalization at the tip of the blade and the formation of a tip-vortex is expected to reduce the performances of the airfoil coefficient at the tip. The 3D nature of the flow can be observed by looking at the streamlines, as in **??**. In [43], streamlines for two-different blade-tip at different operating conditions can be found. It is expected that F_{C_L} will be a function of the blade geometry and the rotor operating condition. Due to the high computational time required for each CFD run an extensive study of how these parameters affects the tip-loss F_{C_l} was not possible, but as much information as possible from existing run cases were used as presented in the following.

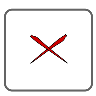

Confidential content removed

Figure 5.5: Streamlines on suction side of the blade tip(2 last percent). Going towards the tip, the streamlines are less and less parallel to the main flow. For chordwise position of x/c approximately above 25%, the flow becomes clearly radial and one can question the validity of using 2D airfoil data in such situation.

5.2.2 Data available

CFD simulations of different blades with different tip-shapes for different operating condition were available. They are summarized on Tab. 5.1. These simulations were run for other purposes than this study so that performing a sensitivity analysis on the parameters that can influence the performances losses is made more difficult. Most of the simulations offer the advantages of covering a wide range of operating conditions for a given blade. From these data it is possible to compare the 3D airfoil performances from 3D CFD with 2D lookup table data, mostly obtained from 2D CFD. A complete overview of such comparisons can be found in Sect. D.2.

Table 5.1: Available CFD cases for investigation of aerodynamic performance losses

Name	**Tip**	**Number of runs**	**Type**
Blade 1	Tip 1	6	"Rough" - pitch sweep with off-design cases
	Tip 2	4	"Rough" - pitch sweep with off-design cases
Blade 2	Tip 1	7	"Rough" - operating conditions
	Tip 1	7	"Clean" - operating conditions
Blade 1 swept	Tip 1	4	"Rough" - rpm sweep with off-design cases

2D airfoil characteristics are known for different thicknesses. The thickness distributions of the two blades considered can be found on Fig. 5.6.

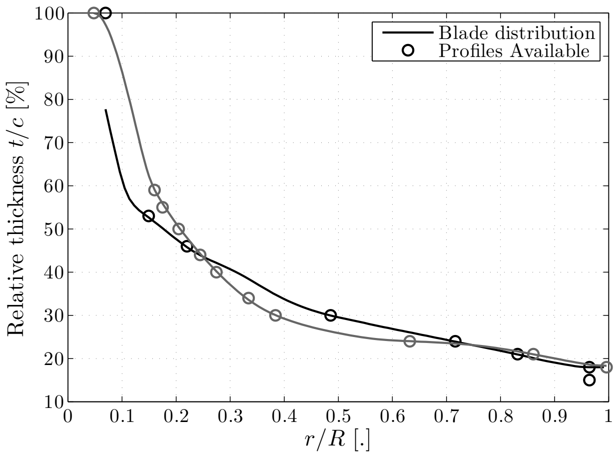

Figure 5.6: Thickness distribution and available 2D profile data of the two blades considered. B1 (black) - B2 (gray)

5.2.3 Polar comparison between 2D and 3D CFD

As a first step, the profile coefficients obtained from 3D CFD are confronted to the 2D lookup table data(obtain with CFD). As seen on Fig. 5.6, only a finite number of 2D airfoil coefficient tabled are known for a given thickness. For each thickness value and each simulation, the lift and drag coefficients together with the angle of attack from CFD data are extracted at the first radial position where this thickness is encountered along the blade span. These values are then compared with the 2D polars. The results for all different polars(i.e. thickness values), all different blades and all different simulations can be found in Sect. D.2. Among these results it is interesting to point out that rotational augmentation is observed for large relative thickness values (inner part of the blade), but of prime interest here are the effects at the tip of the blade. For this reason, the airfoils coefficients obtained for the smallest relative thickness (blade tip) are displayed on Fig. 5.7 for Blade 1.

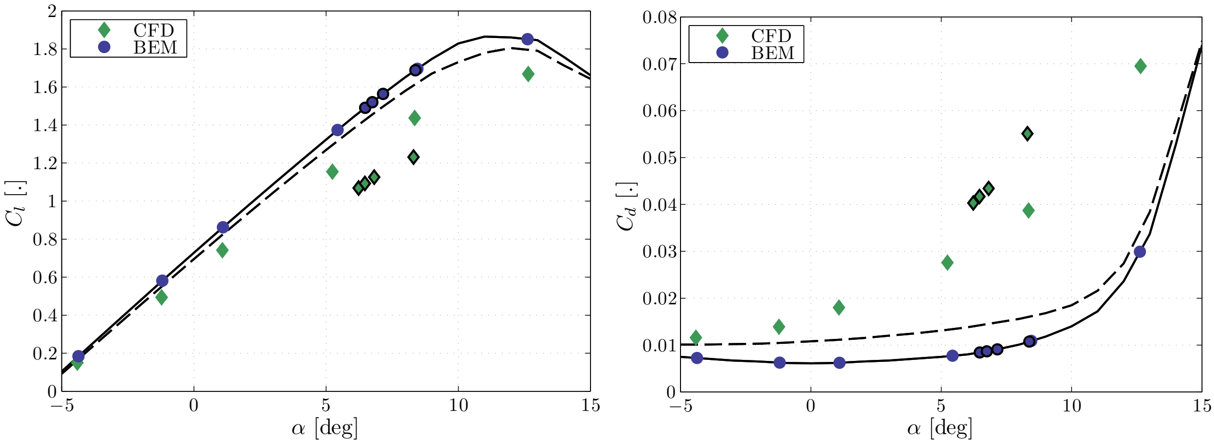

Figure 5.7: Blade 1 airfoil polars for the relative thickness 18%. The 2D data available are plotted with plain and dashed line. For each simulations available, a different couple of value $(\alpha, C_\bullet)$ is extracted from CFD and from BEM computation(using clean profiles). Markers surrounded by a black line are data corresponding to Tip 2, as opposed to Tip 1 for the other markers.

Agreement is fairly good between the 2D data and the 3D data for the relative thickness 18%. By looking at results from Sect. D.2, the agreement is even better for thicknesses above 18% and below 30%, which corresponds roughly to the outer 2/3 part of the blade. This corresponds indeed to the region where the flow is known to behave in good approximation with 2D flow. The differences at the tip will be the focus of the next paragraph.

5.2.4 Tip-loss function from the ratio of Cl

Method In the previous paragraph(Sect. 5.2.3), the 2D and 3D data were compared for radial positions where the relative thickness was exactly the one used for the 2D table. For a complete assessment of the tip-loss though, more radial positions towards the tip are needed. For this study, the range of the blade from $0.8R$ to the end is investigated. The angle of attack and airfoil coefficients from CFD $(\alpha_{3D}, C_{\bullet,3D})$ are extracted for the outer part of the blade. This angle of attack is then inputed to the method used by the BEM code to interpolate airfoil coefficients between different thicknesses and Reynolds number, to obtain a corresponding "2D" airfoil coefficient $C_{\bullet,2D}$. The ratio between the 3D lift coefficient and the interpolated 2D lift coefficient provides the tip-loss function F_{Cl} as defined earlier in Eq. (1.28). As seen on Fig. 5.6, blade 1 has the advantage of keeping a constant profile thickness from $0.95R$ to the blade end. This will ensure a good quality of results in this range as no interpolation is used to obtain the 2D coefficient.

Data overview for Blade 1 Using the method previously described for all six CFD simulations available for Blade 1 with Tip 1, the interpolated 2D and the CFD 3D data are compared on Fig. 5.8. The different simulations were designed so that the angle of attack from one simulation to another would increase by around 3 degrees, thus allowing a nice comparison between 3D polars and 2D polars. For each simulation, the data points should be read from right to left to understand it as data going in the spanwise direction from around $0.8R$ to the very tip. For this blade the angle of attack is indeed decreasing when going towards the tip. Reading each simulation from right to left, it is seen that the 3D and 2D data diverges progressively hence showing a performance loss at the tip. The 2D data don't match the polar when the thickness is over 18% due to the interpolation between the 21% and 18% data sets. Going towards the tip(to the left), the thickness goes to exactly 18%, the 2D data are no more interpolated and match exactly the 2D polar.

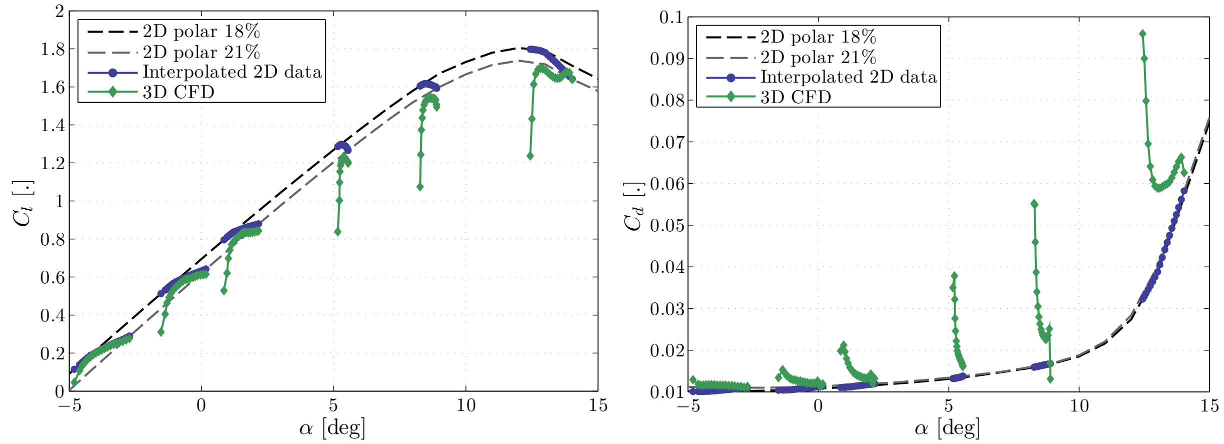

Figure 5.8: 3D and 2D polars for relative thickness between 18% and 21%. The tabulated 2D rough polars are plotted to illustrate the interpolation method on thickness. The ratio between the interpolated 2D data and the 3D CFD data, when read from left to right(i.e. toward the tip) provides the performance tip-loss factor.

Tip-loss results for Blade 1 The results from the left plot of Fig. 5.8 can also be plotted against the radial coordinate as done on Fig. 5.9a and 5.10a. By doing the ratio of the 3D lift coefficient versus the interpolated 2D lift coefficient, the performance tip-loss factor is computed and the results from Blade 1 can be seen on Fig. 5.9b for the first tip, and on Fig. 5.10b for the second tip.

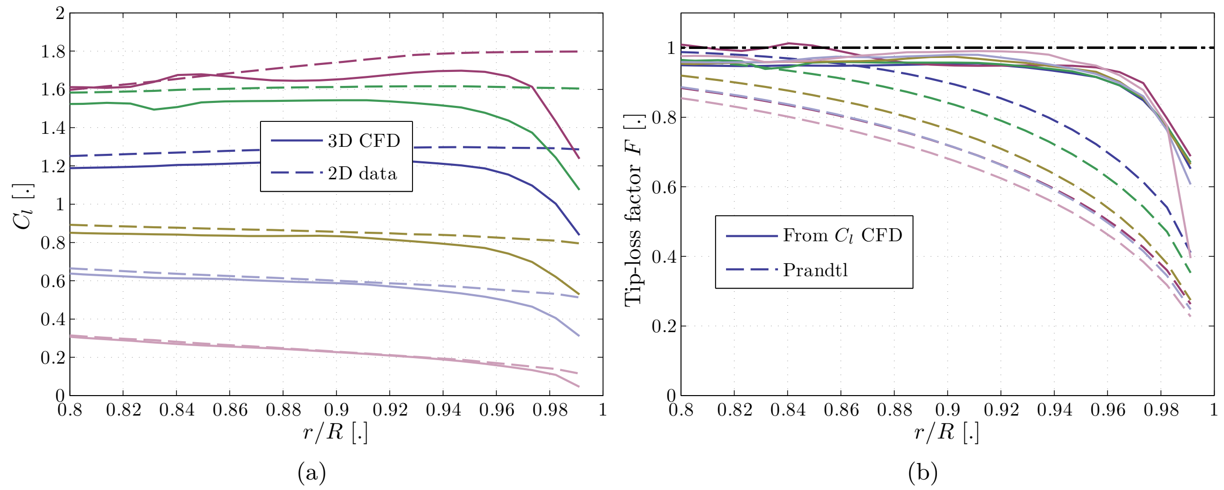

Figure 5.9: Airfoil tip-loss function for Blade 1 and Tip 1. (a) $C_{l,3D}$ and $C_{l,2D}$ - (b) Tip-loss function F_{Cl}. The presence of Prandtl tip-loss factor is for reference only as the comparison is not physically correct. The color scheme between the two figures is preserved. It is interesting to note that despite the wide range of operating conditions studied, the tip-loss function observes few changes.

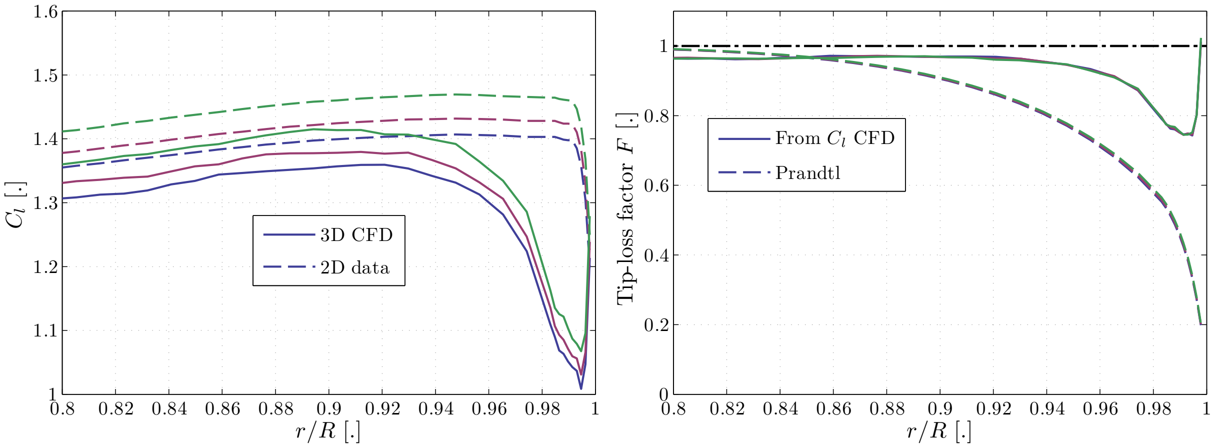

(a) (b)

Figure 5.10: Airfoil tip-loss function for Blade 1 and Tip 2. (a) $C_{l,3D}$ and $C_{l,2D}$ - (b) Tip-loss function F_{Cl}. The presence of Prandtl tip-loss factor is for reference only as the comparison is not physically correct. The color scheme between the two figures is preserved. The tip-loss function observes almost no changes between the different simulations.

Data correction Looking at Fig. 5.9b and Fig. 5.10b, it is seen that the ratio between 3D and 2D data is around 4% lower than one for regions were the flow is expected to be close to 2D (e.g. 0.8%R). For the second blade, the same has been observed but in the order sometime of 10%. This is due to the fact that the 2D tabulated data for Blade 2 comes from wind tunnel measurement and not from 2D CFD as for Blade 1. The "roughness" and turbulence condition between the CFD simulation and measurement don't match, and such differences can results in differences of several percents. Nevertheless, it is expected that the relative variations of aerodynamic coefficients are conserved in a first approximation[2]. As the focus is here to look at the relative variation of coefficients at the tip, the 2D lift coefficients will be adjusted to match in amplitude with the 3D CFD lift coefficient at location $0.8R$. The difference of amplitude in regions "close to 2D" is not what is intrinsically looked after in this analysis. By doing this data correction, the performance tip-loss factor is forced to one for the inner tip, thus allowing an analysis of this effect independently of external simulation or experimental factors.

Comparison of all cases Applying the small data correction mentioned above to ensure that the performance tip-loss goes to one at the inner tip, the tip-loss factor for the different blades and tips is computed, averaged and reported on Fig. 5.11. It is quite interesting to note that for these different designs the shape of the performance tip-loss F_{C_l} seem to follow a similar trend. The only curve that does not quite follow is the one from the "clean" Blade 2 case. Nevertheless, this outlier is expected because "clean", optimistic CFD data is compared with an experimental data which is closer to "rough" CFD. This outlier being kept assside, the comparison between the four different design is really good. Still, it is should be kept in mind that the two tip-design are really close to each other. More tp-shapes are to be studied to investigate the performance tip-loss effect and the proportion in which it occurs.

5.2.5 Ratio of drag coefficient

In the previous analysis, the differences of performances in lift between 2D and 3D situations has been used to define a performance tip-loss factor. For almost no computational cost, the same can

[2]It will appear that this does not hold true when comparing "clean" CFD with experimental data

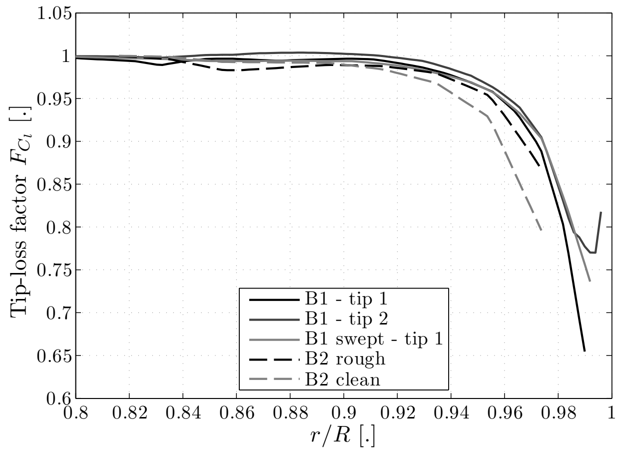

Figure 5.11: Comparison of airfoil performance tip-losses F_{C_l} for different designs. A general trend is found between all the different cases, especially if the expected outlier “Blade 2 - clean” is discarded. Nevertheless, the different designs are quite similar and more should be tested to conclude for trends and relevant parameters.

be evaluated with the drag coefficient. The drag coefficient in 3D has been observed to be higher than its 2D relative. In order to keep a value between 0 and 1, the ratio is inverted as:

$$F_{C_d} = \frac{C_{d,2D}}{C_{d,3D}} \tag{5.1}$$

The computation of the drag ratio for Blade 1 is found on Fig. 5.12. For the different simulations of Blade 1 Tip 1, a large fluctuation on the drag ratio is observed. This is expected due to the drag sensitivity to turbulence, especially in separated regions. Turbulence in separated regions is highly tri-dimensional and hence is badly described by 2D simulations. Moreover, as small error in the estimate of the angle of attack would results in larger relative error in the drag coefficient that in the lift coefficient due to the high lift-over drag ratio. No further analysis of the ratio of drag coefficients for the investigation of tip-losses will thus be done in this study.

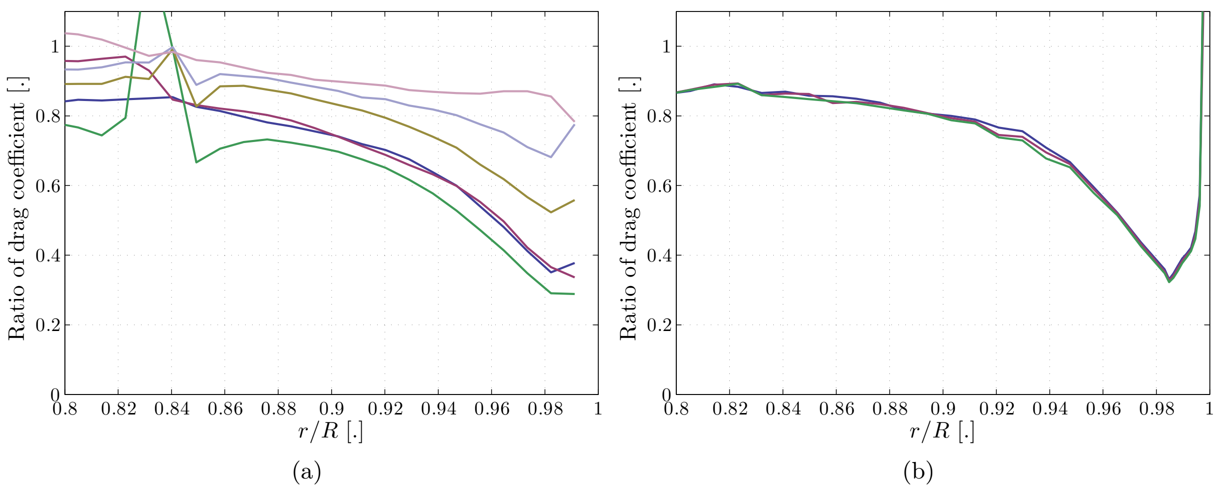

Figure 5.12: Ratio of drag coefficients for Blade 1. (a) Tip 1 - (b) tip 2

5.2.6 Generalization, discussion and comparison with literature

Physical considerations on the performance tip-loss factor At the blade tip the radial gradient of dynamic pressure vanishes progressively. The centrifugal effects and the radial suction associated, should also disappear for radial locations after the tip. This reduction is of course expected to occur progressively. As a results of this Lindenburg[62] argues that at the tip the flow in the boundary layer and in the separation trailing-edge area is not pumped further radially. Nevertheless, the radial flow from sections before the tip result in a reduction of the negative pressure on the airfoil suction side compared to the non-rotating case. Lindenburg hence concludes that "the rotating lift coefficients of the tip sections are smaller than the non-rotating lift coefficients, while the flow is still not in stall".

Suggested model for generalization The small variability of the performance tip-loss function F_{C_l} with regards to operating conditions and tip-shapes, invites to find a simple model that could well represent this function. Whether this model would suit other tip-shapes than the one tried is of course doubtful, but the general trend is expected to be respected though. Analyzing experimental data, a dependence on the performance tip-loss factor with respect to the angle of attack could be expected. This was observed for instance by Lindenburg[62, p 45] by looking at the NREL Phase VI experiment. Early analysis of the CRADA project[65, p 66] seem to show similar behaviors. In the cases considered the angle of attack distribution towards the tip is close to constant and no significant dependence on the operating conditions were observed. For this reason models independent of the angle of attack are presented here but further refinement should be considered in the future. Three generic models are suggested to fit F_{C_l}. These models could be used in another study involving different tip-shapes, or be directly used in BEM codes as explained in Sect. 3.2 in the section involving the correction of the airfoil coefficients. The different functions suggested in this study to fit the tip-loss factor F_{C_l} are:

Acos-Fit $$F_{C_l} = \frac{2}{\pi} \operatorname{acos} \exp\left[-C(1-\overline{r})\right] \qquad \text{with } C = 63 \tag{5.2}$$

Acos shift-Fit $$F_{C_l} = \frac{2}{\pi} \operatorname{acos} \exp\left[-C(1-\overline{r}) + D\right] \qquad \text{with } (C, D) = (48, -0.5) \tag{5.3}$$

F-Fit $$F_{C_l} = 1 - C\frac{(1-\overline{r})^{\nu_1}}{(2-\overline{r})^{\nu_2}} \qquad \text{with } (\nu_1, \nu_2, C) = (0.39, 64, 2.5) \tag{5.4}$$

The first one is an obvious reference to the work of Prandtl and the second one add the flexibility for the tip-loss function not to go to zero when $r = 0$. The third function, referred as "F-fit" has been inspired by the statistical F-distribution. Looking at the cases where the tip-loss function increases back close to the tip, the curve shape reminds the one of a skewed statistical distribution. Canonical distributions that allow skewness are for instance: Weibull, Chi-square, Gamma-distribution, Log-normal. The parametrization from the F-distribution has been chosen for it was believed to provide a good family of curves with different curvatures and an ease to use. The different fit from Eq. (5.2)-(5.4) are plotted on Fig. 5.13.

Discussion The "performance" tip-loss factor based on the lift coefficient as derived above clearly relies on how accurate the angle of attack is determined from 3D CFD data. The method used in this study is a simple form of the averaging technique developed in [48, 43]. Earlier in this report in Sect. 1.2.1, the critical issue of angle of attack determination has been pointed out. Several techniques that account for the bound circulation of the blades seem to give better results and have less dependency on the distance to the rotor plane chosen[47]. Such methods could be investigated in the future to see how much it could affect the performance tip-loss factor developed above. A sufficient amount of CFD simulations and the blade/tip geometries were studied to see general

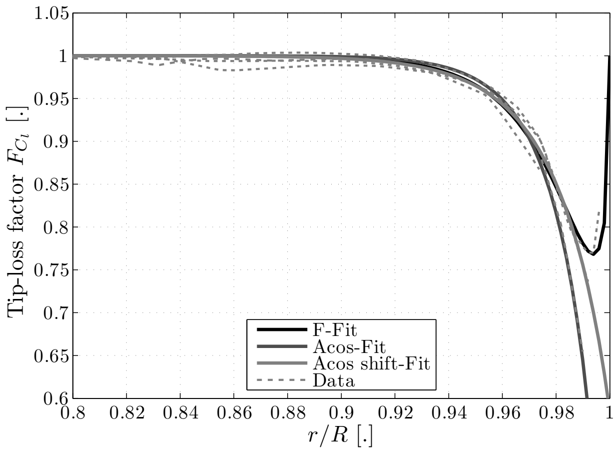

Figure 5.13: Suggested models for the performance tip-loss factor.

trends, but a broader range of tip-shapes with simulations at similar tip-speed ratios would be desired for a more throughout study. Despite of the above, the consistency in the results between the different simulations is comforting, and proves the applicability of the models from Eq. (5.2)-(5.4) as a first approximation before a more complete study is done. At this moment a distinction between these models is not really possible. Data from measurements are usually not available above 0.95% or 0.97% radial positions, and CFD data seem to show different behaviors above 0.97%. In Sect. 1.3, it was mentioned that it could be expected that the loads on the blades have to be zero at the tip due to the pressure equalization. This is the view also shared by Shen[97]. With this argument then, the model from Eq. (5.2) should be used. Nevertheless, the Model from Lindenburg discussed below does no impose this condition, and all the three different models from Eq. (5.2)-(5.4) are left open for discussion.

Comparison with literature In the literature, studies by Shen[97] and Lindenburg[62] performed similar comparisons. These corrections were presented in Sect. 3.1.3. Shen et al used experiments from the NREL rotor and the Swedish WG 500 rotor to find a performance tip-loss function that would fit the experimental C_n and C_t. Shen used a form of tip-loss function that resembles the one from Glauert, with parameters $\{\bar{r}, \phi, \lambda, B\}$. Lindenburg used the data from the NREL phase VI experiment to find a fit for the ratio between the measured 3D lift coefficient and the 2D one(as was done in this chapter). The parameters used by Lindenburg are $\{r, \mathrm{AR}, C_{l,\mathrm{inv}}\}$. Comparisons with these empirical relations and the one derived in this studied were attempted. Nevertheless, it appeared that none of those models could be fitted to the performance tip-loss function found in this study. The parameters attempted to be adjusted for the fit were $(c1, c2, c3)$ for Shen's model, and the coefficient in front of $\mathrm{AR}_{\mathrm{out}}$ for Lindenburg's model. For the latter, due to the large aspect ratio found, the factor was only affecting the last 0.1% of the blade with a minimum amplitude around 0.98. Lindenburg argues indeed that for large wind turbine his correction is expected not to be strong. On the contrary, the model of Shen shows corrections way more important than the model suggested in this study. An example for one simulation is shown on Fig. 5.14. These comparisons were done for all the CFD simulations available and the attention was on finding similar variations and trend between the models. As mentioned earlier, small variations were present in the model of the current study. Even within these small variations, no trend following the tip-speed ratio were found, whereas Shen's factor clearly shows variations for this parameter. Whether this is due to a specific tip design that has a similar behavior invariantly of the tip-speed ratio, a problem in this study for instance in the determination of the angle of attack, or a difference between using CFD data and experimental data, is still to be determined.

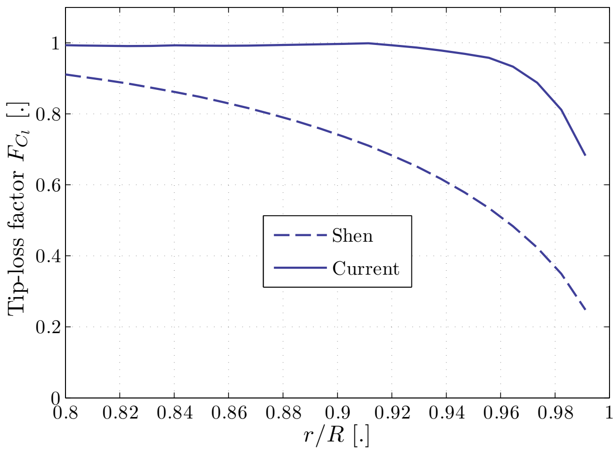

Figure 5.14: Comparison of the performance tip-loss factor from this analysis with the one from Shen for one CFD simulation.

Chapter 6

Results and comparison of the different codes and approaches

In this chapter, final result comparisons between CFD, BEM, and the lifting-line version of the Vortex code implemented are presented. In a first section, general comparative results between the three codes will be presented. For validation results of the vortex code, the reader is referred to Sect. B.2. In Sect. 6.2, the results from the new-tip loss corrections will be shown and the advantages of the approach used in this study will be put to light. In a third section, the BEM code with the new tip-loss model will be compared with CFD data, and a discussion will follow.

6.1 General comparisons

6.1.1 Induced velocities at the rotor plane

The computation of the induced velocities at the rotor from CFD data has been discussed in Sect. 5.2. The methods used either planes distant from 1.3%R or 3.3%R. The vortex code was used to compute the induced velocities in these four planes, and average them to compare the estimated average axial induction at the rotor. Results from CFD and the vortex code are presented on Fig. 6.1 and Fig. 6.2. On these figures the azimuthal angle is indicated according to the rotation of the blades.

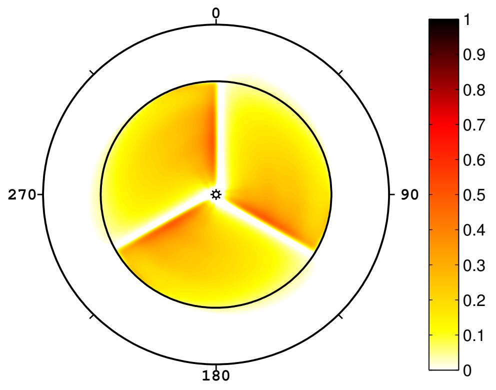

(a)

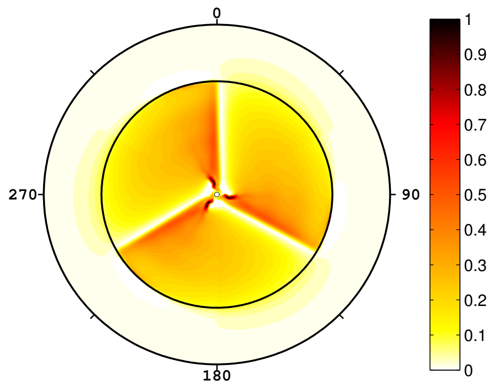

(b)

Figure 6.1: Axial induction obtained by averaging planes at $\pm$3.3%R.

The axial induction obtained by the averaging of closer planes as a slightly higher amplitude

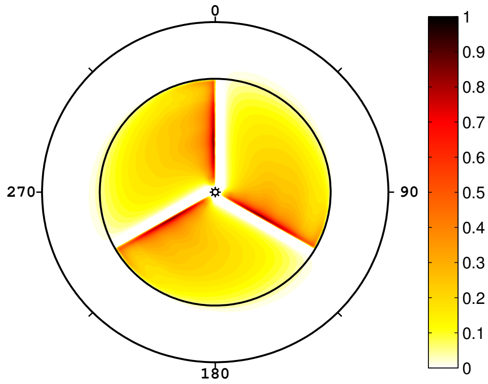

(a)

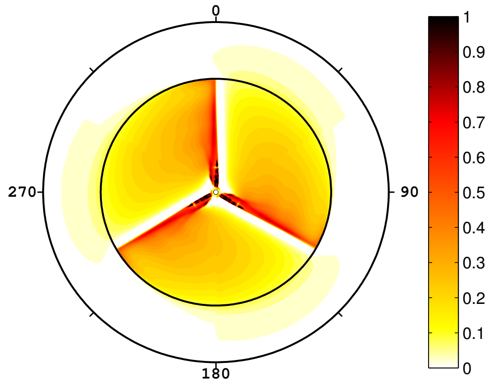

(b)

Figure 6.2: Axial induction obtained by averaging planes at $\pm 1.3\%R$.

and more details. In general the vortex code and the CFD data matches really well and shows the same trends. For any azimuthal direction behind the blade, from the hub to the tip, the axial induction increases, stays rather constant and decreases towards the tip. For azimuthal direction closer to the blade an interesting behavior is observed close to the tip. The axial induction actually increases towards the very tip illustrating the higher values of a_B discussed in this report to define the tip-loss factor. This can be understood with the formation of the tip-vortex. At the tip, the streamlines bends and rolls-up implying that an important part of the axial kinetic energy of the flow is transfered to rotational kinetic energy, i.e. the axial velocity decreases(a_B increases) while the radial and tangential velocities increases. Both codes capture well this behavior. The strong jump of axial velocity on both side of the blade is explained by the bound circulation. The influence of the bound circulation can easily be removed in the vortex code but is more difficult with the CFD. The task is not insuperable though, and should be investigated in the future. This could be done by assessing the circulation on the blade with the Kutta-Joukowski theorem, model the blade as a lifting line and compute with the Biot-savart law the induced velocities due to the bound vorticity only and substract it to the CFD induced velocity.

It should be noted that the small difference in intensity between the two codes is due to a cone angle projection, the blade having indeed a 5°cone angle. The planes outputted by the CFD post-processor appeared to be slanted and their actual definition is still under investigation. The planes used for the vortex code were planes perpendicular to the rotational axis (no tilt angle). For a coned rotor, the questions of which planes planes to use is indeed difficult as the blade follow the surface of a cone as it rotates. The appropriate solution could be to use coned surfaces axially translated from the rotor coned surface. If the rotor is tilted, the situation is even more complex. In any case, for a good comparison with the momentum theory, only the axial velocity, parallel to the ground, should be used, and not the velocity perpendicular to the plane.

6.1.2 Wake deficit plots

As another illustration of the performance of vortex code, it is possible to compute the wake deficit for different axial positions behind the rotor. Such figure is seen on Fig. 6.3 where the vortex code is compared to CFD. Good agreement is found between the two codes, excepts around the rotational axis. This is obviously due to the absence of the nacelle in the vortex code formulation. A way to go around it would be to model the nacelle with a vortex ring such that the flow is blocked in the rotor plane where the nacelle should be located. Such implementation was not considered for this

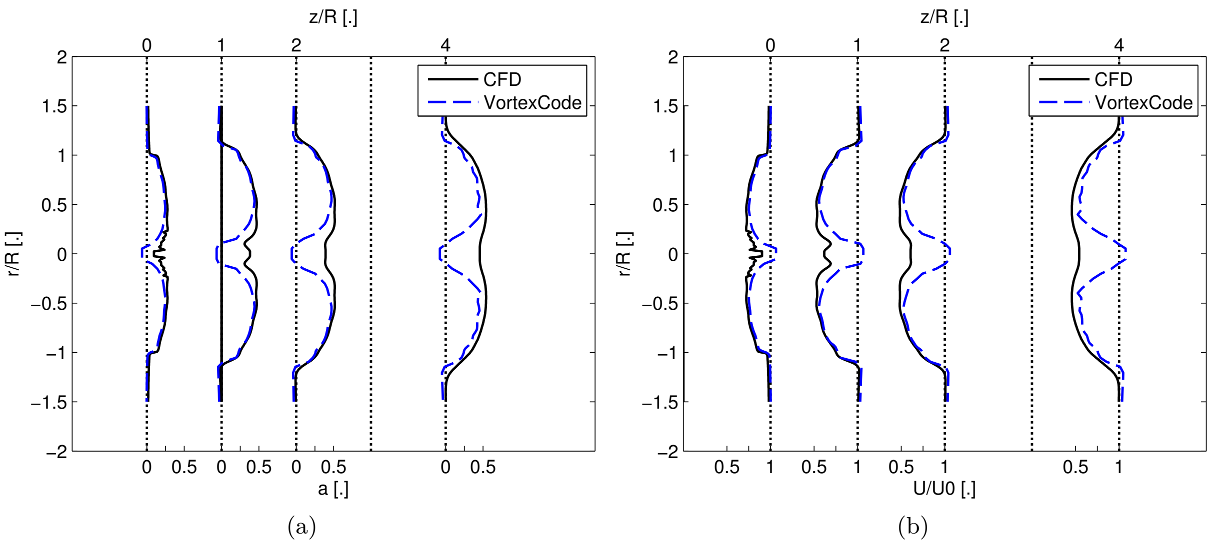

Figure 6.3: Wake deficit computed with the Vortex Code and CFD. Two different representations are given to help conceptualizing the notion of wake deficit: (a) Axial Induction - (b) Velocity ratio

study which was focusing on the tip of the rotor.

6.1.3 General comparison of the different codes

In this section, a wind turbine at one operational point has been simulated with the three different codes available, namely, the BEM, CFD and vortex lattice(VL) code. The wind turbine considered is equipped with a Blade further referred as Blade 2, with a cone angle of 5°. The operating condition is 10.7rpm, 6m/s and $-2.0°$of pitch.

Some key variables obtained by the different codes are compared on Fig. 6.4. Given the large differences between the physical models behind each code the results are quite satisfying. It should be noted that the CFD computations were run in a conservative way, explaining the lower torque performances observed when compared with the two other codes that uses clean 2D data. Also, the axial induction from CFD is computed using an averaging technique over the entire rotor disk and hence does not represent the local axial induction a_B as they other code do. The axial induction obtained with the vortex code is erroneous at the inner part of the blade due to the absence of nacelle's model (this was observed in Sect. 6.1.2). Apart from this differences, the three codes agrees really well which can be considered as a validation of their performance prediction, though (reliable) experimental data are eventually the only judge of such performances.

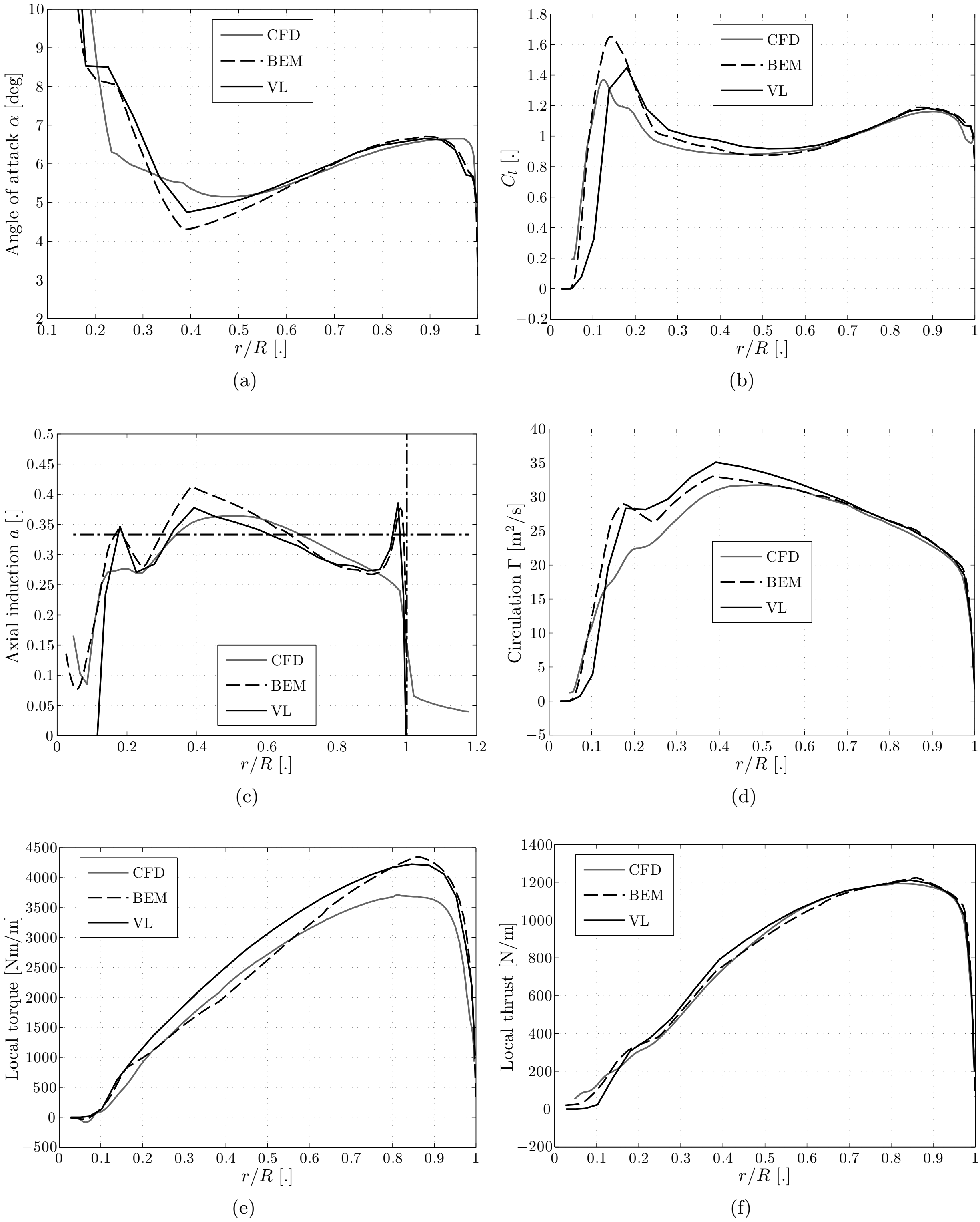

Figure 6.4: Comparison of the results obtained by the different codes when studying a specific wind turbine (Blade 2)

6.2 Examples of BEM results using the new tip-loss models

6.2.1 Comparison between the vortex code and a BEM code with the new tip-loss model

One of the main goal of this analysis is to be able to use the higher degree of description of the unsteady vortex code in the BEM code. The new tip-loss correction derived with the vortex code as explained in Sect. 4.1 is used in a new BEM code implemented as described in Sect. 4.3.3. The unsteady vortex code is accounting for wake roll-up and wake expansion. When used as a descriptive tool(using 2D polar data), it should hence provide a more realistic representation of the flow than a BEM code. The purpose is here to see in which proportion the new BEM code is close to a descriptive vortex code simulation. In other word, can a BEM code perform as well a vortex code when used with the new tip-loss model.

Results for two different blades analyzed with the Vortex code and the BEM code are presented on Fig. 6.5 and Fig. 6.6. It is seen from the two figures that the new BEM code eventually converges using a tip-loss function which is really close to the one obtained with the vortex code. Such results can be seen as the fact that the BEM code is “performing as good” as the vortex code. Using the corrections from the database the BEM code now accounts for wake expansion and roll-up. It is also observed that the tip-loss function obtained by the new BEM code is quite different from the one than Glauert. Though the differences are small, a more physical solution is obtained with the new tip-loss method. Also, it is worth noting that small differences at the tip can have important influence on the torque or flap moments due to the large lever. This can represent significant loss/gain of power and significant change in the loading at the tip which can affect the structural blade design. As an example the local flapwise moment along the blade is represented on Fig. 6.7 for the two BEM codes.

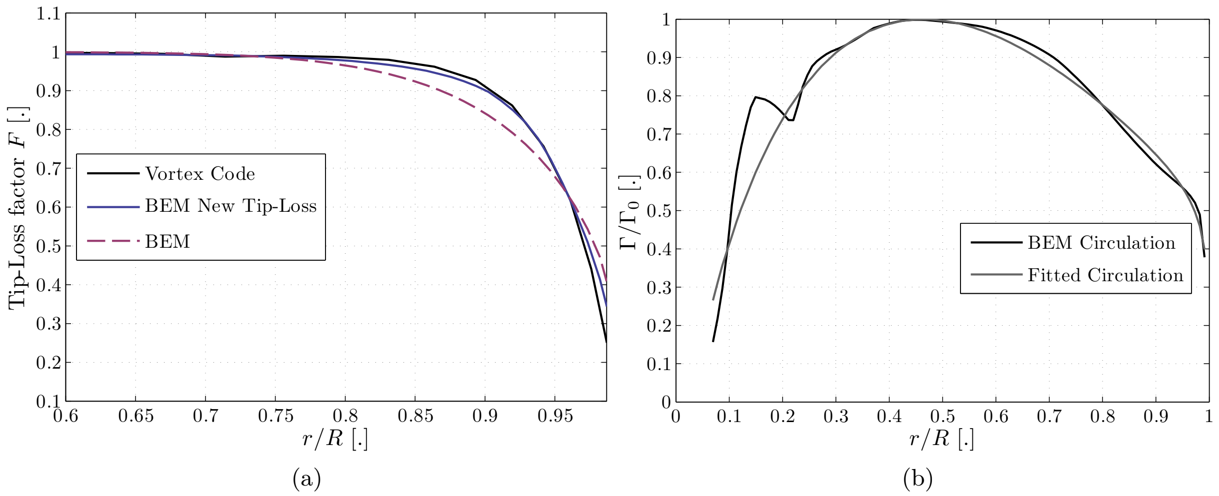

Figure 6.5: Comparison of the new BEM code performances compared to the vortex code - Blade 1. (a) Tip-loss function - (b) BEM circulation and corresponding one from the database

From the results of Fig. 6.5 and Fig. 6.6, it has been observed that the new BEM code performs comparatively to the vortex code. During the BEM iterative process, time is spent looking up the

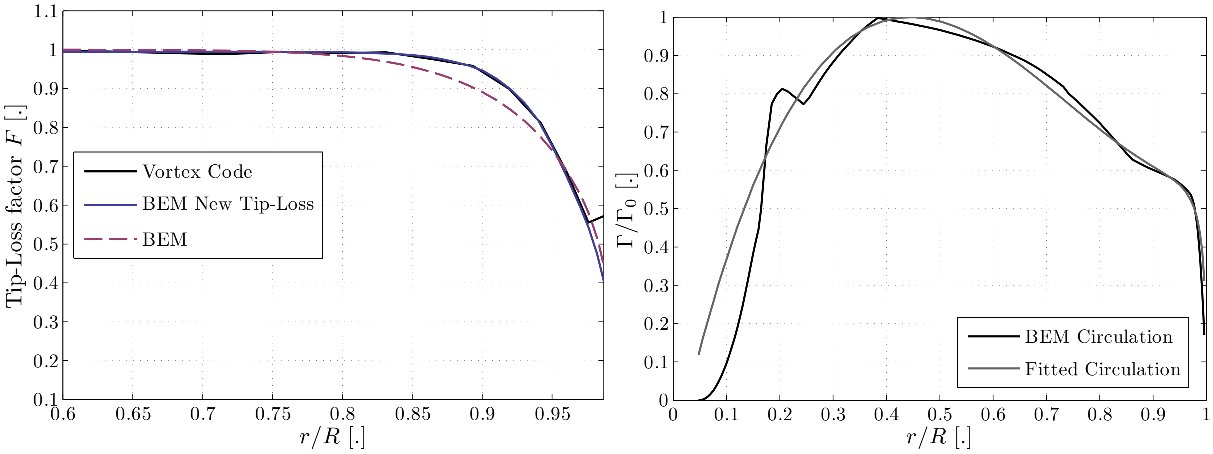

(a) (b)

Figure 6.6: Comparison of the new BEM code performances compared to the vortex code - Blade 2. (a) Tip-loss function - (b) BEM circulation and corresponding one from the database

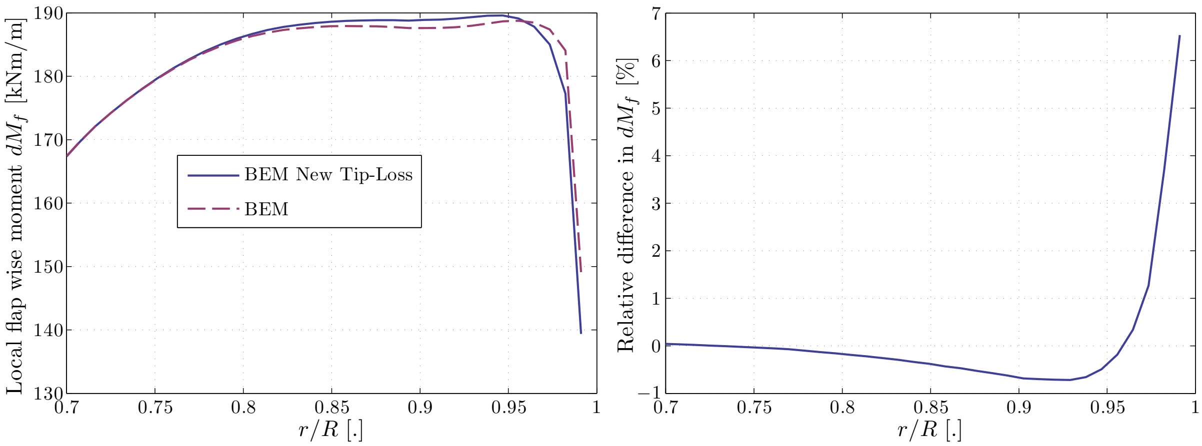

(a) (b)

Figure 6.7: Differences in the local flap moment between the two BEM codes. (a) Physical values - (b) Relative difference

different circulation available and retrieving the corresponding tip-loss. The overall time of this new model is about twice the time of a normal BEM computation. A rough estimate of computational time is seen on Tab. 6.1. The BEM and Vortex code simulations were run on a single core while the CFD computations are usually divided between several dozens of cores(in this example 72 cores). The vortex code can also take strong advantage of parallelization so that the computational could be easily reduced. Even with high complexity, on a single core, the vortex code computation for the resolution required never exceeds 1 hour. From this quick estimate, it is seen that vortex codes are still too slow to be used as designing tools were a lot of iterations are performed in the optimization process. On the other hand, BEM codes are suitable for this, and it is seen that the new BEM code with this new tip-loss model obtains quite similar performances than the vortex code at only a small computational cost.

Table 6.1: Comparison as a rough guide of typical computational time for the different codes. The new BEM code refers to the code using the new tip-loss model described in this report.

Code	BEM	BEM (New)	Vortex Code	CFD
Computational time	2s	4s	12 min	1 day

6.2.2 Comparison of BEM with CFD - Performance tip-loss factor

In the following two different wind turbine designs are analyzed with a BEM code using either Glauert's tip-loss correction or the new tip-loss correction. On top of this correction, the results with or without the "performance" tip-loss function from Eq. (5.2) are studied. For the two blades, Blade 1 and Blade 2, CFD data was also available for comparisons. Results from the different designs are commented in the following paragraphs. On Fig. 6.8, the circulation from the database that was the last(in the BEM iterative process) to fit the best the BEM circulation is displayed.

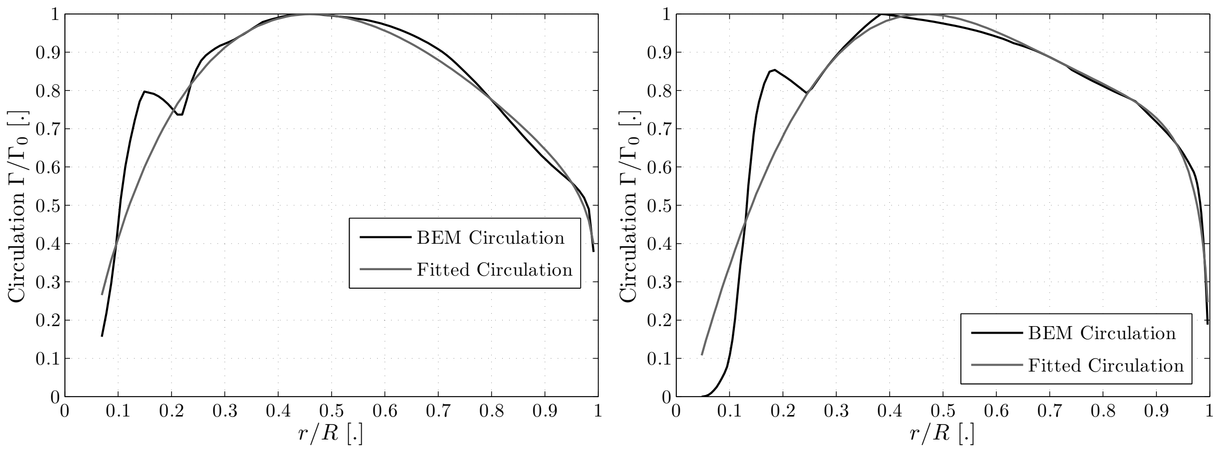

(a) (b)

Figure 6.8: Circulations from the database used by the BEM code. (a) Blade 1 - (b) Blade 2. It is expected that if a circulation curve close to the BEM one is found in the database, then the tip-loss function from the database should be well adapted to this BEM simulation.

Blade 1 Blade 1 was run at 10m/s and 12 rpm with -2.7 degrees of pitch, with some results shown on Fig. 6.9. For this simulation the 2D "clean" coefficients were used, explaining the shift of results between the BEM simulation and the CFD simulations which corresponds more to a "rough" case. The Comparison between Glauert's and the new tip-loss model is rather small in this example. In a sense this is comforting proving that the new-tip loss model is coherent with this common correction. It was also said in Sect. 6.2.1, that small differences at the tip can have large influence on moments. The performance tip-loss factor clearly affects very last part of the tip, and as a result of this, the BEM results match better the CFD ones.

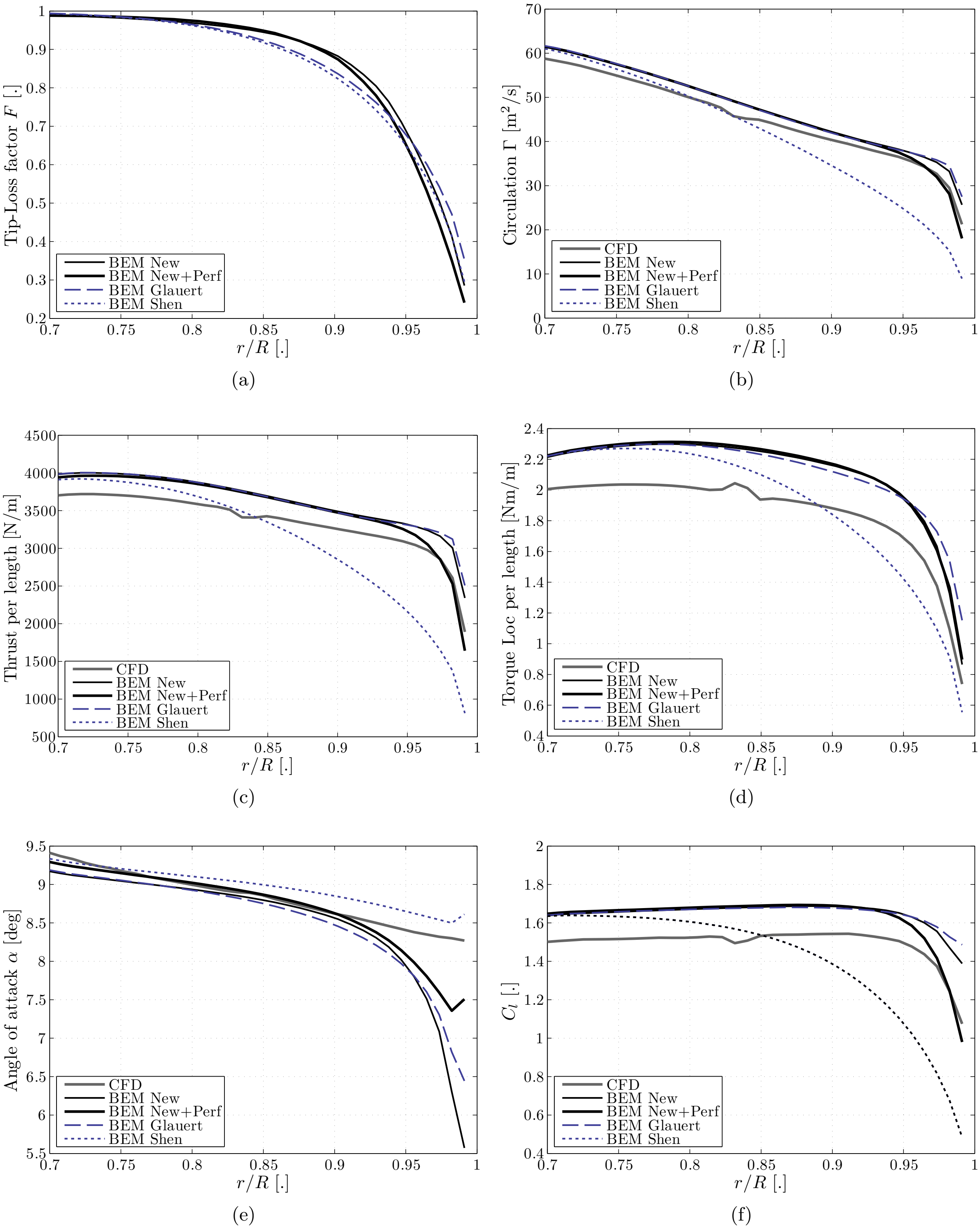

Figure 6.9: Results from the New tip-loss model compared with CFD and BEM for Blade 1

Blade 2 Results for Blade 2 are shown on Fig. 6.10. This simulation was run at 10.7 rpm with a wind speed of 6m/s and -2°of pitch. For this blade the airfoil data matches well the CFD data and the two simulations are in really good agreement. Once again, the difference between the two tip-loss models is rather small.

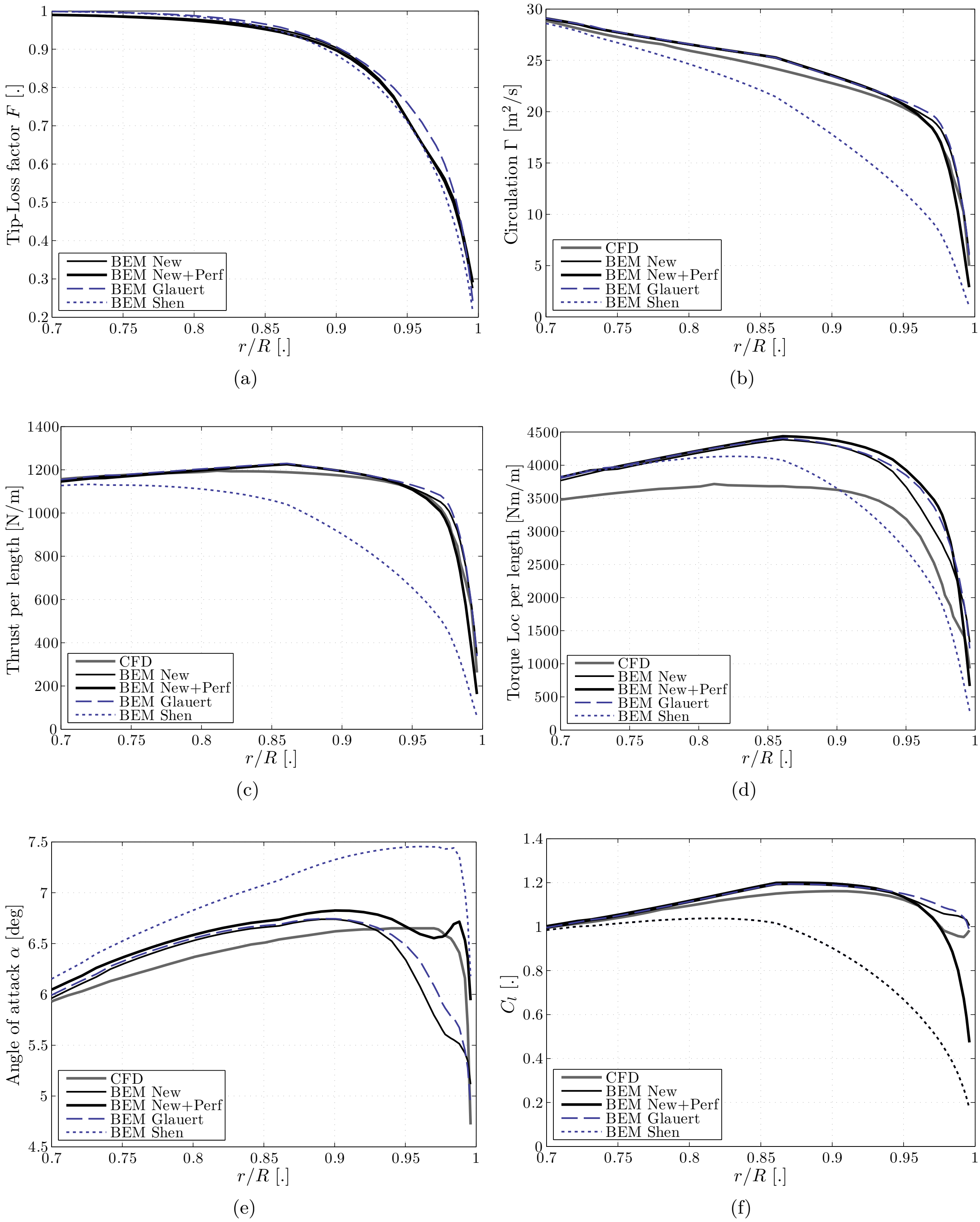

Figure 6.10: Results from the New tip-loss model compared with CFD and BEM for Blade 2

6.3 Comparison of tip-loss factors using CFD as a reference

Comparisons of tip-loss factor without using CFD as a reference were found in Sect. 6.2.1. The discussion whether CFD can be taken as a reference will follow in a next section. In this section the evaluation of the tip-loss function from the BEM code, the vortex code and CFD data is studied. Only the standard "axial induction" tip-loss function is considered, and not the performance tip-loss factor. On Fig. 6.11a on overview of the tip-loss function that is obtained from the three different codes applied on the same blade under the same conditions is found. The two different plane distances used in CFD are represented. As was already discussed, the closer to the rotor plane, the more the effect of finite number of blades is observed. The vortex code and the CFD seem to reveal similar trends, especially when the comparison is done using the same averaging techniques at the same planes (Fig. 6.11b). More information on the averaging technique can be found in Sect. 5.1. The vortex code was run using as prescribed circulation the one from CFD. The spike observed around 0.82% span is actually found in the circulation distribution from CFD.

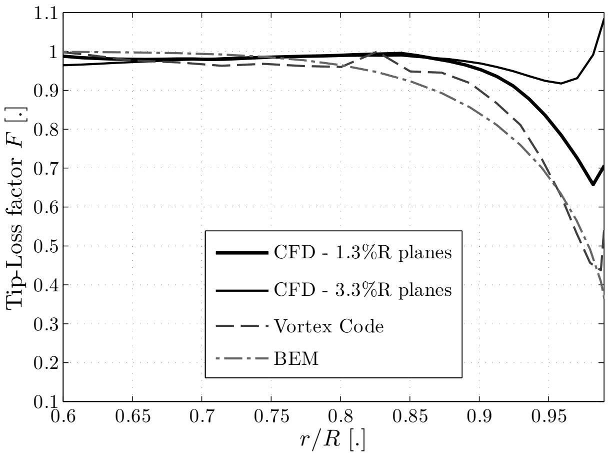

(a)

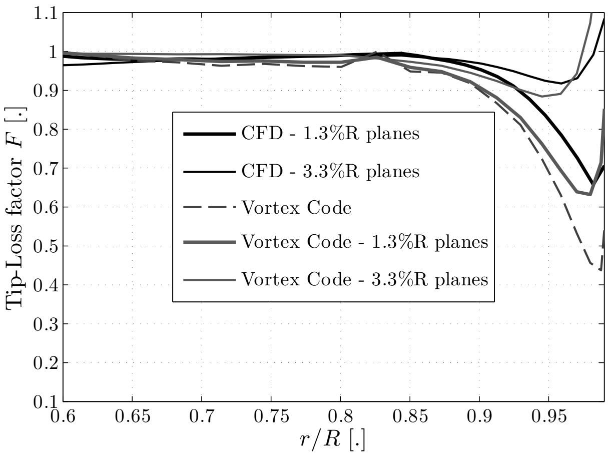

(b)

Figure 6.11: Comparison of the tip-loss function obtained with the three different codes. (a) Results from the three different codes, the BEM code is run with Glauert's tip-loss factor, and the vortex code is run by prescribing the circulation from CFD - (b) Influence of averaging using planes distant to the rotor planes. Accounting for the fact that the vortex code evaluates the tip-loss function at the rotor plane where CFD uses planes distant from the rotor, it seems that the two codes follow similar trends. This is confirmed by figure (b), when the vortex code uses the same averaging method than CFD.

On Fig. 6.12, different approaches are considered. First the vortex code can be used as above with the prescribed circulation from CFD. It has been seen indeed that in this manner the vortex code gives a good estimate of the tip-loss factor at the rotor. *IF* CFD results are assumed to be the goal towards which BEM codes should converge, then this tip-loss function is plotted as a reference on Fig. 6.12a. Nevertheless, it is seen on Fig. 6.12b that the BEM circulation obtained is far from the CFD circulation. The new tip-loss models tries its best to find a circulation in the database that could fit the BEM circulation. The fitted circulation found in the database does not fit the CFD data obviously but it is observed that its derivative follow a similar trend. This could potentially mean that the relative intensity of the trailed vorticity is similar to the CFD one. This could explain why the tip-loss function from the new tip-loss model matches relatively well the CFD tip-loss function between 0.8 and 0.95% span. Above this span, Glauert's tip-loss function agrees better with the CFD results. It can be seen that conclusions are really hard to draw due to the inherent differences between all the different codes. More discussion will follow in the next section.

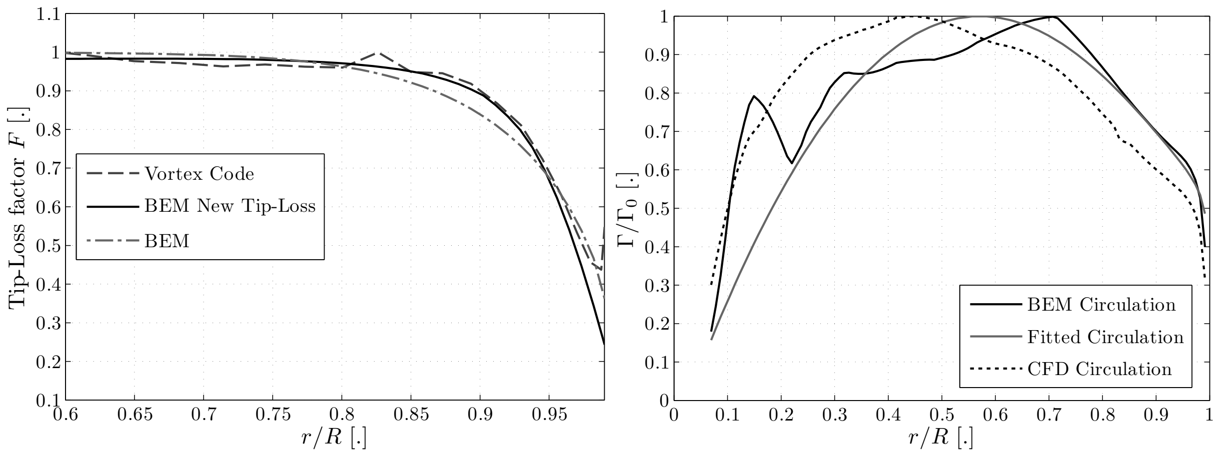

(a) (b)

Figure 6.12: Comparison of different approaches driven by different circulations. (a) Tip-loss function - (b) Normalized Circulations. The color and style schemes between the two plots correspond to each other. Between 0.8 and 0.95% the new tip-loss model seem to better capture the increase of local induced velocity, nevertheless conclusions are really hard to draw.

6.4 Discussion

General observations At a first glance, the difference between Glauert's tip-loss function and the new tip-loss function can be observed to be rather small. Such observation is of course comforting as it shows that the tip-loss corrections obtained with the vortex code are coherent with respect to Glauert's model which has been used in BEM codes that have been validated extensively. Even though the differences between the tip-loss factors are small, it can have important influence on quantities such as moments which benefit from a large lever towards the tip(see Sect. 6.2.1). These small differences can thus mean a lot for structural design of the blade, implying different stiffness and mass repartitions to withstand the loads.

Discussion on the method One of the problem at this stage of development of the new tip-loss model is that the quality of the results depend on how well the database circulations fit the BEM circulations. Only few sets of parameters have been deployed in the database at this stage. Due to the rather high number of parameters (6), having a high resolution database and hence a high resolution of circulation curves and rotor states that can be used in BEM codes requires an important computational time. Using one month of computation on a single machine with four cores, such a high resolution database can be obtained. On top of improving the resolution of the database, an improvement of the methodology can also be considered. Indeed, as was observed in the sensitivity analysis, the shape of the circulation curve appeared to have a small influence on the tip-loss factor, which was rather surprising. On the other hand, from the implementation in the BEM method, it appeared that the quality of the fit between the BEM circulation and the database circulation would affect the overall result. It is believed that other levers could be found in the future, and a better insight on how to handle the vortex code model for the last five percent of the blade is to be investigated.

Comparison with CFD When doing comparisons with CFD the results should be taken with a grain of salt. On one hand, the quality of the 2D coefficients used by the BEM code is one key parameters that influences the quality of the results so that the evaluation of the new tip-loss function is rather difficult. It has been seen for instance in Fig. 6.12b) that the circulation found with a standard BEM code and CFD can be quite different. One can thus questions if it is wise to compare CFD results with the BEM method with the new-tip-loss model knowing that such differences exists. On the other hand, the source of uncertainty from CFD data should not be forgotten. Many parameters come into play in the solving process that can affects the CFD results (turbulence model, transition model, convergence criteria, grid, etc.).

Performance tip-loss factor From the work of Shen[97], Lindenburg[62] and the current, a need to correct airfoil coefficient towards the tip is confirmed.

Performance of the vortex code It has been seen that when used with the prescribed circulation from CFD, the vortex code was giving results in good agreement with CFD. In this sense, it is also expected to give a good assessment of the tip-loss function at the rotor plane, thing which is currently not possible with CFD.

Experimental data A need to compare the existing models with experimental data clearly appears. It is nevertheless difficult to instrument a blade at its tip. Comparisons are of course envisaged for the future of this work using both internal experiments and reference experiments such as the NREL phase six experiment.

Benefit of the method As was discussed in Sect. 4.3.3, there is high potential for such a methodology to give results in many aspects more realistic and more precise than the theoretical approaches of Prandtl and Goldstein. The parametrization and methodology could need to be re-thought and the vortex code slightly improved, but is is believed that such approach can highly improve the knowledge on tip-losses and make BEM codes more realistic. The preliminary study done in Sect. 6.2.1 showed a great benefit of the method. The new BEM code seems to offer performances really close to the vortex code for almost no computational time. The BEM model is improved and can be further used for design and optimization purposes due to the small computational cost added with the new tip-loss model.

Conclusion

From theory to the development of a vortex code A better insight on the origin of tip-losses both historically and physically has been acquired through the first part of this study. Going from simple models with infinite number of blades to more advanced ones, the 3D flow characteristics around a wind turbine were progressively put to light. The notion of tip-losses appeared when studying the 3D effects that affect the wind turbine performances. In this study the distinction between flow characteristics close to the rotor and far behind it was emphasized, giving rise to the notions of near-wake and far-wake. The structure of the wake and its dynamics has been presented. Given the important vorticity found in the wake and its concentration to vortex sheets and tip-vortices, a great descriptive and predictive tool was found to be the vortex theory. On one hand, this theory led to the development of important theorem from Munk and Betz which were later complemented by the only two theoretical studies of tip-losses: the work from Prandtl and Goldstein. On the other hand, vortex theory can be applied for numerical methods which leads to the development of different vortex codes. The implementation of a vortex-lattice code was hence chosen to further study tip-losses and account for higher complexity than the theoretical work from the beginning of the 20$^{\text{th}}$ century.

Historical work on tip-losses Historically, the concept of tip-losses appeared when looking for the circulation that would lead to the minimum energy loss. By focusing on the theories of Betz and Prandtl, the original notion of tip-losses and its applicability was presented. Nevertheless, it was seen that several interpretations could be given due to the simplicity of Prandtl model compared to a real wake flow. The study of Goldstein's theory which model the wake in a better way also led room for discussion. Results from the theories apply to the far-wake and their relations to the rotor parameters is not straightforward. The pitch of the helix, its rotation and the induced velocities are different than the one at the rotor. Using assumptions of no wake expansion and conservation of circulation relations between far-wake parameters and rotor parameters were established. It has been pointed out that the relations used in contemporary articles are different than the one used originally. As many figures as possible were provided to illustrate the different relations and the focus has been on applying this figure to the wind turbine case to avoid any further confusions. Hopefully with this report, the reader can assimilate the historical work of the German school without going through the original articles which uses different notations and conventions. Their reading is nevertheless quite interesting and the author highly recommends the curious reader to discover them.

Different tip-loss factors In this study, a review of all the existing tip-loss correction,s to the author's knowledge, was performed. By using a general formalism for the parameters of the far wake, the theories of Betz, Goldstein and Prandtl were generalized. From these derivations, it was possible to unify all the different tip-loss factors than authors usually refer to as "Prandtl" tip-loss factor even-though they use a different formulation than the one from the original author. Hopefully, more clarity on the matter should follow from this analysis. On top of the existence of many tip-loss factor equations, different definitions, interpretations and implementations are found in BEM codes. This study clearly made the distinction between the standard tip-loss factor and the so called "performance" tip-loss factor which stand in the line of airfoil coefficients corrections.

Standard tip-loss factor The standard tip-loss factor can be defined as a ratio of circulation, like in the original articles of Prandtl and Goldstein, or as a ratio of induced velocities. The later case deserve particular attention. The factor can describe in which proportion the axial induction on the blade is different than the average azimuthal axial induction. In this case though, it should be noted that for a real flow the average azimuthal axial induction goes continuously towards zero in the vicinity of the tip. The axial induction on the blade can take a wide range of values towards the tip due to the formation of the tip-vortex so that the ratio can be hard to define at the very tip of the blade (last 1%). The advantage of this definition of the tip-loss factor, is that is gives a good definition of the angle of attack and thus a better estimate of the loads on the blade using the blade element theory. When used in BEM codes a different definition of the tip-loss factor in terms of induced velocities is found. BEM codes are based on momentum theory which models the rotor with an infinite number of blades and hence no tip-losses are present. In that case the tip-loss factor has conceptually the role of reducing the axial induction from momentum theory to ensure is goes towards zero in the vicinity of the tip. In this sense the tip-loss factor would be the ratio of the real azimuthally averaged axial induction to the momentum theory axial induction. In most BEM code implementations though, the tip-loss factor is applied as a momentum (and sometimes mass flow) change. The tip-loss factor then reduces the loads at the tip. In most BEM equations, the distinction between the average axial induction and the induction on the blade is not done. The introduction of the tip-loss factor in the equations has thus the effect of increasing the axial induction locally to the blade. As a result of this, the velocity triangle is correct as in the previous formulation of the tip-loss factor described. The author believe that BEM equations should be rewritten by carefully making the difference between the axial induction on the blade and the azimuthally averaged axial induction. This is done for instance by Shen[98]. Also, the momentum theory equations should be derived in two steps. The first step consisting in deriving the equations for infinite number of blades. The second step should emphasize the assumption of independence of the different annuli, and hence justify that the axial induction(which is azimuthally averaged by definition), can be changed in each annuli to ensure that it goes towards zero in the vicinity of the tip and hence account for finite number of blades. This should clarify the distinction between $\hat{a}$, $\overline{a}$, and a_B made in this report.

Zero at the tip From the above discussion and the analysis of this report, the question of the tip-loss factor going to zero at the tip was mentioned. Depending on the meaning of the tip-loss factor different conclusions can be drawn. Clearly, the author believes that the average axial induction goes towards zero in the vicinity of the tip. Nevertheless, this is most likely to happen after the tip accounting for the shear stress at the slip stream boundaries. This is observed from CFD data as well. For this reason, forcing the tip-loss factor to go to zero at the tip might be inappropriate. Also, the flow at the tip is very complex close to the blade. Changes in flow direction might even happen in some situations. Hence if the definition $F = \overline{a}/a_B$ is used then the values at the tip is hard to define and is hence not likely to be exactly zero. If on the other hand, the tip-loss is seen as a circulation factor. Then, one can argue that even-though the velocity is none-zero from the above discussion, the loads are likely to be reduced to zero due to the pressure balance occurring at the tip.

Performance tip-loss factor The definition of this performance tip-loss factor and its implementation does not rise as many questions, even though controversy has followed the introduction of Shen's tip-loss factors. This performance tip-loss factor can translate two things. First it can be seen as the results of the pressure equalization at the tip, which should make the loads go to zero at the very tip. Also, it can model the fact that the airfoil does not perform as in 2D in the tip area due to the presence of the tip-vortex and complex flows occurring. Reasons for this are multiple: radial flow, interaction of the tip-vortex with the boundary layer, separation at the very tip and centrifugal forces, etc. This difference in performance is independent to the other tip-loss factor which affects the relative velocity both in amplitude and in direction. Even if the relative velocity is known perfectly, the 2D airfoil data (in the situations observed) do not apply at the very tip. The performance tip-loss factor is hence defined as the ratio between 3D to 2D airfoil polars. The implementation of such correction is straight-forward in BEM codes. The question that remains is the determination of such factor. Experimental data and CFD data can be used but at this time the imprecision in both methods are quite high at the tip of the blade so no conclusion or persistent model can be derived yet.

Tip-losses and CFD data As mentioned in the previous paragraph, the study of the performance tip-loss factor can be done using CFD data. An attempt to derive a model for BEM codes from the available data was done in this study. Nevertheless, imprecisions in CFD and 2D airfoil data leaves the discussion open on the matter. On a different perspective, CFD data was used to analysed tip-losses in terms of axial induction. Interesting results where obtained which matched well the results from the vortex code. This study pointed out the importance of choosing planes as close as possible as the rotor plane in order to assess the tip-loss factor. The definition of the axial induction on the blade was discussed. This definition is difficult due to the spatial extent of the blade and the strong flow fluctuations due to the bound circulation around the blade. Different methods were investigated in this report to assess the axial induction on the blade using CFD data. The method of circular sector with different central angle is preferred by the author for it performs a more physical comparison. On the other hand, only small differences between the methods were found for studying the tip-loss factor only the very tip showed great deviations between the methods.

A new method to investigate tip-losses using a vortex code In this study, a new method was derived to analyse tip-losses using a vortex code. The idea behind this method is that an unsteady free wake vortex code accounts for finite number of blades, wake expansion and wake roll-up. Due to the simple lifting line formulation, the definition of axial induction on the blade and at the rotor plane is made easy, and so is the derivation of the tip-loss factor. To perform a wide range of characteristic analysis, simulations for different tip-speed ratio, thrust coefficients and different family of circulation curves were run. The derivation of the family of circulation curves was done using Bézier curves. The parametrization method derived in this study can be used to characterize typical circulation curve, chord or lift distributions. The author encourages the uses of this method for such applications due to the wide range of curves that can be obtained for only a few parameters. Results from the different vortex code simulations were stored in a database for later use in a BEM code.

Improved BEM code A new BEM code was implemented using the new tip-loss factors derived by the vortex code. The performances of this new BEM code were compared with the one from the vortex code and from a classical BEM code that uses Glauert tip-loss factor. The new BEM code produces results really similar to the vortex code, and quite different at the tip than Glauert's BEM code. It is recalled here that the theory of Prandtl is really simplified and moreover does not account for wake expansion and wake roll-up. The vortex code accounts for this, and the fact that the new BEM code reproduces fairly well the results from the vortex code shows that the goal of improving the physical model of the BEM code has been reached. The computational time for the new BEM code is slightly increased, but still small compared to a vortex code or CFD simulation. From its small computational time the new BEM code can be used as a design tools for new blade, and performance prediction of wind turbine.

Further From the discussions above, it has been seen how difficult the definition of tip-losses was, and how sensitive the implementation of the tip-losses in a BEM code could be. This study intended to give an overview of the existing work on tip-losses and to clarify and distinguish them. Further work is required for the development of BEM equations which clearly distinguish the different axial induction factor introduced in this report. Using either a vortex code, CFD, or experimental data, the link between far-wake and rotor parameters has to be studied in order for the theory of Goldstein to be used more precisely. The use of a vortex code to investigate tip-losses was shown in this study, and the way it could improve BEM code was demonstrated. Methodology similar to the one employed can be derived for further improvements. It is also believed that improvement in the development of vortex code can lead to better results in the determination of the tip-loss factor. The investigation of tangential induction factor is also to be considered. Indeed, one can ponder the validity of using a same correction factor for the axial and tangential induction. Discussions from the definition of tip-loss and their implementation will follow this study, making it a challenging but exciting topic.

Acknowledgements

This master's thesis adventure was made possible thanks to the contribution and help of many people, colleagues and friends. First, I would like to thank Kevin Standish for offering me the opportunity to do my master's thesis at Siemens and to join the dynamic team of Boulder's office. I am grateful for his patience, his perseverance and his generosity and I really appreciated his efforts to make be feel welcomed and part of the team. My thanks are also going to my two supervisors, Kristian Dixon and Mac Gaunaa who regularly followed my work, provided me with valuable advises and guided me with patience. They helped me to focus my study, but discussing with them would arouse my interest and curiosity for the topic and would motivate me to investigate more topics. I hence really appreciated that they offered me this freedom of inquiring and spending time in different directions. During this study I appreciated that several scientists took the time to reply to my emails and questions. Being aware of the few time they have for such considerations, and given the fact that not all my emails received a reply, I am deeply thank full to the one who took this time: Gijs van Kuik, Valery Okulov, Helge Madsen, Christian Bak and Wen Zhong Shen. My experience in Boulder would have not been possible without the help and discussion of Jakob Mann and Jeppe Johansen who oriented me towards Boulder.

I really appreciated the six months spent amongst Boulder's team and I would like to thank them all for welcoming me in such a nice working environment and for bringing a rich human dimension to this project. They all contributed in a way to this work, and it is difficult not of mention all of them. For this reason, I will mention in the following the ones I thank for their direct contribution to this study: Alonzo Zamora for his collaboration and discussion and for providing all the CFD data this study was based on; Paul Medina for some fun and interesting aerodynamic discussions; Arni Steingrimsson for his interest in converting my code to GPU; Khanh Nguyen for looking over my screen once in while to give me feedback and discuss vortex codes with me; Drew Eisenberg for some programming experience exchanges; and of course Kristian Dixon for supervising me with patience. My stay in Boulder would not have been the same without the spare time activities spent with colleagues and friends. Adding to the above my family together with the not mentioned and forgotten ones, I'd like to thank them all for making this project such a rich adventure.

Bibliography

[1] Abbott, I., and Von Doenhoff, A. *Theory of wind sections - Including a summary of airfoil data.* Dover Publications Inc, New York, 1959.

[2] Abramowitz, M., and Stegun, I. *Handbook of Mathematical Functions with Formulas, Graphs, and Mathematical Tables.* Dover, New York, 1964.

[3] Anderson, J. *Fundamentals of aerodynamics - Third Edition.* Mc Graw Hill, 2001.

[4] Bailey, S. *The interaction of a Wing-Tip Vortex and Free-Stream Turbulence.* PhD thesis, University of Ottawa, 2006.

[5] Bak, C. Aerodynamic airfoil characteristics for wind turbines - 2d and 3d. In *DTU courses* (2010).

[6] Bak, C. Aerodynamic design of wind turbine rotors. Risø-I-Report, October 2010.

[7] Bak, C., Johansen, J., and Andersen, P. Three-dimensional corrections of airfoil characteristics based on pressure distributions. *European Wind Energy Conference & Exhibition - Athens, Greece* (2006).

[8] Bertin, J., and Cummings, R. *Aerodynamics for engineers - 5th Edition.* Pearson Prentice Hall, 2009.

[9] Betz, A. Schraubenpropeller mit geringstem energieverlust - mit einem zusatz von l. prandtl. *Göttinger Klassiker der Strömungsmechanik Bd. 3* (1919), p68–88. (in German).

[10] Betz, A. Das maximum der theoretisch möglichen ausnützung des windes durch windmotoren. *Zeitschrift für das gesante Turbinewesen 26* (1920), p307–309. (in German).

[11] Bonnet, A. La portance ou comment tuer un mythe. *I.S.A.E. - SUPAERO* (2005). (in French).

[12] Bonnet, A., and Luneau, J. *Aerodynamique: Theorie de la dynamique des fluides.* Cepades Edition - SUPAERO, 1989. (in French).

[13] Branlard, E. *On the statistics of gusts and their propagation through a wind farm.* ECN - Wind-Memo-09-005, February 2009.

[14] Branlard, E. *Wind power in arctic conditions: The experience of Greenland.* Risø-DTU - Arctic Technologies, December 2010.

[15] Branlard, E. *Wind energy: physics and engineering.* Development version, March 2011.

[16] Bruining, A. Pressure measurements on a rotating wind turbine blade on the open air rotor research facility of the delft technical university. *EWEC* (1993).

[17] Burton, T., Sharpe, D., Jenkins, N., and Bossanyi, E. *Wind Energy Handbook*. J. Wiley & Sons, 2001.

[18] Chattot, J.-J. Optimization of propellers using helicoidal vortex model. *Computational Fluid Dynamics Journal* (2001).

[19] Chattot, J.-J. Design and analysis of wind turbines using helicoidal vortex model. *Computational Fluid Dynamics Journal* (2002).

[20] Chaviaropoulos, P., and Hansen, M. Investigating three-dimensional and rotational effects on wind turbine blades by means of quasi-3d navier stokes solver. *J. Fluids Engineering 122* (June 2000), p330–336.

[21] Corrigan, J., and Schillings, J. Empirical model for stall delay due to rotation. *American Helicopter Society Aeromechanics Specialists conference* (1994).

[22] Crigler, C. Application of theodorsen's theory to propeller design. Tech. rep., NACA report 924, 1949.

[23] De Vries, O. Fluid dynamic aspects of wind energy conversion. *AGARD report AG-243* (1979), p1–50.

[24] Donadon, M., and Iannucci, L. A vortex lattice program for steady state aerodynamic analysis of flapped and twisted uav wing planforms. *Brazilian Symposium on Aerospace Eng. & Applications* (2009).

[25] Drela, M. Assorted views on teaching of aerodynamics. *AIAA Paper 98-2792* (1998).

[26] Drela, M. *XFOIL - http://raphael.mit.edu/xfoil/*. MIT, 2000.

[27] Drzewiecki, S. Méthode pour la détermination des éléments mécaniques des propulseurs hélicoïdaux. *Bulletin de l'Association Technique Maritime No. 3 - Session de 1892* (1893), p11–31. (in French).

[28] Du, Z., and Selig, M. A 3-d stall delay model for horizontal axis wind turbie performance predictio. *AIAA* (1998), p9–19.

[29] Froude, R. On the part played in propulsion by differences of fluid pressure. *Transactions of the Institute of Naval Architects 30* (1889), p390–405.

[30] Froude, W. Unknown title. *Transactions of the Institute of Naval Architects 19* (1878), p47.

[31] Fukumoto, Y., and Okulov, V. The velocity field induced by a helical vortex tube. *Physics of fluids 17* (2005).

[32] Gaunaa, M., Rhétoré, P.-E., and Sørensen, N. Risø contributions to final report efp-vingetipper. Tech. Rep. Riso-R-xxxx, Risø-DTU, 2011.

[33] Gaunaa, M., Sørensen, N., and Døssing, M. Prediction of steady aerodynamic performance of rotors with winglets using simple prescribed ake methods. *AIAA Aerospace Sciences Meeting 543* (2011).

[34] Giguiere, P., and Selig, M. Design of a tapered and twisted blade for the nrel combined experiment rotor. Tech. rep., NREL, 1999.

[35] Glauert, H. Airplane propellers, division l. *Aerodynamic Theory 4* (1935), p169–360.

[36] Goldstein, S. On the vortex theory of screw propellers. Tech. rep., St. John's College, Cambridge, January 1929.

[37] Grasso, F., van Garrel, A., and Schepers, G. Development and validation of generalized lifting line based code for wind turbine aerodynamics. Tech. Rep. ECN-M–11-004, ECN, 2011.

[38] G.T. Houlsby, S. D., and Oldfield, M. Application of linear momentum actuator disc theory to open channel flow. Tech. rep., University of Oxford, Department of Engineering Science, 2008. Report No. OUEL 2296/08.

[39] Gupta, S., and Leishman, J. Comparison of momentum and vortex methods for the aerodynamic analysis of wind turbines. *43rd AIAA Aerospace Scieces and Exhibit* (2005).

[40] Hand, M., Simms, D., Fingersh, L., Jager, D., Cotrell, J., Schreck, S., , and Larwood, S. Unsteady aerodynamics experiments phase vi: Wind tunnel test configurations and available data campaigns. Tech. rep., NREL - TP-500-29955, 2001.

[41] Hansen, K. *Description of Nordtank 500/41 at RisøNational Laboratories.* Risø, 2003.

[42] Hansen, M. *Aerodynamics of Wind Turbines - Second Edition*. Earthscan, London, Sterling, VA, 2008.

[43] Hansen, M., and Johansen, J. Tip studies using cfd and comparison with tip loss models. *Wind Energy 7* (2004), 343–356.

[44] Helmbold, H. Zur aerodynamik der treibschraube. *Zeitschrift f ur Flugtechnik und Motorluftschiffahrt (ZFM) 15* (1924), 150. (in German).

[45] Himmelskamp, H. *Profile investigations on a rotating airscrew.* PhD thesis, MAP Volkenrode, Translation 832, 1947.

[46] Huerre, P. *Mécanique des Fluides - Tome 1.* Ecole Polytechnique - France, 2006. (in French).

[47] Johansen, J., Sørensen, N., Madsen, H., Shen, W. Z., and Okulov, V. Advanced rotor aerodynamics including tip and root aerodynamics. Tech. Rep. Riso-R-1559, Risø - DTU, 2005.

[48] Johansen, J., and Sørensen, N. N. Aerofoil characteristics from 3d cfd rotor computations. *Wind Energy 7*, 4 (2004), 283–294.

[49] Johnson, W. *Helicopter theory.* Dover books on physics. Dover Publications, 1994.

[50] Joukowski, N. Travaux du bureau des calculs et essais aeronautiques. Tech. rep., Ecole Superieure Technique de Moscou, 1918. Republished by editions Gauthier-Villars in "Théorie Tourbillonaire de l'hélice Propulsive", Paris 1929 (in French).

[51] Joukowski, N. Windmill of the nej type. *Transactions of the Central Institute for Aero-Hydrodynamics of Moscow* (1920). Also published in Joukowsky NE. Collected Papers Vol VI. The Joukowsky Institute for AeroHydrodynamics, Moscow: vol VI, 405-409, 1937 (in Russian).

[52] Katz, J., and Plotkin, A. *Low-Speed Aerodynamics, 2nd Edition.* Cambridge University Press, 2001.

[53] Kida, T. A theoretical treatment of lifting surface theory of an elliptic wing. *ZAMM 60* (1980), p645–651.

[54] Kloosterman, M. Development of the near wake behind a horizontal axis wind turbine. Master's thesis, Delft University of Technology, 2009.

[55] Komninos, K. Modeling considerations of the optimum rotor using vortex method. Master's thesis, DTU, 2007.

[56] Kramer, K. The induced efficiency of optimum propellers having a finite number of blades. Tech. rep., NACA - TM - 884, 1939.

[57] Kroo, I. *Applied aerodynamics: a digital textbook*. Desktop Aeronautics, 1996-2007.

[58] Lanchester, F. A contribution to the theory of propulsion and the screw propeller. *Transactions of the Institution of Naval Architects 57* (1920), p98–116.

[59] Larrabee, E. E., and French, S. E. Minimum induced loss windmills and propellers. *Journal of wind Engineering and Industrial Aerodynamics 15* (December 1983), p317–327.

[60] Leishman, J. *Principles of Helicopter Aerodynamics - Second Edition*. Cambridge University Press, 2006.

[61] Lindenburg, C. Stall coefficients - aerodynamic airfoil coefficients at large angles of attack. Tech. rep., ECN - RX01004, 2001.

[62] Lindenburg, C. Investigation into rotor blade aerodynamics. Tech. Rep. ECN-C-03-025, ECN, 2003.

[63] Lindenburg, C. Modelling of rotational augmentation based on engineering considerations and measurements. *European Wind Energy Conference - London* (2004).

[64] Lock, C. N. H., Bateman, H., and Townend, H. C. H. An extension of the vortex theory of airscrew with applications to airscrews of small pitch, including experimental results. *Report and Memoranda 1014* (September 1925).

[65] Machevaux, E. Analysis of airfoil characteristics from pressure distribution. Master's thesis, DTU - Siemens, 2011.

[66] Madsen, H., Bak, C., Døssing, M., Mikkelsen, R., and Øye, S. Validation and modification of the blade element momentum theory based on comparisons with actuator disc simulations. *Wind Energy 13* (2010), p373–389.

[67] Madsen, H., Mikkelsen, R., Øye, S., Bak, C., and Johansen, J. A detailed investigation of the blade element momentum (bem) model based on analytical and numerical results and proposal for modifications of the bem model. *Journal of Physics: Conference Series 75* (2007).

[68] Madsen, H., and Rasmussen, F. Derivation of three-dimensional airfoil data on the basis of experiment and theory. *AWEA Conference* (1988).

[69] Madsen et al. The dan-aero mw experiments - final report. Tech. Rep. Riso-R-1726, Risø-DTU, 2010.

[70] Manwell, J., McGowan, J., and Rogers, A. *Wind Energy Explained*. J. Wiley and Sons, LTD, August 2003.

[71] Mathworld. *http://www.mathworld.wolfram.com/*. Wolfram, 2011.

[72] Melin, T. A vortex lattice matlab implementation for linear aerodynamic wing applications. Master's thesis, Royal Institude of Technology (KTH), December 2000.

[73] Mikkelsen, R., Madsen, H. A., Hansen, M., Shen, W., and Øye, S. Research in aeroelasticity efp-2007 - chapter 2: Analysis of induction near tip. Tech. Rep. Risø-R-1649, Risø-DTU, 2007.

[74] Moffitt, B., Bradley, T., Parekh, D., and D.Mavris. Validation of vortex propeller theory for uav design with uncertainty analysis. unpublished.

[75] Moriarty, P. J., and Hansen, A. *AeroDyn Theory Manual*, 2005.

[76] Munk, M. *The minimum induced drag of aerofoils.* NACA report No. 121, 1923.

[77] NIST. Digital library of mathematical functions from http://dlmf.nist.gov/ - release 2010-05-07.

[78] Okulov, V., and Sørensen, J. Instability of a vortex wake behind wind turbines. *Doklady Physics 49* (2004), p772–777.

[79] Okulov, V., and Sørensen, J. Optimum operating regimes for the ideal wind turbinee. *Journal of Physics - Conference series 75* (2007).

[80] Okulov, V., and Sørensen, J. An ideal wind turbine with a finite number of blades. *Doklady Physics 53* (2008), p337–342.

[81] Okulov, V., and van Kuik, G. The betz-joukowsky limit: on the contribution to rotor aerodynamics by the british, german and russian scientific schools. *Wind Energy 464* (2011).

[82] Olsen, A. *Optimisation of propellers using the vortex-lattice method.* PhD thesis, Technical University of Denmark - DTU, 2001.

[83] Olver, F., Lozier, D., Boisvert, R., and Clark, C. *NIST Handbook of Mathematical functions.* Cambrideg University Press, 2010.

[84] Øye, S. A simple cortex model. *IEA* (1990).

[85] Phillipps, W. *Mechanics of Flight.* John Wiley and Sons, 2004.

[86] Prandtl, L. Tragflügeltheorie. *Göttinger Klassiker der Strömungsmechanik Bd. 3* (1918). (in German).

[87] Prandtl, L. Schraubenpropeller mit geringstem energieverlust - mit einem zusatz von l. prandtl. *Göttinger Klassiker der Strömungsmechanik Bd. 3* (1919), p89–92. (in German).

[88] Prandtl, L. *Applications of modern hydrodynamics to aeronautics.* NACA report No. 116, 1921.

[89] Rankine, W. J. Unknown title. *Transactions of the Institute of Naval Architects 6* (1865), p13.

[90] Rasmussen, F., Petersen, S., Larsen, G., Kretz, A., and Andersen, P. Investigations of aerodynamics, structural dynamics and fatigue on danwin 180 kw. *Riso-M-2727* (1988).

[91] Ronsten, G. Static pressure measurements on a rotating and a non-rotating 2,375m wind turbine blade. *EWEC* (1991).

[92] Sankar, L. Computational studies of horizontal axis wind turbines - annual status report 2000-2001. Tech. rep., NREL - Georgia institute of technology, 2001.

[93] Sant, T. *Improving BEM-based aerodynamics models in Wind turbine design codes.* PhD thesis, DU Wind - Delft University Wind Energy Research Institute, 2007.

[94] Sant, T., van Kuik, G., and van Bussel, G. Estimating the angle of attack from blade pressure measurements on the nrel phase vi rotor using a free wake vortex model: axial conditions. *Wind energy 9* (2006), 549–577.

[95] Savino, J., and Nyland, T. Wind turbine flow visualization studies. *NASA lewis Research Center, Cleeveland, Ohio* (1985).

[96] Schmitz, S., and Chattot, J.-J. Influence of the vortical wake behind wind turbines using a coupled navier-stokes/vortex-panel methodology. *Third MIT Conference on Computational Fluid and Solid Mechanics* (2005), p832–836.

[97] Shen, W., Hansen, M., and Sørensen, J. Determination of angle of attack for rotating blades. *Proceedings of the Euromech colloquium - DTU 37* (2007).

[98] Shen, W. Z., Mikkelsen, R., Sørensen, J. N., and Bak, C. Tip loss corrections for wind turbine computations. *Wind Energy 8* (2005), p457–475.

[99] Shenkar, R. Design and optimization of planar and non planar wind turbine blades using vortex methods. Master's thesis, Technical University of Denmark - DTU, September 2010.

[100] Sissingh, G. Contribution to the aerodynamics of rotating-wing aircraft. Tech. rep., NACA - TM - 921, 1939.

[101] Snel, H., Houwink, R., and Bosschers, J. Sectional prediction of lift coefficient on rotating wind turbine blades in stall. Tech. Rep. ECN-C-93-052, ECN, 1993.

[102] Sørensen, J. *Three-level, viscous-inviscid interaction technique for the prediction of separated flow past rotating wing.* PhD thesis, Technical University of Denmark - DTU, 1986.

[103] Sørensen, J., Shen, W., and Munduate, X. Analysis of wake states by a full-field actuator disc model. *Wind Energ. 1* (1998), 73–88.

[104] Sørensen, J., and van Kuik, G. General momentum theory for wind turbines at low tip speed ratios. *Wind Energy* (2010).

[105] Squire, H. The growth of a vortex in a turbulent flow. *Aeronautical Quaterly 16* (1965), 302–306.

[106] Stepniewski, W., and Keys, C. *Rotary-Wings Aerodynamics.* Dover Publication, 1984.

[107] Tangler, J., and Kocurek, J. D. Wind turbines post-stall airfoil performance characteristics guidelines for blade-element momentum methods. Tech. rep., NREL, 2005.

[108] Theodorsen, T. The theory of propellers i-iv. Tech. rep., NACA reports 775-778, 1944.

[109] Tibery, C., and Wrench, J. Tables of goldstein factor. Tech. rep., Applied mathematics laboratory - Department of the navy - report 1534, 1964.

[110] Troldborg, N., Gaunaa, M., and Mikkelsen, R. Actuator disc simulations of influence of wind shear on power production of wind turbines. *Torque 2010, The science of making torque from wind, EWEA* (2010), p271–297.

[111] Tuck, E. Some accurate solutions of the lifting surface integral equation. *J. Austral. Math. Soc. Ser. B 35* (1993), p127–144.

[112] van Garrel, A. Development of a wind turbine aerodynamics simulation module. Tech. Rep. ECN-C–03-079, ECN, 2003.

[113] van Kuik, G. The lanchester-betz-joukowsky limit. *Wind Energy 10* (2007), p289–291.

[114] Vermeer, L., Sørensen, J., and Crespo, A. Wind turbine wake aerodynamics. *Progress in Aerospace Sciences*, 39 (2003), p467–510.

[115] Viterna, L., and Corrigan, R. Fixed pitch rotor performance of large horizontal axis wind turbines. *DOE/NASA Workshop on large horizontal axis wind turbines* (1981).

[116] Watson, G. *A treatise on the theory of Bessel functions.* Cambridge at the University Press, 1922.

[117] Wilson, R., and Lissaman, P. Applied aerodynamics of wind power machines. Tech. rep., Oregon State University, May 1974.

[118] Wilson, R., Lissaman, P., and Walker, S. Aerodynamic performance of wind turbines. Tech. rep., Oregon State University, June 1976.

[119] Yang, K. Y.-L. Helicopter rotor lift distribution for minimum induced power loss. Master's thesis, M.I.T., 1991.

[120] Zahle, F., and Sørensen, N. On the influence of far-wake resolution on wind turbine flow simulations. *Journal of Physics - Conference Series 75* (2007).

APPENDICES

Appendix A

Goldstein's factor - Derivation and computation

A.1 Short guide to follow Goldstein's article

Below, a short guide to the reading of Goldstein article is presented and two typographic errors are put to light. The notations from the article will be adopted but other variables will be introduced to make some algebra more simple and hopefully clear.

Paragraph §2 The boundary conditions states that the motion imparted to the air is normal to the vortex sheets. In other words, there should be no air passing through the vortex sheet which is assumed to be impermeable. From Betz result, the vortex system is as if the helix was translating at a velocity w, but in reality each section of the helix has a velocity component perpendicular to its section. This is a propriety of helix discusses in Sect. 1.1.5 and illustrated onFig. 1.13. The total contribution of the induced velocities generated by the wake should thus correspond to the velocity of each helix section to satisfy the impermeability condition. Figure A.1 illustrates this condition and hence equation (2) and (3).

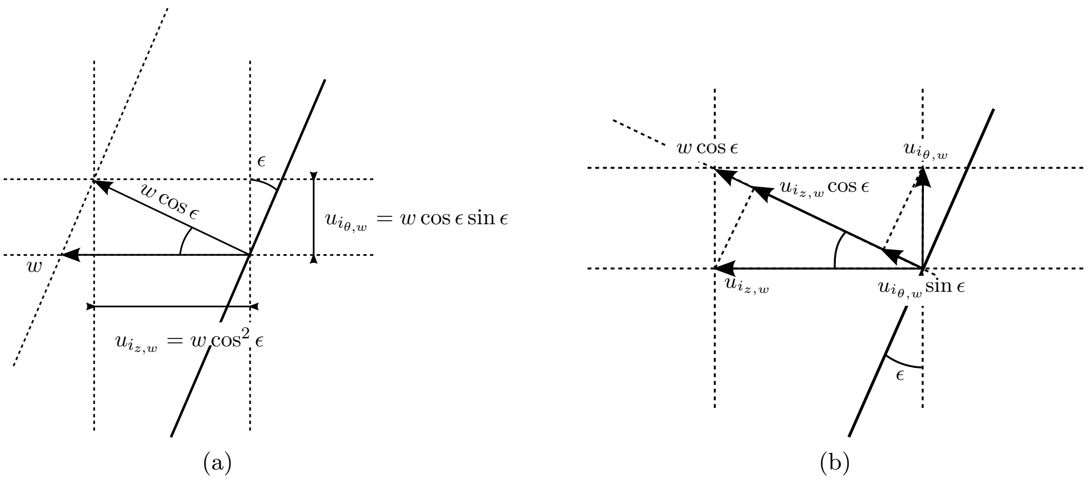

Figure A.1: Induced velocity in the far wake. (a) Induced velocities as function of the wake velocity w - (b) Projections of velocities on the normal

Equation (5) is quickly derived with:

$$\frac{\partial\phi}{\partial z} = \frac{\partial\phi}{\partial\zeta}\frac{-\omega}{v} \tag{A.1}$$

$$\frac{\partial\phi}{\partial\theta} = \frac{\partial\phi}{\partial\zeta} \tag{A.2}$$

Letting the ratio wv/ω equal to 1 is not an assumption, it's just a way to take advantage of linearity. This can be formalized by letting $k = wv/\omega$, and $\tilde{\phi} = \phi/k$, then by linearity both ϕ and $\tilde{\phi}$ satisfy Laplace equation, but ϕ satisfies the BC from equation (5) whereas $\tilde{\phi}$ satisfies equation (7). Once the solution for $\tilde{\phi}$ is found in §3.5, then the solution is simply multiplied by k to obtain the solution for ϕ. That's what Goldstein does but of course dropping the tilde notation. Equation (7) and (8) are easily derived with:

$$\nabla^2 = \frac{\partial^2}{\partial r^2} + \frac{1}{r}\left(\frac{\partial}{\partial r} + \frac{1}{r}\frac{\partial^2}{\partial\theta^2}\right) + \frac{\partial^2}{\partial z^2} \tag{A.3}$$

$$\frac{\partial\phi}{\partial r} = \frac{\omega}{v}\frac{\partial\phi}{\partial\mu} \tag{A.4}$$

$$\frac{\partial}{\partial r} = \frac{\omega}{v}\frac{\partial}{\partial\mu} \tag{A.5}$$

$$\left(\mu\frac{\partial}{\partial\mu}\right)^2\phi = \mu^2\frac{\partial^2\phi}{\partial\mu^2} + \mu\frac{\partial\phi}{\partial\mu} \tag{A.6}$$

Equation (8) is called the homogeneous modified Bessel differential equations and admits for solution the modified Bessel function $I_n(\mu)$ and $K_n(\mu)$ (see for instance [2, p 374] or [83, chap. 10]).

Paragraph §3.1 The form of equation (3) is suggested by the boundary condition. Inserting equation (3) in §2 (8) leads to equation (4), and inserting (3) in the boundary condition leads to equation (5). Now the problem reduces to solving equation (4) with the boundary condition (5).

Equation (6) is simply the Fourier series of the function $f(\zeta) = \zeta$ on $[0\ ;\ \pi]$ (or the Fourier decomposition of $|\zeta|$ on $[-\pi\ ;\ \pi]$). This decomposition will be used for the right-hand side of equation (4). The idea is then to use a decomposition of the same nature for ϕ_1 to allow an identification term by term between the left hand side and the right hand side, hence the assumption of equation (7). Equation (8) and (9) are purely the result of this identification term by term.

Equation (8) can be directly solved: noting H the operator $(\mu\frac{d\mu}{d\mu})^2$, and $g_0 = \pi/2\mu^2/(1+\mu^2)$ then equation (8) is just $H(f_0) = H(g_0)$, which means that $f_0 = g_0 + k$ where k is a function verifying $H(k) = 0$. This writes $\mu^2 k'' + \mu k' = 0$, which can be integrated twice to find that $k = A\ln(\mu) + B$. The term in log has to disappear for finiteness at $\mu = 0$, and the term B is just a constant which is of no interest when dealing with potentials because they are defined relatively. We found that $f_0 = g_0$ which is equation (10).

Going from (9) to (12) is quickly derived using the above notation and some dummy variables A, B, g: Equation (11) is written $f_m = B(g - g_m)$, (9) written $H(f_m) - Af_m = H(Bg)$, in which we can insert the above expression of f_m to get after simplification $-H(-BG_m) - ABg_0 - ABg_m = 0$, simplify by B and get equation (12).

The solving of equation (12) involves some mathematical formalism which will be briefly presented here for clarity and to have a broader perspective of the context. The inhomogeneous Bessel equation of the function $y(z)$ writes:

$$\left(z\frac{d}{dz}\right)^2 y + (z^2 - \nu^2)y = kz^{\tilde{\mu}+1} \tag{A.7}$$

where z can be complex and $k, \tilde{\mu}, \nu$ are constants. The solution for this equation depends on the parity of the terms $\nu + \tilde{\mu}$ and $\nu - \tilde{\mu}$. When none of these terms is an odd negative number(-1,-3, etc.), the solution is in the form:

$$y = s_{\tilde{\mu},\nu}(z) + AJ_\nu(z) + BY_\nu(z) \tag{A.8}$$

with A, B are arbitrary constants, J and Y the Bessel functions of the first and second kind and $s_{\tilde{\mu},\nu}$ is the Lommel function defined as:

$$s_{\tilde{\mu},\nu} = z^{\tilde{\mu}+1} \sum_{m=0}^{\infty} (-1)^m \frac{z^{2m}}{\prod_{j=1}^{m+1} \left((\tilde{\mu} + 2j - 1)^2 - \nu^2 \right)} \tag{A.9}$$

A more general solution which does not depend on the value of $\tilde{\mu} \pm \nu$ is given by:

$$S_{\tilde{\mu},\nu} = s_{\tilde{\mu},\nu} + 2^{\tilde{\mu}-1}\Gamma\left(\frac{\tilde{\mu} - \nu + 1}{2}\right)\Gamma\left(\frac{\tilde{\mu} + \nu + 1}{2}\right) \times \left[\sin\left(\pi\frac{\tilde{\mu} - \nu}{2}\right) J_\nu(z) - \cos\left(\pi\frac{\tilde{\mu} - \nu}{2}\right) Y_\nu(z)\right] \tag{A.10}$$

The above equation is the one referred by Goldstein as "Watson's Bessel Functions §10.71 (3)". The exact title of this reference from Watson and the document itself has been retrieved for this study of Goldstein's article, the document is the following[116]. Other great references on the topic are found to be [77] and [71].

Now it can be seen that Eq. (A.7) corresponds to equation (12) by using $z = i(2m + 1)\mu$, $k = 1$ and $\nu = (2m + 1)$. To avoid manipulating complex numbers, Goldstein evaluates Eq. (A.10) as the following $S_{1,\nu}(iz)$ which leads to equations (13) and (14). A typo-error is found in the first term of equation (14), which is obviously 2^2 instead of 2. To go exactly to equation (13) several manipulation are needed by using the relations between the Bessel functions and the modified Bessel functions.

Lommel's functions comes into the formalism of Hypergeometric functions which are usefully written with the Pochhammer symbol. The Pochhammer notation $(a)_k$ of a number a is:

$$(a)_k = a(a + 1)(a + 2)..(a + k) \tag{A.11}$$

The hypergeometric function ${}_pF_q$:

$${}_pF_q\left((a), (b), z\right) = \sum_{k=0}^{\infty} \frac{a_1..a_p}{(b_1)_k..(b)_k} \frac{z^k}{k!} \tag{A.12}$$

In terms of hypergeometric function then $t_{1,\nu}$ writes:

$$t_{1,\nu} = \frac{-z^2}{\nu^2 - 2^2}\, {}_1F_2\left((1), (2 - \nu/2, 2 + \nu/2), z^2/4\right) \tag{A.13}$$

The hypergeometric functions are better known than Lommel's function, and it is known that when $p \leq q$ the hypergeometric functions have an infinite radius of convergence, which justifies the expression of $t_{1,2m+1}\left((2m + 1)\mu\right)$ for all the values of μ and m. The computation of the T functions is not straight-forward even for modern computers and the asymptotic expression mentioned by Goldstein should be used for high values of z (i.e. high values of the product $(2m + 1)\mu$).

The rest of the paragraph does not present any difficulty.

Paragraph §3.2 In equation (2) Goldstein assumes another form of solution for equation §3.1 (12). There is no obvious reason for it to be exactly the same solution than the one found in the previous paragraph. We will write this series:

$$X = \sum_{k=0}^{\infty} \frac{\tau_{2k}}{Z^{2k}} \tag{A.14}$$

where $Z = 2m + 1$. Introducing this series in equation(12) yields to

$$\sum_{k=0}^{\infty} \frac{1}{Z^{2k}} \frac{1}{1+\mu^2} H(\tau_{2k}) - \sum_{k=1}^{\infty} \tau_{2k} - \tau_0 = \frac{-\mu^2}{1+\mu^2} \tag{A.15}$$

And after some rearrangements on the indexes:

$$\sum_{k=1}^{\infty} \frac{1}{Z^{2k}} \left[\frac{1}{1+\mu^2} H(\tau_{2k-2}) - \tau_{2k} \right] - \tau_0 = \frac{-\mu^2}{1+\mu^2} \tag{A.16}$$

By identifying term by terms the coefficient of $1/Z$ between the left hand side and the right hand side, it yields to equation (4) and (5). The recurrence equation (4) come in handy to calculate the successive τ_i manually. The question is whether the function denoted X above is really $T_{1,(2m+1)}$. Goldstein justifies it by looking at the numerical values. Further is finds that these functions are close to $\frac{\mu^2}{1+\mu^2}$ hence the introduction of F which is expected to go to zero and thus will simplify manual computations and allow further approximation in next paragraphs.

In this paragraph Goldstein introduces two function F and G to conveniently highlight the function $\mu^2/(1+\mu^2)$ and reveal terms that goes to zero. In practice, the definition of these functions is not required. In equation (9) Goldstein uses:

$$\sum_{m=0}^{\infty} \frac{1}{(2m+1)^2} = \frac{\pi^2}{8} \tag{A.17}$$

which can be found from equation §3.1 (6) expressed at $\zeta = 0$.

Paragraph §3.3 Equation (1) is the Fourier decomposition of the function $\cos((2m+1)\zeta)$ on $[0\ ;\ \pi]$. To go between the two equal signs of equation (5), the following result has been used:

$$\sum_{m=0}^{\infty} \frac{1}{(2m+1)^2 \left[4n^2 - (2m+1)^2\right]} = \frac{1}{4n^2} \sum_{m=0}^{\infty} \left[\frac{1}{(2m+1)^2} + \frac{1}{4n^2 - (2m+1)^2} \right] \tag{A.18}$$

$$= \frac{1}{4n^2} \left[\frac{\pi^2}{8} - \frac{\pi \tan(\pi n)}{8n} \right] = \frac{\pi^2}{32n^2} \tag{A.19}$$

The coefficients a_m are determined for the approximate equation first and then a term ϵ_m is added to account for the error. The terms are evaluated numerically only. For the case of any number of blades, Goldstein neglects completely these error terms.

Paragraph §3.4 To obtain equation (2) one should recall our previous discussion on ϕ and $\tilde{\phi}$, notation which isn't used by Goldstein of course. No further difficulties in the different calculations.

Paragraph §5 It should be noted that the definitions for the thrust and torque coefficients are different than the one commonly used in wind energy(differ from a factor 2). A typo-error is found in equation (8) which should be corrected as:

$$\frac{dT}{dr} = p\rho\Gamma(r\omega + \frac{1}{2}u_\theta) \tag{A.20}$$

Computation Even with recent computer the computation of Goldstein's factor is tedious and require some care. Without the help of modern computers, the calculation of Bessel's function for arguments above 50 was difficult and asymptotic approximation of these function had to be used. Recommendations from [109] can still be used for an easier implementation because numerical instabilities can occur, the convergence can be slow, some formulae are indeed more suitable than others and indeed asymptotic expansion should be used. Also, the summations can't be numerically performed to infinity so a trade off has to be found. The Euler-Maclaurin formula can be used for great values of m, when the T functions are close to 1. The computation of the coefficients a_m also requires some attention. The use of a software that does formal algebra greatly simplifies the task. In this study the software Mathematica[71] was used for the calculations.

A.2 Computation of Goldstein's factor using helical vortex solution

The optimal circulation found by Goldstein can be obtained by modelling the wake as a superposition of helical vortex lines. If $h = 2\pi l$ is the dimensional pitch of an helical vortex, then the induced velocities for a helical vortex line of unitary circulation has been approximated by Okulov as:

$$V_f = \begin{cases} 0 - \frac{l}{r} A \left[B \cdot \mathrm{S_l}\left(\frac{r}{l}, \frac{a}{l}, \theta\right) + \mathrm{S_m}\left(\frac{r}{l}, \frac{a}{l}, \theta\right)\right] & r < a \\ \frac{l}{r} - \frac{l}{r} A \left[B \cdot \mathrm{S_l}\left(\frac{a}{l}, \frac{r}{l}, \theta\right) - \mathrm{S_m}\left(\frac{a}{l}, \frac{r}{l}, \theta\right)\right] & r \geq a \end{cases}$$

$$V_z = \frac{1}{2\pi l} \begin{cases} 1 + \quad A \left[B \cdot \mathrm{S_l}\left(\frac{r}{l}, \frac{a}{l}, \theta\right) + \mathrm{S_m}\left(\frac{r}{l}, \frac{a}{l}, \theta\right)\right] & r < a \\ 0 + \quad A \left[B \cdot \mathrm{S_l}\left(\frac{a}{l}, \frac{r}{l}, \theta\right) - \mathrm{S_m}\left(\frac{a}{l}, \frac{r}{l}, \theta\right)\right] & r \geq a \end{cases}$$

$$V_\theta = \frac{1}{2\pi l} \frac{l}{r} \left(1 - \mathrm{V_z}\left(r, a, l, \theta\right)\right)$$

$$V_x = -\frac{r}{l} 2\pi l \, \mathrm{V_z}\left(r, a, l, \theta\right) + \mathrm{V_f}\left(r, a, l, \theta\right)$$

with

$$A = \frac{\left(a^2 + l^2\right)^{\frac{1}{4}}}{\left(r^2 + l^2\right)^{\frac{1}{4}}}$$

$$B = \frac{l}{24} \left(\frac{3r^2 - 2l^2}{\left(r^2 + l^2\right)^{\frac{3}{2}}} + \frac{9a^2 + 2l^2}{\left(a^2 + l^2\right)^{\frac{3}{2}}} \right)$$

$$S_l(x, y, \theta) = \mathrm{Re}\left[-\log\left(1 - e^{i\theta + \log\left(\frac{x\left(1+\sqrt{1+y^2}\right)}{y\left(1+\sqrt{1+x^2}\right)}\right) + \sqrt{1+x^2} - \sqrt{1+y^2}}\right)\right]$$

$$S_m(x, y, \theta) = \mathrm{Re}\left[\frac{e^{i\theta}}{e^{-\left[\log\left(\frac{x\left(1+\sqrt{1+y^2}\right)}{y\left(1+\sqrt{1+x^2}\right)}\right) + \sqrt{1+x^2} - \sqrt{1+y^2}\right]} - e^{i\theta}} \right]$$

The vortex sheet is modelled by a superposition of helical vortex curves of intensity $\gamma_{v,j}$ to be determined using the boundary conditions as follow. Assuming N vortices at radial positions r_j, and $N-1$ control points located at radial positions r_i(for instance taken in between the vortex position), the velocity at the control point r_i, sum of the velocity contribution from all vortices is:

$$\boldsymbol{u}(r_i) = \sum_{j=1}^{N} \boldsymbol{u_j}(r_i) = \sum_{j=1}^{N} \gamma_{v,j} \boldsymbol{a_j}(r_i) \tag{A.21}$$

The above equation can be decomposed on the three components x, θ, z.

The control points are taken to be on the vortex sheet so that they should verify the boundary conditions on this sheet, which is that the velocity reduction is maximum on the vortex sheet.

These boundary conditions (derived in Eq. (2.8) and Eq. (2.7)) are found for u_θ and u_z and can be derived for the u_x component. They write for each point located at radius r on the vortex sheet:

$$u_{\theta,0} = w\frac{-\bar{r}\bar{l}}{\bar{l}^2 + \bar{r}^2} \tag{A.22}$$

$$u_{z,0} = w\frac{\bar{r}^2}{\bar{l}^2 + \bar{r}^2} \tag{A.23}$$

$$u_{x,0} = w\bar{r} \tag{A.24}$$

with $\bar{l} = l/R$ and $\bar{r} = r/R$. Writing the boundary conditions at the control points r_i and combining these with the three component of equation Eq. (A.21) leads to a set of three linear system of equations of size $(N-1)\times N$ which unknowns are the N vortex intensities $\gamma_{v,j}$. These three system equations are written in matrix form:

$$A_\theta \cdot \Gamma_v = U_{\theta,0} \tag{A.25}$$

$$A_z \cdot \Gamma_v = U_{z,0} \tag{A.26}$$

$$A_x \cdot \Gamma_v = U_{x,0} \tag{A.27}$$

The matrices of velocity influence A_* have dimension $N-1\times N$, the vector of vortex intensity Γ_v is $N\times 1$ and the vectors of boundary conditions U_* are $N-1\times 1$. Let us now assume a vector Γ_v (a set of $N-1$ $\gamma_{v,j}$) solution of Eq. (A.21). Inserting the solution Γ_v into Eq. (A.25) it is found that it is also a solution for u_x if the sum of all the helical vortices circulation is equal to zero, i.e.:

$$\sum_{j=1}^{N} \gamma_j = 0 \tag{A.28}$$

This condition is simply added to the A_* matrix and the U_* vectors in order to close the system, and make the problem entirely solvable by inversion of the newly formed $N\times N$ matrices. Any of the three system will give a satisfactory solution for Γ_v so only one system has to be solved. Eventually, the total circulation, or Goldstein's circulation at a radial position r, is the integral of the tangential induced velocity on a circle of perimeter $2\pi r$, or more simply, is the sum of the intensity of the helical vortices contained in this circle:

$$\Gamma(r) = \oint_{C(r)} \boldsymbol{u_\theta}\cdot \boldsymbol{dl} = \sum_{j/\ r_j<r} \gamma_{v,j} \tag{A.29}$$

Results from this calculation have been compared with the results of Tibery and Wrench[109] by Okulov[79] and showed perfect agreement. This simulation was reproduced here and showed perfect agreement as well as seen on Fig. A.2. The circulation has also been calculated for other values of h than the one used by Okulov, and are shown on Fig. 2.14 for reference.

A.3 Computation of optimum power with finite number of blades

In vortex theory, the application of the Kutta-Joukowski leads to the calculation of local loads as function of the relative velocity and the circulation. By decomposing the loads on the normal and tangential component, the total power and thrust can be derived as:

$$P = \Omega\rho B \int_0^R \Gamma\left(U_0 - u_{i_z}\right) r dr \tag{A.30}$$

$$T = \quad \rho B \int_0^R \Gamma\left(\Omega r + u_{i_\theta}\right) dr \tag{A.31}$$

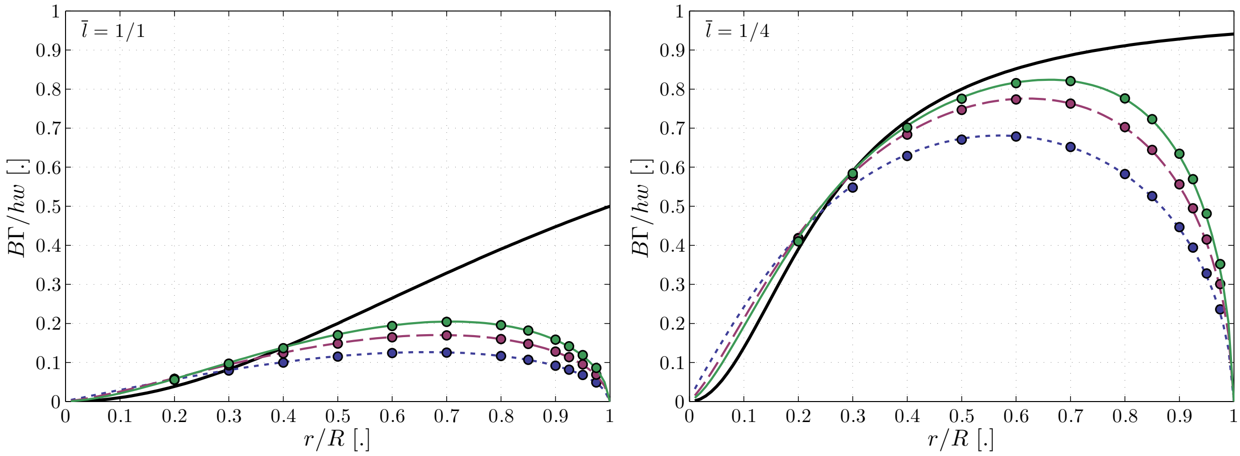

(a) (b)

Figure A.2: Goldstein's circulation function compared to the one from Glauert. (a) $\bar{l} = 1/1$ - (b) $\bar{l} = 1/4$. The computation of Goldstein's factor is performed using the superposition of helical vortex. In this case 150 vortices per blade were used. The thick line represent Glauert's circulation. Goldstein's circulation is computed for $B = 2$(dotted), $B = 3$(dashed) and $B = 4$(thin). Dots are tabulated data from Tibery and Wrench

Using the notations introduced in chapter 2, and the link between rotor parameters and wake parameters, Okulov et al.[80] integrated the power coefficient and thrust coefficient using Goldstein's optimal circulation calculated with the method of the previous paragraph. This yields the optimum coefficients for a rotor with finite number of blades. This computation has been performed here as well as a confirmation and the results are displayed on Fig. A.3.

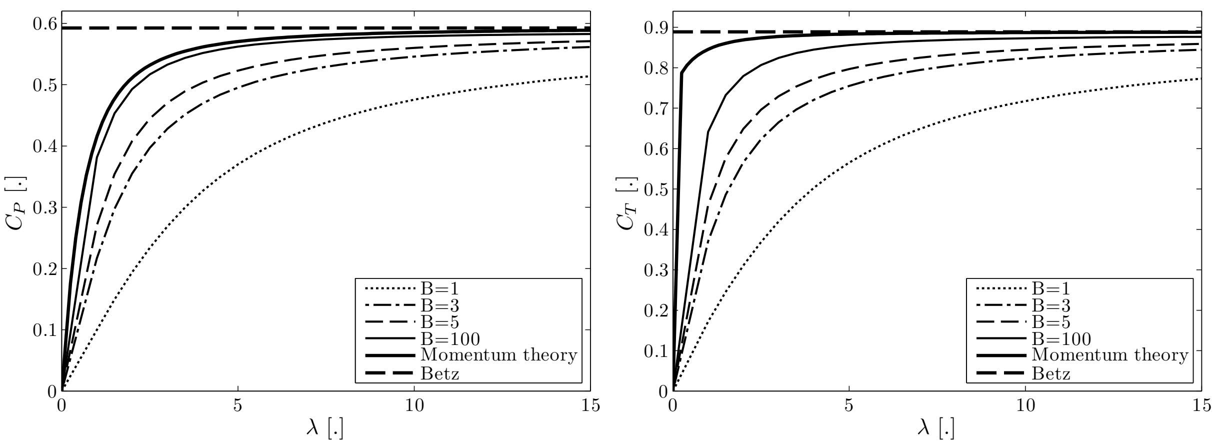

(a) (b)

Figure A.3: Optimum power and thrust coefficient. (a) Power coefficient - (b) Thrust coefficient.

A.4 Fitting functions for fast Goldstein's circulation computation

For engineering applications, or if the methods mentionned above seem to complex or too slow to implement, an explicit parametrization is suggested. Given the shape and values taken by the

Goldstein circulation function, the following form is assumed:

$$G_{\mathrm{Go}} = \frac{B\Gamma_{\mathrm{Go}}}{hw} = \sin\left[P_n\left(\frac{r}{R}\right)\right] \tag{A.32}$$

where P_n is a polynomial of nth degree written as:

$$P(X) = \sum_{k=0}^{n} a_k X^k \tag{A.33}$$

The values of the coefficients a_k that fits the Goldstein's circulation for different values of $\bar{l}$ and for a degree of $n = 8$ can be found in Tab. A.1 and Tab. A.2. If the relation $\lambda = 1/\bar{l}$ is assumed, then this function can be directly used to derive a tip-loss factor as explained in Sect. 3.4.1. The value $w = 1$ is used to recall the linearity in w of the boundary condition, and thus of the solution Γ_{Go} found in Eq. (A.23). The ratio Γ_{Go}/w is independent of w.

Table A.1: Goldstein's circulation function fitted according to Eq.(A.32) for different values of $\bar{l}$, with $w = 1$ and for $B = 2$

$\bar{\mathbf{l}}$	**1/16**	**1/14**	**1/12**	**1/10**	**1/8**	**1/6**	**1/4**	**1/2**
a_0	-0.0	-0.0	-0.0	-0.0	-0.0	-0.0	-0.0	-0.0
a_1	13.7	12.1	10.3	8.5	6.7	5.0	3.2	1.3
a_2	-90.1	-74.2	-58.5	-43.6	-30.8	-21.2	-14.5	-7.4
a_3	446.7	369.3	293.4	223.5	166.8	128.8	102.2	57.3
a_4	-1469.9	-1245.1	-1021.6	-813.1	-643.2	-527.9	-431.3	-238.8
a_5	2978.1	2581.8	2178.3	1790.6	1462.9	1224.1	994.8	541.5
a_6	-3533.1	-3119.3	-2688.3	-2260.9	-1883.2	-1585.0	-1273.3	-684.8
a_7	2242.1	2006.5	1756.7	1502.2	1267.6	1068.8	849.4	453.3
a_8	-587.5	-530.9	-470.3	-407.1	-346.8	-292.6	-230.5	-122.4

Table A.2: Goldstein's circulation function fitted according to Eq.(A.32) for different values of $\bar{l}$, with $w = 1$ and for $B = 3$

$\bar{\mathbf{l}}$	**1/16**	**1/14**	**1/12**	**1/10**	**1/8**	**1/6**	**1/4**	**1/2**
a_0	-0.0	-0.0	-0.0	-0.0	-0.0	-0.0	-0.0	-0.0
a_1	13.3	11.4	9.5	7.6	5.6	3.8	2.3	0.9
a_2	-75.8	-57.7	-41.3	-26.9	-15.1	-7.1	-4.3	-3.8
a_3	339.5	254.2	184.4	129.9	90.1	68.1	65.1	51.0
a_4	-1096.5	-859.1	-680.2	-551.2	-459.0	-400.5	-367.8	-249.7
a_5	2277.3	1867.4	1577.5	1379.5	1230.7	1102.8	965.5	608.7
a_6	-2809.3	-2377.0	-2084.3	-1891.7	-1736.0	-1564.7	-1328.5	-802.8
a_7	1861.6	1606.0	1436.6	1327.1	1233.1	1112.7	927.0	546.3
a_8	-509.9	-445.0	-402.1	-374.2	-349.4	-315.0	-259.2	-150.4

Appendix B

Implementation and validation of a vortex code

B.1 Implementation of a vortex code

Description

The vortex code will not be described in detail in this document. For the implementation of the code and a general descriptions of vortex codes(panel codes, vortex lattice codes,etc.) the following references were used:[52], [8]. For references on lifting line code implementations the reader can refer to the following references:[37],[32],[99],[54][72],[82], [24],[93]. Part of the source code of the vortex code implemented is available in Appendix F. Only the core function on which the vortex code is based is given. This function correspond to the induced velocity created by a vortex segment. Given a vortex line delimited by the points $\boldsymbol{x_1}$ and $\boldsymbol{x_2}$, the velocity induced by this filament at a point $\boldsymbol{x_p}$ is given by:

$$\begin{aligned} \boldsymbol{U_i} &= \frac{\Gamma}{4\pi}\boldsymbol{r_0}\cdot\left(\frac{\boldsymbol{r_1}}{r_1}-\frac{\boldsymbol{r_2}}{r_2}\right)\frac{\boldsymbol{r_1}\times\boldsymbol{r_2}}{\|\boldsymbol{r_1}\times\boldsymbol{r_2}\|^2} && \text{(B.1)}\\ &= \frac{\Gamma}{4\pi}\frac{(r_1+r_2)}{r_1r_2(r_1r_2+\boldsymbol{r_1}\cdot\boldsymbol{r_2})}\boldsymbol{r_1}\times\boldsymbol{r_2} && \text{(B.2)} \end{aligned}$$

with

$$\begin{aligned} \boldsymbol{r_1} &= \boldsymbol{x_p}-\boldsymbol{x_1} && \text{(B.3)}\\ \boldsymbol{r_2} &= \boldsymbol{x_p}-\boldsymbol{x_2} && \text{(B.4)}\\ \boldsymbol{r_0} &= \boldsymbol{x_2}-\boldsymbol{x_1}=\boldsymbol{r_1}-\boldsymbol{r_2} && \text{(B.5)} \end{aligned}$$

and where the relation $\|\boldsymbol{r_1}\times\boldsymbol{r_2}\|^2=(r_1r_2)^2-(\boldsymbol{r_1}\cdot\boldsymbol{r_2})^2$ has been used.

The different vortex code implemented

Core computational methods The core computational methods were implemented in C (see Appendix F for source code fragments). In a later stage of the study, this code has been used as a benchmark for GPU code implementation. Three main functions are implemented:

- Line-by-Line function: computes the induced velocities of a series of vortex segments arbitrarily distributed in space on a series of given control points.
- Lattice function: computes the total induced velocities of a vortex lattice (grid) on a series of given control points

- Lattice Ring-By-Ring function: same as the above but returns the influence of each ring on each control points instead of the total contribution of the whole lattice.

Wake model The wake can be set free or prescribed. The wake can be shed progressively at each time step behind the rotor, or prescribed since the beginning of the simulation. A far wake model consisting of a series of single root-tip rings associated to form an helix of a given pitch can be added behind the free wake. This gives a better estimates of the induced velocities. The pitch of the far wake is determined at each time step depending on the axial induced velocity in the far wake. The number of helix rotations of the far wake is prescribed by the user.

Blade/wing representation The blade or the wing can be represented by a lattice of vortex rings forming a grid of any dimensions $n_{\text{chord}} \times n_{\text{span}}$. In its simpliest form the code can reduce to a lifting line formulation with the wing represented by a lattice of dimension $2 \times n_{\text{span}}$.

Circulation at the blade The way the circulation can be handled depends on the blade/wing representation.

- Prescribed circulation: always possible(blade lattice or lifting line).
- Solved circulation using non-penetration condition: always possible.
- Solved circulation using 2D data: only possible in the lifting line case[1]

Vortex viscous model

To resolve the singularity occurring when a calculation point is close to the vortex line, different corrections are commonly employed. A viscous core radius r_c is used to define the radial location for which the tangential velocity induced by the vortex is maximum. Several methods reduces to a multiplicative factor K_v directly applied to the induced velocity U_i from Eq. (B.2) to eliminate the singularity. These methods are for instance described in [60] and their expressions are:

$$\text{Rankine} \qquad K_v = \max\left\{\ 1\ ,\ r^2/r_c^2\ \right\} \tag{B.6}$$

$$\text{Lamb-Oseen} \qquad K_v = 1 - \exp\left(-\alpha r^2/r_c^2\right) \qquad \alpha = 1.25643 \tag{B.7}$$

$$\text{Vatistas - n} \qquad K_v = \frac{r^2/r_c^2}{\left(1 + (r/r_c)^{2n}\right)^{\frac{1}{n}}} \tag{B.8}$$

$$\text{Vatistas - n=2} \qquad K_v = \frac{r^2}{\sqrt{r_c^4 + r^4}} \tag{B.9}$$

The model of Vatistas for $n = 2$ has been detailed as it is a fairly good approximation of the analytical but simplified result from Lamb-Oseen. In the above, the radial distance r is replaced by the orthogonal distance related to a vortex filament: $h = \|\boldsymbol{r_1} \times \boldsymbol{r_2}\|/r_0$. A common model for the vortex core radius computation is the one from Squire 1965[105][60, p 592] which writes in the form:

$$r_c(t) = \sqrt{4\alpha\delta\nu(t - t_0)} \tag{B.10}$$

where α is the viscous core growth constant from the Lamb-Oseen model, δ is the viscous core diffusivity coefficient (or effective turbulent viscosity coefficient) and ν is the kinematic viscosity.

[1] Methods to extend to vortex lattice are possible using the spanwise distribution of circulation of a flat plate for instance, see e.g. [82]. No time was allowed for this implementation.

The time parameters model the growth of the vortex as the wake ages, and allows the vortex to be already in a stage of decay immediately after it's formation. This model showed good agreement when compared to measurement[60, p 592].

Another way of removing the singularity is to use a cut-off radius that is artificially inserted in the denominator of Eq. (B.2) to prevent it to go to zero:

$$\boldsymbol{U_i} = \frac{\Gamma}{4\pi} \frac{(r_1 + r_2)}{r_1 r_2 (r_1 r_2 + \boldsymbol{r_1} \cdot \boldsymbol{r_2}) + (\delta_c\, r_0)^2} \boldsymbol{r_1} \times \boldsymbol{r_2} \tag{B.11}$$

with r_0 being the length of the vortex filament. Suggested values of cut-off radius parameters δ_c found in [37] are of 1-10% for the wake roll-up computation and 0.01% for bound vortex calculations.

B.2 Validation of Vortex code with prescribed wake

Flat plate

As a first validation step, the lift coefficient for a flat plate of infinite aspect ratio $\mathcal{R}$ is computed with the vortex lattice code. The simulation results seen on Fig. B.1a agree perfectly with the Joukowski result $C_l = 2\pi \sin\alpha$ which approximates to 2π at low angles of attack. The influence of aspect ratio[2] is then studied with results displayed on Fig. B.1b. Prandtl's formula for an elliptic finite wing is slightly modified by introducing a factor τ which is different of 0 for non elliptical wing:

$$C_{l_\alpha} = \frac{C_{l_{\alpha,0}}}{1 + \frac{C_{l_{\alpha,0}}}{\pi \mathcal{R}}(1+\tau)} \tag{B.12}$$

where C_{l_α} is the lift slope of a finite wing and $C_{l_{\alpha,0}}$ the lift slope of the airfoil section, with in general $C_{l_\alpha} < C_{l_{\alpha,0}}$. A modification of this formula has been suggested by Helmbold in 1942[3] for a better fit at lower aspect ratios:

$$C_{l_\alpha} = \frac{C_{l_{\alpha,0}}}{\sqrt{1 + \left(\frac{C_{l_{\alpha,0}}}{\pi \mathcal{R}}\right)^2} + \frac{C_{l_{\alpha,0}}}{\pi \mathcal{R}}} \tag{B.13}$$

Tuck[111] derived an accurate method to assess the lift slope for an flat plate with a lifting surface formulation. He fitted his results with the empirical relation of Koemiawan at high aspect ratio providing the following relation:

$$C_{l_\alpha} = 2\pi - \pi \frac{1}{\mathcal{R}} (\log \mathcal{R} + 2.5620) + 1.404 \frac{1}{\mathcal{R}^2} (\log \mathcal{R} + 3.645) \tag{B.14}$$

Values from the above formulation and experimental data are used for comparison with the simulation results on Fig. B.1b. Perfect agreement is found with the semi-analytical result from Tuck at high aspect ratio, and good agreement is found with the vortex lattice code from Jones 1960. Differences between the lifting surface results and the lifting line results from Prandtl are expected due to the difference in formulation(see for instance [111]).

Elliptical wing

Infinite aspect ratio The lifting line theory is easily verified for an the case of an elliptic wing with infinite aspect ratio. Results for the case $\alpha = 5.7106°$, $U_0 = 1\text{m/s}$ and $c_0 = 1\text{m}$ is displayed on Fig. B.2 where a perfect match with the theory is found.

Influence of aspect ratio Analytical derivation from Kida [53][111] provides the exact lift coefficient C_{l_α} of an elliptical wing from the three-dimensional lifting surface theory. Kida uses trigonometric series of Lamé polynomials for the analytical derivations and resulting numerical tabulated values are provided as function of a geometrical parameter defined as $k^2 = (a^2 - b^2)/a^2$, with a and b the two semi-axis of the ellipse. The notation b should not be mistaken in this context with the full-span of a wing often noted with the same letter. In his table 3[53] Kida separates values for aspect ratio higher and lower than the circular wing. Vortex code simulation of the different wing corresponding to these different values of k^2 and different aspect ratio have been performed to be compared with the numerical values of Kida. Results are shown on Fig. B.3(a-b) where perfect agreement is found.

[2] See Notations on page 3

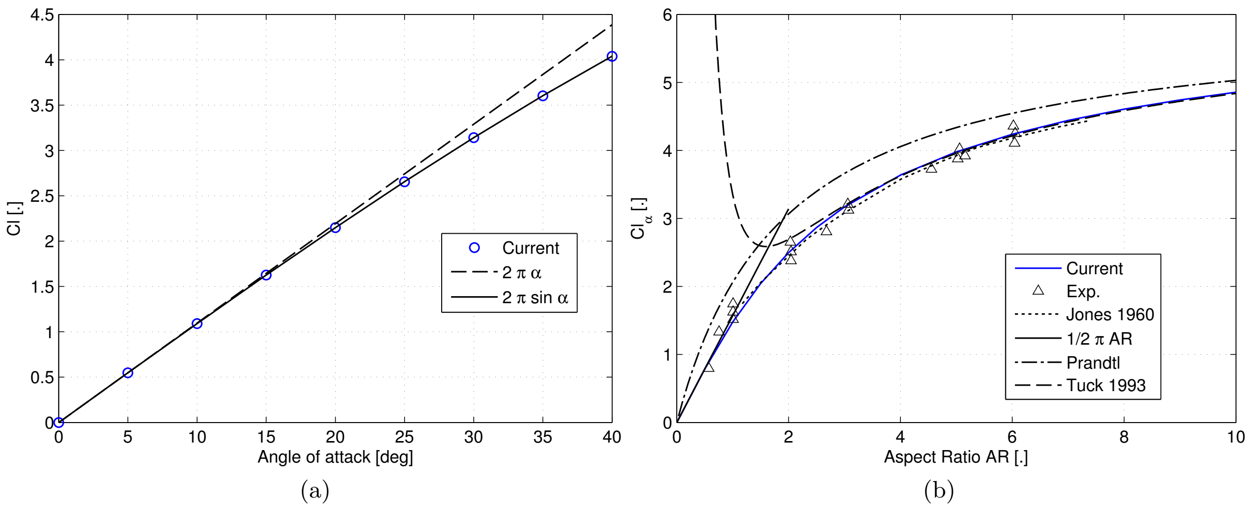

Figure B.1: Lift coefficient for a flat plate. (a) Wing of infinite aspect ratio for different angle of attack - (b) C_{l_α} for a flat plate at different aspect ratio. The experimental and simulation data from Jones 1960 were extracted from [52]. The empirical relation fitted by Tuck[111] derived for high aspect ratio is represented. Current stands for the vortex code implemented in this study. For infinite aspect ratio, C_{l_α} converges exactly to 2π as seen on (a).

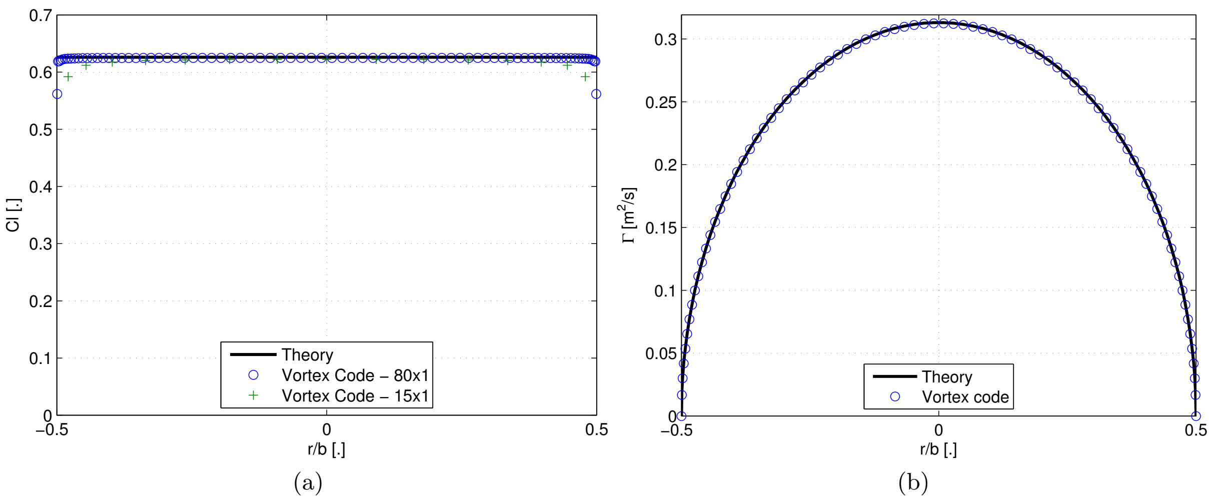

Figure B.2: Elliptical wing with infinite aspect ratio. (a) Lift coefficient - (b) Circulation

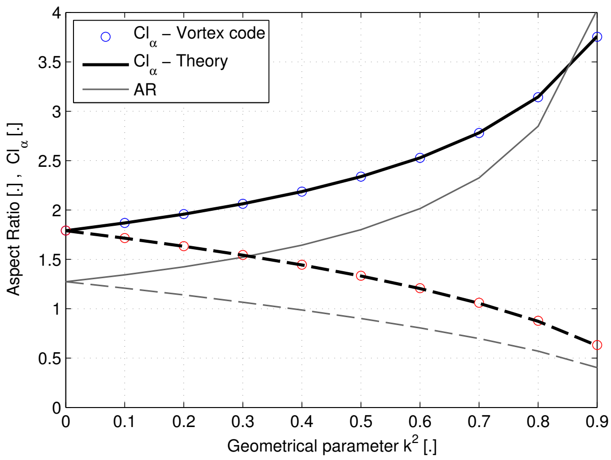

(a)

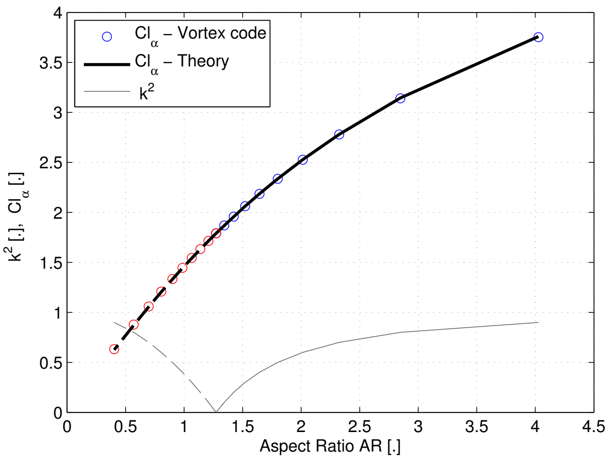

(b)

Figure B.3: Lift coefficient of an elliptical wing for different aspect ratios. Figures (a) and (b) are two different representations of identical results. Plain lines and blue symbols correspond to aspect ratios higher than the circular wing in contrast to dashed lines and red symbols. The smaller semi-axis of the ellipse is always taken as 1/2, hence an aspect ratio of $4/\pi$ for the circular wing.

Swept wing

In their book Bertin et al[8] detail an analytical solution of the vortex-lattice method applied to a swept wing. The wing has a sweep angle of $\Lambda = 45°$, an arbitrary span b, an aspect ratio of $AR = 5$ and is modelled by 8×1 panels. The vortex code applied with this geometry and number of panels showed perfect agreement with the derivation of Bertin as seen on Fig. B.4a. The influence of increasing the grid resolution and the influence of the wake roll-up is also displayed on this figure. Simulation results show good agreement with the experimental results of Weber and Brebner from 1958 found in [8]. A modification of Eq. (B.13) has been suggested by Kuchemann[3] to compute the lift slope of a swept wing as function of the sweep angle Λ. This empirical relation writes:

$$C_{l_\alpha} = \frac{C_{l_{\alpha,0}} \cos\Lambda}{\sqrt{1 + \left(\frac{C_{l_{\alpha,0}} \cos\Lambda}{\pi AR}\right)^2} + \frac{C_{l_{\alpha,0}} \cos\Lambda}{\pi AR}} \tag{B.15}$$

On Fig. B.4b, this relation is confronted to the results from the vortex code. Good agreement is found for low aspect ratio only. For higher aspect ratio, the current vortex code and the one from Jones[52] separates from the empirical relation while staying close to the experimental results.

Goldstein's circulation function

The values of Goldstein's circulation function can be obtained by prescribing an helical wake structure of a given pitch with a sufficiently long extent to be an approximation of the infinite helical wake studied by Goldstein(see Fig. B.6). The method used for the computation is similar to the one described in Sect. A.2. Using the conservation of circulation along the wake, and writing the boundary condition of normal velocity on the screw surface at collocation points located in the center of the wake, the circulation is obtained. Results from such computations displayed on Fig. B.5 show great agreement with the computation of Goldstein's analytical factor by Tibery and Wrench.

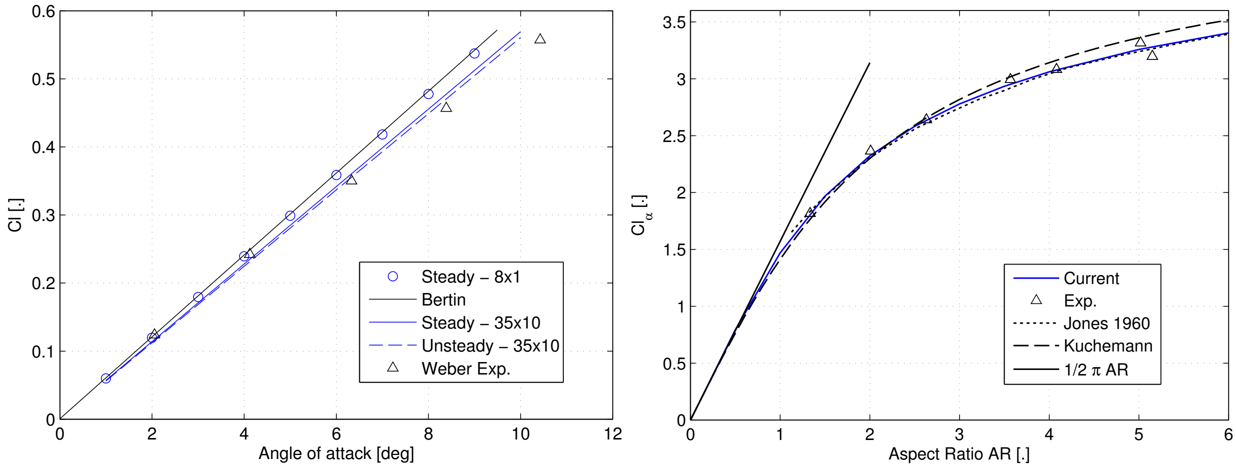

(a) (b)

Figure B.4: Lift coefficient of a swept wing for $\Lambda = 45°$. (a) Swept wing with $\text{Æ} = 5$. The vortex code is in perfect agreement with the analytical derivation of Bertin for 8 panels. An increased number of panels prove better agreement with the experiment of Weber and Brebner. The influence of wake roll up is limited. - (b) C_{l_α} compared to the relation suggested by Kuchemann[3] and data from Jones 1960[52].

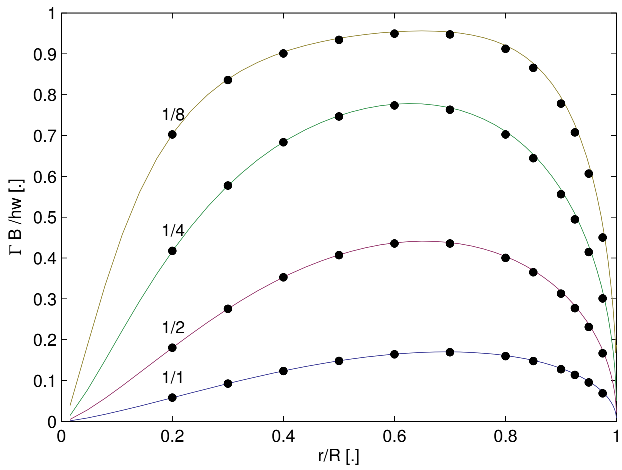

Figure B.5: Golstein circulation function computed with vortex code for different values of $\bar{l}$. Dots are values computed by Tibery and Wrench[109], lines are computed with the current vortex code. Numerical values on the plot refer to the value of $\bar{l}$.

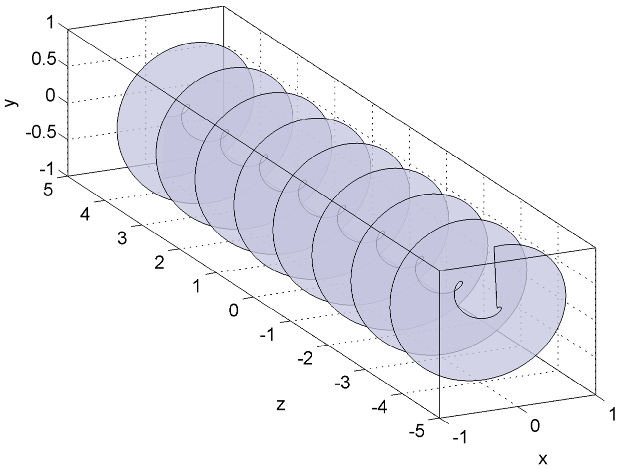

Figure B.6: Illustration of the theoretical helical wake used for the computation of Goldstein's function. Depending on the wake pitch, the number of revolutions sufficient to assume the wake infinite will vary. Control points located at the middle cross section of the wake are used to determine the boundary conditions and solve for the circulation.

B.3 Unsteady vortex code

Sudden acceleration of a flat plate

In this section, a comparison with results from Katz and Plotkin[52], chapter 13 is done. The transient results are unfortunately quite dependent on the way the numerical time integration scheme is done. The reproduction of results from Figure 13.34 of [52] is seen on Fig. B.7 with the superposition of the results obtained with the current vortex code.

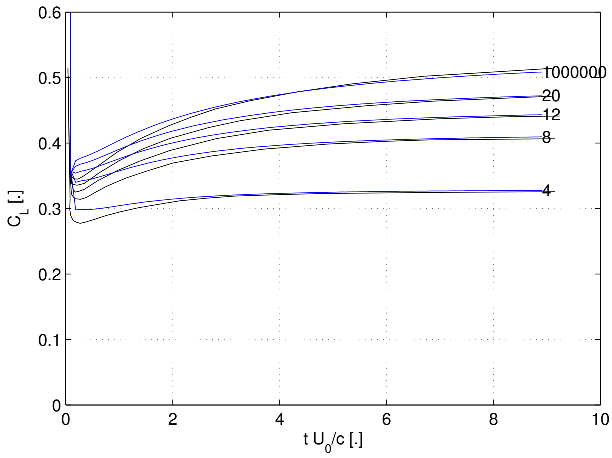

Figure B.7: Transient lift coefficient variation with time for uncambered, rectangular wings that were suddenly set into a constant-speed forward flight. . The calculation is based on four chordwise and thirteen spanwise panels and $U_0\Delta t/c = 1/16$. results from Katz and Plotkin[52] are displayed in black, while the results from the current vortex code are plotted in blue. Numbers on the figure represent the value of the aspect ratio.

The reproduction of results from Figure 13.36 of [52] is seen on Fig. B.8 using the current vortex code.

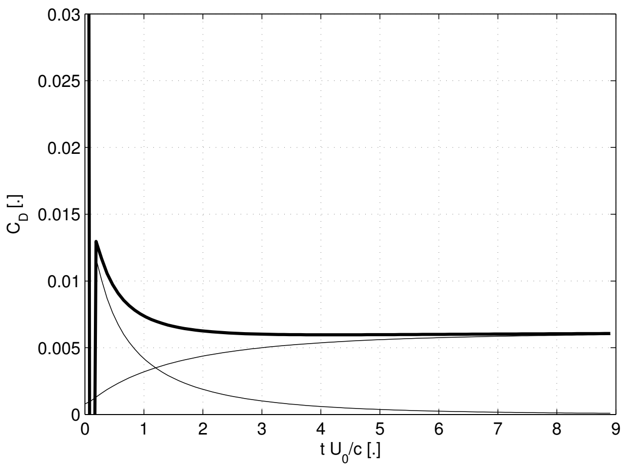

Figure B.8: Separation of the transient drag coefficient for an sudden acceleration of a flat plate. The thin curve going to zero represent the drag due to fluid acceleration, whereas the other thin curve is the drag due to the induced downwash. The thick curve is the total drag. Results were obtained with the current vortex code, comparing really well with the one from figure 13.36 of reference [52].

Wagner function Wagner obtained a solution for the indicial lift on a thin-airfoil undergoing a transient step change in angle of attack in 2D incompressible flow. In its simpliest form, the lift coefficient follows the following variation with time:

$$C_l(t) = \frac{\pi c}{2U_0}\delta(t) + 2\pi\alpha\phi(s) \tag{B.16}$$

with δ the Dirac function, ϕ the Wagner function and $s = 2U_0 t/c$. The analytical expression and computation of the Wagner function being complex, it is often replaced by approximated functions. In [60], two approximations are referenced. The one from Jones (1938) writes:

$$\phi(s) \approx 1.0 - 0.165e^{-0.0455s} - 0.335e^{-0.3s} \tag{B.17}$$

The approximation suggested by Garrick(1938) is:

$$\phi(s) \approx \frac{s+2}{s+4} \tag{B.18}$$

The results from the vortex code of a sudden acceleration of a flat plate of high aspect ratio is displayed on Fig. B.9 and compared with the Wagner function.

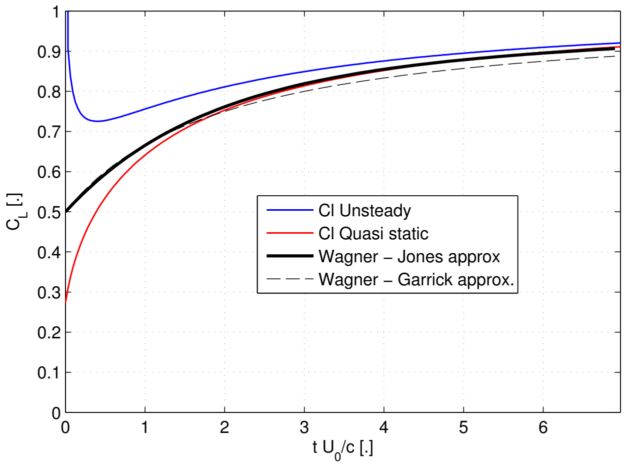

Figure B.9: Sudden acceleration of a flat plate - Comparison with Wagner function. The quasi-static C_l is the lift coefficient without accounting for the fluid acceleration, whereas the unsteady C_l is the total lift coefficient. The result shape is dependent on the time-integration scheme chosen explaining the differences at early times. The vortex code nevertheless converges quickly towards the analytical solution.

Validation against experiment and other vortex code

The experimental campaign described in[93] is used in this section. This rotor has been studied extensively by Sant[93] who developed a free wake lifting line code for comparison with the hot wire measurements. A similar vortex code developed by Kloosterman[54] has also been used for comparison with the TU Delft measurements. The simplicity of the rotor's geometry makes it an easy task to model it, so that results from the current vortex code implementation will be compared with the experimental data and the two vortex code results presented in the above references. The description of rotor's geometry can be found in both of these references. The operating condition of the turbine is the same for all simulations, which is $\lambda = 8$, $U_0 = 5.5$m/s, and $\theta_{\text{tip}} = 2°$. Sant derived a circulation distribution which is prescribed to its vortex code and accordingly to the current vortex code. This circulation is found on the Figure 4.55 of his thesis.

Only a few numerical and experimental results from Sant are selected in order to be compared with the vortex code implemented in this study. The simulation is performed with the following parameters: $n = 21$, $\Delta\phi = 10°$, $n_{\text{rev}} = 3$, $n_{\text{rev,far wake}} = 5$ The longitudinal induced velocity at the lifting line is presented on Fig. B.10. In this figure, the influence of the viscous core parameters and the presence of the far wake model is shown. The same trends are found for the two vortex codes, but small differences are present.

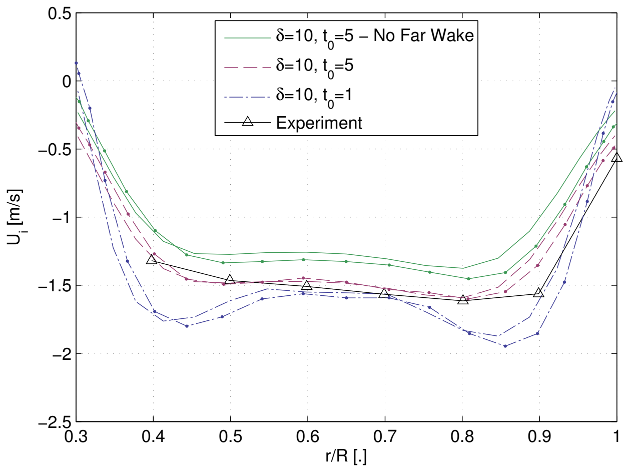

Figure B.10: Comparison of vortex code results compared to experimental data - Induced velocity on the lifting line. Lines marked with dots are data found in Sant 2007[93] using a similar vortex code.

The azimuthal variation of the axial induced velocity for two different radial positions and two different planes downstream paralel to the rotor is found on Figs. B.11 and B.12

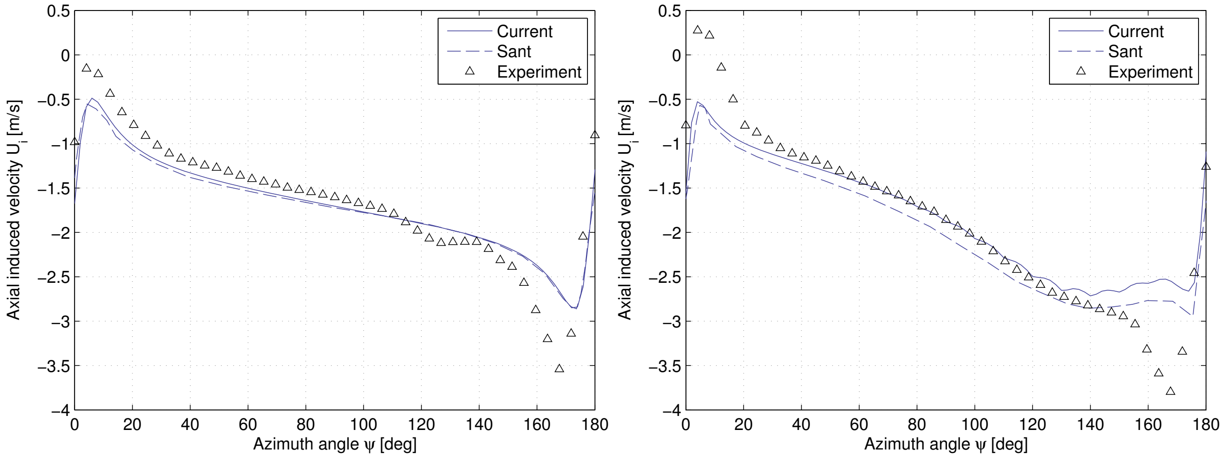

(a) $r/R = 0.6$ (b) $r/R = 0.9$

Figure B.11: Azimuthal variation of axial induced velocity in the plane $z = 0.35$m behind the rotor. Experimental data were taken from the work of Sant[93] together with the results from his vortex code.

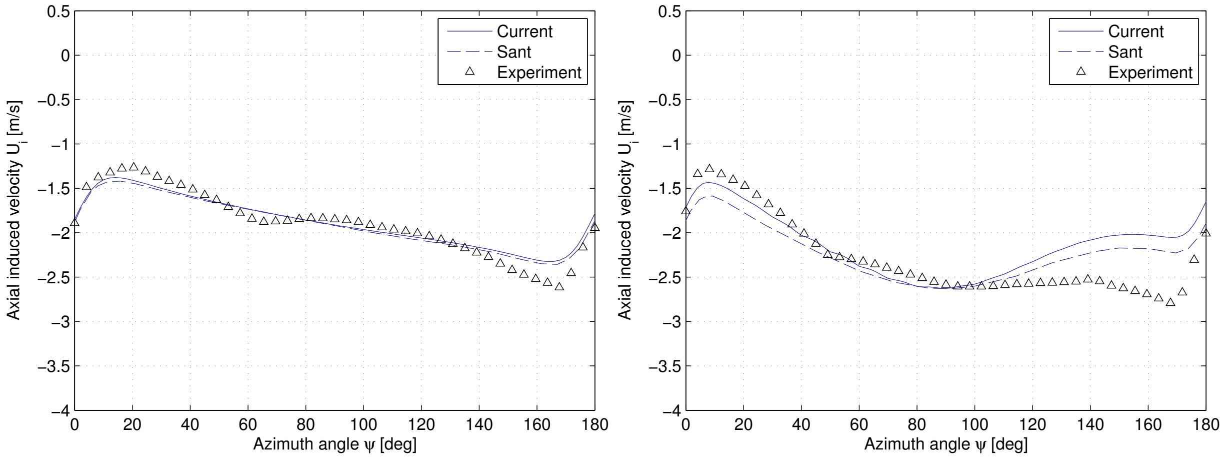

(a) $r/R = 0.6$ (b) $r/R = 0.9$

Figure B.12: Azimuthal variation of axial induced velocity in the plane $z = 0.60$m behind the rotor. Experimental data were taken from the work of Sant[93] together with the results from his vortex code.

On Figs. B.13, contour plots similar to the one found in [54] have been obtained with the current vortex code and compared with the experimental results of Sant and vortex code results of Kloosterman, as reported in [54]. Good agreement is found between Kloosterman's vortex code and the one implemented in this study.

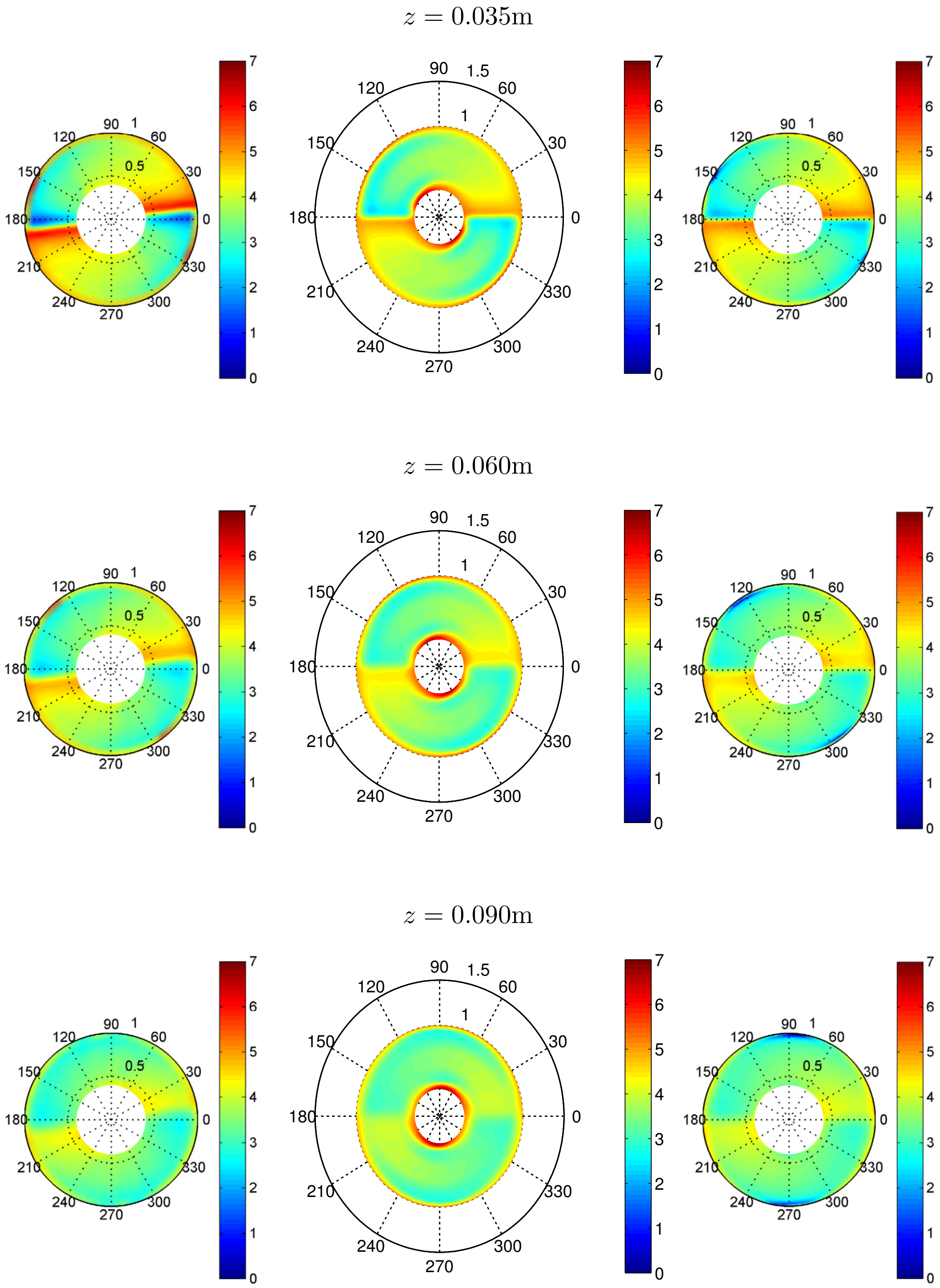

(a) Experiment (b) Current vortex code (c) Kloosterman's code

Figure B.13: Comparison of longitudinal velocity in different plans behind the TUD rotor. Figures (a) and (c) are taken from[54].

The influence of the vortex core parameters on the wake shape has been studied in a similar fashion than Sant. The results obtained are displayed on Fig. B.14 ad can be directly compared with Figure 5.30 from Sant[93]. Similar shapes are found, confirming a same implementation of the vortex core model and a similar implementation of the vortex code. The values from the experimental tip vortices locations used by Sant have also been used for this figure.

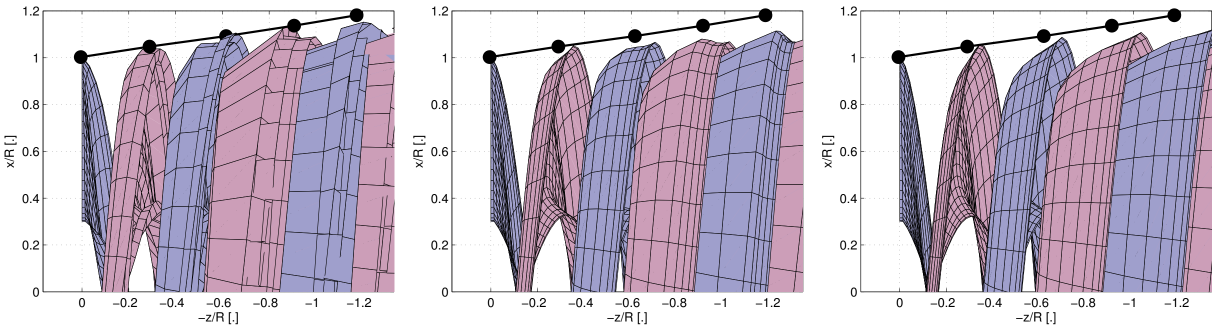

(a) $\delta = 10$, $t_0 = 0.1$ (b) $\delta = 10$, $t_0 = 5$ (c) $\delta = 100$, $t_0 = 1$

Figure B.14: Influence of vortex core parameters on the wake shape. Dots represents the location of tip vortices as measured and reported by Sant[93]

Similar simulations than the one performed by Gupta and Leishman[39, 60] have been performed to study wake shapes and stream lines for different tip speed ratios. Wake deficit has also been studied. Insufficient data were available to study the same rotor than Gupta and Leishman. As a results of this, the case of an existing stall regulated turbine, the Nordtank NTK500 turbine[41] has been used. Results are shown on Fig. B.15. The wake shapes and streamlines agree reasonably well with the results from Gupta and Leishman.

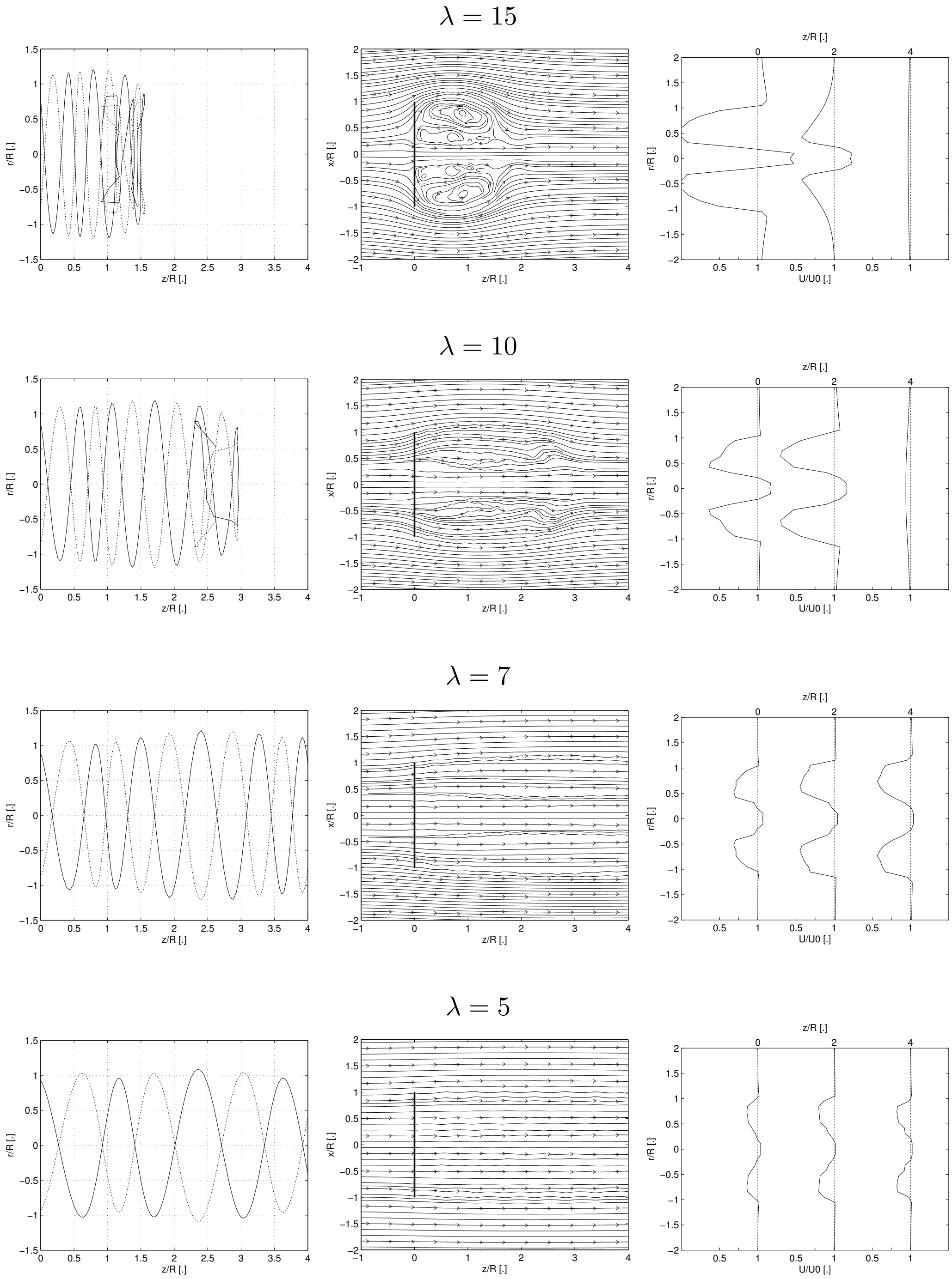

(a) (b) (c)

Figure B.15: Wake shapes(a), streamlines(b) and wake deficit(c) at different tip speed ratios for the NTK 500 turbine as modelled by the vortex code. Five revolutions of the wake have been computed. The last vortex ring's axial position has been used for representation of the wake shape. Due to the tip roll-up this representation is only an approximation. Numerical discretization induces oscillation that can be seen in the streamlines. The wake deficit is not computed correctly for high tip-speed ratio and large distance downstream because the wake was not propagated enough downstream. Increasing values of tip-speed ratio correspond to increasing values of the thrust coefficient. For $\lambda = 10$, $C_T \approx 0.6$, ad for $\lambda = 15$, $C_T \approx 0.9$, so that the turbine is respectively in a turbulent wake state and close to the vortex ring state as confirmed by the streamlines.

NREL rotor In his thesis Sant[93] determines a converged bound circulation for different wind speed for the NREL rotor[34]. Using these prescribed circulation, the current vortex code has been run with the NREL rotor geometry for comparison with the results of Sant. The computation has been performed for the wind speed of 5m/s with the same algorithm parameters than Sant. Results are displayed on Fig. B.16

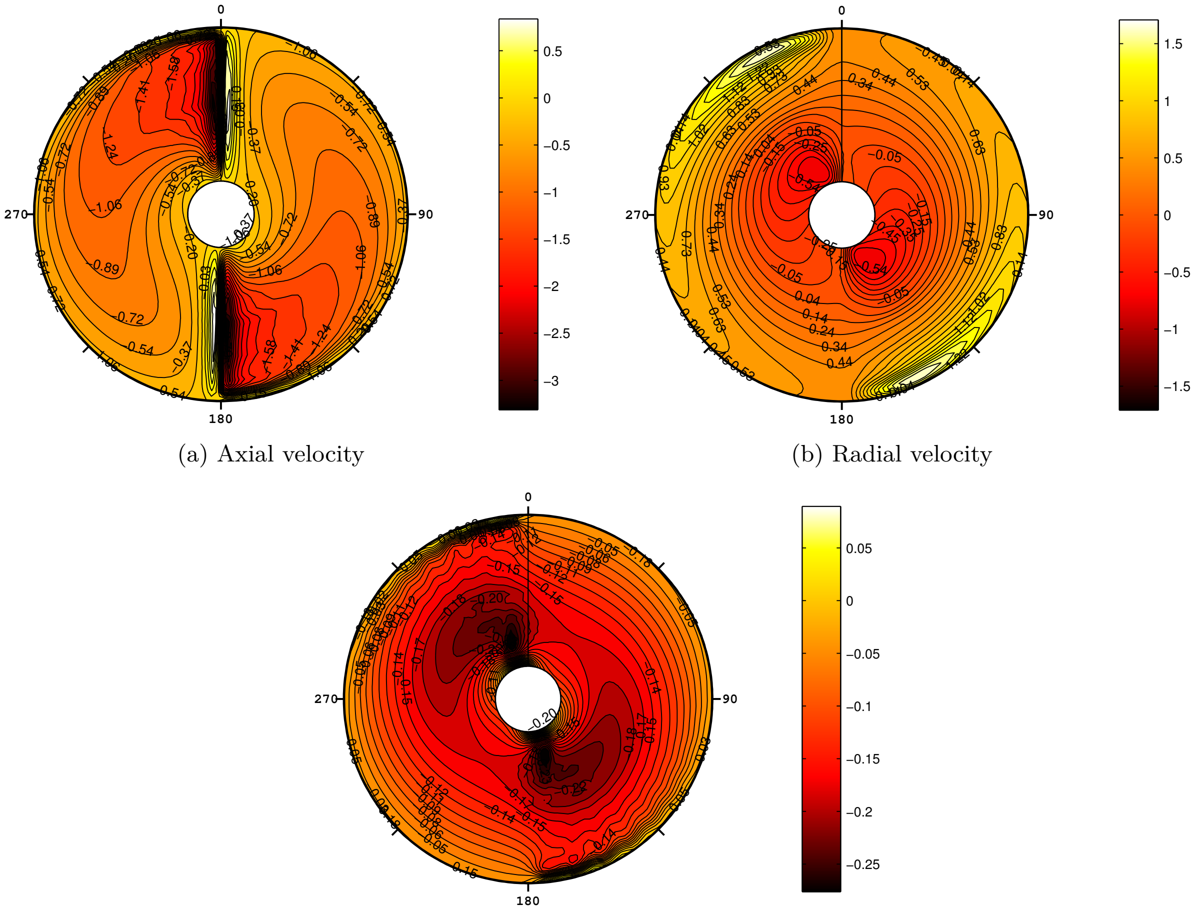

(a) Axial velocity

(b) Radial velocity

(c) Azimuthal velocity

Figure B.16: Induced velocity at the rotor plane for the NREL rotor at 5m/s. The intensity compare very well with the ones found by Sant[93, p 302]

Examples of meshing

To understand the difference between the panels location and the bound vortex rings location, together with the location of the collocation points, an example of "meshing" for a blade is presented on Fig. B.17.

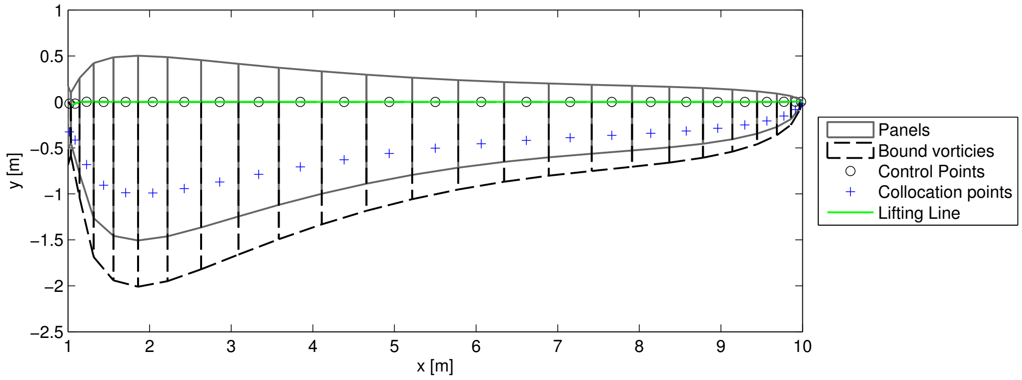

(a) $n_{\text{chord}} = 1$

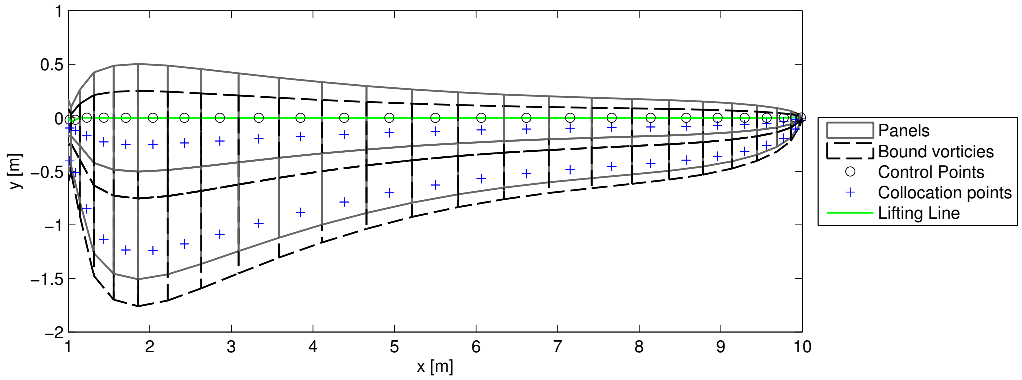

(b) $n_{\text{chord}} = 2$

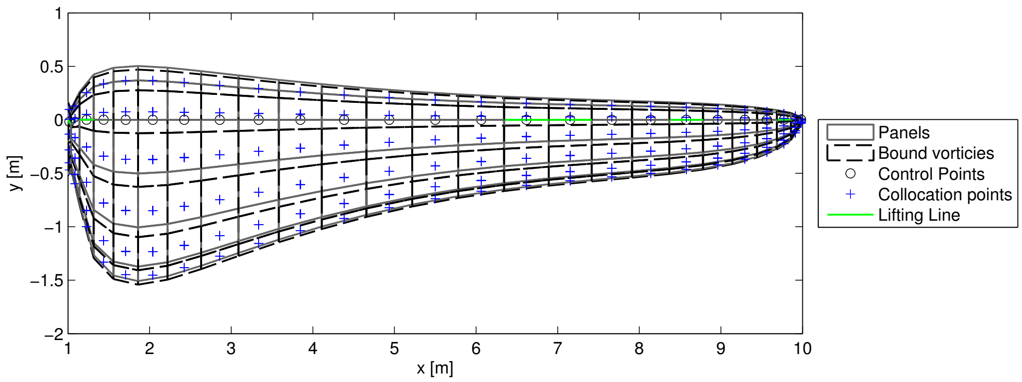

(c) $n_{\text{chord}} = 6$

Figure B.17: Illustration of the meshing method with distinction between panels and vortex rings. the blade geometry is a design from the author. The chordwise and spanwise meshing is done using a "cosine" distribution for a better resolution close the blade extremities and close to the leading edge and trailing edge. The case $n_{\text{chord}} = 1$ corresponds to classic lifting line codes. It is used when the vortex code uses 2D airfoil data to determine the circulation.

Examples of circulation and lift distributions

In the following several examples of lift and circulation distributions obtained by the method of "solving for non-penetration at the collocation points" are shown. The Lift distribution along the span-wise and chord-wise direction for two different wings is illustrated on Fig. B.18.

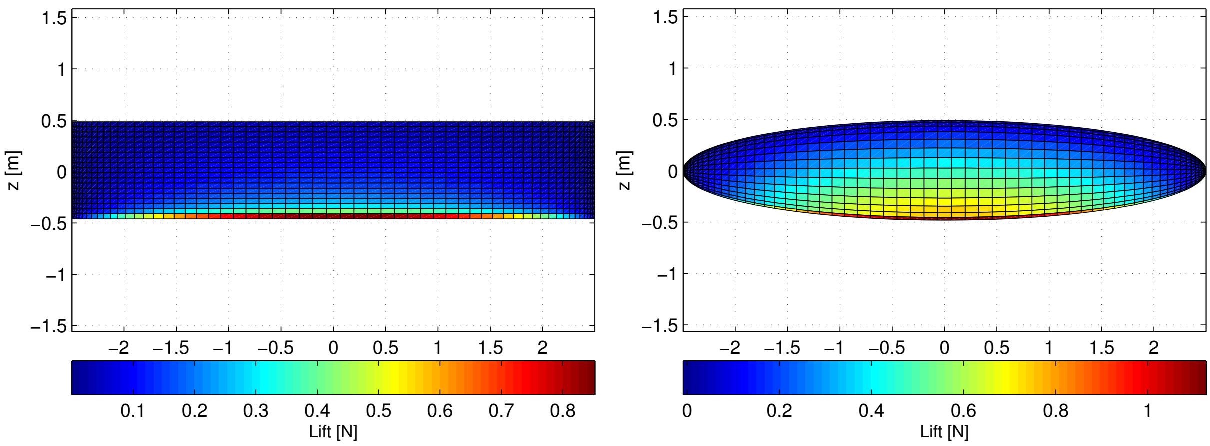

(a) (b)

Figure B.18: Distribution of lift obtained with the vortex code - $U = 10\mathrm{m/s}$ - $\alpha = 5°$. (a) Flat plate - (b) Elliptical wing

Another example of an elliptical wing with a different wing shape together with a trapezoidal wing is considered on Fig. B.19. .

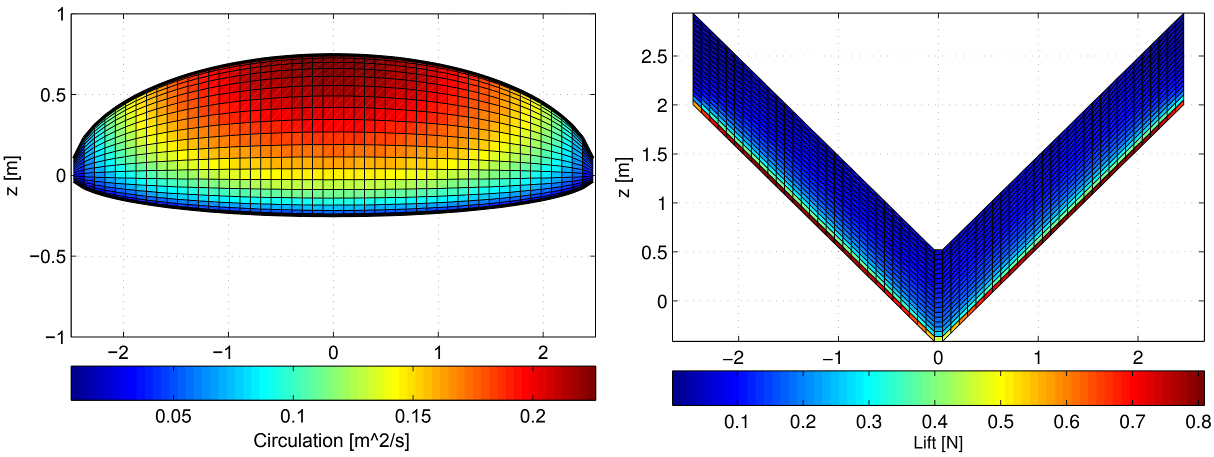

(a) (b)

Figure B.19: Different geometries studied with the vortex code. (a) Circulation distribution on an elliptical wing with $b = 5$, $c_0 = 1$, $\alpha = 5.7106°$, $U_0 = 1\mathrm{m/s}$ - (b) Lift distribution on a trapezoidal wing with $b = 5$, $c_0 = 1$, $U = 10\mathrm{m/s}$ - $\alpha = 10°$

Illustrations of wake shapes

Different wake shapes obtained with the implemented vortex code are presented. On Fig. B.20 the wake shapes behind of an elliptical and trapezoidal wing is displayed.

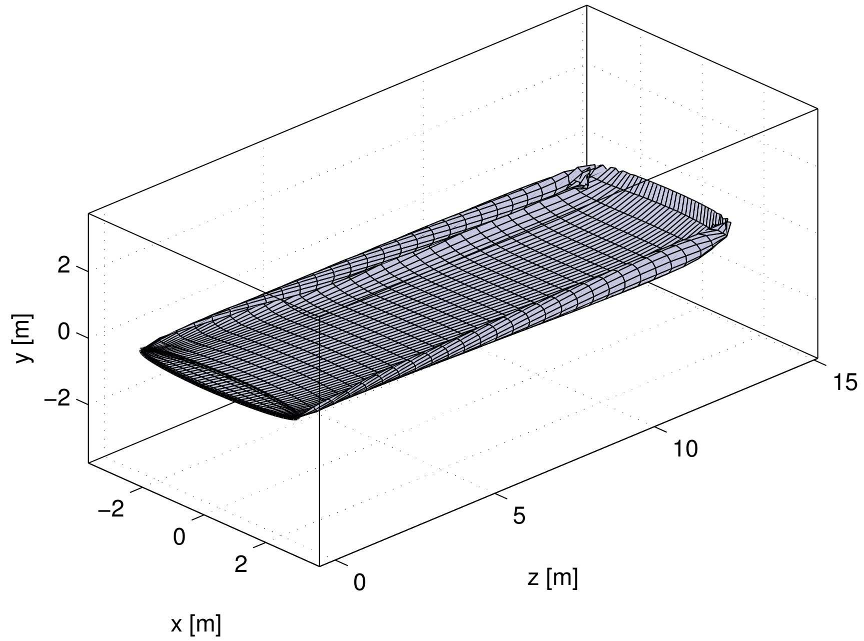

(a)

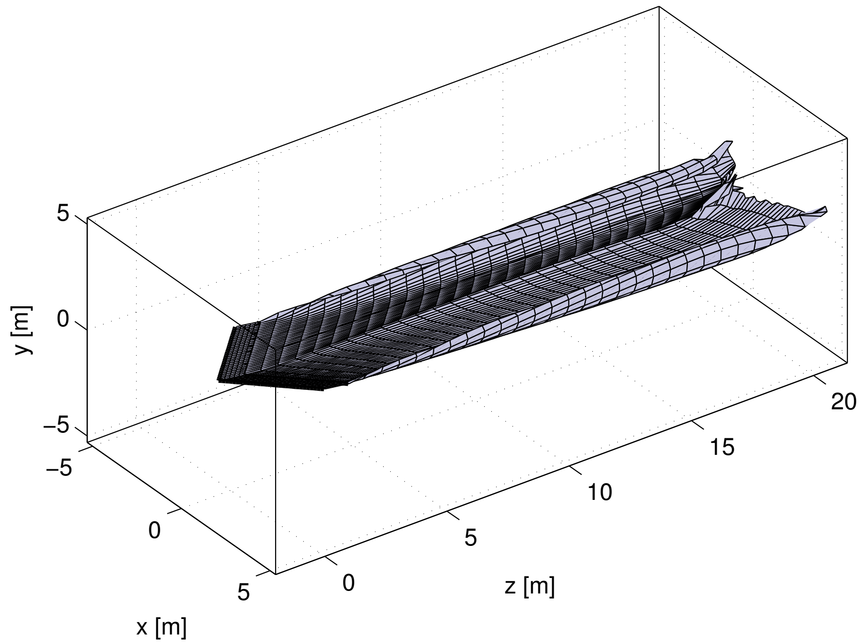

(b)

Figure B.20: Wake shapes behind an elliptical wing and a trapezoidal wing.

Two examples of wake shapes behind a wind turbine cam be found on Fig. B.21.

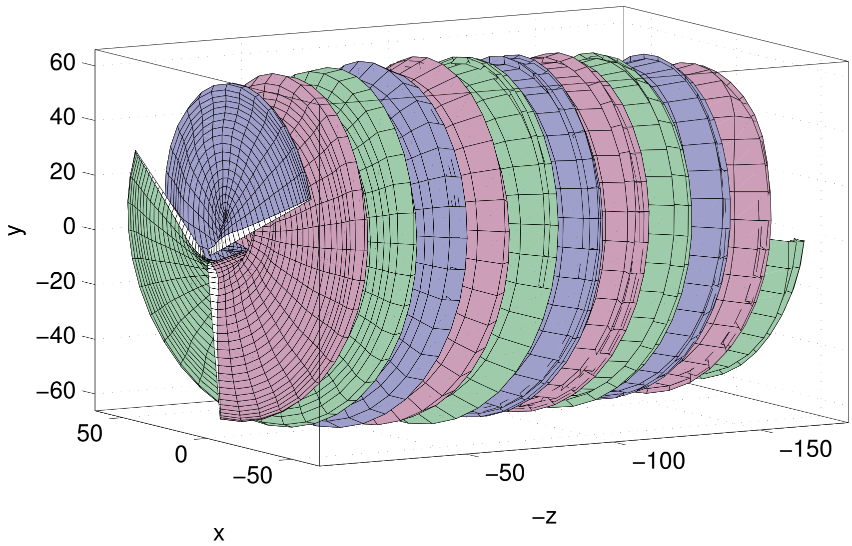

(a)

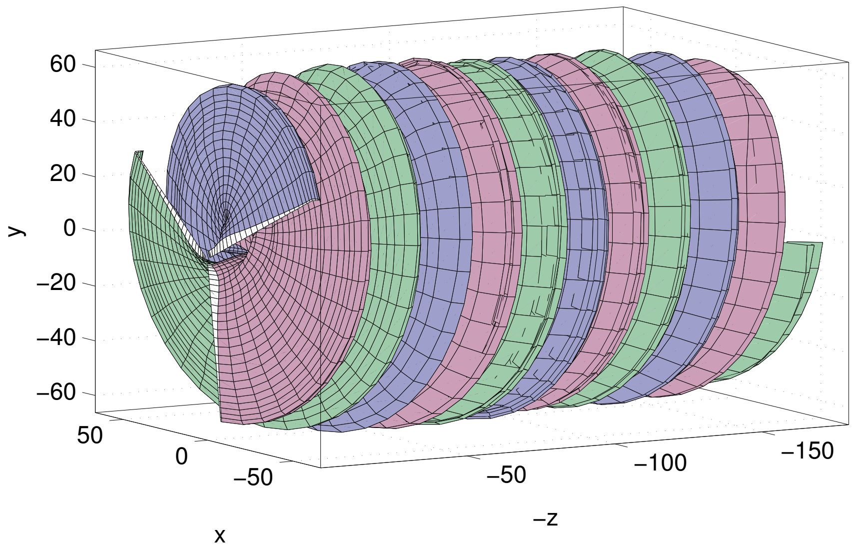

(b)

Figure B.21: Wake shapes behind a wind turbine. (a) Without winglet - (b) With winglet

Appendix C

The BEM method

C.1 Introduction to the BEM method

The blade element momentum(BEM) method results in the combination of the momentum theory and the blade element theory. Figure 1.18 illustrates the differences between these methods and how they are combined to form the BEM theory. The momentum theory applied to a stripe provides the corresponding elementary thrust and torque for a given set of both induction factors. This relation between induction factors and loads is invertible. The velocity triangle from the momentum theory also gives an expression of the flow angle as function of a and a'. On the other hand, the blade element theory requires the airfoil characteristics, the angle of attack and the relative velocity to calculate the forces of lift and drag applied to the blade element, and by projection the elementary thrust and torque. For a given rotor geometry and a given wind condition, a physical solution will be found if both methods returns the same loads for all the different stripes. In order to find this solution, the methods are linked together to form a converging iterative process. The author likes to emphasize two links, or linkage, to clearly distinguish the difference of the methods and how they interact. The first linkage is obtained by comparing the velocity triangles of the two methods. The second linkage consists in equalizing the loads obtained from both methods. It should be noted that due to the hypothesis of independence of each stripe, the convergence loop and the loop over the different stripes can be indifferently switched. Depending on this choice, the convergence criteria can be implemented in several way. The choice of the variable on which the convergence is tested is multiple as well, the most common choices being: the angle of attack, the induction factor or, which is suggested here, the total Power. In practice the implementation of the BEM algorithm is slightly different from the one shown on Fig. 1.18 because the succession of blocks can be simplified mathematically. The final algorithm will be presented in Sect. C.1 after derivation of the linkage equations and simplifications.

Note In the following the BEM algorithm as described by Glauert[35], or [42] is presented. No pressure terms accounting for wake rotations are used. These authors don't explicitly uses the notations a_B and $\hat{a}$ so that the same will be done here to avoid confusion. Controversy also appear as soon as the tip-loss factor is applied. For instance the velocity triangle presented in the next section is for some author local to the blade but on the other hand it is derived from 2D momentum theory which has infinite number of blades. Discussion on BEM formalism are still open.

First link - the energy equation or velocity triangle

The momentum theory with wake rotation, or simplified 2D momentum theory, establishes the following energy equation

$$\lambda_r^2 a'(1+a') = a(1-a) \tag{C.1}$$

which leads to[1]

$$\exists\ \tilde{\phi} \in \mathbb{R}\ /\quad \frac{(1-a)}{(1+a')\lambda_r} = \frac{a'\lambda_r}{a} = \tan\tilde{\phi} \tag{C.2}$$

and hence, this relation can be interpreted as a velocity triangle. Clearly, this triangle defines the flow angle, i.e. $\tilde{\phi} = \phi$, and one can write:

$$\phi = \operatorname{atan}\frac{(1-a)U_0}{(1+a')\Omega r} = \operatorname{atan}\frac{(1-a)}{(1+a')\lambda_r} \tag{C.3}$$

The second part of Eq. (C.2) is interpreted as the orthogonality of the induced velocity with the relative velocity. Figure C.1 explicits the components of the relative velocity U_n and U_t that were used in the blade element theory(see Fig. 1.12), and this allows the expression of $\boldsymbol{U}^2$ that is used in the definition of aerodynamic forces:

$$\boldsymbol{U}^2 = U_0^2(1-a)^2 + \Omega^2 r^2 (1+a')^2 \tag{C.4}$$

To reduce expressions it will more convenient though to use expressions of $\boldsymbol{U}^2$ that uses the flow angle and the induction factors:

$$\boldsymbol{U}^2 \sin^2\phi = U_0^2(1-a)^2 \tag{C.5}$$

$$\boldsymbol{U}^2 \cos\phi\sin\phi = U_0(1-a)\Omega r(1+a') \tag{C.6}$$

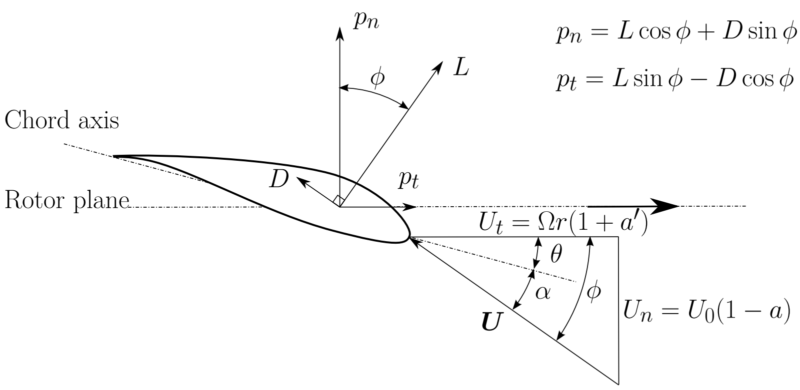

Figure C.1: Velocity triangle illustrating the link between the simplified 2D momentum theory and the Blade Element Theory

Second link - Elementary Thrust and Torque

The aim is here to relate the thrust and torque from the momentum theory to the in-plane and out-of-plane loads from the blade element theory. It should be remembered that the loads in the momentum theory are defined over an annular cross section*(infinite number of blades) of area $dA = 2\pi r dr$ whereas in the blade element theory the loads are defined for one blade element of area $dS = cdr$. To link the two theories, it is thus assumed that if the rotor consists of B blades then the total load from the B blade elements is the same that the one obtained by the momentum

[1] Given the fact that the domain of tan is $\mathbb{R}$

theory for an annular section*. The ratio of these two areas is expected to appear in the linkage, it will be noted σ:

$$\sigma = \frac{\text{Surface blade elements}}{\text{Surface annular element}} = \frac{B\,dS}{dA} = \frac{Bcdr}{2\pi rdr} \qquad [\text{ - }] \tag{C.7}$$

and eventually:

$$\sigma = \frac{Bc}{2\pi r} \tag{C.8}$$

This ratio called solidity is illustrated on Fig. C.2. This solidity is local, i.e. depend on the radius. It does not represent the total solidity of the blade.

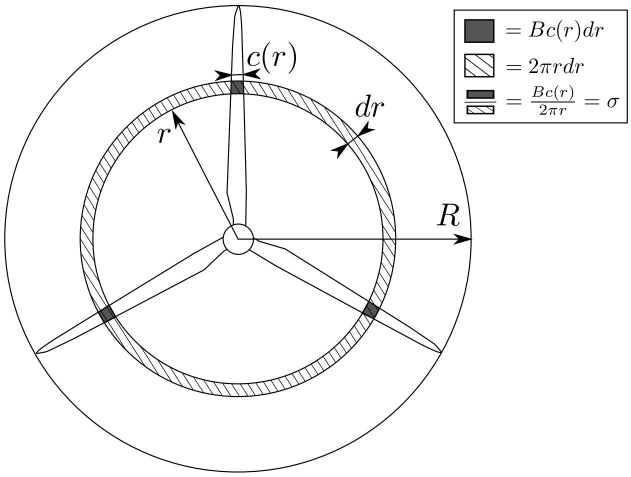

Figure C.2: Illustration of the solidity

Blade Element theory formulation Using the blade element theory(BET) formalism, the total thrust and torque exerted on B blade elements are :

$$dT_{\text{BET}} = BdF_n = \frac{1}{2}\rho \boldsymbol{U}^2(Bcdr)C_n \qquad [\text{N}] \tag{C.9}$$

$$dQ_{\text{BET}} = BrdF_t = \frac{1}{2}\rho \boldsymbol{U}^2(Bcdr)rC_t \qquad [\text{Nm}] \tag{C.10}$$

Momentum theory formulation

$$dT_{\text{MT}} = \frac{1}{2}\rho U_0^2(2\pi rdr)\left[4aF(1-a)\right] \tag{C.11}$$

$$dQ_{\text{MT}} = \frac{1}{2}\rho U_0^2(2\pi rdr)r\left[4a'F(1-a)\lambda_r\right] \tag{C.12}$$

The linkage consists in equalizing the blade element thrust dT_{BET} from equation Eq. (C.9) with it's momentum theory analog dT_{MT} from Eq. (C.11), and doing the same for the blade element torque by equalizing Eqs. (C.10) and (C.12):

$$\frac{1}{2}\rho \boldsymbol{U}^2(Bcdr)C_n = \frac{1}{2}\rho U_0^2(2\pi rdr)\left[4aF(1-a)\right] \tag{C.13}$$

$$\frac{1}{2}\rho \boldsymbol{U}^2(Bcdr)rC_t = \frac{1}{2}\rho U_0^2(2\pi rdr)r\left[4a'F(1-a)\lambda_r\right] \tag{C.14}$$

Introducing the linkage equations to simplify equations

In this section the linkage equations are written in different forms to allow analysis of certain terms and comparison with other references. The equations are presented with or without the inclusion of the drag coefficient in the axial induction.

Simplifications of the Blade Element theory equations using the first link Using the first link, the loads from the BET can be written indifferently in the following forms[2]:

$$dT_{\text{BET}} = \frac{\rho Bc}{2}\frac{U_0^2(1-a)^2}{\sin^2\phi}C_n dr \qquad = \sigma\pi\rho\frac{U_0^2(1-a)^2}{\sin^2\phi}C_n r dr \quad \text{(C.15)}$$

$$dQ_{\text{BET}} = \frac{\rho Bcr}{2}\frac{U_0(1-a)\Omega r(1+a')}{\sin\phi\cos\phi}C_t dr = \frac{\rho Bcr}{2}\frac{U_0^2(1-a)^2}{\sin^2\phi}C_t dr = \sigma\pi\rho\frac{U_0^2(1-a)^2}{\sin^2\phi}C_t r^2 dr \quad \text{(C.16)}$$

From now on, in this paragraph, the subscript BET is dropped, but it should be remembered that no results from the momentum theory are used. The above relations can be expressed with respect to a' as used e.g. in [64]:

$$dT = \sigma\pi\rho\frac{\Omega^2 r^2(1+a')^2}{\cos^2\phi}C_n r dr \quad \text{(C.17)}$$

$$dQ = \sigma\pi\rho\frac{\Omega^2 r^2(1+a')^2}{\cos^2\phi}C_t r^2 dr \quad \text{(C.18)}$$

The *global* thrust and torque coefficients defined with respect to the whole rotor area πR^2 can be written in a differential form(for comparison with e.g. [35]):

$$R\frac{dC_T}{dr} = R\frac{dT}{dr}\frac{1}{\frac{1}{2}\rho U_0^2\pi R^2} = 2\lambda^2\sigma\left(\frac{r}{R}\right)^3\frac{(1+a')^2}{\cos^2\phi}C_n \quad \text{(C.19)}$$

$$R\frac{dC_Q}{dr} = R\frac{dQ}{dr}\frac{1}{\frac{1}{2}\rho U_0^2\pi R^3} = 2\lambda^2\sigma\left(\frac{r}{R}\right)^4\frac{(1+a')^2}{\cos^2\phi}C_t \quad \text{(C.20)}$$

or

The *local* thrust and torque coefficients defined for each annular section of surface $2\pi r dr$ are found to be:

$$C_{T_r} = \frac{dT}{\frac{1}{2}\rho U_0^2 2\pi r dr} = \frac{(1-a)^2\sigma}{\sin^2\phi}C_n \quad \text{(C.21)}$$

$$C_{Q_r} = \frac{dQ}{\frac{1}{2}\rho U_0^2 r 2\pi r dr} = \frac{(1-a)^2\sigma}{\sin^2\phi}C_t \quad \text{(C.22)}$$

or

$$\frac{C_{Q_r}}{C_{T_r}} = \frac{C_n}{C_t} \quad \text{(C.23)}$$

Simplifications using the two links Simplifying Eqs. (C.13) and (C.14) leads to:

$$\frac{a}{1-a} = \frac{1}{4F\sin^2\phi}\frac{cB}{2\pi r}C_n \qquad = \frac{\sigma}{4F\sin^2\phi}C_n \quad \text{(C.24)}$$

$$\frac{a'}{1+a'} = \frac{1}{4F\sin\phi\cos\phi}\frac{cB}{2\pi r}C_t = \frac{\sigma}{4F\sin\phi\cos\phi}C_t \quad \text{(C.25)}$$

[2]There are indeed many variation possible due to the different relations between the parameters. These forms are developed here for an easy comparison with literature

or in a different form (for comparison with e.g. [64])

$$\frac{1}{1-a} = 1 + \frac{\sigma}{4F}\frac{1}{\tan^2\phi}\frac{C_n}{\cos^2\phi} \tag{C.26}$$

$$\frac{1}{1+a'} = 1 - \frac{\sigma}{4F}\frac{1}{\tan^2\phi}\frac{C_t}{\cos^2\phi} \tag{C.27}$$

which solves to:

$$a = \frac{1}{\dfrac{4F\sin^2\phi}{\sigma C_n} + 1} \tag{C.28}$$

$$a' = \frac{1}{\dfrac{4F\sin\phi\cos\phi}{\sigma C_t} - 1} \tag{C.29}$$

Equations without drag In the calculation of induction factors, a and a', it is argued by some authors that C_d should be set equal to zero(see discussion in Sect. 1.3.4, and e.g.[117, 23]). With $C_l = 0$, Eq. (C.24) and Eq. (C.25) reduces to

$$\frac{a}{1-a} = \frac{\sigma\cos\phi}{4F\sin^2\phi}C_l \tag{C.30}$$

$$\frac{a'}{1+a'} = \frac{\sigma}{4F\cos\phi}C_l \tag{C.31}$$

Then Eq. (C.28) and Eq. (C.29) writes:

$$a = \frac{1}{\dfrac{4F\sin^2\phi}{\sigma C_l\cos\phi} + 1} \tag{C.32}$$

$$a' = \frac{1}{\dfrac{4F\cos\phi}{\sigma C_l} - 1} \tag{C.33}$$

Using the two above equations with the first linkage equation and after some algebra an expression can be obtained for the lift coefficient:

$$C_l = \frac{4\sin\phi}{\sigma}\frac{\cos\phi - \lambda_r\sin\phi}{\sin\phi + \lambda_r\cos\phi} \tag{C.34}$$

It can be noted that in the case where the drag is omitted, then then the ratio to the two loading coefficients Eq. (C.23) reduces to a simple function of ϕ:

$$\frac{C_{Q_r}}{C_{T_r}} = \tan\phi \tag{C.35}$$

Also, the ratio of Eq. (C.30) and (C.31) leads to:

$$\tan\phi = \frac{\lambda_r a'}{a} \tag{C.36}$$

which recalls equation Eq. (C.2). Hence when the drag is ignored, the energy equation is satisfied and so is the condition of orthogonality between the induced velocity and the relative velocity.

Note on other conventions Several conventions are found in the old literature for the thrust and torque coefficients. For propellers, due to the large rotational speeds, the velocity taken as a reference is ΩR. In propellers aerodynamics the advance ratio $J = U_0/n_{\text{rot}}D$ plays the equivalent role of the tip-speed ratio. The two are related with: $J = \pi/\lambda$. In[64] the thrust and torque coefficients k_T and k_Q are defined as:

$$T = k_T \cdot \rho n_{\text{rot}}^2 D^4 = k_T \cdot 4\rho \frac{\Omega^2}{\pi^2} R^4 \qquad \Leftrightarrow \qquad C_T = k_T \cdot \frac{8}{\pi^3}\lambda^2 \tag{C.37}$$

$$Q = k_Q \cdot \rho n_{\text{rot}}^2 D^5 = k_Q \cdot 8\rho \frac{\Omega^2}{\pi^2} R^5 \qquad \Leftrightarrow \qquad C_Q = k_Q \cdot \frac{16}{\pi^3}\lambda^2 \tag{C.38}$$

$$P = k_P \cdot \rho n_{\text{rot}}^3 D^5 = k_P \cdot 4\rho \frac{\Omega^3}{\pi^3} R^5 \qquad \Leftrightarrow \qquad C_P = k_p \cdot \frac{8}{\pi^3}\lambda^3 \tag{C.39}$$

In [35], the thrust and torque coefficients are defined as:

$$T = T_c \cdot \rho\pi\Omega^2 R^4 \qquad \Leftrightarrow \qquad C_T = T_c \cdot 2\lambda^2 \tag{C.40}$$

$$Q = Q_c \cdot \rho\pi\Omega^2 R^5 \qquad \Leftrightarrow \qquad C_Q = Q_c \cdot 2\lambda^2 \tag{C.41}$$

Summary of BEM algorithm

Assumptions C.1:

(H C.1a) - The forces of the B blade elements are responsible for the change of momentum of the air which passes through the annulus swept by the elements

(H C.1b) - No aerodynamic interaction between the flow stripes

(H C.1c) - Uniform circulation around the blades (a uniform)

(H C.1d) - Homogeneous, incompressible, steady state fluid flow

(H C.1e) - No frictional drag

(H C.1f) - Infinite number of blades

(H C.1g) - Uniform thrust over the rotor area

(H C.1h) - The static pressure far upstream and downstream is equal to the undisturbed ambient static pressure

A justification on how (HC.1c) can be relaxed can be found in [70, p 63]. This relaxation is primordial to justify the common use of the BEM method.

Dependency Using a and a' as main parameters the following dependencies are observed between the different variables of the BEM code:

$$\text{Parameter at iteration } n+1 = f(\text{Parameters at iteration } n)$$

$$\phi = f(a, a') \tag{C.42}$$

$$\alpha = f(\phi) = f(a, a') \tag{C.43}$$

$$C_n = f(\alpha, \phi) = f(a, a') \tag{C.44}$$

$$C_t = f(\alpha, \phi) = f(a, a') \tag{C.45}$$

$$F = f(\phi) = f(a, a') \tag{C.46}$$

$$a = f(F, \phi, C_n) = f(a, a') \tag{C.47}$$

$$a' = f(F, \phi, C_t) = f(a, a') \tag{C.48}$$

All parameters, including a and a' are dependent of a and a', so that the BEM code is by nature an iterative process

The BEM process is the following for a given geometry and a given tip speed raio:

1. Initial guesses for a and a'
2. Calculation of the flow angle ϕ with Eq. (C.3).
3. Calculation of the angle of attack α from $\alpha = \phi - \beta$
4. Calculation of C_l and C_d from the data
5. Projection of the lift and drag coefficients:

$$C_n = C_l \cos\phi + C_d \sin\phi \tag{C.49}$$
$$C_t = C_l \sin\phi - C_d \cos\phi \tag{C.50}$$

6. Calculation of new values of a and a'(Eq. (C.28) and (C.29)):

$$a_{n+1} = \left.\frac{1}{\frac{4F\sin^2\phi}{\sigma C_n} + 1}\right|_n \tag{C.51}$$

7. Go back to step 2 till convergence of the algorithm

Reproducing the BEM process for different tip speed ratio will allow the plotting of $C_p - \lambda$ or $C_p - WS$ curves characteristic for the studied rotor.

C.2 Common corrections to the BEM method

Discrete number of blades - tip losses

Correction for discrete number of blades are the topic of this document.

Correcting due to the momentum theory break down

The 1D momentum theory with wake rotation assumes no or small expansion of the wake, assumption which fails for large values of the axial induction factor when the rotor is said to be in the turbulent wake state. Moreover, looking at the equation $U_w = U_0(1-2a)$ from 1D momentum theory, it is seen that the momentum theory breaks down for values of a above 0.5 because it would give negative velocity in the far wake.Also, comparison with measurement shows that the BEM code is not in agreement with real rotor flow when the axial induction factor a is over a critical value a_c usually taken around 0.4 which would correspond to a velocity at the rotor equal to 60% the free stream velocity. When operating at high winds induction factors up to 1 are observed, therefore an empirical relation should be found to correct the thrust from the momentum theory for $a > a_c$. These corrections are commonly expressed in terms of the *local* thrust coefficient but they can obviously be written in term of elementary thrust dT as well. The link between the two is recalled here to avoid any confusion between the *local* thrust coefficient C_{T_r} and the *total* thrust coefficient C_T :

$$C_{T_r} = \frac{dT}{\frac{1}{2}\rho U_0^2 2\pi r dr} \tag{C.52}$$

Different corrections close are described below: Glauert's and the Spera's correction. It should be noted that these corrections apply above a certain critical value a_c. Below this value, the momentum theory is assumed to be valid, and Eq. (C.28) is used to compute the axial induction factor. For the physical modelling of the problem, the correction will have to ensure continuity and continuity of the derivative at this critical point. A graphical comparison of the different corrections is found on Fig. C.3.

It should be kept in mind that these corrections are empirical relation. For most practical designs the axial induction factor never exceeds 0.6 and for well-designed blade, it will be in the vicinity of 0.33 for most of its operational range[70].

Glauert's correction

The following correction introduced by Glauert uses a third order polynomial between $a = a_c = 1/3$ and $a = 1$ so that the thrust coefficient at $a = 1$ equals 2:

$$C_{T_r} = 4aF\left(1 - f_G a\right) = \begin{cases} 4aF\left(1-a\right) & \text{when } a \leq \frac{1}{3} \quad \text{i.e. } f_G = 1 \\ 4aF\left(1 - \frac{1}{4}(5-3a)a\right) & \text{when } a > \frac{1}{3} \quad \text{i.e. } f_G = \frac{1}{4}(5-3a) \end{cases} \tag{C.53}$$

In practice, if $a > 1/3$ this relation is inverted using the expression of the local thrust coefficient from the BET (Eq. (C.21)) to obtain a as:

$$a = \text{Root of}\left[-K + a(1+4F+2K) - a^2(5F+K) + 3Fa^3\right] \in \left[\frac{1}{3}\ ;\ 1\right] \tag{C.54}$$

with the following constant defined for simplification:

$$K = \frac{\sigma C_n}{\sin^2\phi}$$

The three complex roots of this polynomial can be obtained analytically, but their expressions are long and won't be written here. Using the analytical solutions also raises the problem of choice between the three real/complex roots. On modern computer solving this equation numerically is not be a problem.

Spera's correction

Spera's correction consists in using a straight line that would be tangent to the momentum theory thrust parabola at the critical point a_c. The slope of this line is thus:

$$\left.\frac{dC_{T_r,\text{parabola}}}{da}\right|_{a=a_c} = 4F(1-2a_c) \tag{C.55}$$

Using as a parameter C_{T_1}, the maximum thrust value at $a = 1$, the equation of the line tangent to the parabola at a_c is:

$$C_{T_r,\text{linear}} = C_{T_1} - 4F(1-2a_c)(1-a) \tag{C.56}$$

For a given value of C_{T_1} the intersection* point a_c is found as:

$$a_c = 1 - \frac{1}{2}\sqrt{\frac{C_{T_1}}{F}} \tag{C.57}$$

So eventually the tangent equation is:

$$C_{T_r,\text{linear}} = C_{T_1} - 4F(\sqrt{\frac{C_T}{F}} - 1)(1-a) \tag{C.58}$$

Spera's correction uses the tangent's equation after the point a_c:

$$C_{T_r} = \begin{cases} 4aF\left(1-a\right) & \text{when } a \leq 1-\frac{1}{2}\sqrt{\frac{C_{T_1}}{F}} \\ C_{T_1} - 4F(\sqrt{\frac{C_T}{F}}-1)(1-a) & \text{when } a > 1-\frac{1}{2}\sqrt{\frac{C_{T_1}}{F}} \end{cases} \tag{C.59}$$

The above formulation used C_{T_1} as a parameter, but it is also possible to use a_c as a parameter which would lead to the following equivalent formulation:

$$C_{T_r} = 4aF\left(1-f_S a\right) = \begin{cases} 4aF\left(1-a\right) & \text{when } a \leq a_c & \text{i.e. } f_S = 1 \\ 4F\left(a_c^2 + (1-2a_c)a\right) & \text{when } a > a_c & \text{i.e. } f_S = \frac{a_c}{a}\left(2-\frac{a_c}{a}\right) \end{cases} \tag{C.60}$$

The value used by is $a_c = 0.2$, but this value will be argued in a following paragraph where the different corrections are compared. Using Eq. (C.57) the correspondence between C_{T_1} and a_c is shown on Tab. C.1 for some typical values. As it was done for Glauert's correction, if $a > a_c$ Eq. (C.60) is inverted using the local thrust coefficient from the BET (Eq. (C.21)) giving:

$$a = \frac{1}{2}\left[2 + K(1-2a_c) - \sqrt{(K(1-2a_c)+2)^2 + 4(Ka_c^2-1)}\right] \tag{C.61}$$

where the following variable has been defined for simplification:

$$K = \frac{4F\sin^2\phi}{\sigma C_n}$$

Table C.1: Maximum thrust coefficient and transitional value for the axial induction factor in the context of Spera's correction

a_c	C_{T_1}	Note/Reference
0.2	2.56	Wilson and walker 1984 Spera 1994 [42]
0.29	2	Glauert's corrections
0.33	1.816	Fit to Glauert's experiment[70]
0.37	1.6	Wilson et Lissaman 1974 [117]
0.46	1.17	Flat disc Hoerner 1965

Glauert's empirical correction

Another empirical correction found in Manwell et al[70] and attributed to Glauert can be used as follow:

$$C_T = \begin{cases} aF\left(1-a\right) & \text{when } a \leq 0.4 \\ \frac{(aF-0.143)^2 - 0.0203 + 0.6427\times 0.889}{0.6427} = 0.96 + \frac{F(a-0.4)[F(a+0.4)-0.286]}{0.6427} & \text{when } a > 0.4 \end{cases} \tag{C.62}$$

Expression which is inverted for $a > 0.4$ as:

$$a = \frac{1}{F}\left[0.143 + \sqrt{0.0203 - 0.6427\left(0.889 - C_{T_r}\right)}\right] \tag{C.63}$$

Comparison of the different corrections

The different corrections are plotted on Fig. C.3.

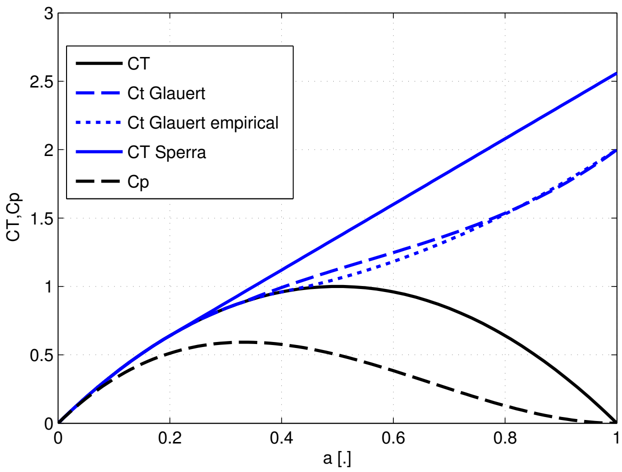

Figure C.3: Power and Thrust coefficients for different high-loading correction models.

General flow conditions

In reality, it is not likely that the flow will arrive perpendicularly to the rotor due to: horizontal and vertical wind shear, turbulence, yaw misalignment, blade coning and relative motion of the blades due to deflection. The only case that can be handled is the coning of the blades(see e.g. [118]) because all the other cases imply an axial induction factor which varies radially and azimuthally. Nevertheless, the different flow conditions mentioned above can be handled by proper geometric transformations and models. With a steady BEM code, sector-wise computations are performed and then averaged, while unsteady BEM codes uses the wind conditions at the current blade position for the computation of loads.

Appendix D

Supplementary notes and results regarding CFD

D.1 Notes on the Post-processing of CFD data

The following reference the basic equations that were used for post-processing of CFD data.

The total force applied on an obstacle is:

$$\boldsymbol{F} = -\iint_S p\boldsymbol{n}\,dS + \iint_S (\underline{\underline{\boldsymbol{\tau}}} \cdot \boldsymbol{n})\,dS \tag{D.1}$$

where p and τ are respectively the static pressure and the viscous shear stress tensor of the flow on the obstacle surface S. The wall shear stress is given by:

$$\tau_w = \mu \left(\frac{\partial u}{\partial y}\right)_{y=0} \tag{D.2}$$

with u the velocity parallel to the wall and y the distance to the wall. The drag force is the component parallel to the upstream velocity, and the drag the force perpendicular to it:

$$\boldsymbol{F_d} = \boldsymbol{F} \cdot \frac{\boldsymbol{U_\infty}}{\|\boldsymbol{U_\infty}\|} \tag{D.3}$$

The skin friction coefficient is defined as

$$C_f = \frac{\tau_w}{\frac{1}{2}\rho U_\infty^2} \tag{D.4}$$

An approximate formulation for flat plate with $5 \cdot 10^5 Re_x < 10^7$ is:

$$C_f = 0.0576 Re_x^{-1/5} \tag{D.5}$$

The pressure coefficient is defined as:

$$C_p = \frac{p - p_\infty}{\frac{1}{2}\rho U_\infty^2} \tag{D.6}$$

It typically takes negative values of the suction sides and positive values at the pressure side. In the free stream, $C_p = 0$, and at a stagnation point the pressure is maximum and the pressure coefficient is 1.

The normal aerodynamic coefficient can be computed from the pressure distribution as:

$$C_n = \int_{\mathrm{LE}}^{\mathrm{TE}} \left(C_{p,\mathrm{sup}}(x) - C_{p,\mathrm{inf}}(x)\right)\, d\frac{x}{c} \tag{D.7}$$

The integration of the frictional coefficient was also performed but had insignificant contribution to the lift as expected. The contribution of the frictional coefficient on the drag has a large influence, but only small investigations were done on this subject. This method of integration was used to compare with the values obtained with the post-processor and double check the determination of the angle of attack. This steps also allowed a clearer exportation of C_p data. After this step, values from the post-processors were directly used. An example of integration of the C_p coefficient is displayed on Fig. D.1.

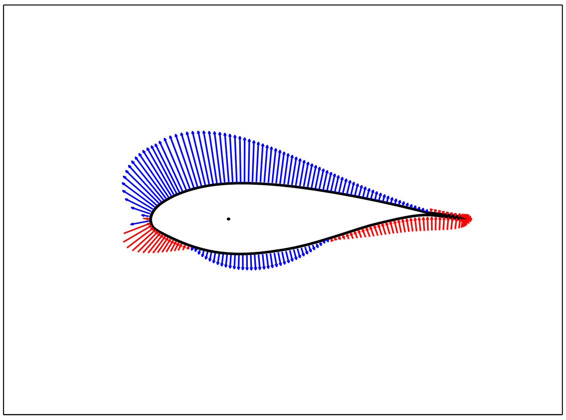

(a) $r/R = 50\%$

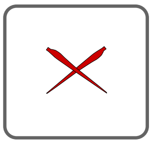

Confidential content removed

(b) $r/R = 70\%$

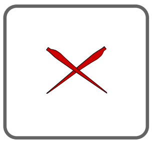

Confidential content removed

(c) $r/R = 80\%$

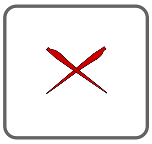

Confidential content removed

(d) $r/R = 90\%$

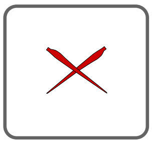

Confidential content removed

(e) $r/R = 95\%$

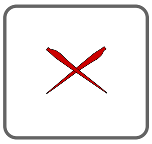

Confidential content removed

(f) $r/R = 98\%$

Figure D.1: Post-processing of CFD data - Integration of C_p at different radial positions. The scaling factor for the elementary forces is the same for all plots. The intensity of the vectors is function of the C_p but also the grid size which is not linear. The airfoil shape has been modified for the position 50%.

D.2 Aerodynamic Coefficients for Blade 1

Comparisons of 2D versus 3D polar for different thicknesses(i.e.) locations on the blades, are found on Fig. D.2 and Fig. D.3 for Blade 1.

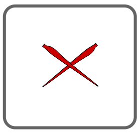

Confidential content removed

(a)

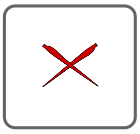

Confidential content removed

(b)

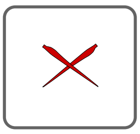

Confidential content removed

(c)

Figure D.2: Comparison of 2D and 3D polars for Blade 1 at different thicknesses

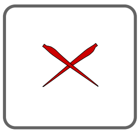

Confidential content removed

(a)

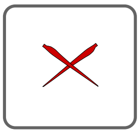

Confidential content removed

(b)

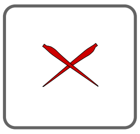

Confidential content removed

(c)

Figure D.3: Comparison of 2D and 3D polars for Blade 1 at different thicknesses

D.3 Aerodynamic Coefficients for Blade 2

Comparisons of 2D versus 3D polar for different thicknesses(i.e.) locations on the blades, are found on Fig. D.4 and Fig. D.5 for Blade 2.

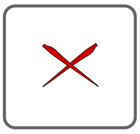

Confidential content removed

(a)

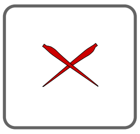

Confidential content removed

(b)

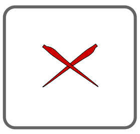

Confidential content removed

(c)

Figure D.4: Comparison of 2D and 3D polars for Blade 2 at different thicknesses

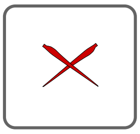

Confidential content removed

(a)

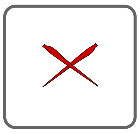

Confidential content removed

(b)

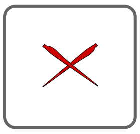

Confidential content removed

(c)

Figure D.5: Comparison of 2D and 3D polars for Blade 2 at different thicknesses

D.4 CFD visualization of tip-vortex formation

The formation of the tip-vortex and its propagation is illustrated on Fig. D.7 and Fig. D.6 for a medium speed configuration.

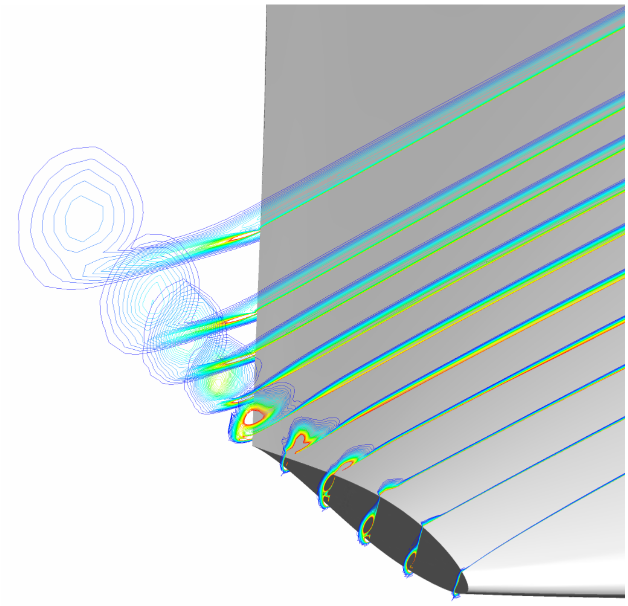

Figure D.6: Vorticity at the tip and formation of the tip-vortex. Figure realized with Ansys. Scales and dimensions are voluntarily hidden. Property of Siemens, reproduction forbidden.

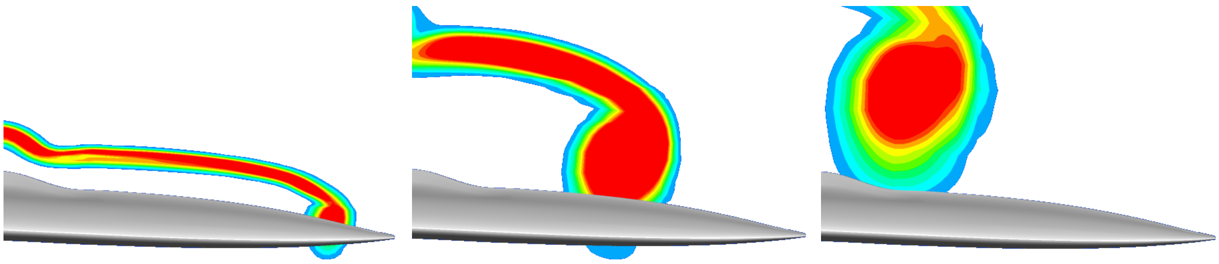

(a) (b) (c)

Figure D.7: Vorticity behind the blades. (a) 1m - (b) 3m - (c) 5m. Figure realized with Ansys.Scales and dimensions are voluntarily hidden. Property of Siemens, reproduction forbidden.

Appendix E

German abstracts

Few german abstracts of the original article from Betz and Prandtl[9] are presented here as they have been used for the understanding of this article. Such abstracts don't exists in a numerical form.

> Die Ergebnisse dieser Betrachtung, die ebenso wie die Betz'sche Theorie nur für den Grenzfall sehr schwach belasteter Schrauben streng gültig sing, lassen sich auf stark belastete Schrauben erweitern, wenn man, wie Herr Betz in einer anderen noch zu veröffentlichenden Untersuchung gezeigt hat, in den obigen Formeln für "v" und "r w' die genauen Werte der Strömungsgeschwindigkeiten relativ zu den Flügelprofilen "v+wa" und "rw-wt" setzt, wobei unter "v" die Zuflussgeschwindigkeit im Unendlichen vor der Schraube und unter "wa" und "wt" die zusätzlichen Geschwindigkeitskomponenten weit hinter der Schraube verstanden werden. Eine brauchbare Näherung für mässig belastete Schrauben erhält man übrigens schon dadurch, dass in den obigen Formeln "v" durch "v+w/2" ersetzt wird, wobei die einfache Vorstellung von in die Luft geschnittenen Schraubenflächen, die sonst hinfällig wird, beibehalten werden kann. Von dieser letzteren Näherung ist in Formel 8 Gebrauch gemacht.
>
> Diese Radialgeschwindigkeiten klingen aber, wenn die Schraubenflächen hinreichend dicht stehen, nach dem Innern zu sehr rasch ab, so dass es hier ausreicht, die tangentiale Komponente "wt" und die axiale Komponente "wa" der Luftbewegung zu betrachten. Die Bewegung, die bei dem Stoss erzeugt wird, erfolgt im Innern, wie leicht zu stehen, normal zu den Schraubenflächen, mittelst derer der Stoss auf die Flüssigkeit ausgeübt wird. Ist "v" die Geschwindigkeit, mit der die luftschraube gegen die Luft fortschreibet, "w" deren Winkelgeschwindigkeit, dann ist die Steigung der Schraubenflächen "H=vT", wo "T=2pi/ww" die Umlaufszeit ist.
>
> [...] Für due Randzone gilt die folgende Sonderbetrachtung. Es sei "a" der senkrechte Abstand von zwei benachbarten Randkurven der Schraubenflächen. An die Stelle der Umströmung der Ränder der Schraubenflächen mag nun die Umströmung der Ränder eines äquidistanten Ebenensystems vom Abstand "a", gemäss fig2, gesetz werden, um den Abfall der Zirkulation an der Flügelspitzen zu studieren [...]
>
> Mit "a" nach Gleichung (4), in der ebenfalls gemäss der Anmerkung "v" durch "v+w/2" ersetzt werden kann. Die Gleichung gilt um so genauer, je mehr Schraubenflügel vorhan-

den sind, es ist aber zu erwarten, dass sie auch bei wenigen, ja selbst bei zwei Flügeln, immer noch brauchbare Resultate ergibt.

Appendix F

Source Codes

F.1 C code for vortex code

Confidential content removed

Confidential content removed

Confidential content removed

Confidential content removed

List of Figures

List of Tables

Index